



*Structuring pea*  
TOWARDS  
*meat analogues*



FLOOR K.G. SCHREUDERS

## *Propositions*

1. Thorough insight in meat analogues requires even more thorough insight of meat as a reference.  
(this thesis)
2. Proper understanding of industrial processes can only be achieved by measuring at actual processing conditions.  
(this thesis)
3. Additional insight in food product heterogeneity can be obtained by considering the deviations from average values as source of information.
4. The more attention is given to the design of a graph, the simpler it looks to the reader.
5. Heterogeneity is appreciated when eating foods but not when studying it.
6. Joint scientific activities during corona times energize young scientists.
7. “Gezelligheid” is the Dutch secret for achieving productivity in a workplace.

Propositions belonging to the thesis, entitled

*Structuring pea towards meat analogues*

Floor K.G. Schreuders

Wageningen, 26 November 2021

# *Structuring pea towards meat analogues*

Floor K.G. Schreuders

*Thesis committee*

*Promotors*

Prof. Dr A.J. van der Goot

Personal chair at Food Process Engineering

Wageningen University & Research

Prof. Dr R.M. Boom

Professor of Food Process Engineering

Wageningen University & Research

*Other members*

Prof. Dr E. van der Linden, Wageningen University & Research

Prof. Dr M. Corredig, Aarhus University, Denmark

Dr G. Della-valle, INRAE, Nantes, France

Prof. Dr J.P.M van Duynhoven, Unilever, Wageningen University & Research

This research was conducted under the auspices of the Graduate School VLAG

(Advanced studies in Food Technology, Agrobiotechnology, Nutrition and Health Sciences)



# *Structuring pea towards meat analogues*

Floor K.G. Schreuders

## **Thesis**

submitted in fulfilment of the requirements for the degree of doctor

at Wageningen University

by the authority of the Rector Magnificus,

Prof. Dr A.P.J. Mol,

in the presence of the

Thesis Committee appointed by the Academic Board

to be defended in public

on Friday 26 November, 2021

at 1:30 p.m. in the Aula.

Floor K.G. Schreuders

*Structuring pea towards meat analogues*

286 pages

PhD thesis, Wageningen University, Wageningen, the Netherlands (2021)

With references, with summaries in English and Dutch

ISBN: 978-94-6395-886-8

DOI: <https://doi.org/10.18174/549711>

# *Content*

<i>Chapter 1</i>	Introduction and thesis outline	1
<i>Chapter 2</i>	Comparing structuring potential of pea and soy protein with gluten for meat analogue preparation	13
<i>Chapter 3</i>	Water redistribution determined by Time Domain NMR explains rheological properties of dense fibrous protein blends at high temperature	33
<i>Chapter 4</i>	Small and large oscillatory shear properties of concentrated proteins	59
<i>Chapter 5</i>	Mapping the texture of plant protein blends for meat analogues	87
<i>Chapter 6</i>	Structure formation and non-linear rheology of blends of plant proteins with pectin and cellulose	111
<i>Chapter 7</i>	Non-linear rheology reveals the importance of elasticity in meat and meat analogues	143
<i>Chapter 8</i>	Texture methods for evaluating meat and meat analogue structures	167
<i>Chapter 9</i>	Near infrared spectroscopy and chemometrics for non-destructive quantification of fats in dense protein mixes	195
<i>Chapter 10</i>	General discussion	211
<i>References</i>		229
<i>Summary &amp; Samenvatting</i>		261
<i>Appendices</i>		271



# *Chapter 1*

*Introduction and thesis outline*

## 1.1 *Pea as ingredient for meat analogues*

For a sustainable supply of food for the growing world population, a shift is needed from animal-based foods towards plant-based foods. A reduced meat consumption and at least partial transition to plant-based proteins may lead to a lower environmental footprint of human diets (Tilman & Clark, 2014; Weinrich, 2019). Traditional plant-based protein alternatives have been widely available on the market for decades. Many of those products are based on soy (e.g., tofu and tempeh) or wheat gluten (e.g., seitan) (Figure 1.1). However, consumers have not transitioned largely towards these products yet, which suggests that these products do not completely cover their needs and expectations. Therefore, a lot of activity in the development of novel plant-based products is with special focus on meat analogues that mimic meat in all its sensory aspects. High resemblance to meat is considered an important enabler for consumers to migrate towards plant-based protein foods (Michel et al., 2021).

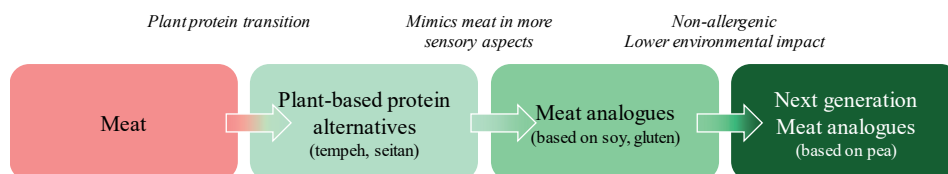


Figure 1.1. Plant protein transition towards the next generation meat analogues.

Proteins used for meat analogues are mostly derived from dairy, soy and wheat, because those proteins can be processed into products having texture, appearance and functionality similar to meat. Despite the clear advantages of using proteins from wheat and soy, they also have some disadvantages. Both wheat gluten and soy protein are allergens. Estimates suggest that around 3-6% and 0.4% of the population has a gluten sensitivity or soy protein allergy, respectively (Leonard & Vasagar, 2014; Sicherer et al., 2000; Thrane et al., 2017). A further disadvantage of soy is that it cannot generally be grown in temperate zones, such as Europe, which connects its use to deforestation, for example in Brazil (Harvey & Phillips, 2020).

Pea protein is an emerging alternative to soy protein due to its good functionality, low potential for allergens, and the ability of pea to grow readily in temperate climate zones (Bashi et al., 2019; Lam et al., 2018; Stone et al., 2015). There are indications that it can be transformed into a fibrous structure using high moisture extrusion cooking at high temperatures (Osen et al., 2014) (Figure 1.2), which makes it an interesting raw material for further investigation.

## 1.2 *Formation of fibrous structures*

Meat analogues are often defined as plant-based products that mimic the sensorial properties of meat as much as possible. An ideal meat analogue 1) has a fibrous structure similar to that of meat, 2) has a juicy mouthfeel during mastication, and 3) possesses a meat-like flavour (Elzerman et al., 2013, 2015; Hoek et al., 2011; Weinrich, 2019). The structure of meat is characterized by muscle tissue structure that consists of myofibrillar protein and myoglobin. Those proteins are positioned in a unique spatial layout, creating textural characteristics. Naturally, globular plant proteins are not fibrillar in nature and therefore structuring processes are required for imposing this fibrillar structure (Fuhrmeister & Meuser, 2003; Sun & Arntfield, 2010; Taherian et al., 2011).

Different approaches to structure plant proteins have been developed. These techniques can be divided into two strategies of approach: bottom-up and top-down, as described by Dekkers, Boom, et al. (2018a). For the bottom-up strategy, each structural component is first created and then combined to into a complete product. Examples of such techniques are tissue engineering (cultured meat) using biological self-assembly, fermentation (mycoproteins) using the mycelia as structural element, wet spinning and electrospinning. For the top-down strategy, a fibrous product is created at once through the use of processes that structure protein blends. Though the bottom-up methods can create structures that are much closer to that of meat potentially, scaling of these methods towards industrial production capacity is not trivial. Besides, waste streams generation is significant in many cases (Warner, 2019). The top-down methods are more robust, better scalable and have better resource efficiency. Examples of those processes are freeze structuring, mixing (proteins and hydrocolloids), extrusion and shear cell technology.

Extrusion cooking is widely used for the production of meat analogues. However, for extrusion cooking, quantitative understanding of the structuring mechanism is difficult to achieve due to the complexity of the process, with many different physical and chemical phenomena impacting the structure and other product attributes simultaneously. This makes translation of this process towards new proteins complicated. A related technology is the so-called shear cell, which can employ similar conditions, but can also simplify the conditions by imposing just plain shear flow and independent control of the temperature. These shear cells were originally meant to mimic and better understand extrusion-relevant conditions by using only well-defined flow (van den Eijnde et al., 2004, 2005). However, it was found that

calcium caseinate could be transformed into hierarchically fibrous materials at relatively mild conditions in a shear cell (Figure 1.2) (Manski et al., 2007). Later, these insights were translated to plant-based ingredients. Blends of soy protein isolate (SPI)-wheat gluten (WG) and SPI/pectin could be transformed into fibrous product in a shear cell by heating the blend at 95 and 140°C while shearing for 15 min, respectively (Dekkers, Nikiforidis, et al., 2016; Grabowska et al., 2014).

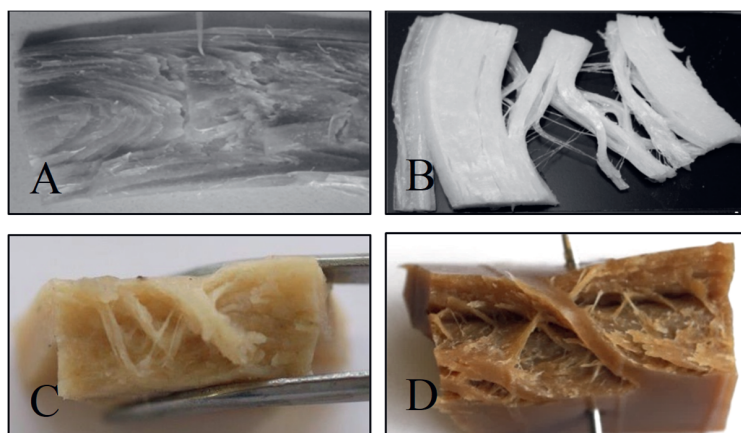


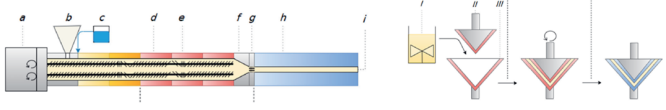
Figure 1.2. Macrostructure from A) high moisture extruded pea protein isolate (This article was published in *Journal of Food Engineering*, 127, Osen, R., Toelstede, S., Wild, F., Eisner, P. and Schweiggert-Weisz, U., High moisture extrusion cooking of pea protein isolates: Raw material characteristics, extruder responses, and texture properties, 64-74, Copyright Elsevier (2021)), B) shear-induced structuring of calcium caseinate, C) soy protein isolate-wheat gluten blends, D) soy protein isolate-pectin blends.

Recently, the similarities and differences between extrusion and shear cell technology were described in depth. Both high-moisture extrusion cooking (HMEC) and shear cell processing are thermo-mechanical processes (Table 1.1) and are comparable in their basic operations: 1) mixing and hydration, 2) thermo-mechanical treatment, and 3) cooling (Cornet et al., 2021). A main difference is that HMEC is a continuous process, while a shear cell is only described as a batch process so far. Other differences lie in the residence time and the necessity for cooling. The residence time of the material during HMEC is shorter than in a shear cell, while in HMEC the conditions in the extruder and in the cooling die are different. Those differences also imply that the structure formation process may be different. In case of extrusion, the fibrous product may be formed in the cooling zone (Akdogan, 1999; Cheftel et al., 1992; Sandoval Murillo et al., 2019; Tolstoguzov, 1993), while cooling seems less essential in a shear cell.



For both processes, similar plant protein blends can be used. With HMEC, the screening of plant protein formulations and process conditions to create fibrous structures is still predominantly based on trial-and-error based experiments. Greater insight into the fibrous structure formation of plant protein during and after thermomechanical processing would improve understanding and development of meat analogues.

Table 1.1. Comparison of HMEC (high moisture extrusion cooking) and shear cell technology.

	HMEC	Shear cell
		
Basic operational units	Mixing and hydration step Thermo-mechanical treatment Cooling step	Mixing (*external) and hydration step Thermo-mechanical treatment Cooling step
Temperature	100-175°C	95-140°C
Pressure	10-60 bar	5 bar
Residence time	2-5 min	~20 min
Shear rates	1-45 s <sup>-1</sup> (in cooling die)	39 s <sup>-1</sup> (during heating)

### 1.3 Characterization of texturization

Up to now, the exact structural and textural characteristics of meat analogues are difficult to fully quantify. The structure and texture characteristics of meat have been widely studied, but dedicated methods used to analyse meat analogues are still limited (McClements et al., 2021). Instrumental techniques to measure the texture of meat and meat analogues are often used, while descriptive (trained panel) and affective (consumer) sensory trials then help to reveal the texture and flavor characteristics and perception relevant for consumption with the goal to determine the similarities between meat analogues and meat. However, sensory experiments are expensive, time-consuming, difficult to make fully quantitative and not trivial to translate back towards modifications in processing.

Therefore, instrumental techniques are widely used, as these provide more objective information on different structural parameters, which can then be more easily translated towards changes in process or formulation. In addition, these techniques give the opportunity to better understand the underlying mechanisms that drive structure formation. The macrostructure, microstructure and mechanical properties of the fibrous products is currently analysed with texture analysis, spectroscopy, microscopy and rheology.

The microstructure can be investigated with several methods. Confocal laser scanning microscopy (CLSM) has been used to study the alignment along the shear direction in SPI-WG blends after staining with Rhodamine B. SPI and WG showed fluorescence; the intensity difference in different parts of the samples is used to indicate differences in protein concentration (Dekkers et al., 2018). Dekkers, de Kort, et al. (2016) presented a method to determine the water distribution in SPI-WG blends using Time-Domain Nuclear Magnetic Resonance (TD-NMR) and described consequences for the rheological properties of the blend, which is an important aspect of the microstructure: the (re)distribution of water over the dispersed and the continuous phase co-determines the volume and rheology of the fractions and thus the behaviour during deformation by shearing. In addition, these products tend to also be at least somewhat porous. Air is entrapped in the structure which could be considered as a weak/disperse phase that is deformed in the shear flow direction and enhances the fibrous structures in calcium caseinate (Wang et al., 2018). X-ray tomography (XRT) reveals the porosity in the structure. The microstructural characteristics ultimately give rise to the macrostructure and the macroscopic mechanical properties.

A way to characterise the macroscopic anisotropy in these materials, is to measure the tensile strength parallel and perpendicular to the shear flow direction. However, this does not yet give us sufficient information on how the structural elements interact during processing, and create the macroscopic characteristics. Rheological measurements can provide insight into the behaviour of the materials during their thermomechanical processing. Most conventional rheometers are not capable of operating at the rather extreme conditions during a thermomechanical treatment (i.e. high protein concentrations, high pressures, high temperatures, and high shear rates). Recently, a ‘closed cavity rheometer’ (CCR) developed for investigating properties of rubbers, was used to mimic the process conditions inside a shear cell or even an extruder (Dekkers et al., 2018; Emin & Schuchmann, 2017). Dekkers et al. (2018) created the rheological fingerprint of blends of SPI and WG at processing conditions in a CCR and related this to the formation of fibrous structures in a shear cell. The outcomes of those measurements resulted in the hypothesis that for fibrous structures, the two phases in a blend must have similar rheological properties during processing at high temperatures, to allow for extensive deformation of the dispersed phase, which was hypothesized to yield the fibrous structure.

Traditional rheological analysis is done using small deformations, but these are less relevant for the phenomena that take place during thermomechanical processing, because large-scale deformation is the fundamental principle of both HMEC and the shear cell techniques. This is why, large amplitude oscillatory shear (LAOS) experiments are used in this thesis to describe and understand the behaviour in the non-linear region (Hyun et al., 2011). This allows the investigation of the fundamental microscopic deformations occurring during processing that give rise to the macroscopic anisotropy.

## 1.4 Research aim and thesis outline

The aim of this thesis is to identify the determining properties of the constituents to the microstructures obtained during and after thermomechanical treatment, and to relate those to the macroscopic characteristics of the products created. To do so, pea protein isolate (PPI) and blends of PPI with other components are characterised using non-linear (large deformation) rheological measurements, and compared with more conventional products and materials, such as SPI, but also meat.

This aim can be subdivided into three objectives. Objective I is the investigation of blends containing PPI and selected other biopolymers on their structuring potential using shear cell technology. Objective II is (further) development of analytical tools to study product structure and structure formation with emphasis on rheological analysis of the materials using deformation in both linear and non-linear regimes under relevant conditions, such as high temperature and intensive shear. The results can be presented in compact maps and schemes to help relating the results to the macroscopic properties. The results and methodology of Objective I and II are combined in Objective III, where the focus is on a quantitative comparison of meat, meat analogues and the products made in this project. The rheological benchmarking reveals how closely meat analogues resemble the originals. Besides, it identifies parameters for research to further improve meat analogues, especially when using newer materials, like pea protein.

Figure 1.3 graphically outlines how the objectives are covered in the various thesis chapters.

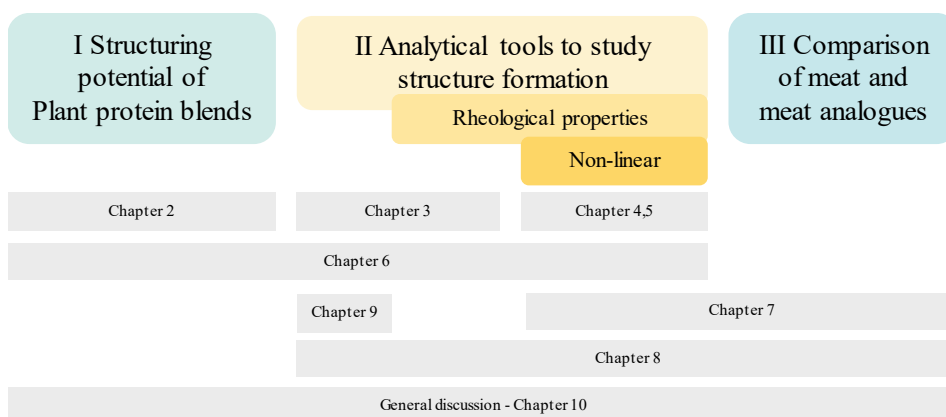


Figure 1.3. Graphical outline of the thesis content and chapter division.

**Chapter 2** explores the structuring potential of blends of PPI-WG and SPI-WG using shear-induced structuring combined with heating. The mechanical properties of the plant protein blends are compared to that of cooked chicken. In **Chapter 3**, insight into the internal structure of the blends is obtained by a combination of Time-Domain Nuclear Magnetic Resonance (TD-NMR) and rheological characterization using the polymer blending law. For this polymer blending law, the prediction of the water distribution of the phases after blending are obtained with TD-NMR. A closed cavity rheometer (CCR) is used to quantify the rheological properties of the separate phases. The polymer blending law is used to combine both outcomes to describe the rheological properties of protein blends. The analysis of the polymer blending is extended by fitting the polymer blending law to the experimental data, which yields insight into the morphology development of the phases in the blend over time and temperature.

A next step in rheological characterisation is the evaluation of the non-linear properties of plant protein blends at high temperatures, and stress and strain. This has not been studied before, thus this is the focus of **Chapter 4**. The large-deformation oscillatory shear properties of concentrated PPI, SPI and WG dispersions are measured before, during and after a thermomechanical treatment. The analysis is done using Lissajous curves and the energy dissipation ratio, which characterizes the plasticity of the materials. The rheological properties are linked to shear-induced microstructures that can be obtained. **Chapter 5** extends these rheological analyses to PPI-WG and SPI-WG blends with different protein ratios and processing conditions. The rheological properties are visualized in a compact way by texture maps and colour schemes to demonstrate the difference between the blends.

In previous chapters, commercial PPI-WG and SPI-WG blends were investigated. While these blends can give fibrous structures, it is of interest to study whether PPI can result in fibrous structures with other ingredients than WG; for example in combination with carbohydrates. **Chapter 6** describes the exploration of the structuring potential of PPI, SPI and blends of these with pectin/and or cellulose. The linear and non-linear rheological properties of the blends are studied with the CCR at structuring conditions to gain insight into the structure formation as well as physical and chemical changes.

In previous chapters, plant protein blends are used to gain insight into shear-induced structuring. These blends contain a high protein content and water only, while commercial meat analogues contain also flavourings, oil or fat, binding agents and colouring agents. Thus

**Chapter 7** describes the rheological properties of various meat and meat analogues before and after heating and mapping those in texture maps and colour schemes. Differences and similarities between meat and meat analogues are described. **Chapter 8** reviews texture methods that are typically used to characterize the structure of meat products and discusses the potential to apply those methods to prepare meat analogues. The need for new methods that characterize specific texture and structure properties that are different than meat is described. **Chapter 9** introduces near-infrared (NIR) and hyperspectral imaging (HSI) to non-destructive and rapidly quantify the composition and the spatial distribution of the blend using chemometric modelling. For this, blends of PPI, water and oil are used to mimic meat analogues.

**Chapter 10** reflects on the findings of all previous chapters. The main findings are summarized and new insights in structuring protein blends are presented. The developments made in characterization methods are critically discussed. Suggestions for future development on meat analogues are provided.







# *Chapter 2*

*Comparing structuring potential of pea and soy protein  
with gluten for meat analogue preparation*

*This chapter has been published as* Schreuders, F. K. G., Dekkers, B. L., Bodnár, I., Erni, P., Boom, R. M., & van der Goot, A. J. (2019). Comparing structuring potential of pea and soy protein with gluten for meat analogue preparation. *Journal of Food Engineering*, 261, 32-39.

## 2.1 *Abstract*

Pea protein isolate (PPI) can be combined with wheat gluten (WG) into materials with a fibrous morphology using shear-induced structuring combined with heating. Results are partly in-line with soy protein isolate (SPI)-WG blends, but the latter yields anisotropic materials in a much broader temperature range. Both blends also have the ability to include air. Air bubbles were aligned and deformed at process conditions that gave the most pronounced fibrous products. Mechanically, the PPI-WG materials processed at 140°C had a similar strength as SPI-WG blends. At 110 and 120°C, the PPI-WG blends had a strength that was comparable to a chicken meat reference (50-100 kPa) but weaker than their counterparts with SPI-WG (220-300 kPa). Blends of PPI-WG show potential for preparing structured plant protein materials, but the application area might be different compared with potential applications of SPI-WG blends.

## 2.2 Introduction

The awareness of our overexploitation of natural resources has given rise to a quest for plant-based protein foods that mimic the fibrous texture of meat (Elzerman et al., 2015; Hoek et al., 2011). These foods can be created from plant-based proteins by extrusion cooking, by solidifying proteins with a mixture of hydrocolloids and divalent cations, or by using the newly emerging shear cell technology (Cheftel et al., 1992; Grabowska et al., 2014; Osen et al., 2014). This latter technique was used previously for studying structure formation processes with soy protein isolate (SPI) and wheat gluten (WG) (Grabowska et al., 2014) and later extended to SPI/pectin blends and soy protein concentrate (Grabowska et al., 2016). Recently it was found that air held up in the materials influences the mechanical anisotropy of these materials (Dekkers et al., 2018; Dekkers, Nikiforidis, et al., 2016).

Currently, mostly soy proteins are used to mimic animal proteins because of their favorable gelling properties and the resulting creation of an interlaced, fibrous matrix (Banerjee & Bhattacharya, 2012; Day & Swanson, 2013). SPI combined with WG or pectin could be used to create a range of fibrous structures. This structure formation was based on the fact that the biopolymers formed two separate phases of which the rheological properties are dependent on the moisture content, the ratio between the different biopolymers and on the processing conditions (Grabowska et al., 2014, 2016). For a fibrous structure, the two phases should have a sufficiently high viscosity to allow deformation and alignment upon shearing, and structure entrapment during cooling.

Pea proteins are increasingly used as an alternative for soy protein since the pea plants may be grown in more moderate climates than soy. In addition, pea proteins are less connected to GMO questions, and are not listed as allergenic (Lam et al., 2018). Structuring of pea protein however remains a challenge because it has a much lower gelling capacity than soy protein (Bildstein et al., 2008). In addition, heat induced gels of SPI are stronger than heat induced gels of pea protein isolate (PPI) (Hsu, 1982; O’Kane et al., 2005; Shand et al., 2007; Sosulski et al., 1976). Only a few studies reported success in structuring pea protein isolates with low moisture extrusion (Beck et al., 2017; Wang et al., 1999) and high moisture extrusion (Osen et al., 2014). In this study, it was decided to include WG next to PPI and SPI in the blend, since the WG network can contribute to the viscosity, elasticity and strength (Ng & McKinley, 2008; Pietsch et al., 2016). WG acts as structurant in these blends and renders anisotropy due to elongation of the domains according (Grabowska et al., 2014).

Here, we report on the morphologies obtained by blending PPI and WG relative to those obtained with SPI and WG. We postulate that the use of WG with PPI may result in solidified protein materials by heating, which may become anisotropic when they are sheared concurrently. However the exact processing conditions will have to be adjusted to the different type of materials. We expect that the inclusion of air will play a similar role for structure formation as found earlier with SPI/pectin.

## 2.3 *Materials and methods*

### 2.3.1 *Materials*

Pea protein isolate (PPI) (NUTRALYS® F85G) and vital wheat gluten (WG) (VITENS® CWS) were both obtained from Roquette Frères S.A., (Lestrem, France). Soy protein isolate (SPI) (SUPRO® EX 37 IP) was obtained from Solae (St. Louis, MO, USA). PPI was composed of 78.6 wt.% protein (N x 5.7), WG was composed of 72.4 wt.% protein (N x 5.7), SPI was composed of 80.0 wt.% protein (N x 5.7) (Breese Jones, 1931) on a dry basis, according to Dumas measurements. The manufacturer's specification indicated that the PPI contained 1% dietary fiber, 9% lipids, 4% ash. The manufacturer's specification indicated that the SPI contained ≤1% lipids, ≤5% ash. PPI, SPI and WG had an average dry matter content of 93.2 wt.%, 92.8 wt.%, and 92.3 wt.%, respectively. Sodium chloride and Rhodamine B were both obtained from Sigma-Aldrich Co., LLC. (Zwijndrecht, the Netherlands). The mechanical properties of the processed SPI-WG and PPI-WG mixture were compared to chicken fillet as a reference more specifically the breast of a chicken (Jumbo, Wageningen, The Netherlands), composed of 74.7 wt.% water, 23.6 wt.% protein, 1.6 wt.% fat and 0.1 wt.% salt.

### 2.3.2 *Protein mixtures*

Two protein mixtures (SPI-WG and PPI-WG) were prepared with at 40 wt.% concentration. The SPI-WG and PPI-WG mixtures were prepared with a combination of 19.5 wt.% protein isolate (SPI or PPI), 19.5 wt.% WG, 1 wt.% sodium chloride and 60 wt.% demineralized water. Firstly, the sodium chloride was dissolved in distilled water. Then SPI or PPI was added and mixed with a spatula. The protein mixture was hydrated with the saline solution for 30 min. After hydration, WG was mixed with a spatula to the protein mixture and added directly before processing.

### 2.3.3 *High-temperature and shear-induced structure formation of protein mixtures*

A high-temperature conical shear cell (HTSC) (Wageningen University, the Netherlands), which was developed in house (Grabowska et al., 2016), was used to process the SPI-WG and PPI-WG mixtures. The HTSC is a cone-in-cone device, of which the bottom cone rotates. The cavity between the two cones is closed, preventing escape of steam during heating. The protein mixtures were processed in the pre-heated shear cell of different processing

temperatures (95-140°C) at 39 s<sup>-1</sup> (controlled by a Haake PolyLab QC drive, Germany). After 15 min constant shearing and heating, the HTSC was cooled down to 25°C within 5 min. The products were left at room temperature in a closed plastic bag for at least one hour before further measurements were performed. Each product was prepared and analysed three times independently.

#### 2.3.4 *Chicken*

Chicken fillet was used as a reference for the mechanical properties to the SPI-WG and PPI-WG products. First, the fillet was vacuum sealed in a plastic bag and frozen overnight. Then it was partly defrosted to facilitate cutting parallel and perpendicular to the fibers to a specimen of approximately 7 mm thick, 7 mm width, 45 mm length. Each specimen was again vacuum sealed in a plastic bag and heated in a water bath at 65°C for 20 minutes. The heated chicken had an average dry matter content of 28.6%. Mechanical measurements were conducted with the samples at room temperature.

#### 2.3.5 *Confocal laser scanning microscopy*

The morphologies of the SPI-WG and PPI-WG products were visualized with a confocal laser scanning microscope (CLSM). Samples of the SPI-WG and PPI-WG materials were cut into samples with dimensions 3 by 8 by 10 mm and rapidly frozen with liquid nitrogen. A cryo-microtome (Micron CR50-H, ADAMAS-instruments Corp., Rhenen, The Netherlands) was used to create slices with approximately 40 µm thickness at a temperature of -20°C. A solution of 0.2 mg/mL Rhodamine B was used to stain the specimens (Sigma-Aldrich Chemie GmbH, Steinheim, Germany). A Confocal Laser Scanning Microscope type 510 (Zeiss AG, Oberkochen, Germany) using a 543 nm HeNe laser with a 405 nm Blue/Violet diode laser was used with a 20x EC Plan-Neofluar/0.5.A lens. The images were analysed with the software ZEN, the blue edition (Carl Zeiss Microscopy).

#### 2.3.6 *X-ray microtomography*

An X-ray microtomographer, GE Phoenix v|tome|x m (General Electric Go., Wunstorf, Germany), was used to study the inclusion of air in the SPI-WG and PPI-WG products. A 240 kV microfocus tube with tungsten target was employed. X-rays were produced with a voltage of 80 kV and a current of 90 mA. The images were recorded by a GE DXR detector array with 2,024 x 2,024 pixels (pixel size 200 µm). The detector was located 815 mm from the X-ray source. A sample was cut to a dimension of 3 by 4 by 20 mm and placed in a closed

Eppendorf tube to avoid moisture loss. The sample was placed 28.55 mm from the X-ray source, which resulted in a spatial resolution of 7.00  $\mu\text{m}$ . The sample was placed on a rotary stage to allow a full scan consisting of 1,500 projections over 360°, with a step ratio of 0.24°. The first image was skipped. The saved projection was the average of three images where every image is obtained over 250 ms exposure time. GE image reconstruction software (Wunstorf, Germany) was used to calculate the 3D structure via back projection. The 3D images, obtained using the v|tome|x XRT, were analysed using Avizo imaging software version 9.4.0. The measurements were performed in duplicate.

### 2.3.7 Tensile strength analysis

Tensile strength analyses were performed with a Texture Analyzer (Instron Corp. 5564, USA) using a static load cell of 100 N. A uniaxial tensile test was performed at room temperature with a displacement rate of 1 mm/s. Tensile bars were taken from the materials with a dog bone-shaped mold in two directions: *i*) parallel, and *ii*) perpendicular to the direction of shearing. The bone-shaped mold was used to cut the samples, the dimensions (thickness and width) of the cut sample varied. Therefore, the dimensions were measured and accounted for in the tensile strength determination. The ends of the tensile bars were placed into the two clamps such that 15.5 mm was the initial length of the sample. The results obtained from these tensile test analyses were depicted as force-displacement curves. The true stress ( $\sigma, \text{Pa}$ ) and fracture strain ( $\epsilon, -$ ) were defined as

$$\epsilon_h = \ln \frac{h(t)}{h_0} \quad [-] \quad 2.1$$

$$A(t) = \frac{h_0}{h(t)} \cdot A_0 \quad [\text{m}^2] \quad 2.2$$

$$\sigma(t) = \frac{F(t)}{A(t)} \quad [\text{Pa}] \quad 2.3$$

Where  $h_0$  is defined as the length of the sample of the tensile bar (15.5 mm),  $h(t)$  defined as the length all time  $t$ ,  $A(t)$  is defined as the contact surface area  $A$  of the tensile bar all time  $t$ ,  $A_0$  is the initial contact surface area of the tensile bar and  $F(t)$  is the force per unit of area  $A(t)$ . It was assumed that the volume of the tensile bar did not change during stretching and the shape was retained. The point following a dramatically decrease in stress in the stress-strain curve was taken as the fracture point. Young's modulus was calculated from the slope

of the tensile stress-strain curve of the first 1.5 mm. For the SPI-WG and PPI-WG products, three samples were prepared per condition. For every sample, three parallel and three perpendicular specimens were taken. Therefore, in total nine parallel and nine perpendicular specimens per conditions were tested. The results of the three specimens for every sample were averaged and the standard deviations were determined based on the variation between the average values of those three samples. For the chicken, three different chicken breasts were tested, and four parallel and four perpendicular samples (chicken strips) were taken. In total 12 parallel and 12 perpendicular chicken strips were tested. The four chicken strips were averaged and the standard deviations were determined based on the variation between the three samples.

#### 2.3.8 *Statistics*

The experiments were performed in duplicate unless stated otherwise. Duncan's test was performed to evaluate the statistical significance between samples at a significant level of 95% ( $P < 0.05$ ) analysed using SPSS statistics Version 25.0 (IBM, Armonk, NY).



## 2.4 Results and discussion

The morphologies of sheared and heated mixtures of pea protein-gluten were explored and compared with the morphology obtained from mixtures of soy protein-gluten.

### 2.4.1 Macrostructure

First, the morphologies of sheared and heated mixtures of pea protein isolate (PPI) and wheat gluten (WG) processed at different temperatures were analysed by manually deforming the samples and then visually inspecting the fibrousness (Figure 2.1). It was observed the soy protein isolate (SPI)-WG blends yielded stronger and more fibrous materials than the PPI-WG blends for most process conditions. The PPI-WG blends were often darker in colour than the SPI-WG blends.

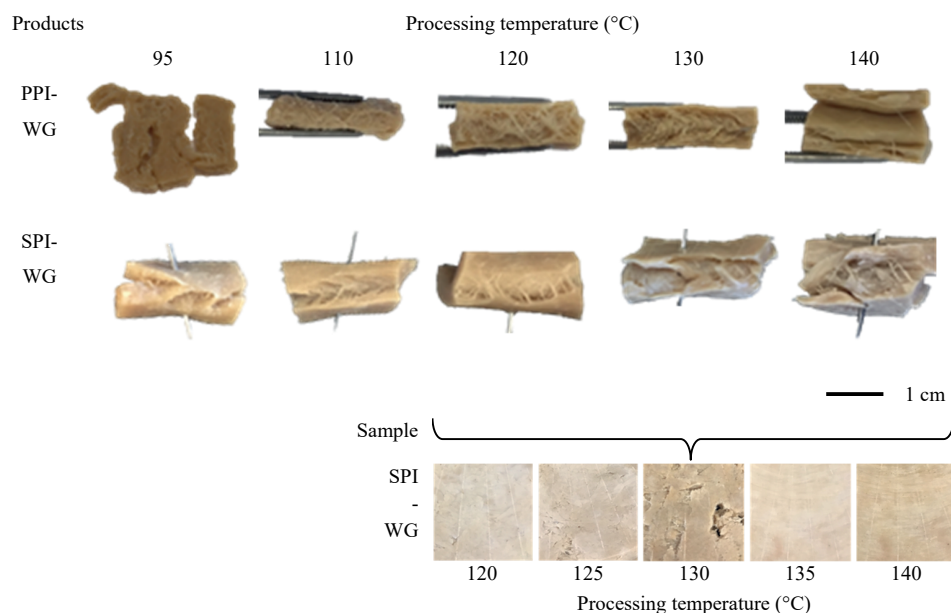


Figure 2.1. Visual observation of shear-induced structuring (15 min,  $39\text{ s}^{-1}$ ) of pea protein isolate (PPI)-wheat gluten (WG) blends and soy protein isolate (SPI)-WG blends at different temperatures, which were deformed manually. The surfaces of the SPI-WG products were depicting at a specific temperature range (120-140°C), demonstrating holes at 130°C.

The processing temperature was much more critical for the PPI-WG blend than for the SPI-WG blend. The PPI-WG blend gave a fragile and weak product when processed at 95°C. At higher temperature, 110°C resulted in a weak gel with small fibers, while a fibrous product was obtained at 120°C. A brittle product was formed upon processing at 130°C, and a layered product at 140°C. Shearing of the SPI-WG blends yielded a distinct fibrous morphology at

all temperatures, even though shearing at 130°C resulted in a more brittle product, in which we observed larger holes (Figure 2.1).

### 2.4.2 Microstructure

The shape and orientation of protein domains in the direction of the shear flow was examined with CLSM. The effect of shearing on those domains was revealed by comparing a sheared and a non-sheared PPI-WG product heated at 120°C (Figure 2.2). Previous studies (Dekkers et al., 2018; Peters et al., 2017) showed that WG typically takes up much less water than SPI. Given the similar water holding properties of PPI, we may therefore assume that WG also absorbs less water than PPI in PPI-WG blends (Peters et al., 2017). After staining with Rhodamine B, both the SPI/PPI and WG showed fluorescence. The WG phase is expected to exhibit higher fluorescence intensity due to its higher protein concentration. Indeed, we observe high intensity red domains in the non-sheared PPI-WG blend. After shearing the PPI-WG blend at 120°C, those high-intensity domains were aligned in the shear flow direction. The latter observation coincides with the fibrous product observed visually.

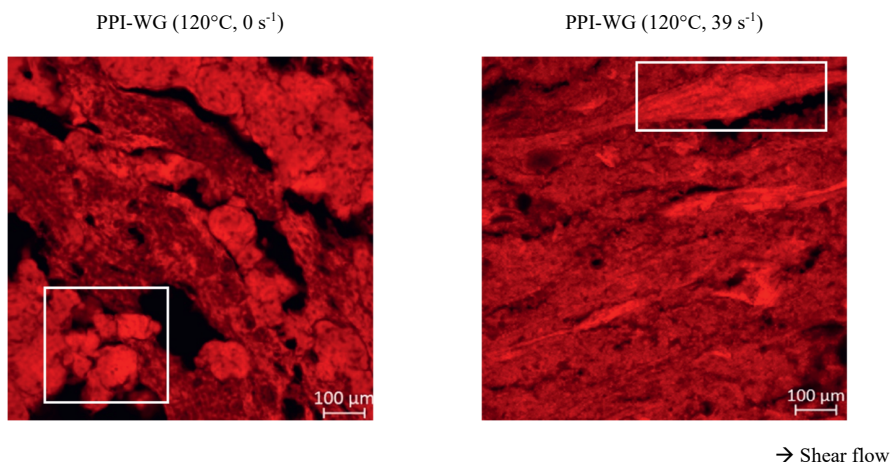


Figure 2.2. CLSM images of the fluorescence channel of the 40 wt.% PPI-WG (50/50 by weight) product at 120°C at 0 and 39 s<sup>-1</sup> stained with Rhodamine B. High-intensity red - WG. Low-intensity red - PPI.

Shearing may deform and orient the dispersed domains in the materials, but the extent of the effect depended on process temperature. CLSM images of the PPI-WG and SPI-WG product at several processing temperatures are shown in Figure 2.3. As a reference, we also measured non-heated and sheared PPI-WG and SPI-WG blends that showed no alignment of protein domains. Shear-induced structuring at 120 and 140°C for SPI-WG mixtures and at 120°C for PPI-WG mixture resulted in elongated protein domains along the direction of the shear flow,

which as appeared as aligned fibers in the product. However, shearing at other processing temperatures gave no alignment of the protein domains; instead these proteins domains (both in PPI-WG and SPI-WG blends) were randomly oriented after processing at 95, 110 and 130°C. At higher processing temperatures (e.g. at 140°C for PPI-WG), the PPI and WG domains became less evident. Hardly any differences in intensities could be observed anymore. A possible explanation is that the PPI and WG become more compatible or associate due to interactions between both phases while shearing.

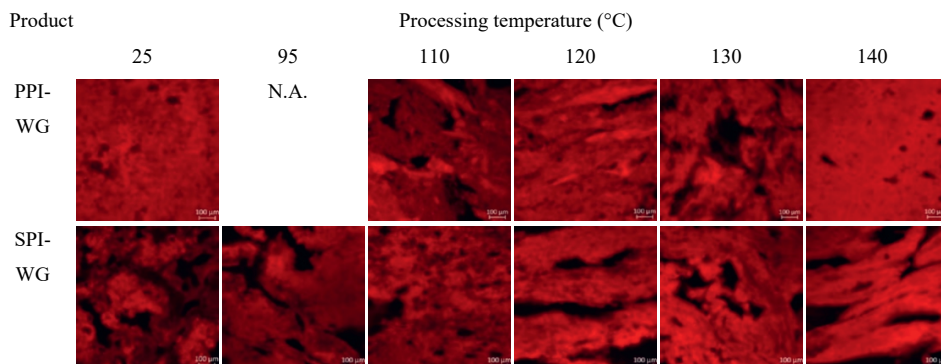


Figure 2.3. CLSM images of the fluorescence channel of the 40 wt.% SPI-WG (50/50 by weight) and PPI-WG (50/50 by weight) product at 25, 95, 110, 120, 130 and 140°C at 39 s<sup>-1</sup> stained with Rhodamine B. High-intensity red - WG. Low-intensity red - SPI/PPI. N.A. - not available.

### 2.4.3 Entrapment of air

Previous research revealed the importance of air inclusion in those dense protein blend used for making fibrous materials. X-ray microtomography (XRT) was therefore used to quantify the air void fraction in the protein blends.

The reconstructed 3D X-ray tomography image showed that almost all blends contained air to a certain extent, and the exact amount depended on the processing temperature (Figure 2.4). The reconstructed 3D images of both blends are used for the quantification of the voids fraction as well as the void geometry in the blends after processing (Figure 2.5). As a reference, we also measure non-heated and sheared SPI-WG and PPI-WG blends (25°C, 40 wt.%, 50/50 by weight, at 39 s<sup>-1</sup>), yielded a void fraction of 6 to 11 vol.%. In case of PPI, the shearing process resulted in a decrease of air inclusion. The SPI-WG was able to keep air inside up to a process temperature of 120°C. Nevertheless, the heating temperature was found to be an important parameter in both the PPI-WG and SPI-WG products, and a higher temperature during shearing resulted in a reduced void fraction of air (Figure 2.4 and Figure

2.5). The use of a temperature of 110°C gave a void fraction of 6 to 7 vol.%, while processing at 140°C led to an air fraction of only 0.2 to 0.1 vol.%, meaning that processing at 140°C did leave hardly any air in the product. The coalescence of air bubbles to larger bubbles and even holes is observed, which is probably the first step in air escaping at higher processing temperature.

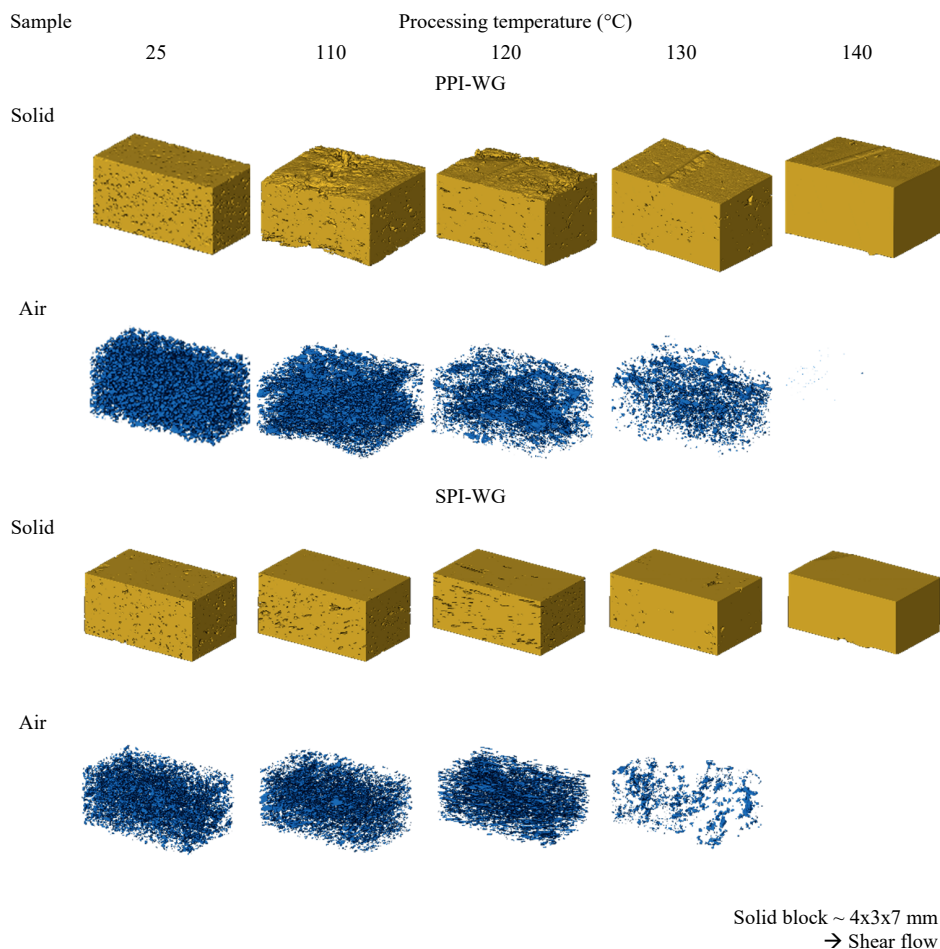


Figure 2.4. X-ray microtomography images of a reconstructed trimetric image of the solid (in yellow) of SPI-WG and PPI-WG products at 25, 110, 120, 130 and 140°C (where a structure without large fractures and holes was chosen and the small line on top was formed by the curves of the cone in the shear cell and a smaller reconstructed trimetric image was shown for 25°C since the weak products gave difficulties during cutting) and a reconstructed trimetric image of the air (in blue) in SPI-WG and PPI-WG products at 25, 110, 120, 130 and 140°C.

The SPI-WG blends specifically show extensive deformation of the air bubbles when sheared and heated at 120 to 140°C; we do not see this with the PPI-WG blends, which does not show any significantly different deformation of the air bubbles (Figure 2.5). Deformation of air bubbles shows this with the average ratio of the longest ( $l$ ) over the shortest ( $w$ ) dimension of the bubbles.

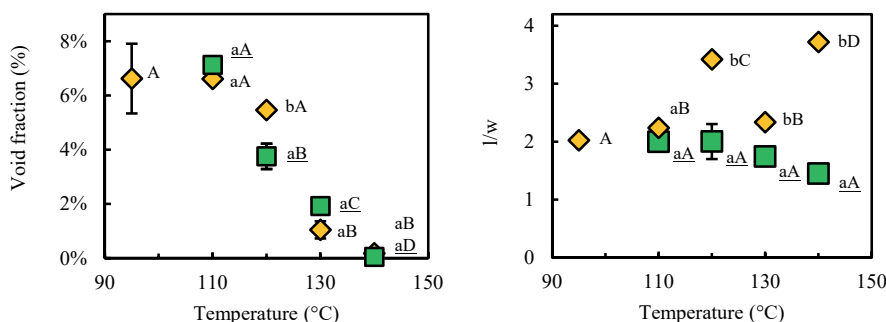


Figure 2.5. X-ray microtomography analysis of air cavities when heating the SPI-WG (♦) and PPI-WG (■) products at 110, 120, 130 and 140°C: void fraction, deformation of the air cavities ( $l/w$  = length of the deformed air cavities in the shear flow direction (defined as  $l$ ) and the diameter of the deformed air cavity in the velocity gradient direction (defined as  $w$ )). Please note: Means with the same lower-case letter within a column (sample) were not significantly different ( $p < 0.05$ ). Means with the same capital letter within a row (temperature) were not significantly different ( $p < 0.05$ ). The underlined letters are related to PPI-WG and the others to SPI-WG.

#### 2.4.4 Mechanical properties

On microscale, we observed alignment of the protein domains and air bubbles in the direction of the shear flow for the SPI-WG blend when sheared at 120 and 140°C, and for PPI-WG when sheared at 120°C. It is expected that this structure will influence the macroscopic mechanical properties. Therefore, the resulting materials were subjected to a tensile strength analysis parallel and perpendicular to the direction of shearing during processing. The ratio between the tensile strengths (stress and strain) parallel and perpendicular to the direction of shearing was used as a measure for the anisotropy of the product. Figure 2.6 shows the Young's modulus, the tensile stress and tensile strain of the SPI-WG and PPI-WG materials sheared at different temperatures in parallel and perpendicular direction to the shear flow. As a reference fibrous product, a cooked piece of chicken was taken.

As Figure 2.6 shows, the Young's modulus of the SPI-WG blend increased after processing at 95°C (statistical analysis in Appendix Table A 2.1). It was observed that the Young's modulus was hardly affected by the shearing temperature, except for a brief, but reproducible decrease at 130°C. In addition, it is found that Young's moduli were hardly different when measured in both directions. The tensile stress at 120 and 140°C shows stronger anisotropy. The SPI-WG blends exhibit an increasing tensile stress (parallel to direction to shear flow) after 95°C and a similar tensile stress and strain value irrespective of the shearing temperature employed, and once more show a lower value at 130°C.

The Young's modulus for PPI-WG blends increased with increasing temperature. A decrease at 130°C can also be seen in the tensile strain (parallel to the direction of shear flow). The PPI-WG blends also show increasing tensile stress- and strain values at a shearing temperature of 140°C, indicative of the gradual solidification of the PPI-WG blend at higher temperatures. At high shearing temperatures (i.e. 140°C) the PPI-WG products showed similar strength to the SPI-WG products, except for the tensile stress perpendicular to the shear flow direction

Young's modulus (parallel to the shear flow direction) of the chicken strips was comparable to the values of the SPI-WG blend at 110°C and to the values of PPI-WG blend at 120, 130, 140°C. Young's modulus (perpendicular to the shear flow direction) of the chicken strips was comparable to the values of PPI-WG blend at 110°C, and therefore lower than those for the SPI-WG and PPI-WG blends measured at the other processing temperatures. The anisotropy in Young's moduli was limited in all materials, except the chicken meat. Comparison to the chicken shows that especially the stress of the SPI-WG products at 110 and 120°C is higher than the chicken, while the PPI-WG products are in the same range.

We therefore hypothesize that the PPI gel forms a weaker phase during processing as well compared with the SPI gel, which could impact the deformation and alignment of the protein domains in the direction of the shear. Our earlier observation (Figure 2.5) that deformed air bubbles can be retained in their anisotropic state in the SPI-WG system, but not in the weaker PPI-WG system, appears to support this hypothesis. A low viscous PPI phase is less capable of retaining the air bubbles.

The lower values for Young's modulus and in the tensile stress and strain at 130°C is remarkable. While the decrease is mostly visible for SPI-WG products, it can also be seen in

the tensile strain for PPI-WG products. We speculate that this effect is caused by two effects. We expect that shearing gluten at higher temperatures will lead to collapse and disintegration of the gluten network (Emin & Schuchmann, 2017). This will lead to a decrease in the strength of the material and a more brittle appearance (Figure 2.1). At the same time, the increased temperature will also decrease the viscosity of both SPI and PPI. A lower viscosity leads to faster coalescence and possible escape of the air bubbles. At 130°C, we observe clearly the effect of coalescence leading big air holes that act a defect during tensile tests. At 130°C, the effect of those effects are more dominant than matrix properties.

A second observation is that the SPI-WG blends exhibit anisotropy irrespective of the shearing temperature, while for PPI-WG, this is only observed when shearing at 120°C. We attribute this to the similarity in the viscoelastic behaviour of SPI and WG when present in a blend after equilibrium of the moisture distribution over the two phases according to water distribution as determined with TD-NMR (Dekkers et al., 2018). The viscosity of WG was expected to be comparable to the viscosity values of SPI. The similarity in viscosities allows the deformation of the WG domains into long fibres, or perhaps even a bicontinuous structure, as may be seen in Figure 2.3. Further study should focus on understanding how the viscoelastic behavior of PPI-WG blend dependency is on temperature. The viscosity of WG was expected to be comparable to the values of SPI, and lower than those for PPI. It is expected that only in the temperature range where the PPI phase has sufficiently solidified, while the WG phase still retains sufficient strength, is there a match between the viscosities that allows strong deformation of the WG domains.

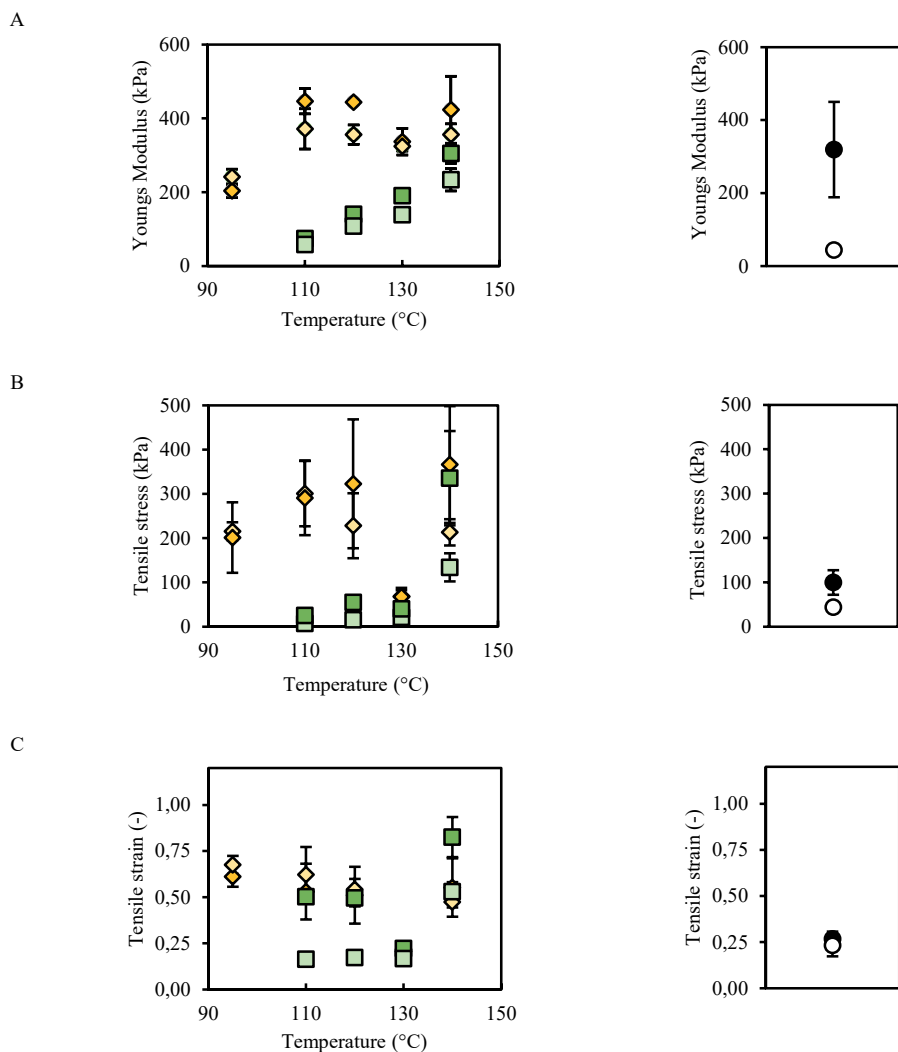


Figure 2.6. A) Young's modulus, B) tensile stress, C) tensile strain of SPI-WG product (♦) and PPI-WG product (■) at different temperatures (15 min, 39 s<sup>-1</sup>) and chicken (●). (parallel (darker color, ♦, ■, ●) and perpendicular direction (lighter color, ◆, □, ○) to the direction of shearing, mean value  $\pm$  absolute deviation). Please note: Statistical analysis in appendix Table A 2.1.



## 2.5 Conclusion

Pea protein isolate (PPI) blended with wheat gluten (WG) resulted in distinct fibrous morphology, when sheared and heated at 120°C. Processing at a lower temperature resulted in a weak product without fibers, while higher temperature gave a strong and layered product. In contrast, soy protein isolate (SPI)-WG blends yield similar fibrous, anisotropic materials at a broader range of shearing temperatures (i.e. 110-140°C). Mechanically, blends with SPI-WG resulted in three times stronger materials than the PPI-WG blends at lower shearing temperatures (i.e. 120°C). At higher shearing temperatures (i.e. 140°C) the SPI-WG and PPI-WG products showed similar strength. There is a distinct decrease in strength in both the SPI-WG and PPI-WG blends, when processed at 130°C.

## 2.6 Appendix

*Table A 2.1. Analysis of significantly differences of the tensile strength in Figure 2.6 of the Young's modulus, tensile stress and tensile strain of pea protein isolate-wheat gluten (PPI-WG) blends, soy protein isolate-wheat gluten (SPI-WG) blends and chicken processed at different temperatures. Please note: Means with the same lower-case letter within a column (sample) were not significantly different ( $p < 0.05$ ). Means with the same capital letter within a row (temperature) were not significantly different ( $p < 0.05$ ).*

	Parallel						Perpendicular					
	Samples	Processing temperature (°C)					Samples	Processing temperature (°C)				
		95	110	120	130	140		95	110	120	130	140
Young's modulus	PPI-WG		aA	aB	aC	aD	PPI-WG		aA	aB	aC	aD
	SPI-WG	A	bB	bB	aC	aB	SPI-WG	A	bB	bB	bC	bB
	Chicken		b	a	a	a	Chicken		a	c	c	c
Tensile stress	Samples	Processing temperature (°C)					Samples	Processing temperature (°C)				
		95	110	120	130	140		95	110	120	130	140
	PPI-WG		aA	aA	aA	aB	PPI-WG		aA	aA	aA	aB
Tensile strain	SPI-WG	A	bB	bB	abA	aB	SPI-WG	A	bA	bA	bB	bA
	Chicken		a	a	b	b	Chicken		a	a	c	c
	Samples	Processing temperature (°C)					Samples	Processing temperature (°C)				
		95	110	120	130	140		95	110	120	130	140
	PPI-WG		aA	aA	aB	aC	PPI-WG		aA	aA	aA	aB
	SPI-WG	B	aB	aB	aA	aB	SPI-WG	A	bA	bAB	aC	aB
	Chicken		b	b	a	b	Chicken		a	a	a	B





# *Chapter 3*

*Water redistribution determined by Time Domain NMR  
explains rheological properties of dense fibrous protein  
blends at high temperature*

*This chapter has been published as Schreuders, F. K. G., Bodnár, I., Erni, P., Boom, R. M., & van der Goot, A. J. (2020). Water redistribution determined by time domain NMR explains rheological properties of dense fibrous protein blends at high temperature. *Food Hydrocolloids*, 101, 105562.*

### 3.1 *Abstract*

Blends of different plant proteins can form excellent basis for meat analogues by subjecting those to shear and heating. We here want to obtain more information of the internal structure of pea protein isolate (PPI)-wheat gluten (WG) and soy protein isolate (SPI)-WG blends, by using the polymer blending law to explain rheological responses. For this polymer blending law the water distribution over the two phases is the blend was obtained with time domain  $^1\text{H}$  NMR measurements using the NMR measurements of individual protein phases and on the blend. By matching the relaxation rate ( $R_2$ ) of the individual phases with those of the blend, the water distribution over the two phases could be obtained. Water is preferentially taken up by SPI or PPI phase leaving less water for WG, which effect strongly changes the volume fractions of the phases. Rheological properties of the separate phases as function of their hydration resulted in higher apparent modulus for the WG phase, and a lower one for the PPI and SPI phase. From the results, it was concluded that both blends show signs of a bi-continuous morphology. The SPI-WG blend showed an intermediate value between bi-continuous and SPI continuous. PPI-WG at lower temperatures showed a bi-continuous structure, while at higher processing temperatures and time was probably WG continuous.

### 3.2 Introduction

Proteins used in meat replacing foods are mostly derived from dairy, soy and wheat gluten. However, because of dietary restrictions, food allergies and vegetarianism alternative protein sources (e.g. pulses) are also being explored (Adebiyi & Aluko, 2011; Akintayo et al., 1998; Betancur-Ancona et al., 2004; Karaca et al., 2011; Sánchez-Vioque et al., 1999; Traina & Breene, 1994). An important requirement for meat analogues is to mimic the fibrous structure of meat. Such structures were successfully created from blends of concentrated solutions of pea protein isolate (PPI)-wheat gluten (WG) and soy protein isolate (SPI)-WG blends (Chapter 2). This was achieved by subjecting the blends to shear at high temperature. These blends basically are water-in-water emulsions, as a result of the thermodynamic incompatibility of the proteins (Tolstoguzov, 1993).

The mechanical properties of these protein products depend on the rheology of the blend during the process. The rheological properties of a blend depend on the distribution of water over the phases and the properties of the polymer in each phase. When the rheological properties of both phase are known, the response of the blend can be described with an empirical polymer blending law (Morris, 1992). This polymer blending law assumes that either the strain is equal over the two phases (isostrain), or that the stress is equal over the two phases (isostress) (Takayanagi et al., 1963) or that the structure would divide over these phases (Davies, 1971). The polymer blending law reads in its general form as:

$$G_{XY}^n = \phi_X G_X^n + \phi_Y G_Y^n \quad 3.1$$

Where  $G_X$ ,  $G_Y$  and  $G_{XY}$  are the moduli of the two polymers  $X$  and  $Y$  and the blended material  $XY$ , and  $\phi_X$  and  $\phi_Y$  are the volume fractions of phase  $X$  and  $Y$ . The value of the parameter  $n$  depends on the spatial distribution of the two components in the blended material and their moduli, with  $n = 1$  for isostrain,  $n = -1$  for isostress, and  $n = 0.2$  for bi-continuous. Blends that obey isostrain behaviour generally consist of a stronger continuous phase and a weaker discontinuous phase. The behaviour of those blends can be described best using  $n = 1$  in a polymer blending law as described above. The continuous and dispersed phases are deformed to the same extent. Blends that obey isostress behaviour generally consist of a weaker continuous phase and a stronger discontinuous phase. The behaviour of those blends can be described best using  $n = -1$  in a polymer blending law as described above. The strength of the weaker phase limits the force that can be transmitted to the stronger phase, implying that

both phases are subjected to the same stress. For products having phases that are both continuous (a bi-continuous product), the overall modulus of products can be related to the moduli of the individual phases ( $G_X$  and  $G_Y$ ). A bi-continuous structure is described by using  $n = 0.2$ . The polymer blending law developed by Davies (1971) for bi-continuous products was initially used to describe the behaviour of composites of condensed materials. Also in biopolymer products, bi-continuous structures are possible. Piculell et al. (1992) first applied the polymer blending law to hydrated biopolymer networks, and found that the experimental moduli of co-gels of a mixture of iota and kappa carrageenan gave good agreement with a prediction for a bi-continuous product.

The rheological properties of blends in which both phases contain water and a biopolymer depend on the distribution of the water in the blend. In case two proteins that do not have the same interaction with water, there will be two phases with different individual protein concentrations. In several studies (Clark et al., 1983; Fitzsimons et al., 2008; Kasapis & Tay, 2009; Shrinivas et al., 2009), the relative amount of water in each polymeric phase is calculated with the “solvent avidity parameter”,  $p$ . This parameter is fitted based on the rheological properties with a polymer blending law. Direct determination of the water distribution by NMR relaxometry was proposed by Clark et al. (1983) to overcome the difficulty of solvent avidity parameter between the polymeric phases. More recent, it was shown that time domain nuclear magnetic resonance (TD-NMR) could be used to quantify the water content in a concentrated protein blend (Dekkers, de Kort, et al., 2016). The proton relaxation rate ( $R_2$ ) was determined for products with different protein concentrations of the individual (protein) component similarly as described by (Peters et al., 2017) as well as the individual (protein) components used in the blend as described by Dekkers, de Kort, et al. (2016). Then, the  $R_2$  of the individual phases were matched with those of the blend to obtain the water distribution over the two phases. Further, Dekkers et al. (2018) measured the rheological properties. Based on the outcome of the TD-NMR measurements and the rheological responses at 95°C, they concluded that two phases of the SPI-WG blend have similar rheological properties under process conditions in the high temperature shear cell (i.e. 95°C, 15 min, 39 s<sup>-1</sup>), which they hypothesized to be a requirement for the creation of a fibrous product (Dekkers et al., 2018). This study applies this procedure to blends of PPI and WG, subjected to higher temperatures (110-140°C). Those temperatures allow formation of fibrous, anisotropic structure when subjected to shearing (Chapter 2).



Here, we study the distribution of water in the PPI-WG blend with TD-NMR and the rheological properties of both the individual components and the PPI-WG blends as function of their hydration at high temperatures. Results are compared with those of SPI-WG blends. A detailed analysis of the rheological properties of the individual biopolymer and biopolymer blends made it possible to fit the exact  $n$ -value of the polymer blending law. The  $n$ -value of the polymer blending law was used to obtain information on the internal structure of the blends. The outcomes were mirrored against products structures formed upon shear structuring (Chapter 2).

### 3.3 *Materials and methods*

#### 3.3.1 *Materials*

Pea protein isolate (PPI) (NUTRALYS® F85G) and vital wheat gluten (WG) (VITENS® CWS) were both obtained from Roquette Frères S.A., (Lestrem, France). Soy protein isolate (SPI) (SUPRO® EX 37 IP) was obtained from Solae (Europe S.A.). PPI was composed of 78.6 wt.% protein (N x 5.7), WG was composed of 72.4 wt.% protein (N x 5.7), SPI was composed of 80.0 wt.% protein (N x 5.7) on a dry basis, according to Dumas measurements. PPI, SPI and WG had an average dry matter content of 93.2 wt.%, 92.8 wt.%, and 92.3 wt.%, respectively. Sodium chloride was obtained from Sigma-Aldrich (Zwijndrecht, the Netherlands).

#### 3.3.2 *Preparation of protein blends*

Protein blends (PPI, SPI, WG, PPI-WG and SPI-WG) were prepared with 20-55 wt.% concentration. For the PPI-WG, blends different ratios of protein were mixed (20/80, 50/50, 80/20). First, 1 wt.% sodium chloride was dissolved in distilled water. Then PPI, SPI or WG was added and mixed with a spatula. The protein blend was then hydrated for 30 min. For the PPI-WG and SPI-WG blends, the WG was mixed with in with a spatula to the hydrated PPI or SPI solution, directly before processing.

#### 3.3.3 *Proteinaceous product*

Products were made with the protein blends (PPI, WG, PPI-WG) with and without applying any shear in a high-temperature conical shear cell or in air-tight cylindrical vials, respectively. A high-temperature conical shear cell (Wageningen University, the Netherlands), developed in house (Grabowska et al., 2016), was used to process the protein blends. This device is a cone-in-cone device, of which the bottom cone rotates. The cavity between the two cones is sealed, preventing escape of steam during heating. The protein blends were processed with a pre-heated shear cell at 95°C at 0 and 39 s<sup>-1</sup> (controlled by a Haake PolyLab QC drive, Germany). After 15 or 7.5 min shearing and heating at constant shear rate (at 0 and 39 s<sup>-1</sup>) and temperature (95°C), the HTSC was cooled down to 25°C within 5 min. Furthermore, gels were made with the protein blends without applying any shear. The proteins blends were placed in air-tight cylindrical vials with a diameter of 25 mm and a height of 4 mm. These cylindrical vials were overfilled, to remove most of the air from the blend. The surplus of the blend could escape from a hole on the top of the vial. After

filling, the hole was sealed before heating. The vials were heated in a water bath at 95°C or an oil bath at 110, 120, 130, 140°C for 15 min. The gels were cooled for 5 min in a cold water bath. The products were left at room temperature in a closed and vacuum sealed plastic bag for at least one hour before further measurements were performed.

### 3.3.4 TD-NMR

The proton relaxation time  $T_2$  of the PPI, WG and PPI-WG products (see Table 3.1 for an overview of the composition and processing conditions of the protein blends used) was determined with TD-NMR according to the method that was described by Dekkers, de Kort, et al. (2016). Components with significantly different  $T_2$  represent populations of protons ( $^1\text{H}$ ) with different rotational mobility, and can therefore be assigned to different classes of proton-bearing moieties in the sample. A sample, taken from the gels or processed blends were placed into 7 mm NMR-tubes. The tubes were closed with a cap to prevent moisture loss. A Maran Ultra NMR spectrometer at a magnetic field at 0.72 T and a  $^1\text{H}$  resonance frequency of 30.7 MHz was used. Data was interpreted using RINMR software (Resonance Instruments Ltd., Witney, UK).  $T_2$  values were measured with a Carr-Purcell-Meiboom-Gill pulse train with 12288 echoes (five data points per echo). The sample time between the data points in each echo was 10  $\mu\text{s}$  resulting in a spectral width of 100 kHz. The time between each echo was 407  $\mu\text{s}$ . In total, 16 transients were recorded with phase cycling resulting in no baseline offset, with a repetition time of 30 s. Each CPMG echo train was averaged to one data point using the IDL package (ITT Visual Information Solutions, Boulder, CO, USA). The experimental error (upper and lower bound) was measured by repeating all experiments four times.

Transverse magnetization decay curves were analysed with the Levenberg-Marquardt non-linear least squares algorithm implemented in SplMod (Vogel, 1988), which fits a sum of exponential curves (“components”)  $\sum_i A_i e^{-t/T_{2,i}}$  to the decay, resulting in an amplitude,  $A$ , and a transverse relaxation time  $T_2$  for each component  $i$ . The inverse of  $T_2$  is the relaxation rate,  $R_2$ . The number of decay components needed to describe the data was estimated from the decrease of the standard deviation when fitting an additional component. For all experiments, we found that the data could be accurately described with four components. Laplace inversion of the data (by CONTIN (Provencher, 1982)) predicts three separate  $T_2$  distributions shown by different authors (Dekkers, de Kort, et al., 2016; Hinrichs et al., 2003,

2007; Peters et al., 2017). The longest relaxation time represents just a small proton population in the sample. This relaxation time is shorter than that of pure water (which is  $\sim 2$  s (Ruan, et al., 1999)), but still suggests presence of relatively mobile water, probably within pores of the fibrous product (Grabowska et al., 2014). The fraction of “free” water is small and negligible above  $\sim 20$  wt.% protein, reflecting the strong water binding capacity of PPI and SPI. The component with the shortest  $T_2$  represents protein-bound protons: its amplitude increases linearly with concentration, which is in line with the idea that it represents the protein-bound proton population. The two middle components in a 4-component fit together were used to describe the large and slightly dispersed middle population. These two middle components were averaged, which represents the vast majority ( $>90\%$ ) of the NMR relaxometry signal intensity and was therefore assigned to “absorbed” water following previous studies (Dekkers, de Kort, et al., 2016; Hinrichs et al., 2003, 2007; Peters et al., 2017). The concentration ( $C_i$ ) dependency of  $R_2$  of “absorbed” water was fitted with a stretched exponential

$$R_2 = A \cdot e^{B \cdot C_i^C} \quad 3.2$$

in which A, B and C were fitting parameters.

### 3.3.5 Prediction of water distribution with TD-NMR

The  $R_2$ -dependency on the dry matter content can be used to predict the water distribution (and phase volume fraction) in the PPI-WG blends, similarly as described by Dekkers, de Kort, et al. (2016) for SPI and WG. A mass balance (explained in Appendix C) was used to calculate all the theoretical possible water redistribution after combining the two phases, given the originally added amount of water. The  $R_2$ -value of the two separated phases at various theoretical water distributions in the blend were calculated. The  $R_2$ -value of the two separated phases were summed (based on their protein concentration) and were compared to the experimentally determined  $R_2$ -value of the PPI-WG blends. The water distribution in the blend was taken at the point where the summed  $R_2$ -values corresponded to the experimentally determined  $R_2$ -value of the PPI-WG blend. Here, it was assumed that PPI and WG form separate phases with only PPI or WG present in each phase, since swollen WG will severely hinder mixing molecular level with another biopolymer due to its densely crosslinked network. Further, both phases do have a high viscosity, which also prevents molecular mixing.

### 3.3.6 Rheological properties

The rheological properties of the PPI, SPI, WG, PPI-WG and SPI-WG blends (see Table 3.1 for an overview of the composition and processing conditions of the protein blends used) were measured at elevated temperature with a closed cavity rheometer (CCR) (RPA elite, TA instruments, New Castle, Delaware, USA) (Emin & Schuchmann, 2017). The PPI-WG and SPI-WG blends were measured at a ratio of 50/50. This ratio resulted a fibrous structure upon shear cell processing (Chapter 2). Approximately 6 g of the hydrated blends was placed between two plastic films in the cavity (disk geometry), which were sealed to each other to allow a pressure of 4.5 bar to prevent water evaporation. The closed cavity rheometer has a radius of 2.25 mm and maximum height of the inner cavity of 4 mm and biconical opening with an angle of  $3.35^\circ$  for homogeneous transmission of the shear stress to the protein blends. The grooves on the surface of the cones prevent slippage. Mechanical treatment is applied through oscillatory movement of the lower cone. Three rheological tests were performed with PPI, WG and PPI-WG blends at a ratio of 50/50. First, an isothermal measurement was performed at a high temperature 110, 120, 130 and  $140^\circ\text{C}$  while applying a shear treatment of 15 min using high strain (80%) and frequency (10 Hz). The response of these materials was studied over longer times under these conditions to mimic the shearing process in the high temperature shear cell. A frequency sweep (10-0.1 Hz, 1% strain) and an amplitude sweep (1 Hz, 0.1-100%) were performed at  $40^\circ\text{C}$  to determine the linear viscoelastic (LVE) regime. Since this test is done outside the LVE regime, the stress response is no longer a single-harmonic sinusoid and therefore we refer to it as an apparent  $G^*$ .

Table 3.1. An overview of the experimental design and the composition and processing conditions of the samples (the underlined numbers are related to the mass fraction determined with TD-NMR).

Method	Gelled	Sheared
TD-NMR (replicate four times)	20-45 wt.% PPI at $95^\circ\text{C}$	40 wt.% PPI at $95^\circ\text{C}$ at $39\text{ s}^{-1}$
	25-55 wt.% WG at $95^\circ\text{C}$	40 wt.% WG at $95^\circ\text{C}$ at $39\text{ s}^{-1}$
	25-40 wt.% PPI-WG (20/80, 50/50, 80/20) at $95^\circ\text{C}$	40 wt.% PPI-WG (50/50) at $95^\circ\text{C}$ at $39\text{ s}^{-1}$
	40 wt.% PPI-WG (50/50) at 25, 110- $140^\circ\text{C}$	
Rheology with CCR (duplicates)		<u>32</u> and 40 wt.% PPI at 110- $140^\circ\text{C}$
		40, <u>48</u> , <u>51</u> wt.% WG at 110- $140^\circ\text{C}$
		40 wt.% PPI-WG (50/50) at 110- $140^\circ\text{C}$
		<u>33</u> , 40 wt.% SPI at 110- $140^\circ\text{C}$ 40 wt.% SPI-WG (50/50) at 110- $140^\circ\text{C}$

### 3.4 Results and discussion

#### 3.4.1 Water distribution with TD-NMR for PPI and WG products

Time domain nuclear magnetic resonance (TD-NMR) results of the single phases and the blends are presented in Figure 3.1. These outcomes of the single phases and the blends are used to predict the water distribution in the blends. For all systems, there was a clear relation between the dry matter content and the relaxation rate ( $R_2 = 1/T_2$ ) of the protons of the absorbed water (Figure 3.1 A). The  $R_2$  of the component increased as function of the dry matter content, reflecting the decreasing mobility of these fractions with increasing dry matter content. Results were in agreement with results of Peters et al. (2017) for pea protein isolate (PPI), soy protein isolate (SPI) and wheat gluten (WG) and Dekkers, de Kort, et al. (2016) for SPI, WG and SPI-WG. It was observed that WG calibration curve of the  $R_2$  versus dry matter content increased more gradually than for SPI and PPI. The differences in isoelectric point of WG (around 7.5) and the other proteins (around 4.5) are hypothesized to be a cause for different responses of  $R_2$  upon dry matter content. However, there is hardly any difference in  $R_2$  for heated PPI-WG products prepared under shear or without shear (Figure 3.1 B), in agreement with the results reported by Dekkers et al. (2018) for SPI-WG (50/50, 20-40 wt.% at 95°C for 15 min).

Figure 3.1 A shows  $R_2$ -values for PPI, WG and PPI-WG as function of the dry matter content. The  $R_2$ -value for PPI was always larger than that for WG at similar dry matter content, but close to  $R_2$ -values for SPI. The measurements therefore suggest a lower mobility of water within the PPI-phase than within the WG-phase at similar dry matter concentration. This result aligns with results obtained with blends of SPI and WG. The  $R_2$  of the PPI-WG blends were in between those of pure PPI and pure WG. Blends with more PPI (i.e. 80/20) have  $R_2$ -values closer to PPI, and blends with more WG (i.e. 20/80) had  $R_2$ -values closer to those of only WG. A similar trend was observed for SPI-WG blends (Dekkers, de Kort, et al., 2016).

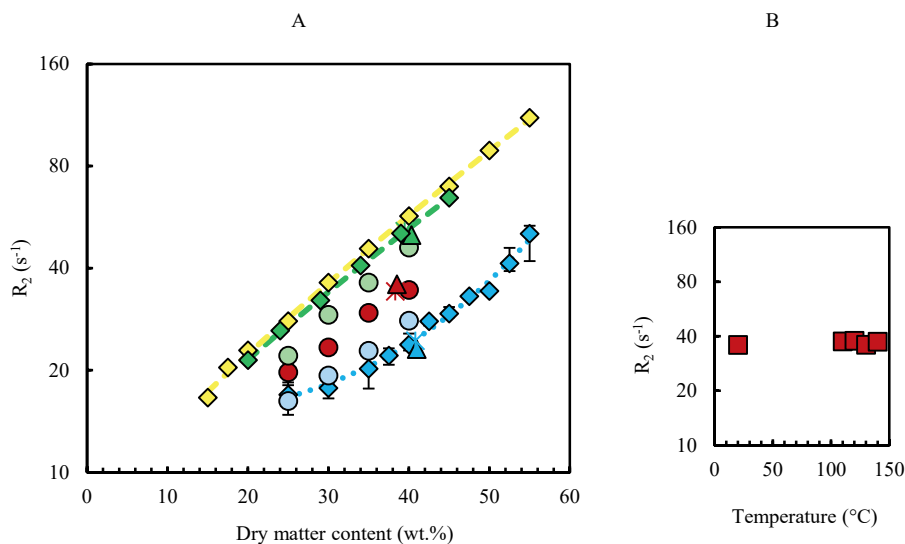


Figure 3.1. Relaxation rate ( $R_2$ ) of A) PPI (♦), SPI (♦), WG (♦) and PPI-WG gels at various ratios: 20/80 (●), 50/50 (●), 80/20 (●) by weight of the PPI-WG blend as function of the dry matter content. The sheared PPI-WG (50/50) (▲), PPI (▲), WG (▲) at 39 s<sup>-1</sup>, and the gelled PPI-WG (50/50) (\*), PPI (\*), WG (\*) at 0 s<sup>-1</sup> in high temperature shear cell. The right hand Figure B) shows the  $R_2$  values for PPI-WG (50/50) as function of the temperature used during processing or gelling.

### 3.4.2 Translation of TD-NMR values into volume fractions

The  $R_2$ -dependency on the dry matter content was used to predict the water distribution and phase volume fractions in the PPI-WG blends similarly as performed earlier for SPI-WG blends by Dekkers, de Kort, et al. (2016). The experimentally determined  $R_2$ -values of the PPI-WG blend at different dry matter contents and ratios are shown in Table 3.2. The table also reports the corresponding concentrations of PPI and WG in their phases and the phase volumes of PPI and WG after water distribution in the PPI-WG blend. The  $R_2$ -values of the PPI-WG gels increased with increasing dry matter content in all ratios, indicating a lower mobility of water by increasing dry matter content. The calculated volume fractions of PPI/WG at different ratios and dry matter contents reveal that PPI absorbed more water. This implies that the volume fraction of the individual phases was not similar to the mass fraction anymore. Consequently, the volume of the PPI phase was larger and thus the concentration of PPI in its phase was lower than the concentration of WG in its phase.

For the 25 wt.%, 30 wt.% and 35 wt.% PPI-WG products with a ratio of 20/80, there was no match between the experimentally determined  $R_2$ -value of the PPI-WG and the sum of the predicted  $R_2$  of PPI and predicted  $R_2$  of WG. The experimentally  $R_2$ -value was lower than

the predicted  $R_2$  indicating more mobile/free water than predicted. The fact that WG was not available to absorb all the free water made determination of the volume fractions with this method not possible, because the presence of free water was not considered in the mass balances that was used to relate concentration of the proteins in both phases and their volume fractions. That relation is explained in Appendix C .

*Table 3.2. Overview of estimated concentration PPI in its phase and WG its phase and volume fractions of the PPI and WG phases determined using TD-NMR.*

Ratio PPI/WG (-)	Dry matter (wt.%)	$R_2$ PPI- WG (s <sup>-1</sup> )	[PPI] in its phase (wt.%)	[WG] in its phase (wt.%)	$R_2$ PPI (s <sup>-1</sup> )	$R_2$ WG (s <sup>-1</sup> )	Volume fraction PPI phase (-)	Volume fraction WG phase (-)
80/20	25	22	21	37	23	22	0.88	0.12
	30	29	28	45	29	29	0.88	0.12
	35	36	30	50	35	37	0.87	0.13
	40	46	35	55	43	48	0.87	0.13
50/50	25	20	21	32	23	19	0.59	0.41
	30	23	25	35	27	21	0.60	0.40
	35	30	27	45	30	29	0.65	0.35
	40	34	32	48	37	33	0.63	0.37
20/80	25	16	17	33	18	20	0.34	0.66
	30	19	20	36	21	21	0.33	0.67
	35	23	23	40	25	24	0.32	0.68
	40	28	29	41	32	25	0.27	0.73

### 3.4.3 Rheological properties of protein blends at similar dry matter content

The strain and frequency sweeps of PPI at 40°C are shown in Figure 3.2. The strain sweep results of PPI (Figure 3.2 A) showed that a strain of 1% was within the linear viscoelastic (LVE) regime and a strain of 80% was in the non-LVE regime. The stress response is no longer a single-harmonic sinusoid and therefore we refer to it as an apparent  $G^*$ . Similar conclusions were drawn for WG, SPI, PPI-WG and SPI-WG blends at a ratio of 50/50 prepared at 40 wt.%. Therefore, a 1% strain was selected for frequency sweep tests, shown in Figure 3.2 B. There is only minor dependency of the complex modulus on the oscillation frequency, which was also observed earlier for WG, SPI, PPI-WG and SPI-WG blends at a ratio of 50/50 prepared at 40 wt.% (Dekkers et al., 2018). Similar behaviour was observed at different dry matter contents or processing temperature, even though the absolute values of the apparent complex modulus differed.



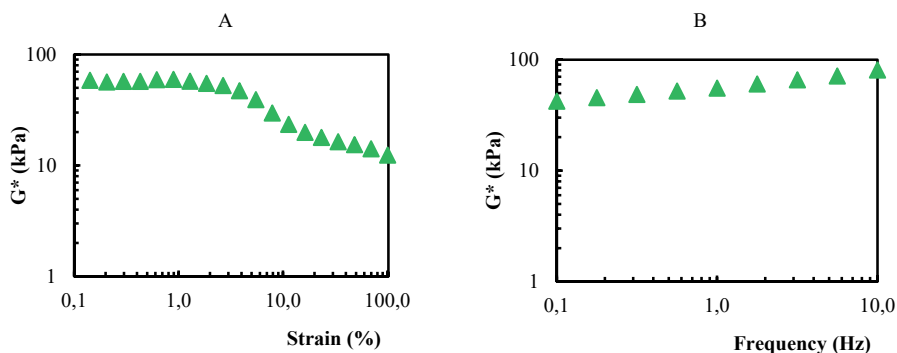


Figure 3.2. Complex shear moduli ( $G^*$ ) for PPI measured at 40°C after an isothermal experiment at 120°C for 15 min at high strain (80%) and high frequency (10 Hz) with a A) strain sweep (1 Hz, 0.1-100%) and B) frequency sweep (1%, 0.1-10 Hz).

In Figure 3.3, the complex moduli of PPI, WG, PPI-WG are depicted for a blend having a dry matter content of 40 wt.% and measured under conditions relevant for structure formation (i.e. at 120°C for 15 min at 80% and 10 Hz). The apparent  $G_{SPI}^*$  was comparable to the apparent  $G_{WG}^*$ , while the apparent  $G_{PPI}^*$  was much lower. The fast initial changes in the moduli are attributed to sample heating from room temperature to the operating temperature of 120°C. After the initial heating period, the apparent  $G_{PPI}^*$  and  $G_{SPI}^*$  was almost constant, but the  $G_{WG}^*$  first increased, until after approximately 4 min, started to decrease. This effect was previously explained as gluten polymerization (Pietsch et al., 2018), which became more pronounced at higher temperature.

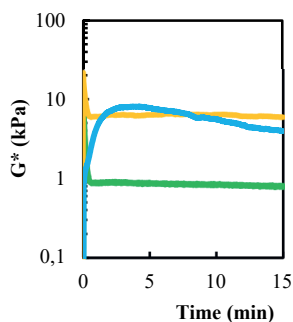


Figure 3.3. Complex shear moduli ( $G^*$ ) measured during a time sweep at 120°C at high strain (80%) and high frequency (10 Hz) for 40 wt.% PPI, 40 wt.% SPI and 40 wt.% WG.

#### 3.4.4 Combination of TD-NMR and rheology

In Figure 3.4, the  $G_{PPI-WG}^*$  is between the values of the  $G_{PPI}^*$  and  $G_{WG}^*$  at a dry matter content of 40 wt.%. However, the TD-NMR measurements showed that the water does redistribute between the PPI and WG; therefore the phases will have different volume fractions and local protein concentrations. We combined the information on water distribution from TD-NMR and rheology to determine the expected rheological properties of the phases present in the PPI-WG blend. Our TD-NMR results show that the water distribution while processing at different temperatures remains the same; so we used the water distribution that was obtained by measuring at room temperature (after having heated to the processing temperature) for determining the rheological properties of the blends at elevated temperatures. It is still unclear how water distributes in a blend during heating at high temperatures, which would be relevant for understanding shear-based structuring processes. A measurement of a protein-water mixture at high temperature (above 100°C) would require a pressure cell inside the NMR device. Measuring this is to our knowledge beyond the current possibilities. However, given the high water activities in both phases (Peters et al., 2017), there is not a clear driving force for water migration upon heating. Given the fact that water distribution was similar before and after heating, and the lack of driving force for water migration justifies the assumption that the water distribution does not change upon heating.

Figure 3.4 shows the apparent complex modulus of PPI and WG at a moisture content as predicted by the TD-NMR measurements of the phases present in the PPI-WG blend. As described above it means that PPI has a lower concentration of 0.32 g/g (but a larger volume fraction of that phase), and WG has a correspondingly higher concentration of 0.48 g/g. Lowering the concentration from 0.40 g/g to 0.32 g/g resulted in a lower modulus for PPI. An opposite trend is visible for WG, in which the modulus increased. We see that the modulus of PPI and WG now differ by almost two orders of magnitude (Figure 3.4).

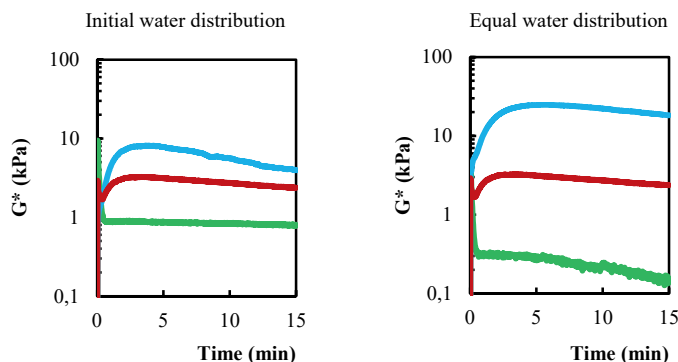


Figure 3.4. Complex shear moduli ( $G^*$ ) measured during a time sweep at 120°C at high strain (80%) and high frequency (10 Hz) for A) 40 wt.% PPI, 40 wt.% WG and 40 wt.% PPI-WG (50/50), B) 32 wt.% PPI, 48 wt.% WG and 40 wt.% PPI-WG (50/50).

Figure 3.5 shows the effect of temperature on the rheological properties. At higher temperatures, the modulus of PPI slowly decreased. The exact reason for this decline is not clear yet. WG still shows a similar maximum in its curve, albeit that the maximum is earlier and more pronounced than at lower temperatures. This is probably caused by polymerization as described by (Pietsch et al., 2018). In all cases, we see that the PPI phase is much weaker than the WG phase. It would be expected that a continuous PPI phase would not be able to deform a dispersed WG phase.

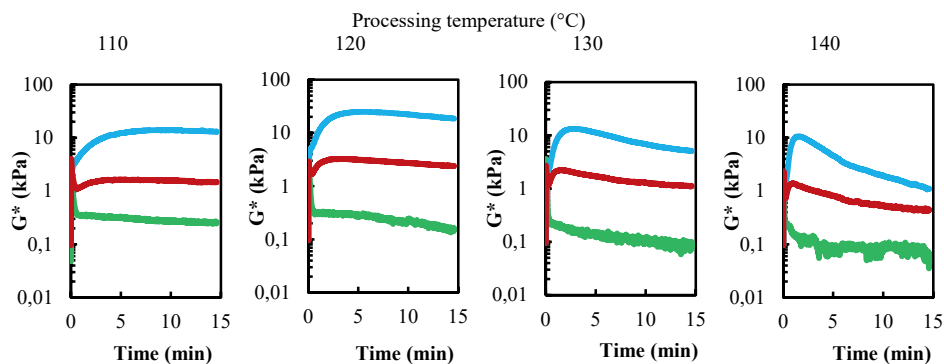


Figure 3.5. Complex shear moduli ( $G^*$ ) measured during a time sweep at 110-140°C at high strain (80%) and high frequency (10 Hz) for 32 wt.% PPI, 48 wt.% WG and 40 wt.% PPI-WG (50/50).

We can now compare this behaviour to that of a SPI-WG blends. Similarly as to the PPI-WG blend, more water is absorbed by SPI than by WG, as observed with TD-NMR (Dekkers, de Kort, et al., 2016). The mass fractions of SPI and WG are in this case 0.33 g/g and 0.51 g/g

in their respective phases and the phase volumes of SPI and WG are 0.62 and 0.38 after water redistribution, according to Dekkers et al. (2018). In Figure 3.6, the moduli using these concentrations are followed at several temperatures. We see a similar trend as in the PPI-WG system: the water redistribution implies a higher modulus for the WG phase, and a lower one for the SPI phase. At lower temperatures the SPI modulus was almost constant over time, but at 130 and 140°C a decreasing trend can be seen. At 95°C, the apparent modulus of the WG phase is only slightly higher than that of the SPI phase, after water redistribution according to Dekkers et al. (2018). At 110-140°C, the SPI modulus was always lower than the one of the WG phase, but especially at lower temperatures the values were not too far apart. At higher temperatures, the difference between the two phases becomes larger. At 140°C, the WG modulus is again two orders of magnitude larger than the SPI modulus.

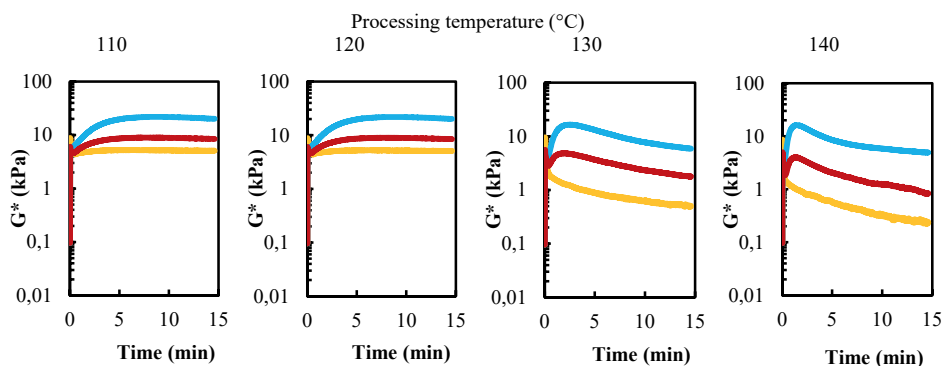


Figure 3.6. Complex shear moduli ( $G^*$ ) measured during a time sweep at 110-140°C at high strain (80%) and high frequency (10 Hz) for 33 wt.% SPI, 51 wt.% WG and 40 wt.% SPI-WG (50/50).

### 3.4.5 Analysis of rheological properties of PPI-WG and SPI-WG with a polymer blending law

We used a polymer blending law to predict the moduli of the blends, using the values of the individual phases, when assuming that the water redistributed based on the TD-NMR measurements. Figure 3.7 and Figure 3.8 show the predictions accordingly when assuming an isostrain ( $n = 1$ ), isostress ( $n = -1$ ) and bi-continuous ( $n = 0.2$ ) model. To depict the mean deviation of the calculated isostrain, isostress and bi-continuous model from the experimentally measured moduli of the PPI-WG and SPI-WG blends, the root mean square error (RMSE) is shown in Appendix Figure A 3.1. We see in Figure 3.7 that for PPI-WG, the only model that predicts the values the best, is the bi-continuous model, even though the bi-continuous model slightly underestimates the measured values at 120, 130 and 140°C. Thus,

given the fact that it is a bi-continuous model, both the PPI and WG phase contribute equally to the final product properties.

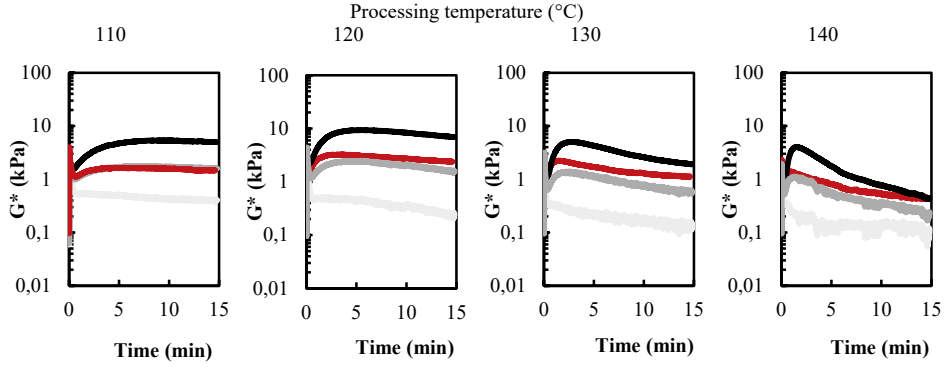


Figure 3.7. Complex shear moduli ( $G^*$ ) measured during a time sweep at 110-140°C at high strain (80%) outside of the linear viscoelastic (LVE) regime and high frequency (10 Hz) for 40 wt.% PPI-WG (50/50) and calculated 40 wt.% PPI-WG (50/50) based on the volume fraction (0.63/0.37) with (—) isostrain, (—) bi-continuous models, (—) isostress.

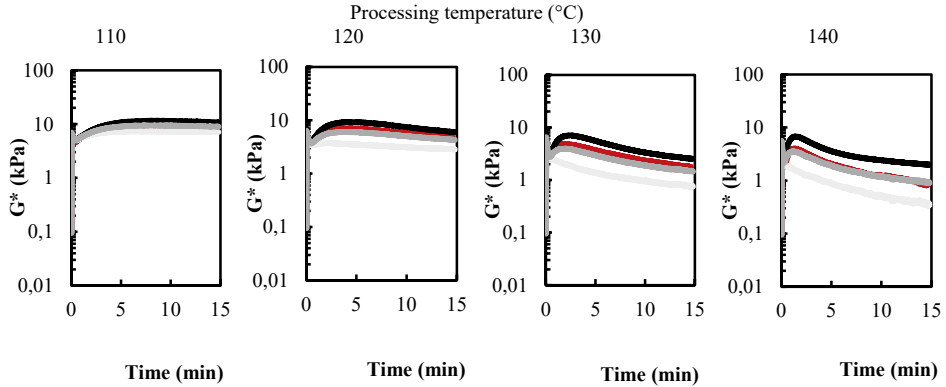


Figure 3.8. Complex shear moduli ( $G^*$ ) measured during a time sweep at 110-140°C at high strain (80%) outside of the linear viscoelastic (LVE) regime and high frequency (10 Hz) for 40 wt.% SPI-WG (50/50) and calculated 40 wt.% SPI-WG (50/50) based on the volume fraction (0.62/0.38) with (—) isostrain, (—) bi-continuous models, (—) isostress.

A previous study according to Dekkers et al. (2018) found that the moduli of the individual SPI and WG phases could well predict the moduli of SPI-WG blends, using the isostrain model. Figure 3.8 and in Appendix Figure A 3.1 show that the values as predicted by the isostress and the isostrain models are quite close. In fact, also the bi-continuous model would match well with the experimental moduli. Therefore we find that these measurements give

no insight on which model is valid, and therefore on which type of morphology a SPI-WG blend has. We see the same trend at 110 and 120°C: the isostress, isostrain and bi-continuous models all yield similar predictions (Figure 3.8) and thus give no decisive insight into the morphology.

Apart from the final morphology of the blends, it is interesting to understand how this morphology develops. Therefore, we follow the development of the complex moduli over time. This was done for the PPI-WG blend with 40 wt.% overall in the blend and the corresponding concentration in the single phases of 32 wt.% PPI and 48 wt.% WG; and for the SPI-WG blend again 40 wt.% overall, and in the corresponding single phases 33 wt.% SPI and 51 wt.% WG. We then used a polymer blending law to fit the modulus of the blend, by using the exponent  $n$  as fit parameter. For this fit parameter,  $n$ , the mean deviation of the calculated fit parameter to the experimentally measured  $G_{PPI-WG}^*$  and  $G_{SPI-WG}^*$ , the root mean square error (RMSE) is minimalized (using ‘Solver’ function in Microsoft Excel) and shown in Appendix Figure A 3.1. Figure 3.9 shows the parameter  $n$  for the PPI-WG and SPI-WG blends after different times of processing at different temperatures. For the PPI-WG blend, the  $n$ -value increases with increasing processing temperature from around 0.2 to 1. At 110°C, the  $n$ -value of the blending law indicated a bi-continuous system ( $n = 0.2$ ) as was discussed before. At 120°C, the  $n$ -value of the blending law resulted in slightly higher  $n$ -values. At increasing processing temperature, the  $n$ -value shifts to a higher  $n$ -value. This shift was more pronounced over longer times of processing, indicative of a transition towards an isostrain system ( $n = 1$ ). With SPI-WG blends, we see a very different behaviour. Here the  $n$ -value at 110°C is zero, indicative of a product with a strong internal phase. At higher temperatures we see  $n$ -values around 0.4; an intermediate  $n$ -value between a bi-continuous network, and an isostrain system; it is possible that this implies that there is some connection between the domains of the dispersed phase, but it does not percolate fully. At 140°C, the system evolves over time, with a  $n$ -value decreasing from decreasing from 0.3 to 0.1. This may well indicate that the SPI-WG is an intermediate system between a bi-continuous structure and a system with a stronger dispersed phase.

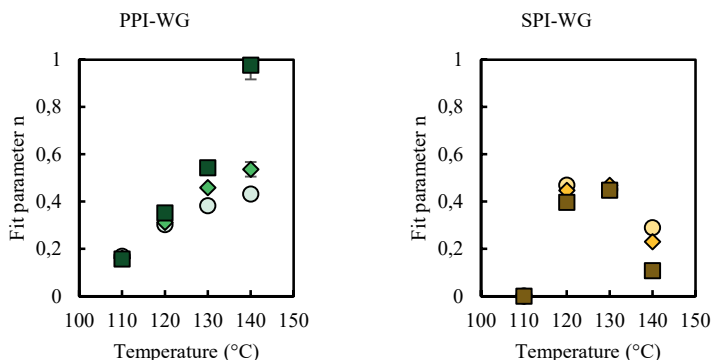


Figure 3.9. Fit parameter,  $n$ , of a polymer blending law for PPI-WG and SPI-WG blends as function of temperature and different times (● 5 min, ◆ 10 min, ■ 15 min).

The behaviour of the two protein blends is markedly different at high temperature. The results indicate that SPI-WG at 140°C for 15 min give the good fit between a bi-continuous structure and a system with a stronger dispersed phase ( $n = 0.1$ ), whereas PPI-WG at 140°C for 15 min give the good fit when using an isostrain approach ( $n = 1$ ). This difference is probably due to the difference in physical properties of these proteins: SPI tends to form strong gels, while PPI is known to form weaker gels. This then explains the different processing temperatures. The fit of the exact  $n$ -value of the polymer blending law indicated that the morphology of the SPI-WG blend may in fact be more or less bi-continuous as well as it is possible to create a SPI gel, interspersed with WG. With PPI-WG at 110 and 120°C it could be possible that WG ultimately also interconnects, just like in kneaded wheat dough, to form a more or less bi-continuous network, which also gives a fibrous structure upon shear cell processing (Chapter 2). Rheological characterization of PPI-WG at 140°C for 15 min suggest that the product structure could change to a dispersion with a weak dispersed phase, give the good fit when using an isostrain approach ( $n = 1$ ). Indeed, shear cell processing resulted in a layered product rather than a fibrous product (Chapter 2). We expect that this effect of time and temperature is because of partial polymerization of the WG phase as shown in the study of Pietsch et al. (2018), becoming interconnected, probably forming the continuous phase at some point (compare the gluten network formation in bread), and incorporating the PPI as weaker internal phase. At 110°C, the  $n$ -value did not depend on the processing time, implying stable behaviour. Remarkably, shorter processing at 140°C gave somewhat fibrous product (in Appendix Figure A 3.2). The rheological measurements indicated a structure that was in between bi-continuous and isostrain based on the best fit-value for  $n$ . It is therefore

hypothesized that a bi-continuous structure is an indication of a blend to form fibrous products upon shearing.



### 3.5 Conclusion

The combination of TD-NMR and rheological characterization using CCR was successfully applied to blends of pea protein isolate (PPI)-wheat gluten (WG) and soy protein isolate (SPI)-WG blends, being processed at high temperature. The analysis of the rheological properties of the blends and the separate phases as function of their hydration was extended by fitting the exact  $n$ -value in the polymer blending law. The results revealed different structuring behaviour of PPI-WG and SPI-WG blends. The SPI-WG blend showed that the fitted  $n$ -values was hardly dependent on processing temperature. The  $n$ -value in case of PPI-WG blend was more temperature dependent, indicating the presence of a bi-continuous structure at 110-120°C, while a higher processing temperature resulted in a WG continuous structure, analogous to the development of gluten dough. We therefore conclude that the fit of the exact  $n$ -value allows indications in the morphology development over time and temperature of plant protein blends. Potentially, it could be a factor that indicates the potential of a protein blend to form fibrous products.

## 3.6 Appendix A

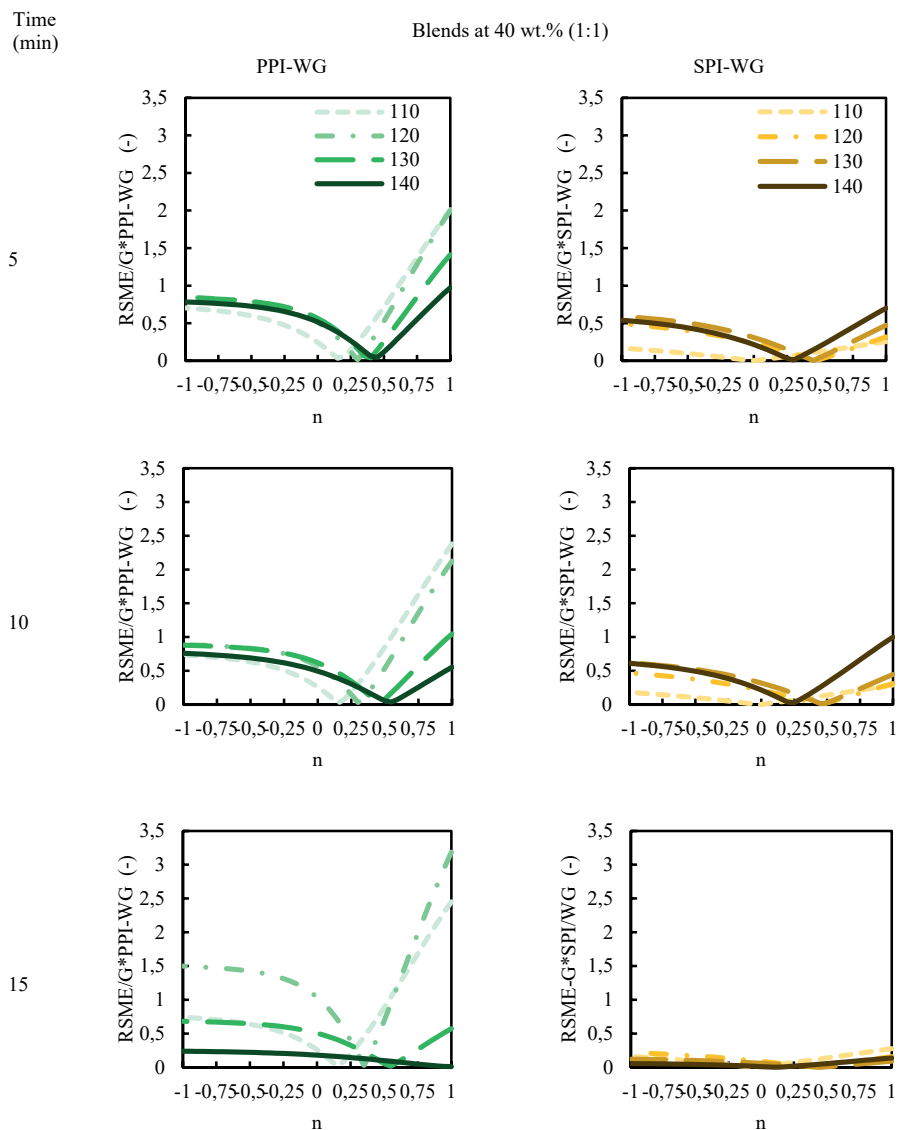


Figure A 3.1. Root mean square error (RMSE) of the parameter  $n$  of a polymer blending law divided by  $G_{PPI-WG}^*$  and  $G_{SPI-WG}^*$  as function of temperature and at different times. The minimum  $RMSE/G_{PPI-WG}^*$  or  $G_{SPI-WG}^*$  resulted in the fit parameter  $n$ .

## Appendix B

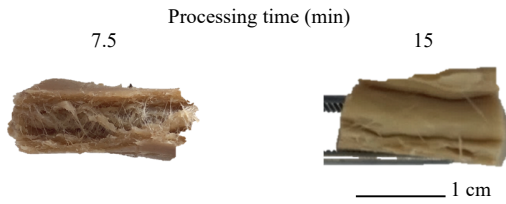


Figure A 3.2. Visual observation of shear-induced structuring ( $140^{\circ}\text{C}$ ,  $39\text{ s}^{-1}$ ) of pea protein isolate (PPI)-wheat gluten (WG) blends at 7.5 and 15 min, which were deformed manually.

### Appendix C. Mass balances: Relation between the concentration and the volume fraction

A blend (Figure A 3.3) consisting of biopolymer X with water (phase i) and Y with water (phase j) is considered. Here, we assume a two phase system with complete de-mixing, which means that no biopolymer X is present in phase j and no biopolymer Y in phase i. In this study phase i with biopolymer X can be for example considered as a mixture of pea protein isolate or soy protein isolate with water, while phase j with biopolymer Y can be for example considered as a mixture of wheat gluten with water.

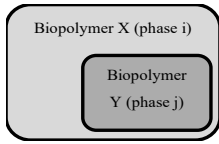


Figure A 3.3. Schematic picture of the blend of biopolymer X and Y.

The following equations are derived from mass balances to relate concentration and the volume fraction:

Total mass ,  $m_{tot}$ , of the blend (kg) is defined as

$$m_{tot} = m_i + m_j \quad 3.3$$

where, the mass of phase i is defined as  $m_i$  (kg) and the mass of phase j is defined as  $m_j$  (kg).

Total mass of phase i or j consisting of the mass of biopolymer X ,  $m_{X,i}$ , and water in phase i  $m_{w,i}$ , or the mass of biopolymer Y ,  $m_{Y,j}$ , and water in phase j  $m_{w,j}$ .

$$m_i = m_{X,i} + m_{w,i} \quad m_j = m_{Y,j} + m_{w,j} \quad 3.4$$

Concentration of each biopolymer X ,  $C_{X,i}$  (kg/kg) , or Y ,  $C_{Y,j}$  (kg/kg), in each phase i or j.

$$C_{X,i} = \frac{m_{X,i}}{m_i} \quad C_{Y,j} = \frac{m_{Y,j}}{m_j} \quad 3.5$$

Concentration of each biopolymer X ,  $C_X$  (kg/kg) , or Y ,  $C_Y$  (kg/kg), in the blend.

$$C_X = \frac{m_{X,i}}{m_{tot}} \quad C_Y = \frac{m_{Y,j}}{m_{tot}} \quad 3.6$$

Volume fraction of phase i ,  $\phi_i$  ( $m^3$ ), and phase j ,  $\phi_j$  ( $m^3$ ), in the blend and the combination with equation 3.4.

$$\phi_i = \frac{\frac{m_i}{\rho_i}}{\frac{m_{tot}}{\rho_{tot}}}$$

$$\phi_j = \frac{\frac{m_j}{\rho_j}}{\frac{m_{tot}}{\rho_{tot}}}$$

Rewritten as:

Rewritten as:

3.7

$$\phi_i = \frac{\frac{m_{X,i} + m_{w,i}}{\rho_i}}{\frac{m_{tot}}{\rho_{tot}}}$$

$$\phi_j = \frac{\frac{m_{Y,j} + m_{w,j}}{\rho_j}}{\frac{m_{tot}}{\rho_{tot}}}$$

where  $\rho_i$  is the density of phase i ( $\frac{kg}{m^3}$ ),  $\rho_j$  being the density of phase j ( $\frac{kg}{m^3}$ ) and  $\rho_{tot}$  being the density of the blend ( $\frac{kg}{m^3}$ ).

The relation between the concentration and the volume fraction can be calculated. To do so, we have to find an equation for  $m_{w,i}$  and  $m_{w,j}$ . This needs rewriting of equation 3.4 and equation 3.5

$$m_{w,i} = m_i - m_{X,i}$$

$$m_{w,j} = m_j - m_{Y,j}$$

Rewritten as:

Rewritten as:

3.8

$$m_{w,i} = \frac{m_{X,i}}{C_{X,i}} - m_{X,i}$$

$$m_{w,j} = \frac{m_{Y,j}}{C_{Y,j}} - m_{Y,j}$$

Then equation 3.7 can be combined with equation 3.8, showing the relation between the concentration and volume fraction.

$$\phi_i = \frac{\frac{m_{X,i} + \frac{m_{X,i}}{C_{X,i}} - m_{X,i}}{\rho_i}}{\frac{m_{tot}}{\rho_{tot}}}$$

$$\phi_j = \frac{\frac{m_{Y,j} + \frac{m_{Y,j}}{C_{Y,j}} - m_{Y,j}}{\rho_j}}{\frac{m_{tot}}{\rho_{tot}}}$$

Rewritten as:

Rewritten as:

3.9

$$\phi_i = \frac{\frac{\frac{m_{X,i}}{\rho_i}}{C_{X,i}}}{\frac{m_{tot}}{\rho_{tot}}} = 1 - \phi_j$$

$$\phi_j = \frac{\frac{\frac{m_{Y,j}}{\rho_j}}{C_{Y,j}}}{\frac{m_{tot}}{\rho_{tot}}} = 1 - \phi_i$$

Those equations can now be combined with a polymer blending law.



# *Chapter 4*

## *Small and large oscillatory shear properties of concentrated proteins*

*This chapter has been published as* Schreuders, F. K. G., Sagis, L. M. C., Bodnár, I., Erni, P., Boom, R. M., & van der Goot, A. J. (2021). Small and large oscillatory shear properties of concentrated proteins. *Food Hydrocolloids*, 110, 106172.

#### 4.1 *Abstract*

A closed cavity rheometer was employed to assess the properties of concentrated protein materials before, during and after thermal treatment, using conditions that are relevant to the production of meat analogues. Pea protein isolate (PPI), soy protein isolate (SPI) and wheat gluten (WG) were used as model matrices. The analysis was done using Lissajous curves, both for small and large amplitude oscillatory shear deformation. The energy dissipation ratios based on the enclosed area inside the Lissajous curves characterize the plasticity of the materials. The results show that the modulus of WG increases during heating and remains elevated after cooling. In contrast, the moduli of PPI and SPI decrease during heating. Subsequent cooling leads to properties that are similar to the rheological properties of unheated PPI and SPI. Lissajous curves and energy dissipation ratios provide insight in the non-linear response. At 30°C, PPI and SPI have a higher dissipation ratio than WG. Upon a heat treatment and even after cooling, the dissipation ratio was smaller at similar strain amplitude compared with 30°C. This indicates that heating induced more elasticity. Upon heating, PPI loses its elastic properties faster than SPI, while WG showed abrupt dissipation after extensive deformation. The observed characteristics are consistent with the behaviour during extrusion and shearing, in which WG forms extended filaments, while SPI and PPI form a homogeneous matrix. Studying the large oscillatory shear behaviour during and after thermal treatment provides a more detailed picture of the rheological changes during processing, than one would obtain through classical rheology. The dissipation ratio summarizes the information in the Lissajous curves. These insights help to better identify material-structure-process relationships for concentrated plant protein materials during thermomechanical conversions, such as extrusion.



## 4.2 Introduction

The interest in using plant proteins as alternative for animal protein is strongly growing, currently (Bashi et al., 2019; Jones, 2016; Lu et al., 2019; Mattice & Marangoni, 2020; Thrane et al., 2017; Tulbek et al., 2016). Soy, pea and wheat gluten are most commonly used ingredients in plant-based products. Wheat gluten is known for its characteristic viscoelastic behaviour when mixed with water (Belton, 1999). It is often described as a polymeric network (Belton, 1999; Ng & McKinley, 2008; Singh & MacRitchie, 2001). The rheological behaviour of soy protein isolate (SPI) was previously explained by considering the protein dispersion as a particle gel (Berghout et al., 2015). The protein particles are created in the fractionation process, in which the final step is drying. Drying requires heating, which leads to denaturation and partial insolubility of the protein particles.

Extrusion is widely used to transform these plant proteins into fibrous or layered products such as meat analogues (Cheftel et al., 1992; Osen et al., 2014). During extrusion, the final product properties (i.e. anisotropy, colour or strength of the material) are determined by process parameters (i.e. temperature, rate of deformation and cooling temperatures), in addition to the protein properties. Understanding of the rheological properties of the materials processed inside the extruder is considered as an important step to further optimize the extrusion process and to develop novel plant-based products. So far, most studies on viscoelastic properties of foods and other materials use small amplitude oscillatory shear (SAOS) analysis. SAOS measurements are characterized by the fact that the modulus is independent of the applied strain and strain rate amplitude. The oscillating stress or strain amplitude input results in a sinusoidal response that provides the properties in the linear viscoelastic (LVE) regime. Often materials are studied in devices that measure very precisely, but only at low torque value, which limits the materials that can be tested. Besides, regular rheometers are mostly used to measure at room temperature or slightly elevated temperature. Unfortunately, industrial extrusion processing is characterised by the use of high temperature, stresses and strains when making texturized protein products. Recently, a closed cavity rheometer (CCR) was suggested as a device which provides measurements on concentrated plant materials at extrusion relevant conditions (Emin & Schuchmann, 2017). This device allows oscillatory rheometry in a sealed environment with precise temperature control and can be used to characterize the rheological properties while heating and cooling of dense proteinaceous materials. Besides, it allows deformations outside the LVE regime. Nowadays,

large amplitude oscillatory shear (LAOS) measurements are analysed in more detail through using Lissajous curves. These provide insight in the non-linear response as the modulus depends on the applied strain and strain rate amplitude. For a large amplitude sinusoidal strain input, the shape of the resulting stress waveform often deviates from a sinusoidal wave, with a significant contribution from higher-order harmonics. Information from LAOS experiments is typically extracted either using Fourier-transform based methods, wherein Fourier-transform analysis may be applied directly on the measured signals, or using a geometric approach (Hyun et al., 2011). Only a few studies reported both the linear and non-linear response for protein and/or polysaccharides (Chong-hao Bi et al., 2013, 2019; Duvarci et al., 2017; Fuongfuchat et al., 2012; John et al., 2019; Klost, Giménez-Ribes, & Drusch, 2019; Precha-Atsawanan et al., 2018; Yazar et al., 2016). Previous studies on pea protein isolate (PPI), SPI and wheat gluten (WG) describe rheological measurements outside the LVE regime, but only in terms of the apparent moduli (Dekkers et al., 2018 and Chapter 3).

Here, we considerably extend the characterization of PPI, SPI and WG, within and outside the LVE regime, by using Lissajous curves. We compare the SAOS and LAOS behaviour of these three proteins at conditions that are relevant (i.e. 40 wt.% and temperature between 100-140°C) for the production of meat analogues. The linear and non-linear behaviour is studied under conditions approaching the large-shear conditions of interest during heating and cooling and cooled down again, the latter reveals the recovery of the material after a pre-heating step. The LAOS parameter, dissipation ratio, as proposed by Ewoldt et al. (2008) and Ewoldt et al. (2010) was used to quantitatively compare the observed dissipation to that of a perfectly plastic material. The insight in the non-linear rheological properties of these composite protein materials is essential for rational design of extrusion or other thermomechanical processes for creating meat analogues, based on material-structure-process relations.

## 4.3 *Materials and methods*

### 4.3.1 *Materials*

Pea protein isolate (PPI) (NUTRALYS® F85G) and vital wheat gluten (WG) (VITENS® CWS) were both obtained from Roquette Frères S.A., (Lestrem, France). Soy protein isolate (SPI) (SUPRO® EX 37 IP) was obtained from Solae (St. Louis, MO, USA). PPI was composed of 78.6 wt.% protein (N x 5.7), WG was composed of 72.4 wt.% protein (N x 5.7), SPI was composed of 80.0 wt.% protein (N x 5.7) on a dry basis, according to Dumas measurements. PPI, SPI and WG had an average dry matter content of 93.2 wt.%, 92.8 wt.%, and 92.3 wt.%, respectively. Sodium chloride was obtained from Sigma-Aldrich (Zwijndrecht, the Netherlands).

### 4.3.2 *Preparation of proteinaceous materials*

Proteinaceous materials (PPI, SPI and WG) were prepared with 30, 40, 50 and 60 wt.% concentration (corrected for the dry matter content of the protein). First, 1 wt.% sodium chloride was dissolved in distilled water. Then PPI, SPI or WG was added and mixed with a spatula. The samples were then hydrated for 30 min.

### 4.3.3 *Rheological properties*

The rheological properties of the protein materials were measured at elevated temperature with a closed cavity rheometer (CCR) (RPA elite, TA instruments, New Castle, Delaware, USA) (Emin & Schuchmann, 2017). Approximately 6 g of the protein material was placed between two plastic films in the cavity, which were sealed to each other to allow a pressure of up to 4.5 bar to prevent water evaporation. The geometry of the closed cavity rheometer has a radius of 2.25 mm and maximum height of the inner cavity of 4 mm and biconical opening with an angle of 3.35° for homogeneous transmission of the shear stress to the protein materials. The grooves on the surface of the cones prevent slip. In this setup the lower cone oscillates in strain-controlled mode while the upper cone remains stationary. First the materials (40 wt.%) were heated for 2 min at elevated temperatures (i.e. 30, 100, 120 and 140°C) without a shear treatment. Subsequently, strain sweep experiments were performed at these elevated temperatures at a constant frequency (1 Hz). Next, the materials (40 wt.%) were heated for 2 min at elevated temperatures (i.e. 30, 100, 120 and 140°C) and cooled to 30°C with a cooling rate of 5°C/min without a shear treatment. After that, strain sweep experiments were performed at 30°C at a constant frequency (1 Hz). A frequency sweep of

the protein materials (40 wt.%) was performed at constant strain amplitude of 1% (within the linear viscoelastic regime). The frequency was varied from 0.1 - 20 Hz at 30°C. The dry matter content dependence of  $G'$  and  $G''$  of 30, 40, 50 and 60 wt.% protein materials were determined with a frequency sweep experiment at a constant strain amplitude (1%) at 30°C.

#### 4.3.4 LAOS

The stress and strain data obtained from the LAOS measurements were analysed using the MITlaos software (Version 2.1 beta, freeware distributed from MITlaos@mit.edu). The strain amplitude was varied in the range of 0.01-1000% at a constant frequency of 1 Hz at 30°C. Lissajous curves were used to relate the response of the protein materials to the imposed oscillatory strain.

The area enclosed in a Lissajous curve can be interpreted as the energy dissipated per unit volume during one complete cycle of the oscillatory strain that is imposed. The energy dissipated per unit volume in a single cycle is a function only of the first-order viscous Fourier coefficient ( $G_1''$ ; calculated from the intensity and phase of the first-harmonic);

$$E_d = \oint \sigma d\gamma = \pi G_1'' \gamma_0^2 \quad 4.1$$

The energy dissipated by a perfect plastic material in a single cycle is equal to

$$(E_d)_{pp} = 4 \gamma_0 \sigma_{max} \quad 4.2$$

for a given strain amplitude ( $\gamma_0$ ) and a maximum stress ( $\sigma_{max}$ ). The Lissajous curve for a perfectly plastic material has a rectangular shape (see Figure 4.1), and this shape corresponds to a material that initially gives a perfectly rigid response, at the maximum deformation of the cycle (lower left and upper right corners), and subsequently yields, and displays a constant stress ( $+/-\sigma_{max}$ ), independent of the strain in the rest of the cycle (i.e. purely plastic behaviour).

Comparing the actual dissipated energy to the perfect plastic dissipation, gives the energy dissipation ratio ( $\varphi$ ) as proposed by Ewoldt et al. (2010).

$$\varphi = \frac{E_d}{(E_d)_{pp}} = \frac{\pi G_1'' \gamma_0}{4 \sigma_{max}} \quad 4.3$$

The physical meaning of the dissipation ratio is illustrated in Figure 4.1.

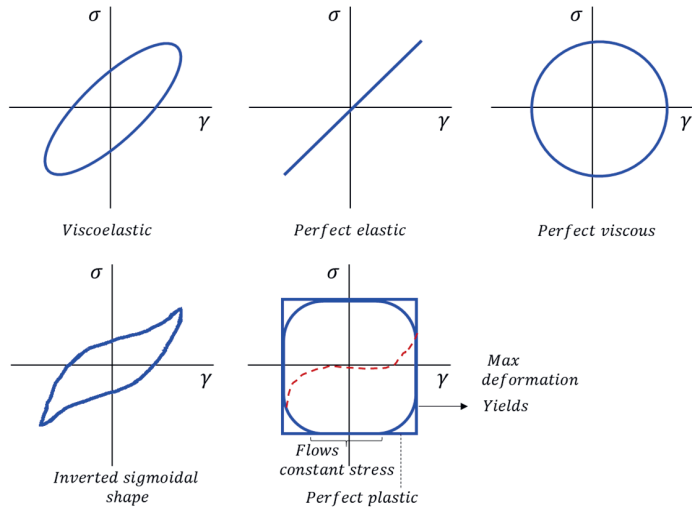


Figure 4.1. Stress-strain Lissajous curve for linear viscoelastic, perfect elastic, perfect viscous, inverted sigmoidal shape and perfect plastic behaviour. The energy dissipation coefficient ( $\phi$ ) represents the enclosed area of the Lissajous curve for the viscoelastic response divide by the enclosed area of the perfect plastic response.

## 4.4 Results and discussion

### 4.4.1 Strain-dependence of $G'$ and $G''$ as a function of the temperature profile

Figure 4.2 shows storage ( $G'$ ) and loss ( $G''$ ) moduli as a function of the strain amplitude for materials at 40 wt.% at 1 Hz frequency. Three different conditions were tested: (i) unheated (i.e. 30°C), (ii) elevated temperatures and (iii) cooled down after heating. Measurements were performed to determine  $G'$  and  $G''$  and the extent of the linear viscoelastic (LVE) regime of the protein materials with respect to the temperature, and the recovery after heating, using a frequency of 1 Hz (Figure 4.2). In the linear viscoelastic regime, the moduli were independent of the applied strain amplitude and  $G'$  was always larger than  $G''$ , indicating predominantly solid-like behaviour. At 30°C, pea protein isolate (PPI) had a maximum linear strain amplitude in the LVE regime of about ~10%, and a  $G'$  of 95 kPa (tan delta of 0.25). For soy protein isolate (SPI), the LVE regime extended slightly further up to strain amplitudes up to 14%, and it had a higher value for  $G'$  of 180 kPa (tan delta of 0.2). Those measurements show that SPI leads to stronger material than PPI. Wheat gluten (WG), though had a lower modulus at 30°C.

The effect of heating at 120°C on  $G'$  and  $G''$  is shown in Figure 4.2 B. For PPI and SPI,  $G'$  and  $G''$  decreased almost two orders of magnitude, while the LVE regime became larger. Both materials remain predominantly elastic at 120°C. The modulus of PPI was lower, and its LVE regime was narrower than that of SPI, which indicates a weaker and slightly more brittle material compared with SPI. For WG,  $G'$  increased almost one order of magnitude when the temperature was increased from 30°C to 120°C. In addition, the ratio of the storage (elastic) to the loss (viscous) modulus representing tan delta decreased (30°C~0.6 while at 120°C ~0.15). Along with the slight decrease in absolute  $G''$ , this change towards a much more elastic material was previously explained as gluten polymerization (Pietsch et al., 2018; Strecker et al., 1995). WG heated to 120°C had a slightly higher modulus than PPI and SPI. The temperature dependence of  $G'$  and  $G''$  in the LVE regime (frequency of 1 Hz and strain amplitude of 1%) for PPI, SPI and WG is summarized in Figure 4.3 A. The moduli of PPI and SPI decreased with increasing temperature while the moduli of WG increased with increasing temperature. This confirms that the response of WG to heating is significantly different from that of PPI and SPI.

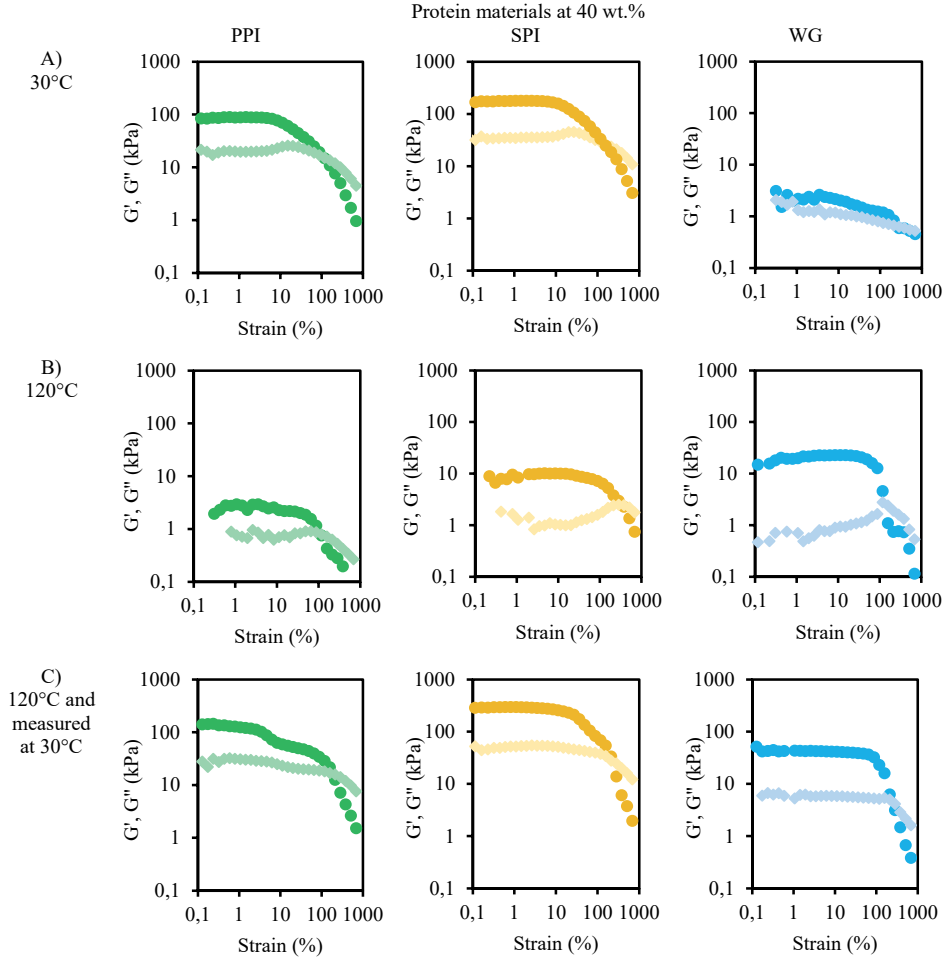


Figure 4.2. Storage ( $G'$ ) (●, ●, ●) and loss modulus ( $G''$ ) (◊, ◊, ◊) of 40 wt.% PPI, SPI and WG as function of strain amplitude at a frequency of 1 Hz at 30°C, 120°C and heated to 120°C and subsequently cooled to 30°C.

The recovery of  $G'$  and  $G''$  after heating and cooling of the protein materials is presented in Figure 4.2 C. The heat pre-treatment at 120°C had little influence on PPI and SPI, and the moduli of these materials after a heat pre-treatment recovered to a similar order of magnitude as the untreated material at 30°C. The heat pre-treated PPI showed a narrower LVE regime, while SPI gave a larger LVE regime compared with PPI or SPI at 30°C. Furthermore, the heat pre-treated SPI showed a larger modulus and a larger LVE region than the same heat pre-treatment compared with PPI. The heat treatment had a large influence on WG. Its  $G'$  and  $G''$ -values increased by almost two orders of magnitude. Overall, PPI and SPI showed

higher moduli that resulted in stronger material than WG. However, a larger LVE region was observed for WG than for PPI and SPI. The network of WG could be stretched and aligned at a higher strain amplitude than PPI and SPI. The larger LVE region for WG is probably due to a larger density of crosslinks formed (Pietsch et al., 2018). The effect of the heat pre-treatment on  $G'$  and  $G''$  in the LVE regime is summarized in Figure 4.3 B. The moduli of PPI and SPI did not change with increasing temperature upon heating, while the modulus of WG increased with increasing temperature for the heat pre-treatment.

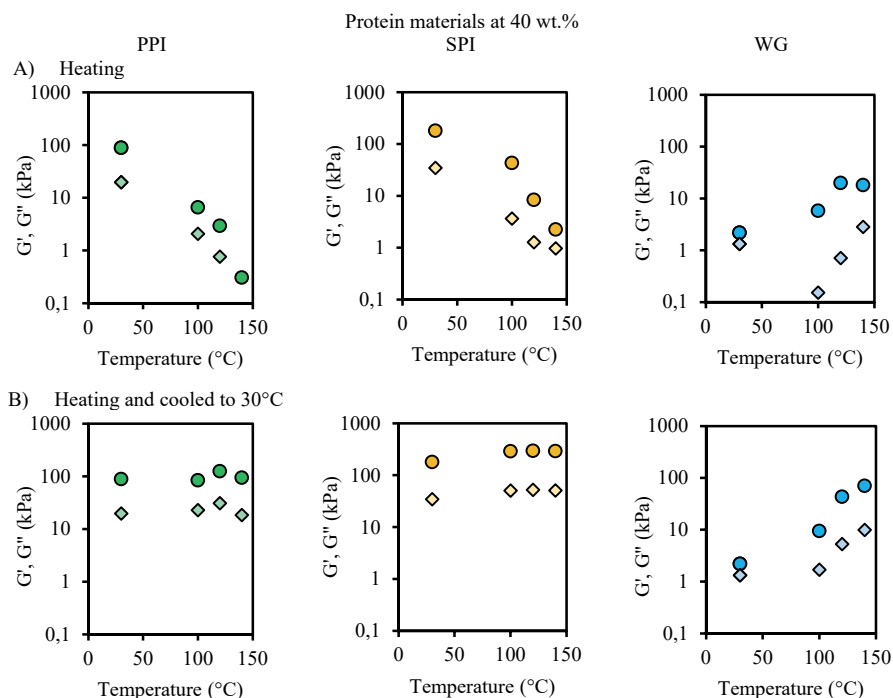


Figure 4.3. Temperature dependence of the storage ( $G'$ ) (●, ●, ●) and loss modulus ( $G''$ ) (◆, ◆, ◆) in the LVE regime for 40 wt.% PPI, SPI and WG A) during heating at 30, 100, 120 and 140°C and B) during cooling from a heat treatment from 100, 120 and 140°C to 30°C with strain amplitude of 1% and frequency of 1 Hz. The strain amplitudes of PPI, SPI and WG when heated at 100 and 140°C are shown in Appendix Figure A 4.1 and heated at 100 and 140°C subsequently cooled to 30°C are shown in Appendix Figure A 4.2.

The effects of the dry matter content at 30°C on  $G'$  and  $G''$  in the LVE regime are shown in Figure 4.4. As the dry matter content (DM) increased, the  $G'$  and  $G''$  for PPI, SPI increased more than the modulus of WG increased. All responses were fitted with a power law  $G' \sim DM^c$ , in which  $c$  is a scaling exponent. The concentration dependence  $c$  for PPI and SPI was almost similar ( $c = 4.96$  and  $4.56$ , respectively), but different compared to WG ( $c = 1.59$ ).



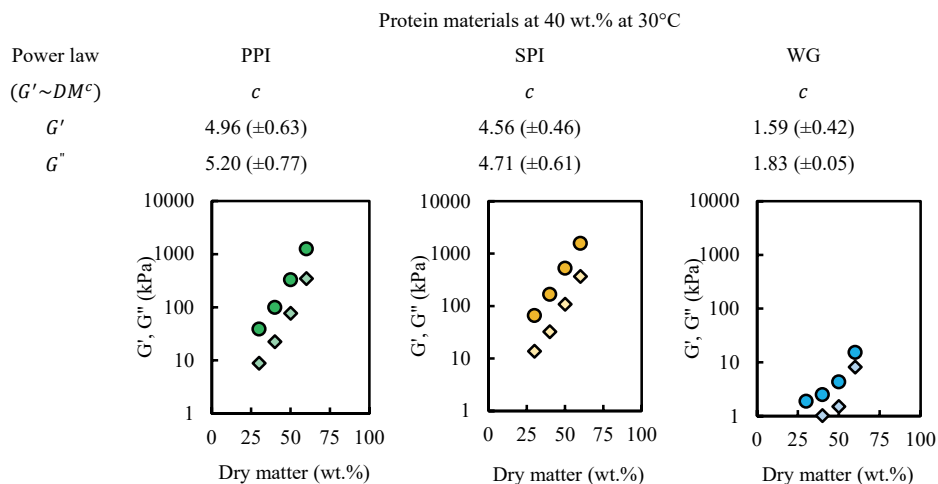


Figure 4.4. Dependence on the dry matter content (wt.%) of the storage ( $G'$ ) (●, ●, ●) and loss modulus ( $G''$ ) (●, ●, ●) in the LVE regime for 40 wt.% PPI, SPI and WG at 30°C with strain amplitude of 1% and frequency of 1 Hz, including the power law ( $G' \sim DM^c$ ) value  $c$  of the  $G'$  and  $G''$  for each material.

The frequency dependence of the storage and loss moduli is shown in Figure 4.5. As the frequency increased, the  $G'$  and  $G''$  for PPI, SPI and WG showed a small increase. The response could be fitted with a power law  $G' \sim \omega^n$ , in which  $\omega$  is the frequency, and  $n$  is a scaling exponent. The frequency dependence  $n$  for PPI and SPI moduli was similar ( $n = 0.14$  and  $0.13$  respectively). This weak power law behaviour is often associated with materials that behave as a soft glassy material. Here, the term “glassy” refers to a condition of metastable structural disorder, in which thermal motion is not enough for relaxation to take place. The term “soft” is used to indicate the possibility for flow upon increasing strain amplitude (Bandyopadhyay et al., 2006). Several soft glassy materials are characterized by a power law value  $n$  ranging between 0.1 - 0.3 (Bandyopadhyay et al., 2006; Ketz et al., 1988; Khan et al., 1988; Mackley et al., 1994). SPI and PPI are provided as granular material, which is only partly soluble. In presence of limited water, we expect that the granular nature is (at least partly) preserved (Berghout et al., 2015). Upon water addition, the particles will swell, and become deformable. Particle interaction will strongly increase due to jamming, leading to fast increasing moduli upon increased concentration. After heating, such protein dispersion can form a particle gel (Berghout et al., 2015). This was also supported by the stronger concentration dependence for PPI and SPI ( $c = 4.56$  and  $4.96$  respectively) in Figure 4.4. The frequency dependence of WG was with  $n = 0.28$  much larger than that of PPI and SPI. Similar frequency dependence for  $G'$  ( $n = 0.3$ ) was reported for WG at 41 wt.% (Georgopoulos et al.,

2004). This value for  $n$  corresponds with a swollen polymer network behaviour, which is an appropriate description for WG indeed (Ng & McKinley, 2008). Also the concentration dependence for WG ( $c = 1.59$ ) was significantly different compared with PPI and SPI as observed in Figure 4.4. If these protein materials are indeed so different we would expect a completely different response in the LAOS measurements, which we will investigate now in the next section.

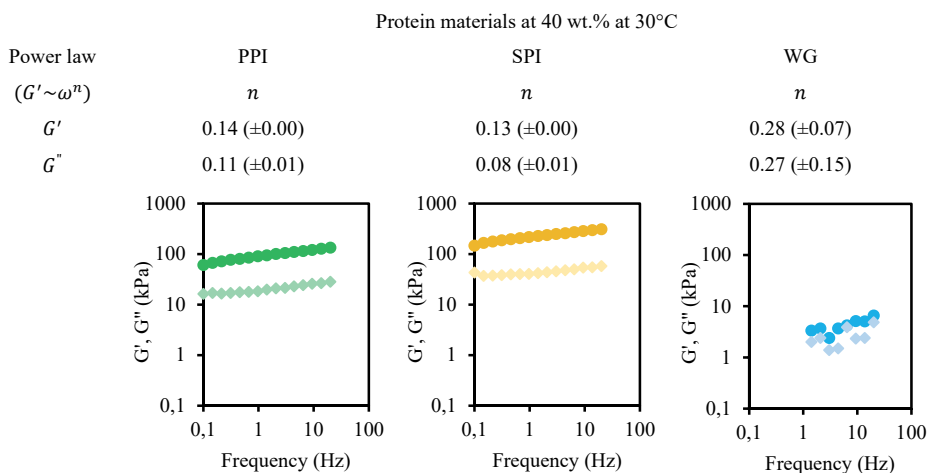


Figure 4.5. The storage ( $G'$ ) (●, ●, ●) and loss modulus ( $G''$ ) (◆, ◆, ◆) of 40 wt.% PPI, SPI and WG as function of frequency (frequency sweep at a strain amplitude of 1% at 30°C), including the power law ( $G' \sim \omega^n$ ) value  $n$  of the  $G'$  and  $G''$  for each material.

#### 4.4.2 Large amplitude oscillatory shear (LAOS): Intra-cycle rheology and temperature-dependence

Upon increasing the strain amplitude beyond the LVE regime, all materials show a decrease of  $G'$  and  $G''$ , implying shear-softening and shear-thinning behaviour. In the beginning of the non-linear viscoelastic regime,  $G'$  is larger than  $G''$  representing solid behaviour. At even larger strains, both  $G'$  and  $G''$  decreased, and eventually  $G''$  exceeded  $G'$  (Figure 4.2). A more detailed assessment of the non-LVE behaviour of protein materials was obtained through Lissajous curves.

Figure 4.6 shows these curves at three different strain amplitudes for PPI at 30°C. The elastic Lissajous curves (stress versus strain) had a line or narrow ellipse shape for small strain amplitudes, implying that the response of this material was elastic at these strains. With a further increase of the strain amplitude, the area encompassed by the curve became wider.

This is an indicator of viscous dissipation, suggesting structure breakdown. In Figure 4.6 the total stress was decomposed in an elastic and viscous contribution. In the plots of stress versus strain, the red dashed lines indicate the elastic contributions to the total stress. In the plots of stress versus shear rate, the red dashed lines indicate the contribution of the viscous stress to the total stress. The large deviations from the dashed lines at larger strains indicate that the elastic-dominated behaviour is changed into more viscous-dominated behaviour. At large strains, the area encompassed by the curve increased and changed gradually into an almost rectangular shape, indicating plastic behaviour eventually.

Figure 4.6 also shows the viscous Lissajous curves of the stress versus strain rate amplitude for PPI at 30°C. At small strain amplitudes, the viscous Lissajous curve had a circle or ellipse shape, with near zero contribution of the viscous stress (red dashed line). With the increase of strain rate amplitude into the non-linear region, the Lissajous curve narrowed, indicating more viscous dissipation. At the highest strain rate-value, the curve changed to a sigmoidal curve, indicating a strong shear thinning behaviour in the viscous response.

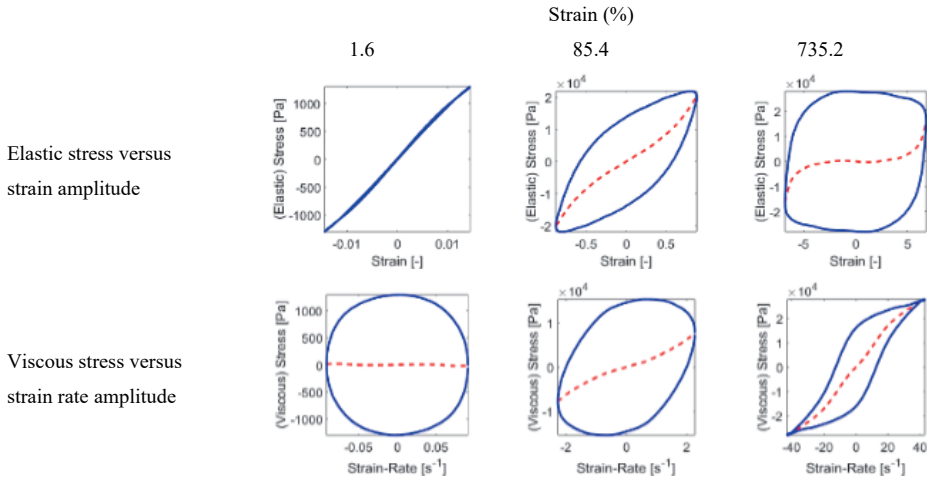


Figure 4.6. Lissajous curve of stress versus strain amplitude and stress versus strain rate amplitude at three different amplitudes for 40 wt.% PPI at 30°C. (individual plots of normalized stress (solid lines) and elastic stress (dashed lines) vs. strain, individual plots of normalized stress (solid lines) and viscous stress (dashed lines) vs. strain rate.)

Figure 4.7 shows Lissajous curves at different strain amplitudes for PPI, SPI and WG, after a heat pre-treatment at various temperatures (100, 120 and 140°C), and measured at 30°C. The elastic Lissajous curves of stress versus strain amplitude are shown in Figure 4.7 and in Appendix Figure A 4.3, and the viscous Lissajous curves of stress versus strain rate amplitude

are shown in Appendix Figure A 4.4. The behaviour of PPI, SPI and WG at high temperature is provided in the Appendix Figure A 4.5 and 4.6. Lissajous curves of PPI, SPI and WG at high temperature show a comparable trend to the Lissajous curves of PPI, SPI and WG when heated and subsequently cooled as discussed below. At low strains, heating and subsequent cooling hardly affected the properties of PPI compared to PPI at 30°C. At higher strain amplitudes (i.e. 33.9% and 85.4%), heat pre-treatment affected the shape of the Lissajous curves. PPI with a heat pre-treatment resulted in a more pronounced inverted sigmoidal curve with a smaller enclosed area than PPI at 30°C. The area enclosed within the Lissajous curve represents the dissipated energy in one cycle. The change in the curve shown in the figure indicates that the heat pre-treatment reduces the dissipation in the material during deformation. At high strains, the shape of the Lissajous curve changed to an almost rectangular shape. It means that PPI showed plasticity: yielding at all processing temperatures, followed by flow (the horizontal part of the loop), followed by recovery (as explained in Figure 4.1).

The Lissajous curve of SPI after different heat pre-treatment showed a similar trend as for PPI: pre-heating affected the shape of the Lissajous curve to lower viscous dissipation. At the highest strain amplitude an “overshoot” was observed after yielding, where the elastic contribution to the stress (the dashed red line) decreased after reaching a maximum value. At high strains for SPI, self-intersections appear in the viscous Lissajous curve (shown in Appendix Figure A 4.4), which leads to secondary loops (Ewoldt et al., 2010). This means that the stress response remained similar at constant strain rate amplitude while the corresponding strain amplitude values were different. This might be related to the strong non-linearities in the elastic stress. These self-intersections may emerge when the time scale for restructuring of the microstructure is shorter than the oscillatory deformation time scale. These self-intersection in the Lissajous curve were also observed in soft wheat flour dough (Yazar et al., 2017), foam prepared from egg white protein (Ptaszek, 2015) and tomato paste (Duvarci et al., 2017).

The Lissajous curves of WG after heat pre-treatment show a different trend compared with PPI and SPI. WG is not predominately elastic at low strains measured for the non-treated sample at 30°C, and is primarily viscous. At increasing strain amplitude, the area enclosed within the Lissajous curve increased, which indicates that the material dissipates more energy with increasing strain amplitude, while no clear yielding behaviour was observed. Heat

treatment rendered the WG predominantly elastic, as evident in the narrow ellipse shape at low strains and the circular shape at low strain rate amplitude. Predominantly elastic behaviour was observed at a strain of 157.9%. A further increase of the strain amplitude resulted in an abrupt transition to non-linear behaviour, that was observed for WG pre-heated at 120°C at strain amplitudes above 292.1% and for WG pre-heated at 140°C even at lower strain amplitudes of 157.9% (shown in Appendix Figure A 4.3). At high strain amplitude for WG, self-intersections appear in the viscous Lissajous curves (shown in Appendix Figure A 4.4) leading to secondary loops (Ewoldt et al., 2010). Again, this is indicative of the reformation of crosslinks within timescale shorter than the oscillatory deformation

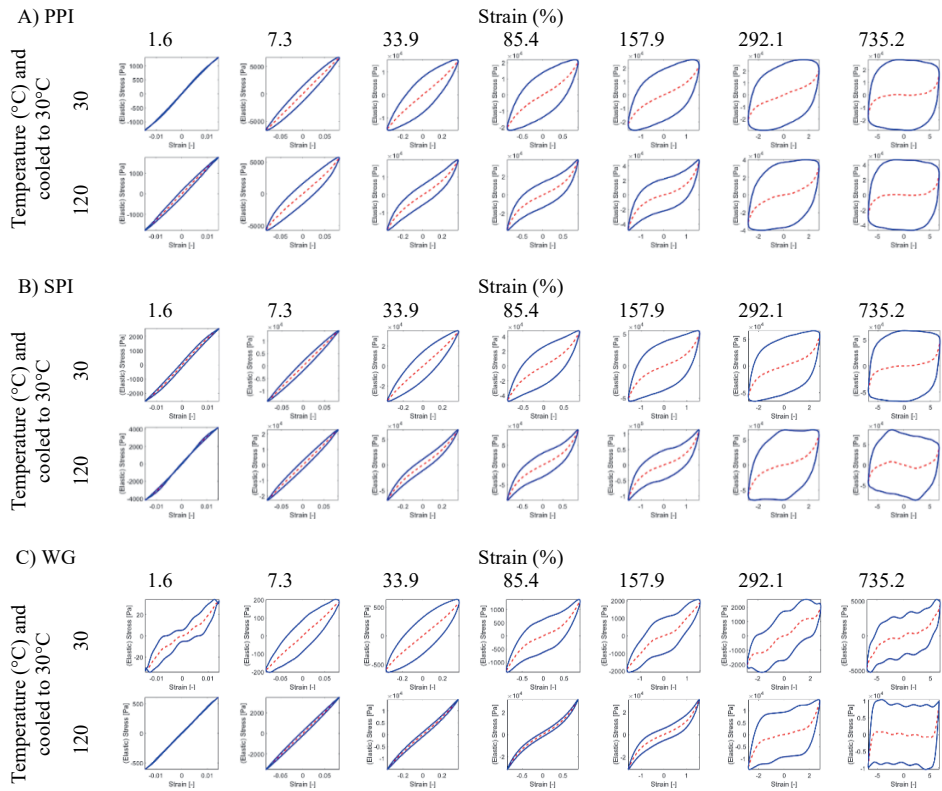


Figure 4.7. Lissajous curve of stress versus strain amplitude for A) PPI, B) SPI, C) WG at 30°C and heated to 120°C and subsequently cooled to 30°C, at several strain amplitudes. (normalized stress (solid lines) and elastic stress (dashed lines)).

To better quantify the dissipation and the non-linear behaviour, we calculated the energy dissipation ratio ( $\phi$ ) as defined in equation 4.3. The total energy dissipated per cycle is only

a function of the first-order viscous Fourier coefficient. When  $\varphi=0$ , the response is purely elastic as no energy is dissipated, and when  $\varphi=1$ , material exhibits perfect plasticity (Ptaszek, 2014). A  $\varphi$  of  $\pi/4$  corresponds to a material that behaves as a Newtonian liquid.

The dissipation ratio as function of the strain amplitude is shown in Figure 4.8. At small strain amplitudes, the  $\varphi$  is small for all materials indicating a predominantly elastic response. A larger strain amplitude leads to a larger dissipation ratio. Eventually a maximum ratio of around 0.8 was obtained implying viscous behaviour (Figure 4.8). At 30°C, the dissipation ratio for WG is higher at low strain amplitude and lower at high strain amplitude as compared with the dissipation ratio of PPI and SPI. This difference indicates elastic behaviour for PPI and SPI at low strain amplitudes and viscous behaviour at high strain (since  $\varphi$  is close to 0.79). At 30°C, the dissipation ratio for PPI and SPI is similar. In contrast, once these two materials are heated at high temperatures, a different behaviour for PPI and SPI emerged: PPI was now more dissipative at low strain amplitudes than SPI. This suggests that PPI loses its elastic properties faster upon heating and that viscous behaviour becomes more predominant than for SPI. As the strain amplitude increases, the dissipation ratio of PPI first increases more strongly than that of SPI, even though its maximum value is similar for both. At high temperatures and low strain, WG and SPI both had a low dissipation ratio indicating predominantly elastic behaviour, different from PPI. WG shows a sharp increase in the dissipation ratio at ~100% strain amplitude.

The dissipation ratios of PPI and SPI were almost similar at 30°C. After heat pre-treatment, there was generally a slight difference in the ratios of PPI and SPI, but this difference was smaller than for the case of heated-only samples. This result indicates that PPI lost its elastic properties at a lower strain amplitude than SPI after cooling. WG after a heat pre-treatment followed by cooling showed a similar trend compared to when heated-only samples as discussed above; at increasing strain amplitude the dissipation ratio of WG shows a sharp increase at ~100% strain amplitude for heat pre-treatment at 100, 120 and 140°C. This additional information on the dissipation behaviour of the materials related to high temperatures and recovery supported the change in the enclosed area of the Lissajous curve. This dissipation ratio reveals the main information in the Lissajous curves in a compact manner.

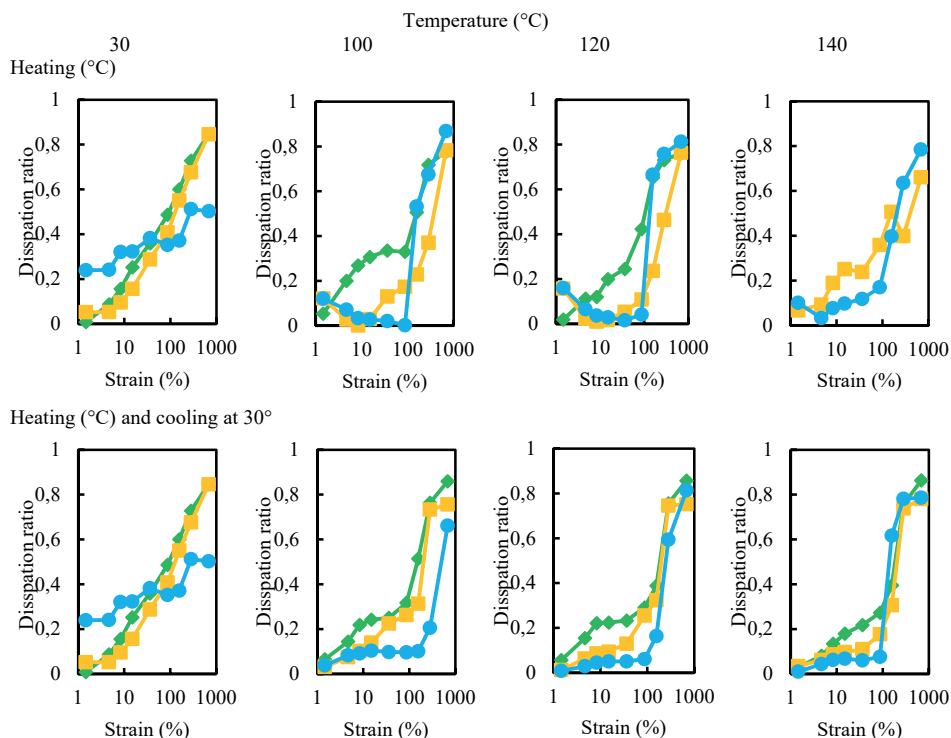


Figure 4.8. Dissipation ratio of PPI (♦), SPI (■) and WG (●) heated at 30, 100, 120 and 140°C and heated at 30, 100, 120 and 140°C and subsequently cooled to 30°C. For PPI at 140°C the stress values were too small to measure accurately and therefore the dissipation ratio is not shown.

#### 4.4.3 Connection of SAOS and LAOS to structure formation

The rheological properties of protein materials at a high dry matter content (i.e. 40 wt.%) and high temperature (i.e. 100-140°C) are relevant for understanding their behaviour in processes that combine heating and deformation, such as extrusion. This paper discusses the rheological behaviour of protein materials with SAOS and LAOS. LAOS is important to understand the behaviour of the materials during industrial processing. Therefore, protein materials were heated and simultaneously subjected to a shear treatment by applying a frequency of 1 Hz and increasing strain amplitude in an oscillation experiment. In this section, we connect the outcomes of the experiments to the observations made in structuring equipment like shear devices and extruders, even though the oscillatory shear as occurring in the closed cavity rheometer differs from the continuous shear inside a shear cell or extruder. However, we believe that the study done here still offers the closest study to these processes that is currently available.

From the strain-dependence of  $G'$  and  $G''$ , we conclude that PPI and SPI behaved quite differently from WG. The moduli of PPI and SPI in the LVE regime at 30°C were similar, but that the extent of the LVE regime differed. Both the modulus and the extent of the LVE regime of PPI and SPI were different compared with WG at 30°C. Both PPI and SPI had a large modulus at 30°C in the LVE regime and after a heating and subsequent cooling the moduli of PPI and SPI were almost similar to the original values. The rheological measurements (low frequency dependence and large scaling exponent with dry matter) indicated that both PPI and SPI could be considered a particle gel. Therefore we expect that part of the interactions between the domains will be broken with increasing strain, allowing them to flow past each other, resulting in viscous or plastic behaviour. Whether this structural breakdown occurs homogeneously, or is accompanied by a complex local strain field with different shearing zones within the sample, will need further clarification. The behaviour of WG resembled more the rheological response of a crosslinked polymeric network. WG had a low modulus at 30°C in the LVE regime, but heating and subsequent cooling resulted in a much higher modulus. This difference is probably due to additional crosslink formation. With increasing strain amplitude, crosslinks in the WG network break, allowing the strands of protein to slide past each other, explaining a shift towards more viscous behaviour. If crosslinks are indeed the determinant factor for extending the LVE regime, future research should be focused on how to induce additional crosslinks in PPI.

Lissajous curves were constructed to evaluate the deformation in the linear and non-linear viscoelastic regime. The shapes of these Lissajous curves for PPI and SPI were quite similar but different from WG. This supported the SAOS data that these protein dispersion are fundamentally different indeed. Energy dissipation ratios based on the analysis of the integrated area inside the Lissajous curves were calculated and used to characterize plasticity of the materials. Strain amplitude and heat treatment alter the ratio of elastic to viscous behaviour. We conclude that the materials change from elastic to plastic upon increasing strain amplitude. As the deformation increases, the strain amplitude on the network eventually causes breakage and plasticity. At high temperature, the dissipation ratio was smaller than at 30°C at similar strains. Even after cooling, the dissipation ratio remained smaller. This indicates that heating induces irreversible changes, generating induced more elasticity. This elasticity is most pronounced for WG as observed by the higher dissipation ratio in Figure 4.8. This dissipation ratio of WG increased at a higher strains than SPI and



PPI. Those observations are in line with confocal light microscopy images. Those reveal that WG forms strongly elongated domains under continuous shear which appeared as aligned fibres in SPI-WG and PPI-WG blends, while SPI and PPI both do not show this clear elongated domains, even after extensive deformation (Chapter 2). We further observed that PPI loses its elasticity quickly, which is probably connected to its low strength as a matrix during processing. The SPI network is stronger, and retains its elasticity better during heating. Indeed after structuring, SPI-containing products are stronger than PPI-based product at similar dry matter content (Shand et al., 2007).

These insights of the rheological properties of three concentrated protein materials (PPI, SPI and WG) at extrusion-like conditions were linked to the structure formation process observed in other studies. Lissajous curves and dissipation ratios at different temperatures were used as a rheological fingerprint of the protein dispersions. As a next step, this fingerprint will be linked to structure formation process allowing a “design type of thinking” approach and better selection of the optimal process condition. This could enable to develop new plant protein-based matrices for meat analogues in the future.

## 4.5 Conclusion

Small and large amplitude oscillatory shear deformation with a closed cavity rheometer was successfully applied before, during and after thermal treatment, giving insight in the structural changes during thermomechanical treatment, such as extrusion and shear cell treatment. Pea protein isolate (PPI) and soy protein isolate (SPI) at 40 weight% behaved similarly, but different from wheat gluten (WG). The modulus of WG increased with increasing temperature, and did not recover after cooling. Heat pre-treatment did not significantly change the modulus of PPI and SPI. The LAOS analysis reveals the rheological changes occurring at large shear strains more clearly than one would obtain through classical rheology. The energy dissipation ratio showed a simplified perspective to reveal the complex information in the Lissajous curves in a compact manner. At 30°C, PPI and SPI show a higher dissipation ratio than WG. At high temperature and even after cooling, the dissipation ratio was smaller at similar strain amplitude compared with 30°C. This indicates that heating induced more elasticity. Upon a thermal treatment, PPI lost its elastic properties more quickly than SPI, while WG showed abrupt dissipation after extensive deformation. These observations are consistent with observations from shear deformation processing, in which WG is seen to deform into elongated structural domains, while SPI and PPI show less extension. These insights are useful for the rational design of thermomechanical processes to prepare structured plant protein matrices, based on mechanistic material-structure-process relationships.

## 4.6 Appendix

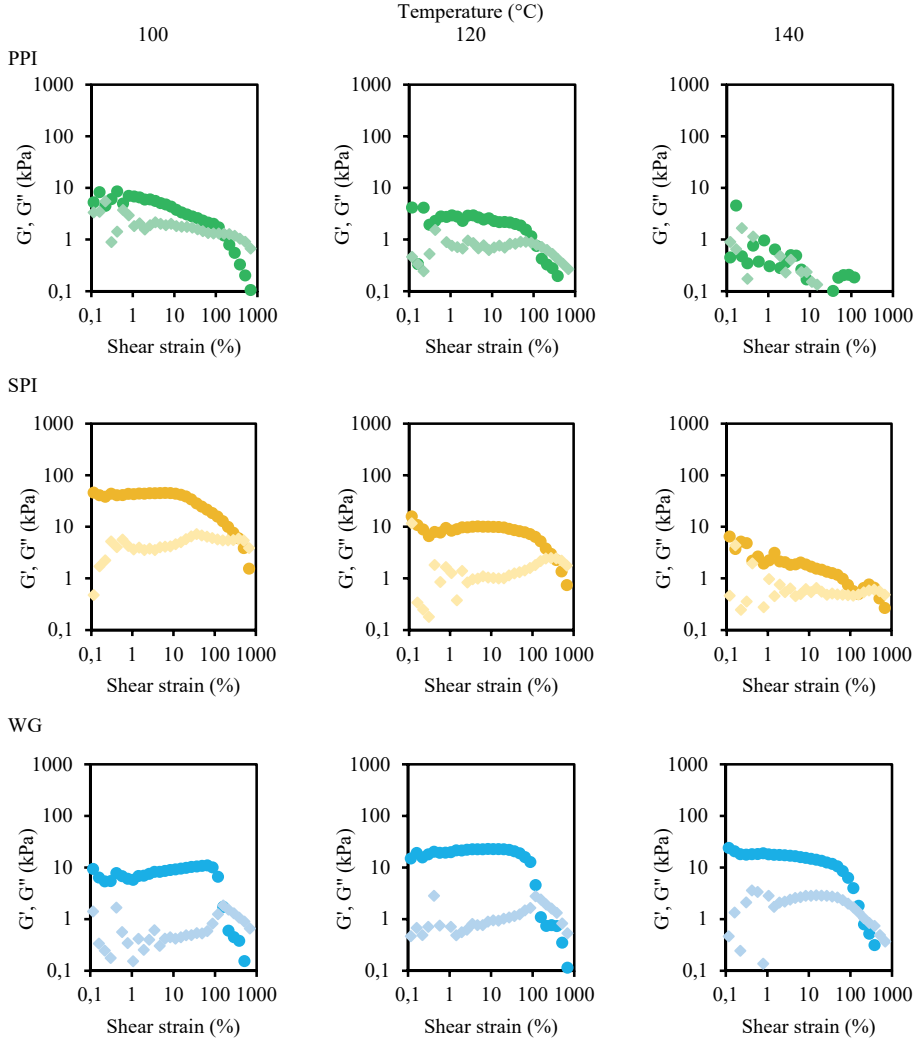


Figure A 4.1. Storage ( $G'$ ) (●, ●, ●) and loss modulus ( $G''$ ) (◊, ◊, ◊) of 40 wt.% PPI, SPI and WG as function of strain amplitude at a frequency of 1 Hz at 100°C, 120°C and 140°C.

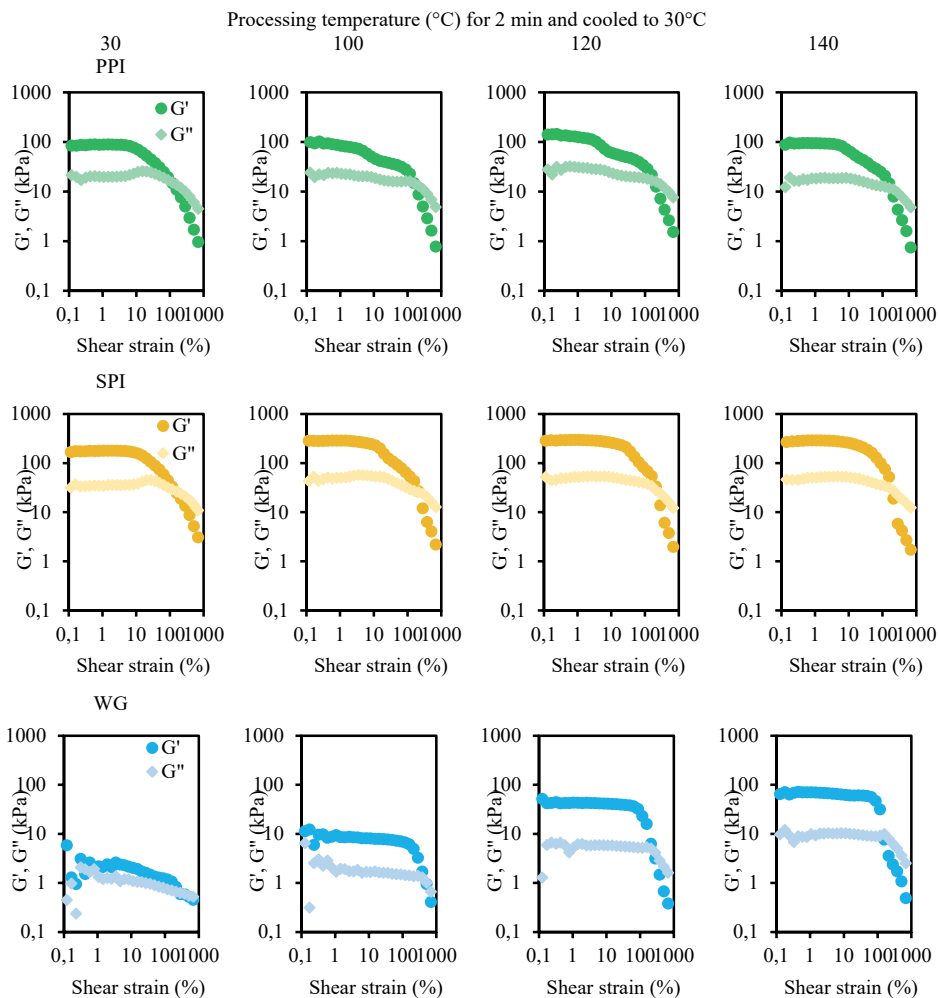


Figure A 4.2. Storage ( $G'$ ) (●, ●, ●) and loss modulus ( $G''$ ) (◐, ◐, ◐) of 40 wt.% PPI, SPI and WG as function of strain amplitude at a frequency of 1 Hz heated to 100°C, 120°C and 140°C and subsequently cooled to 30°C

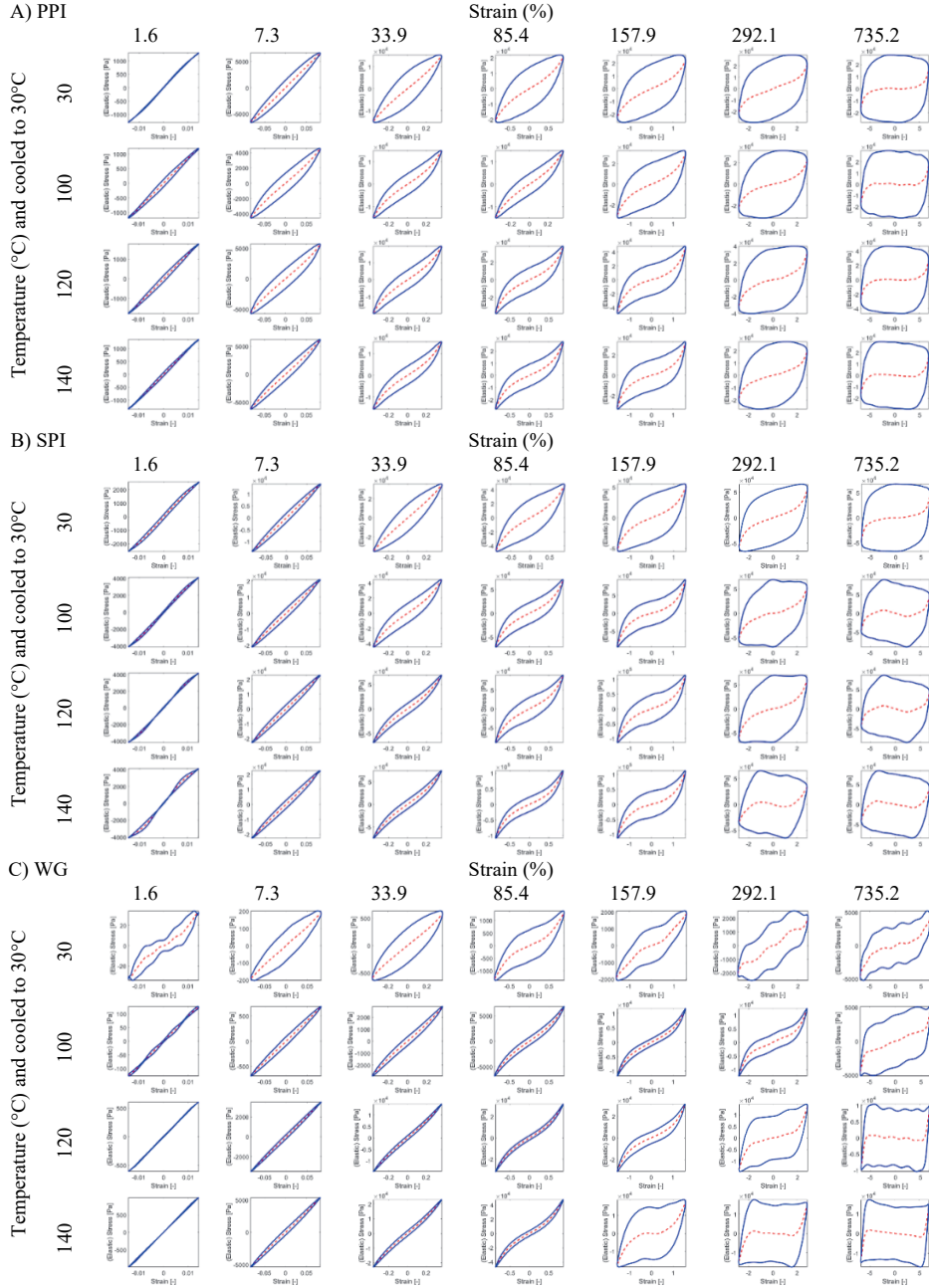


Figure A 4.3. Lissajous curve of stress versus strain amplitude for A) PPI, B) SPI, C) WG at 30°C and heated to 100, 120 and 140°C and subsequently cooled to 30°C, at several strain amplitudes. (normalized stress (solid lines) and viscous stress (dashed lines) vs. strain rate amplitude.)

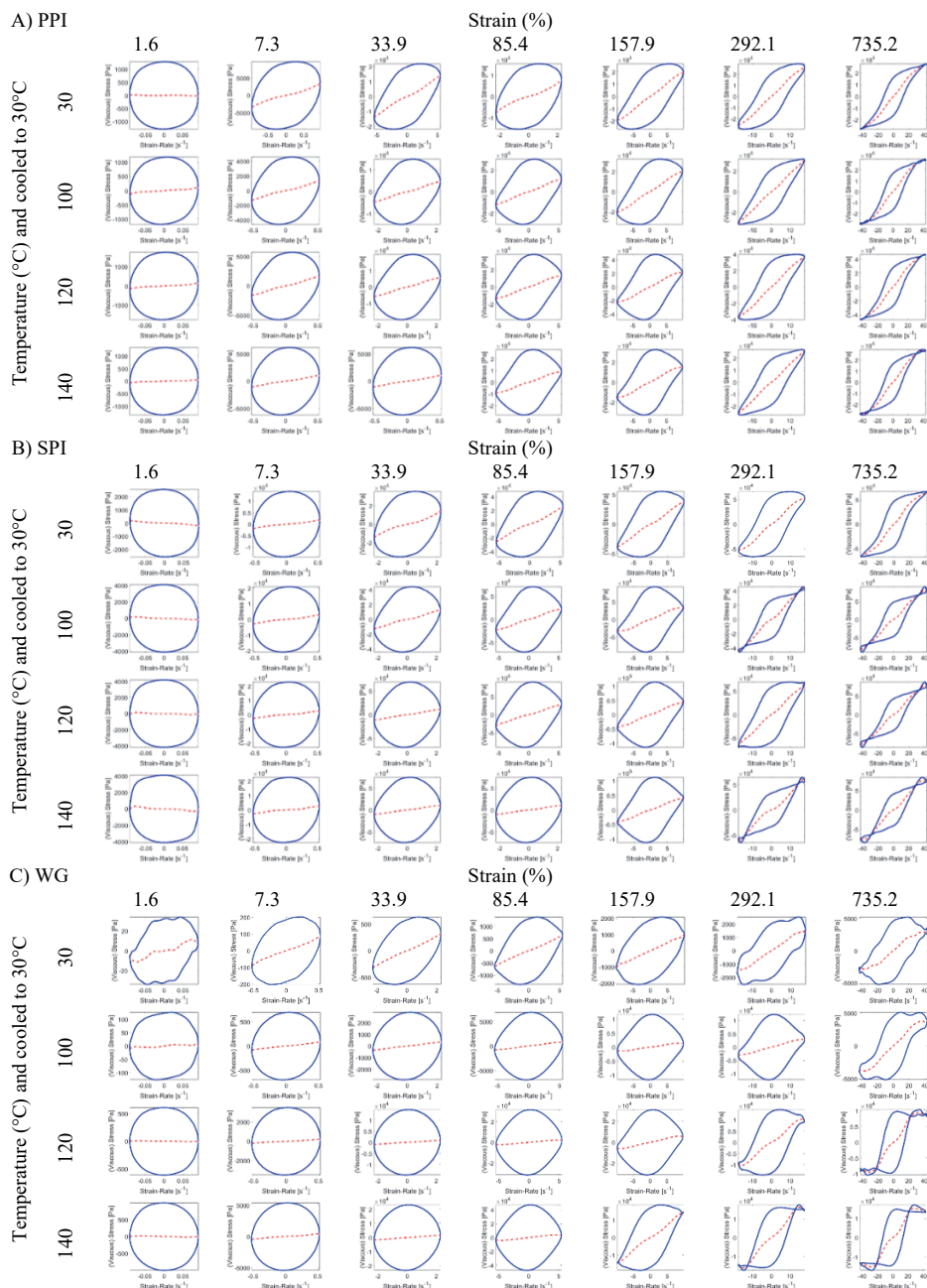


Figure A 4.4. Lissajous curve of stress versus strain rate amplitude for A) PPI, B) SPI, C) WG at 30°C and heated to 100, 120 and 140°C and subsequently cooled to 30°C, at several strain amplitudes. (normalized stress (solid lines) and viscous stress (dashed lines) vs. strain rate amplitude.

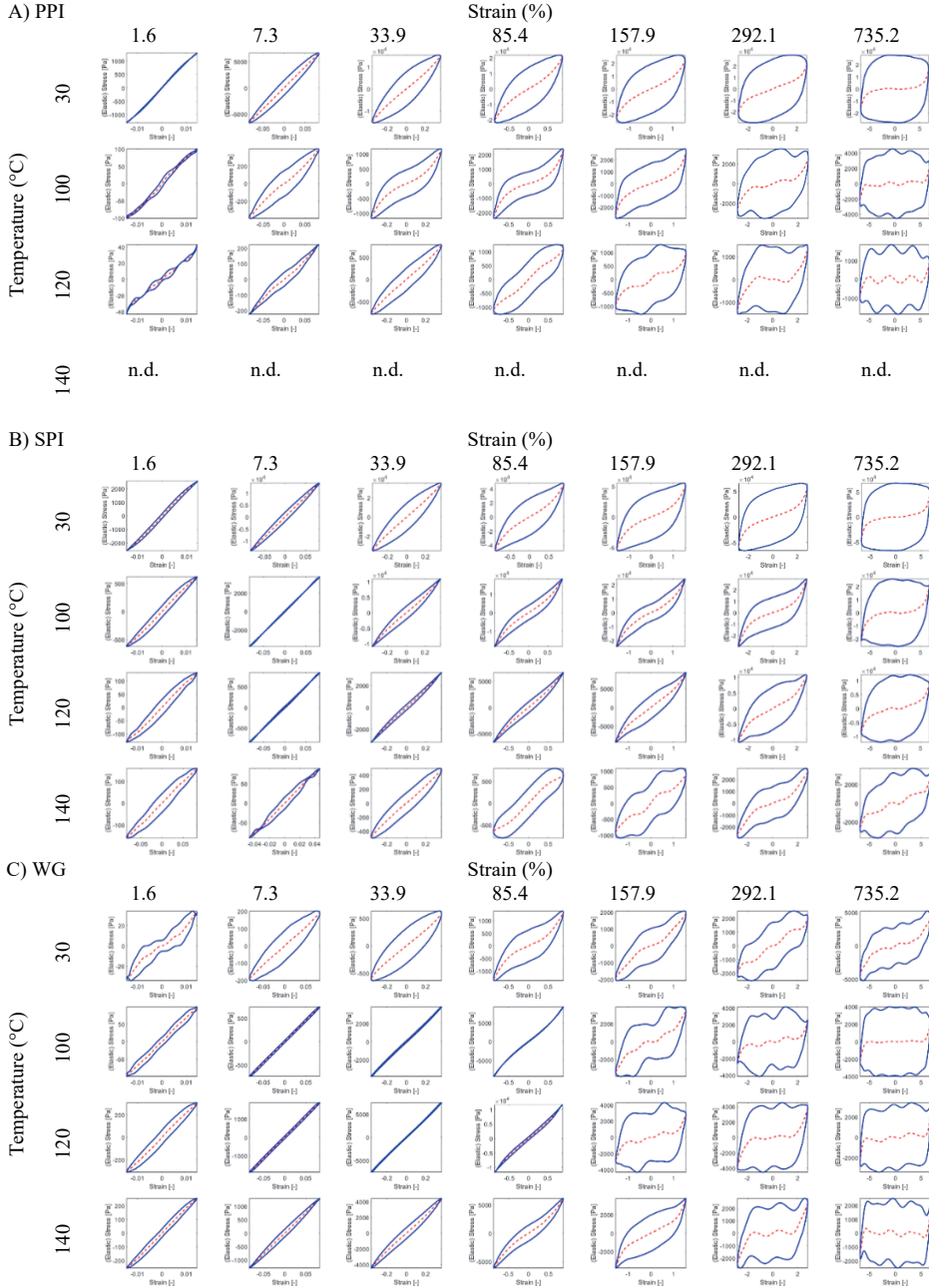


Figure A 4.5. Lissajous curve of stress versus strain amplitude for A) PPI, B) SPI, C) WG at 30, 100, 120 and 140°C, at several strain amplitudes. (normalized stress (solid lines) and elastic stress (dashed lines)). The curves in particular shape in the Lissajous curve indicated an overshoot in the stress, most likely due to a coupling of the elasticity of the sample with instrument inertia effect. For PPI at 140°C the stress values were too small to measure accurately and therefore the Lissajous curves are not shown (n.d. = not determined).

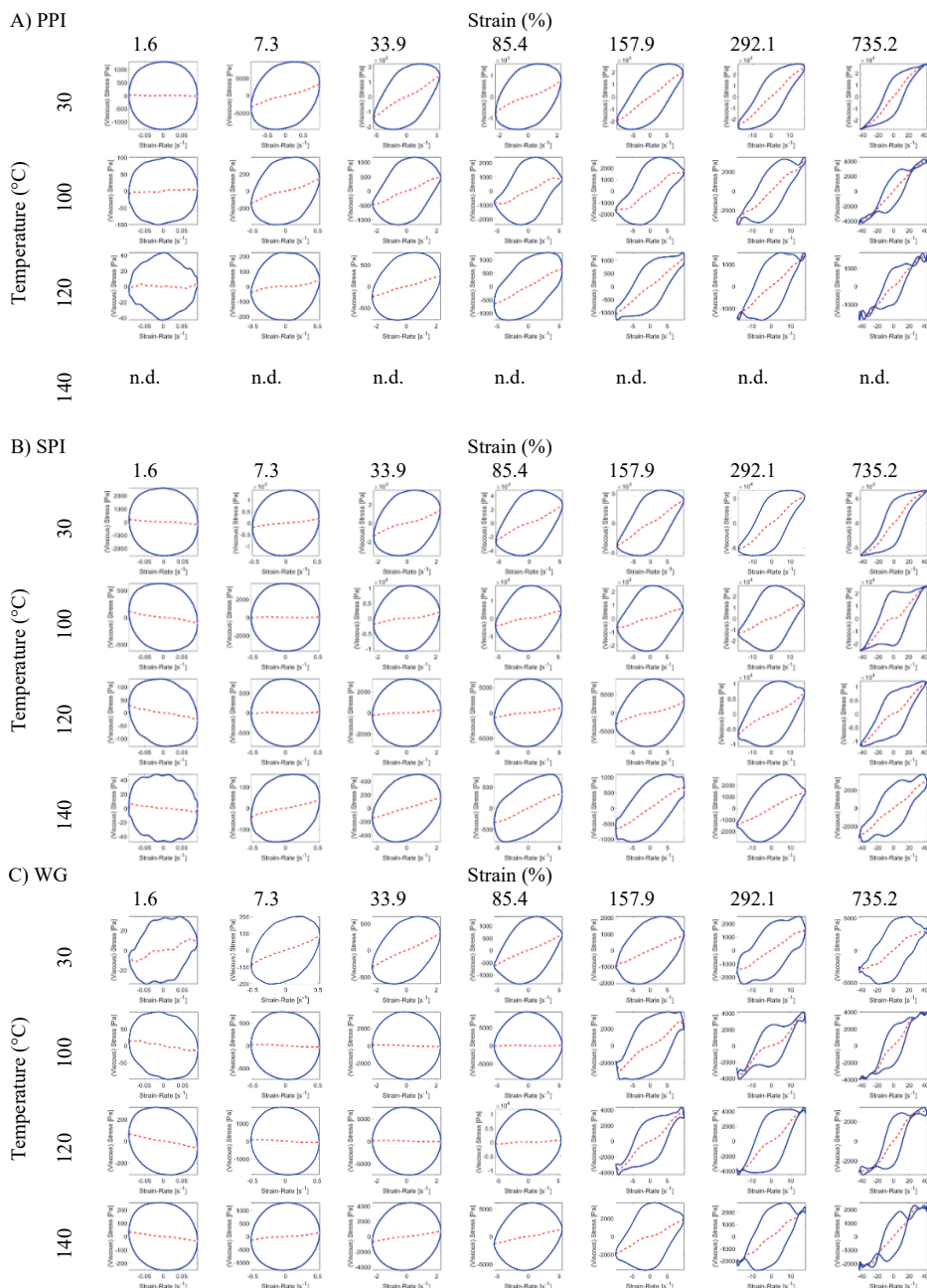


Figure A 4.6. Lissajous curve of stress versus strain rate amplitude for A) PPI, B) SPI, C) WG at 30, 100, 120 and 140°C, at several strain amplitudes. (normalized stress (solid lines) and viscous stress (dashed lines) vs. strain rate amplitude.) For PPI at 140°C the stress values were too small to measure accurately and therefore the Lissajous curves are not shown (n.d. = not determined).







# *Chapter 5*

## *Mapping the texture of plant protein blends for meat analogues*

*This chapter has been published as* Schreuders, F. K. G., Sagis, L. M. C., Bodnár, I., Erni, P., Boom, R. M., & van der Goot, A. J. (2021) Mapping the texture of plant protein blends for meat analogues. *Food Hydrocolloids*, 118, 106753.

## 5.1 *Abstract*

The development of next-generation meat analogues can be accelerated by in-depth knowledge of the rheological properties of dense biopolymer blends. Blends comprising plant proteins such as pea protein isolate (PPI) or soy protein isolate (SPI) combined with wheat gluten (WG) can be used to create a wide range of structures. The objective of this study is to demonstrate the use of texture maps to systematically show the rheological properties of plant proteins under conditions relevant to processing of meat analogue products. The first texture map was constructed by plotting the stress and strain at the end of the linear viscoelastic regime of the strain sweeps and a second map was based on the stress and strain at the crossover point of those sweeps. Next, a colour scheme was used to visualize the relative importance of the viscous and elastic contributions as a function of the strain amplitude and different ratios of each protein in the blend. The maps and schemes showed that heating induced elasticity. In PPI-WG blends, lower strain, stress and elasticity values were obtained for PPI compared with WG. In SPI-WG blends, the texture properties were almost similar for the two components. SPI-WG blends are tougher and more elastic than PPI-WG blends.

## 5.2 Introduction

Despite recent progress, meat analogues still differ from genuine meat in terms of mouthfeel, texture, taste and flavour (Samard & Ryu, 2019b). Therefore, more insight is needed into the functionalities of plant proteins to transform them into materials with even better meat-resembling properties. Rheology can be used to characterize plant protein blends with regard to their functionality for use in meat analogue applications. Meat analogues often contain often ingredients derived from soy, wheat or pea, and blends comprising these plant proteins can be used to create a wide range of structures (Bashi et al., 2019; Jones, 2016). Recent research revealed that fibrous structures were successfully created from pea protein isolate (PPI)-wheat gluten (WG) blends and soy protein isolate (SPI)-WG blends (Grabowska et al., 2014 and Chapter 2). High moisture extrusion cooking of these ingredients is generally done with a dry matter content between 30 and 50 wt.%, maximum temperatures between 100°C and 170°C, and short residence times (2-5 min) (Cornet et al., 2021). Structure formation processes of plant protein blends involve large deformations of the materials. Recently, it was found that a closed-cavity rheometer used in the rubber industry allows accurate determination of the rheological properties of concentrated plant-based protein materials under extrusion relevant conditions (Emin & Schuchmann, 2017). In Chapter 4, single ingredient dispersions (SPI, PPI and WG) were studied under conditions approaching the large-shear conditions relevant for structuring during heating and cooling. Here, we extend these analyses to blends of PPI-WG and SPI-WG with different protein ratios in the blends (20/80, 50/50, 80/20). Measurements of these protein blends under different processing conditions and ratios lead to a large amount of experimental data, but the data do not naturally lead to straightforward insights. Therefore, we propose the use of texture maps and colour schemes to provide overviews of a broad set of rheological measurements.

The starting point of the study is the use of large amplitude oscillatory shear (LAOS) measurements to characterize viscous and elastic properties under conditions relevant for structuring processes. LAOS provides insight into the non-linear response because the modulus depends on the applied strain and strain rate amplitude. For a large amplitude sinusoidal strain input, the shape of the resulting stress waveform often deviates from a sinusoidal wave, with a significant contribution from higher-order harmonics. The LAOS information is typically extracted using Fourier-transform based methods (Hyun et al., 2011). Lissajous curves are used to facilitate the interpretation of a broad set of complex

measurements. The so-called test space of the Lissajous curves is formed by two key parameters of LAOS deformation: frequency and strain amplitude. This test space is often shown in a Pipkin plot (Ewoldt & McKinley, 2017; Pipkin, 1972; Szopinski & Luinstra, 2016; Zhou et al., 2010). To better quantify the transitions in non-linear behaviour, the energy dissipation ratio was calculated and presented by colour contours in the Pipkin plot (Ewoldt et al., 2008; Tao et al., 2019). The energy dissipation ratio ( $\phi$ ) as proposed by Ewoldt et al. (2008) and Ewoldt et al. (2010) is the ratio between the actual dissipated energy and the dissipation of a material showing perfect plastic behaviour. When  $\phi = 0$ , the rheological response is purely elastic, while  $\phi = 1$  implies that the material displays perfect plastic (Ptaszek, 2014). A  $\phi$  of  $\pi/4$  corresponds to a material that behaves as a Newtonian liquid. Texture maps provide a compact overview of the rheological properties for any material of interest. They summarize non-linear rheological information into two-dimensional plots involving only characteristic key parameters. This allows us to map the non-linear rheological behaviour of a great number of samples in an intuitive way. Figure 5.1 exemplifies this approach and includes stress and strain values from previous studies. Although different parameters can be chosen for these plots, most texture maps are based on the stress and strain at the end of the linear viscoelastic (LVE) regime to classify products into four quadrants (Figure 5.1) (Hamann & MacDonald, 1992). Materials in quadrant 1 on the lower left, with low shear stress and shear strain, are classified as a soft, non-shaped texture commonly referred to as “mushy” (such as for grits and similar food materials). Materials in quadrant 2 on the lower right, with low shear stress and high shear strain, are often described as “rubbery” (such as gelatin). Quadrant 3 on the top right, with strong materials with high shear stress and shear strain that are not easily broken, indicates a “tough” texture (for example, fruit leather and dried fruits). Quadrant 4 on the top left, with delicate and easily broken materials with high shear stress and low shear strain, clusters products with a “brittle” texture (such as many baked or confectionery food products; Tunick & Van Hekken, 2010). Although the texture of food can be considered as a sensory property related to the human response, it is also often measured instrumentally in terms of mechanical or rheological proprieties (Altay & Gunasekaran, 2013). The latter studies relate “texture” and used texture maps for instrumental responses such as the shear stress and strain at failure and classify those responses as rubbery, mushy, brittle and tough. Good examples of this approach are available for cheese (Truong & Daubert, 2001), soybean protein (tofu) and gellan gum gels (Truong & Daubert, 2000), cross-linked waxy maize, tapioca, and Amioca

starch dispersions (Genovese & Rao, 2003), mixed gelatine/SPI gels (Ersch et al., 2015) and heat-induced PPI with microbial transglutaminase (Shand et al., 2008).

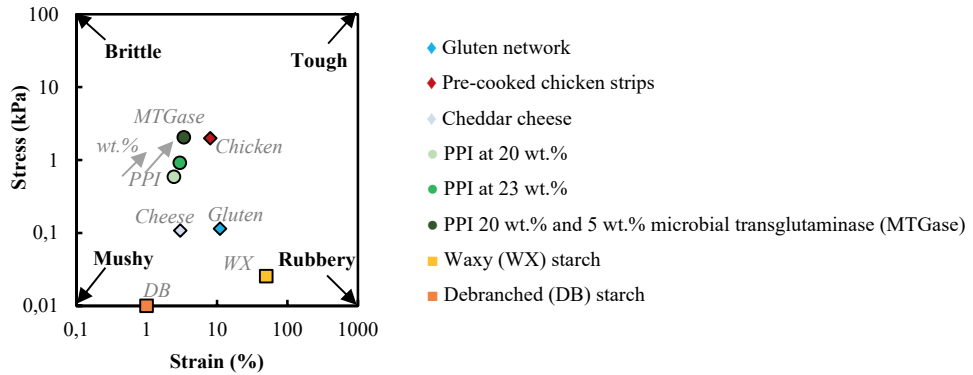


Figure 5.1. A texture map plotting stress versus strain to classify food products into four quadrants. Texture map of different literature values at the end of the LVE regime was analysed for a gluten network, pre-cooked chicken strips and cheddar cheese at 50°C and 0.48 Hz (Mattice & Marangoni, 2020), PPI at 20 wt.%, 23 wt.% and 20 wt.% and 5 wt.% microbial transglutaminase (MTGase) at 20°C and 2 Hz (Moreno et al., 2020), waxy (WX) and debranched (DB) starch at 15 wt.% at 20°C and 0.16 Hz (Precha-Atsawan et al., 2018).

The objective of this study is to map the rheological properties of plant protein blends under conditions relevant to meat analogue processing in a compact way using texture maps and colour schemes. In this article, three rheological parameters are mapped: stress at the end of the LVE regime and the stress-strain crossover point are captured in texture maps, and the energy dissipation ratio is demonstrated with colour schemes. The dissipation ratio is represented by colour contours in strain-protein ratio diagrams.

### 5.3 *Materials and methods*

#### 5.3.1 *Materials*

Pea protein isolate (PPI) (NUTRALYS® F85G) and vital wheat gluten (WG) (VITENS CWS) were both purchased from Roquette Frères S.A. (Lestrem, France). Soy protein isolate (SPI) (SUPRO EX 37 IP) was purchased from Solae (St. Louis, MO, USA). PPI was composed of 78.6 wt.% protein ( $N \times 5.7$ ), WG was composed of 72.4 wt.% protein ( $N \times 5.7$ ), SPI was composed of 80.0 wt.% protein ( $N \times 5.7$ ) on a dry weight basis, according to Dumas measurements. The manufacturer's specifications indicated that the PPI contained 1 wt.% dietary fibre, 9 wt.% lipids, 4 wt.% ash; SPI contained  $\leq 1$  wt.% lipids,  $\leq 5$  wt.% ash; and WG contained 10 wt.% starch, 0.5 wt.% cellulose fibre, 3 wt.% lipids and 1 wt.% ash. PPI, SPI and WG had an average dry matter content of 93.2 wt.%, 92.8 wt.%, and 92.3 wt.%, respectively. Sodium chloride was obtained from Sigma-Aldrich (Zwijndrecht, the Netherlands).

#### 5.3.2 *Preparation of proteinaceous materials*

Different ratios of protein were mixed (20/80, 50/50, 80/20) for the PPI-WG and SPI-WG blends. The sample preparation procedure has been described in detail previously by Grabowska et al. (2014). Protein blends (PPI, SPI, WG, PPI-WG and SPI-WG) were prepared with a final dry matter content of 40 wt.% (Figure 5.2). First, 1 wt.% sodium chloride was dissolved in distilled water. Then the PPI, SPI and WG materials were prepared by dispersing PPI, SPI or WG powder in the saline solution (at room temperature), followed by mixing by hand using a spatula until a homogeneous paste was obtained. The protein material was then hydrated at room temperature for 30 min and the material was covered with Parafilm (Pechiney Plastic Packaging, Chicago, IL, USA) to prevent water evaporation. For the PPI-WG and SPI-WG blends, the WG was mixed into the hydrated PPI or SPI dispersion with a spatula directly before the rheological measurement.

#### 5.3.3 *Rheological properties*

The rheological properties of the protein materials were measured with a closed-cavity rheometer (CCR) (RPA Elite, TA instruments, New Castle, DE, USA) (Emin & Schuchmann, 2017). Approximately 6 g was placed in between two plastic films in the closed cavity, which was sealed with a closing pressure of 4.5 bar to prevent water evaporation at high temperature. The transformation of PPI dispersion into a solid mass can be observed in



Figure 5.2 before and after measurement in the CCR, suggesting a kind of melting of the particles during the measurement. The geometry of the CCR has a radius of 22.5 mm, maximum height of the inner cavity of 4 mm and a biconical opening with an angle of  $3.35^\circ$  for homogeneous transmission of the shear stress to the protein materials. The grooves on the surface of the cones prevent slippage. In this setup, the lower cone oscillates in strain-controlled mode while the upper cone remains stationary. First, the protein material was heated for 2 min at constant temperatures (i.e.  $30^\circ\text{C}$ ,  $100^\circ\text{C}$ ,  $120^\circ\text{C}$  and  $140^\circ\text{C}$ ) without a shear treatment. Subsequently, strain sweep (0.01%-1000%) experiments were performed at these temperatures at a constant frequency (1 Hz). In a second type of test, the protein material was heated at constant temperatures (i.e.  $30^\circ\text{C}$ ,  $100^\circ\text{C}$ ,  $120^\circ\text{C}$  and  $140^\circ\text{C}$ ) for 2 min and cooled to  $30^\circ\text{C}$  at a cooling rate of  $5^\circ\text{C}/\text{min}$  without shear treatment. After that, strain sweep experiments were performed at  $30^\circ\text{C}$  at a constant frequency (1 Hz).

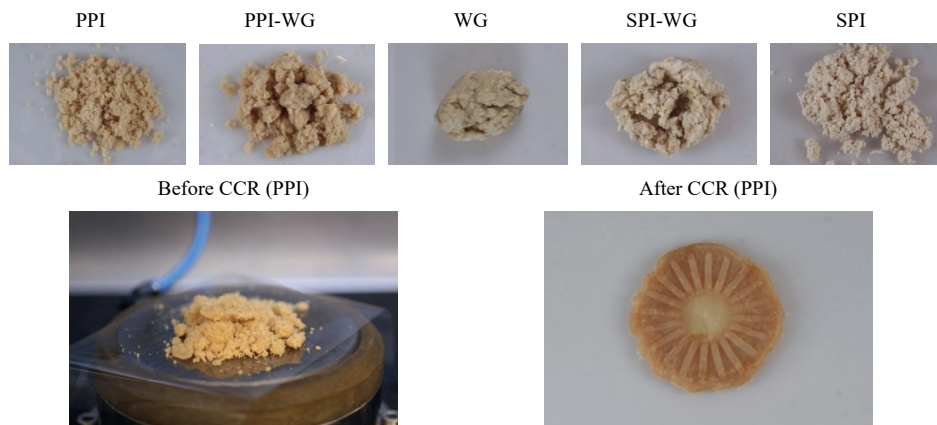


Figure 5.2. Protein blends (PPI, SPI, WG, PPI-WG (50/50) and SPI-WG (50/50)) were prepared with a final dry matter content of 40 wt.%. Pea protein isolate blend with a moisture content of 40 wt.% before (left) and after (right) a rheological measurement in a closed cavity rheometer.

A strain sweep experiment is used to determine the yield stress and the flow stress of a material. The yield stress is defined as the value of the shear stress at the end of the LVE regime. Here, we define this stress as the point where  $G'$  differs more than 5% from its strain-independent value in the LVE regime (Figure 5.3). The flow stress is defined as the value of shear stress at the crossover point where the storage modulus is equal to the loss modulus ( $G' = G''$ ).

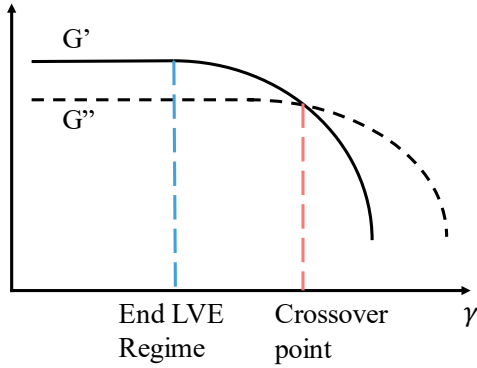


Figure 5.3 The storage modulus ( $G'$ ) and loss modulus ( $G''$ ) versus strain. Vertical lines indicate the crossover point ( $G' = G''$ ) and the end of the linear viscoelastic (LVE) regime (Wereley et al., 2006).

#### 5.3.4 Large amplitude oscillatory shear

The stress and strain data obtained from the LAOS measurements were analysed using the MITlaos software (version 2.1 beta, freeware distributed from MITlaos@mit.edu). The strain amplitude varied in the range of 0.01%-1000% at a constant frequency of 1 Hz at 30°C. Lissajous curves were used to relate the response of the protein materials to the imposed oscillatory strain.

The area enclosed in a Lissajous curve is equal to the energy dissipated per unit volume during one complete cycle of the imposed oscillatory strain. The energy dissipated per unit volume in a single cycle is a function only of the first-order viscous Fourier coefficient ( $G_1''$ ); calculated from the intensity and phase of the first-harmonic):

$$E_d = \oint \sigma d\gamma = \pi G_1'' \gamma_0^2 \quad 5.1$$

The energy dissipated by a perfectly plastic material in a single cycle is equal to

$$(E_d)_{pp} = 4 \gamma_0 \sigma_{\max} \quad 5.2$$

for a given strain amplitude ( $\gamma_0$ ) and a maximum stress ( $\sigma_{\max}$ ).

The ratio of the actual dissipated energy and the perfectly plastic dissipation gives the energy dissipation ratio ( $\varphi$ ) as proposed by Ewoldt et al. (2010).

$$\varphi = \frac{E_d}{(E_d)_{pp}} = \frac{\pi G_1'' \gamma_0}{4 \sigma_{\max}} \quad 5.3$$

## 5.4 Results and discussion

### 5.4.1 Texture maps at the end of the LVE regime

Figure 5.4 presents the texture map of the pea protein isolate (PPI)-wheat gluten (WG) blends at ratios of 0/100, 20/80, 50/50, 80/20 and 100/0 at 30°C, at high temperature (100°C), and heating at 100°C and cooling to 30°C. At 30°C, PPI materials generally became brittle, whereas WG materials were rubbery. A blend of PPI and WG yielded products with intermediate values in hardness and deformability. More PPI in a blend led to increased stress and reduced strain making the product more brittle. Those values are compared with the stress and strain values obtained from products depicted in Figure 5.1. PPI at 40 wt.% is tougher than at 20 wt.% and 23 wt.% PPI (Moreno et al., 2020). The texture properties of PPI (20 wt.%) with 5 wt.% transglutaminase are tougher compared with only PPI (20 wt.%), which have texture properties similar to pre-cooked chicken strips (Mattice & Marangoni, 2020). Upon heating, PPI products changed to more mushy behaviour, whereas WG products became tough (as indicated by the grey arrow in Figure 5.4). More PPI in a blend led to lower stress and strain, making the product mushier. The addition of WG led to higher stress and strain, making the product stronger, but also more stretchable. To summarize, upon heating, a shift in the texture map is observed compared with that at 30°C from brittle to mushy for PPI and from rubbery to tough for WG. A similar shift was observed for blends heated at 120°C and 140°C (Appendix Figure A 5.1). After heating and cooling, more PPI in a blend led to reduced stress and strain, making the product more mushy. More WG, however, resulted in an increase in the stress and strain, making the product tougher. A similar trend from mushy to tough texture upon higher WG content in the blend was observed when blends were heated at 120°C and 140°C and cooled to 30°C (Appendix Figure A 5.1). The strengthening of WG and PPI-WG blends after heating and cooling compared with those at 30°C suggests the formation of additional physical interactions; for example, hydrogen bonding. PPI-only dispersions gave a lower stress and strain after the complete measurement, implying that the network is weakened; for example, a lower ability to form additional physical interactions during cooling.

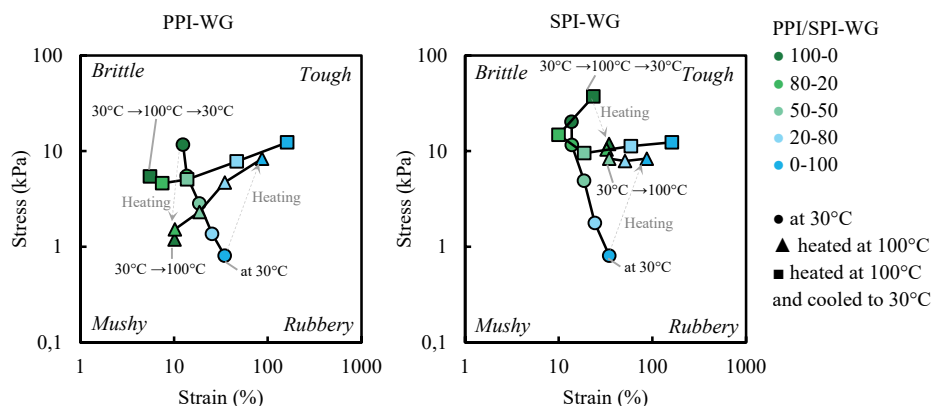


Figure 5.4. Texture map at the end of the LVE regime for PPI-WG and SPI-WG at 40 wt.%. Lines are drawn for visual guidance.

We compared the behaviour of PPI-WG blends with that of soy protein isolate (SPI)-WG blends. Figure 5.4 presents a texture map of the SPI-WG blends at ratios of 0/100, 20/80, 50/50, 80/20, and 100/0. At 30°C, SPI products were commonly brittle. The combination of SPI and WG yielded products with intermediate values in hardness and deformability. The SPI-WG products showed slightly higher stress values compared with PPI-WG products. Heating SPI to 100°C slightly transformed the material to rubbery behaviour (as indicated by the grey arrow in Figure 5.4). The reduced stress observed in the texture maps of both PPI and SPI compared with 30°C could be the effect of weakening of the physical interactions that stabilize the protein material, because the protein materials can now be considered as a melt. Heating WG resulted in tougher behaviour, whereas the SPI-WG blend gave slightly smaller strain values with higher SPI content, making the product less stretchable. An opposite trend was observed at higher temperatures (i.e. 120°C and 140°C) (Appendix Figure A 5.1) and resulted in a higher strain for SPI and a lower strain for WG. The SPI-WG blend showed products with minimum values for stress and strain. For the SPI-WG blends, small differences were observed in the stress and strain values. This is on contrast to the outcomes with PPI-WG blends, where larger differences were observed in the stress and strain values between the components in the blend. After heating and cooling, both SPI and WG products have higher stress and strain compared with those at 30°C and both show strengthening of the network, suggesting the formation of additional physical interactions. This is most pronounced for WG. After heating and cooling, the SPI-WG blend did not show products

with intermediate values in hardness and deformability. This blend showed slightly higher stress compared with at that at 30°C and higher stress values compared with the PPI-WG blend.

The effect of temperature on both PPI-WG and SPI-WG blends at a 50/50 ratio is presented in a texture map in Figure 5.5, at 30°C, at high temperature (100°C, 120°C, 140°C) and after heating at 100°C, 120°C, 140°C and cooling to 30°C. The plant protein blends heated to different temperatures covered a wide range of stresses and strains. Without heating, the stresses and strains of the SPI-WG and PPI-WG blends were similar. For the PPI-WG blends, heating at higher temperatures leads mainly to softer products, whereas, for the SPI-WG blends, heating leads to a tougher/rubbery character. After heating and cooling, both PPI-WG and SPI-WG products became tougher, meaning that heating resulted in a stronger material for the blends. This increase after 140°C was also observed in a previous study in a tensile test at room temperature on PPI-WG product, sheared ( $39 \text{ s}^{-1}$ ) and heated (140°C) in the shear cell (Chapter 2). In general, the SPI-WG blends are tougher than the PPI-WG blends.

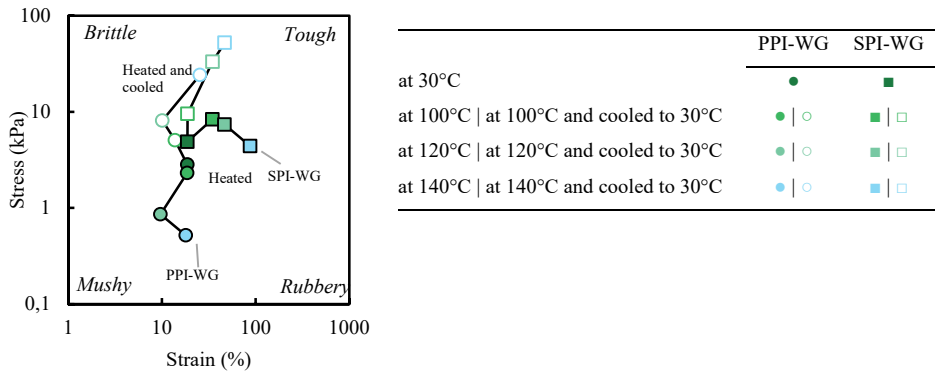


Figure 5.5. Texture maps at the end of the LVE regime of 40 wt.%, 50/50 blend of PPI-WG and SPI-WG. Lines are drawn for visual guidance.

#### 5.4.2 Texture maps at the crossover point

The texture properties at the crossover point of both the PPI-WG and SPI-WG blends are shown in Figure 5.6. At 30°C, PPI is characterized as brittle, whereas WG is characterized as rubbery. Combining PPI and WG in a blend yielded a lower intermediate crossover point in hardness and deformability. Heating made PPI products softer and WG products became less deformable. More PPI in a blend led to reduced crossover stress, whereas more WG in

the blend led to increased crossover stress. Heating to higher temperature resulted in a decreased stress for PPI (Appendix Figure A 5.2). After heating and cooling, the PPI and WG materials became comparable with those at 30°C, however, for WG a further increase in the temperature (i.e. 120°C and 140°C) resulted in larger crossover stress and smaller crossover strain (Appendix Figure A 5.2).

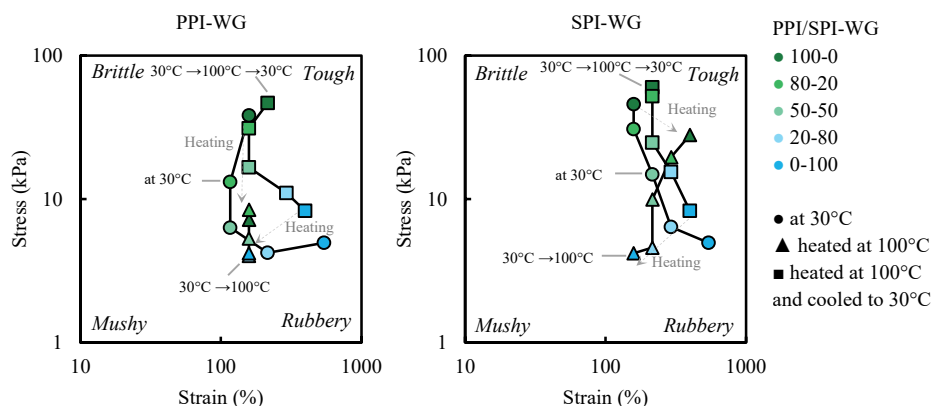


Figure 5.6. Texture map at the crossover point for PPI-WG and SPI-WG at 40 wt.%. Note that the scales of the x-axis and y-axis are different from those in Figures. 5.4 and 5.5. Lines are drawn for visual guidance.

SPI-based products were commonly brittle, whereas WG products were rubbery at 30°C. With both SPI and WG, intermediate values in hardness and deformability were obtained in those products. Heating SPI shifted the crossover point to higher strain values and slightly lower stress values, whereas WG products became less deformable upon heating. Higher temperatures resulted in decreased stress for SPI. By combining SPI and WG in a blend, products with intermediate values in hardness and deformability were obtained. A further increase in the heating temperature (i.e. 140°C) gave a smaller difference between the stress and strain values of SPI and WG (Appendix Figure A 5.2). After heating and cooling, the SPI and WG products became comparable to those at 30°C, however, increasing the temperature (i.e. 120°C and 140°C) resulted in increased stress of the crossover point for SPI and increased stress and decreased strain of the crossover point of WG (Appendix Figure A 5.2).

A texture map for the crossover points is presented in Figure 5.7 for both PPI-WG and SPI-WG blends at a 50/50 ratio at 30°C, at high temperature (100°C, 120°C, 140°C) and after

heating at 100°C, 120°C, 140°C and cooling down to 30°C. At 30°C, the crossover stress and strain values indicated that the SPI-WG blend became tough, whereas the PPI-WG blend became mushy. For both PPI-WG and SPI-WG blends, heating at higher temperatures led to reduced crossover stress, making the product softer. After heating and cooling, both PPI-WG and SPI-WG products had higher stress compared with those at 30°C, meaning that heating resulted in a stronger material. After heating and cooling, the PPI-WG and SPI-WG blends at high temperatures resulted in higher stress, making both materials stronger. The results presented here confirm that the SPI-WG blends are tougher than the PPI-WG blends.

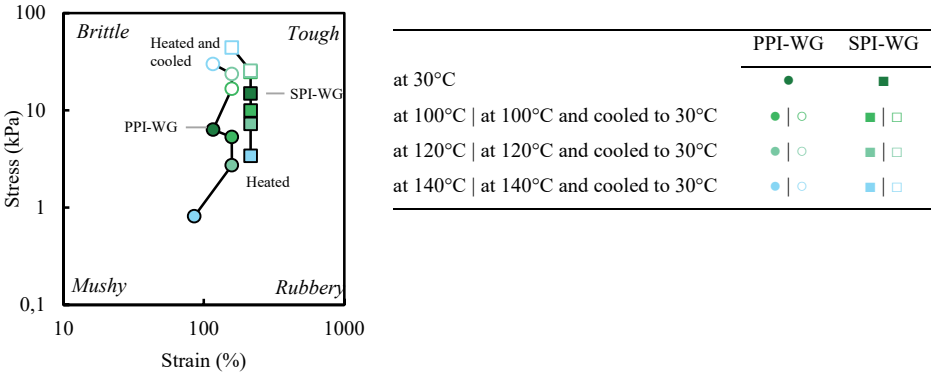


Figure 5.7. Texture maps at the crossover point of PPI-WG and SPI-WG at 40 wt.%. Note that the scales of the x-axis and y-axis are different from those in Figures. 5.4 and 5.5. Lines are drawn for visual guidance.

### 5.4.3 Colour scheme to describe the dissipation ratio

A more detailed assessment of the non-linear viscoelastic behaviour of protein materials was obtained with Lissajous curves. The dissipation ratio was then calculated to summarize the essential non-linear behaviour (Ewoldt et al., 2008, 2010; Klost et al., 2020; Tao et al., 2019). The values are presented in a colour scheme to facilitate comparison. The left-hand panel of Figure 5.8 shows these colour schemes for PPI-WG and SPI-WG. In the right-hand panel of Figure 5.8, the corresponding elastic Lissajous curves are shown for the grid values of imposed strain amplitude and protein ratios marked by the crosses in the left-hand panel (colour scheme of the dissipation ratio). In the following, the dissipation ratios with increasing strain amplitudes of the PPI-WG and SPI-WG blends at ratios of 0/100, 20/80, 50/50, 80/20, and 100/0 (Figure 5.8) are discussed. At 30°C, PPI showed an increasing dissipation ratio for increasing strain amplitude. The elastic Lissajous curves had a line or

narrow ellipse shape for small strain amplitudes, implying that the response of this material was mostly elastic at these strains. With a further increase in the strain amplitude, the area encompassed by the curve became wider. This is an indicator of increased viscous dissipation that allows the protein particles in the matrix to flow past each other, and eventually structure breakdown. The red dashed lines indicate the elastic contributions to the total stress. The dissipation ratio for increasing strain amplitudes remained constant for WG. The PPI-WG blend yielded products with intermediate dissipation ratios. At equal strain amplitude, more PPI in a blend gave a larger dissipation ratio. Heating WG lowered the dissipation ratios for almost all strain amplitudes and a more sudden transition to viscous behaviour. For WG, narrow ellipses were observed at low strain amplitude, indicating the predominant elastic behaviour. The dissipation ratio of PPI did not change upon heating, as indicated by only minor changes in the Lissajous curves of PPI. More PPI in the blend resulted in a gradual increase in the dissipation ratio for increasing strain amplitudes. Most PPI-WG blends yielded intermediate dissipation ratios. After heating and cooling, both PPI and WG became more elastic for a longer strain amplitude compared with the unheated materials. Again this abrupt transition in dissipation ratio for increasing strain amplitude was most pronounced for WG and also present in the blend containing a higher WG content.



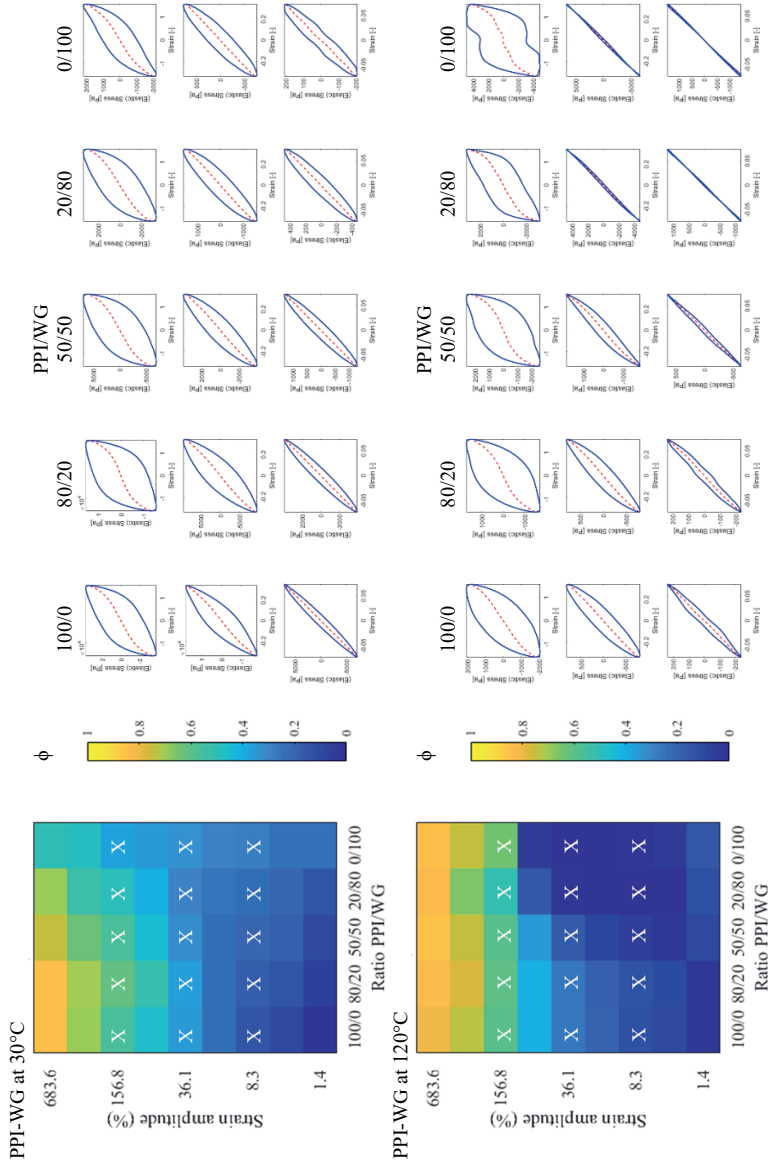


Figure 5.8. Colour scheme of the dissipation ratio ( $\phi$ ) in a strain-protein ratio diagram for a PPI-WG and SPI-WG blend at different ratios at 30°C, heated at 120°C, and heated at 120°C and cooled to 30°C. The colour corresponds to the value of the dissipation ratio ( $\phi$ ) in the colour bar:  $\phi = 0$ , elastic;  $\phi = \pi/4$ , Newtonian liquid;  $\phi = 1$ , perfect plastic. The colour scheme of the dissipation ratio at increasing temperatures is shown in Video 1 (including heating at 100°C and 120°C and heated at 100°C and 120°C and cooled to 30°C). Right: Lissajous curve of stress versus strain amplitude at three different strain amplitudes corresponding to the X symbol in the left panel (individual plots of normalized stress [solid lines] and elastic stress [dashed lines] vs. strain).

PPI-WG heated at 120°C and cooled to 30°C

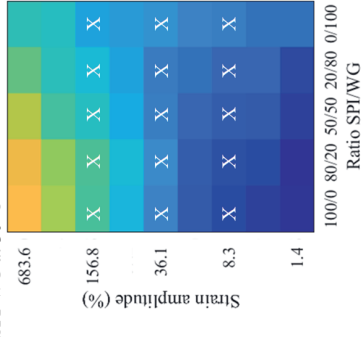
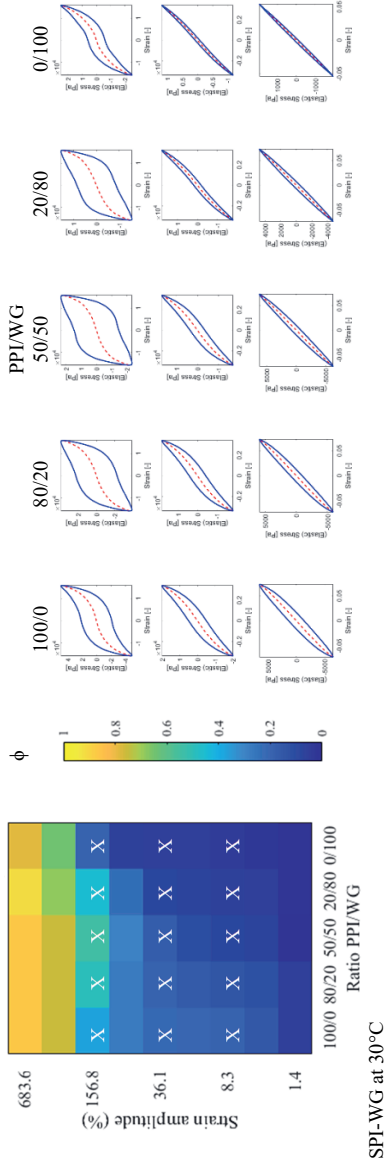
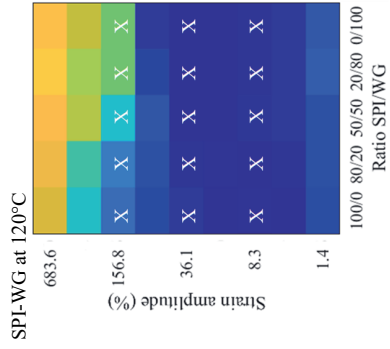


Figure 5.8 (continued)



SPI-WG heated at 120°C and cooled to 30°C

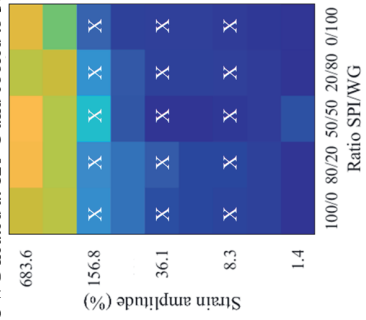
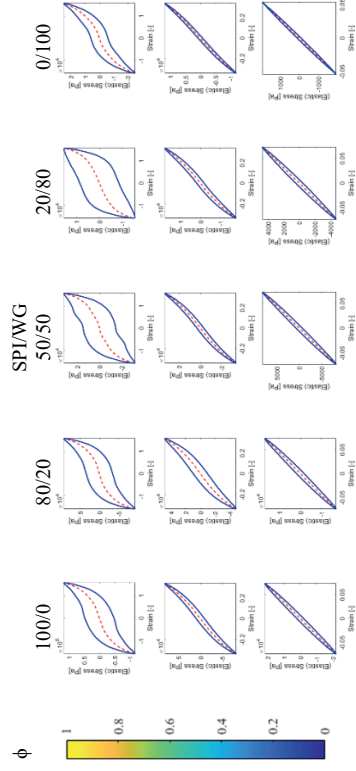
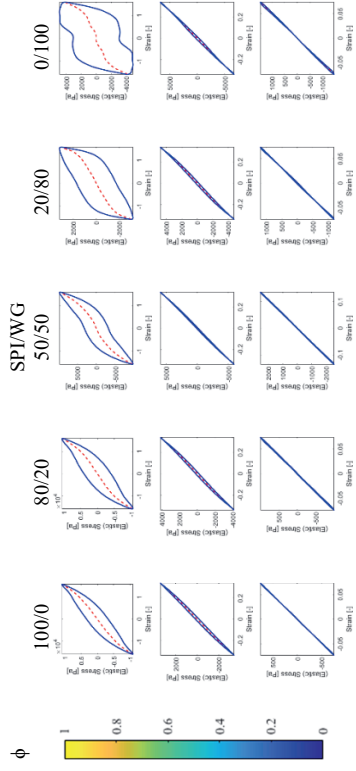


Figure 5.8 (continued)



We now compare the dissipation behaviour of PPI-WG blends with that of SPI-WG blends at different temperatures. The dissipation ratios of unheated SPI-WG and PPI-WG blends at ratios of 20/80, 50/50 and 80/20 were comparable. SPI only showed a larger dissipation ratio for increasing strain amplitudes. Both SPI-WG and PPI-WG blends resulted in products with intermediate dissipation ratios. Heating led to lower dissipation ratios for SPI, WG and SPI-WG blend and resulted in similar elastic behaviour in the case of the SPI-WG blend for different protein ratios. In the Lissajous curves, narrow ellipses were observed at low strain amplitude, indicating the predominant elastic behaviour. Extensive deformation led to a sudden onset of viscous/plastic behaviour. After heating and cooling, both SPI and WG became more elastic across a wider range of strain amplitudes compared with untreated materials. The SPI-WG blend (50/50) showed lower dissipation ratios (~36% strain amplitude) compared with SPI and WG at similar strain amplitude, indicating increased elasticity. That could indicate synergetic effects between SPI and WG, indicative of specific interactions.

#### *5.4.4 Combining texture maps and colour schemes to describe the dissipation ratio*

Texture maps give an efficient and quantitative summary that give food product development teams and process engineers insight into the effects of ingredients and processing conditions on the material properties relevant to product texture. Table 5.1 gives an overview of all the results presented in the texture maps and colour schemes. Both maps revealed that SPI-WG is tougher than PPI-WG and that an increase in WG in the blend resulted in a more rubbery material. Similar differences between the protein materials were described in previous studies even though a much lower protein concentration (~10 wt.%) was investigated than the concentration commonly used in high moisture extrusion cooking (>30 wt.%). As observed in previous studies, PPI forms weaker and less elastic gels compared with SPI (Batista et al., 2005; Lam et al., 2018; O’Kane et al., 2004). Batista et al. (2005) established a relationship between a stronger gel and more protein unfolding during and after thermal treatment. After protein unfolding, protein aggregates are formed through hydrophobic interactions and strengthened further due to the formation of disulphide bridges. The total number of cysteine residues differs between types of protein and the number of potential disulphide bonds that can be formed. The accessibility of free thiol groups and disulphide bonds are both important

to network formation. Gluten contains relatively large amounts of cysteine (Shewry & Tatham, 1997), whereas pea protein contains relatively low amounts.

*Table 5.1. Summary of the texture maps and colour schemes presented in this paper (marked with an asterisk) after heating and cooling.*

	Texture map		Colour scheme
	End of the LVE regime	Crossover point	Dissipation ratio
Difference between products*			
SPI-WG compared to PPI-WG	Tougher	Tougher	More elastic
Effect of heating*			
WG	Tougher	Slightly more brittle	More elastic
SPI	Slightly tougher	Slightly tougher	More elastic
PPI	Mushy	Slightly tougher	Slightly more elastic
SPI-WG	Stronger/tougher	Stronger/tougher	More elastic
PPI-WG	Stronger	Stronger/tougher	Slightly more elastic
Increased ratio the WG in blend			
SPI-WG	Rubbery	Rubbery	-*
	Rubbery/more deformable*	Rubbery*	
PPI-WG	Rubbery	Rubbery	More elastic*
	Tougher*	Rubbery*	

Also, differences between the texture maps were observed. The effect of heating was observed differently in both maps. When comparing the texture map at the end of the LVE regime with the texture map at the crossover point, we actually compare the effect of small strain in the LVE regime and larger strain in the non-linear regime. At small strains, the material is deformed more after heating and cooling, making the material mushier for PPI. However, WG became a tougher material. This could be related to weakening of the physical interaction for PPI and the formation of additional physical interactions for WG upon heating. At larger strains, at the crossover point in the texture map, both the temperature and strain amplitude will influence the material. At larger strain, the protein aggregates in the matrix start to flow past each other. Heating and cooling transformed PPI into a slightly tougher product and WG into a more brittle product. This texture map in the non-linear region is

especially interesting for shear-induced structuring where the material is sheared beyond the linear regime. The linear and non-linear regimes also explain the different response of the protein materials after heating. Therefore, we conclude that analysing the combination of the two texture maps is important.

The texture of plant-based protein products is influenced by both composition and process conditions. The main question is the mechanisms underlying the differences in stresses and strains of the blends. Two different situations can be observed in the texture maps:

- 1) A blend gives intermediate hardness and deformability, and intermediate values in stress and strain values. Heating PPI makes the blend weaker and less deformable, whereas WG increases the strain and stress making the gels tougher. For PPI-WG blends, the end of the LVE regime was observed in the blend with intermediate values in hardness and deformability of PPI and WG. Similarly for non-linear rheology, intermediate dissipation ratio values were observed.
- 2) Blends yield intermediate values in hardness and deformability but minimum stress and strain values. For SPI-WG, this behaviour was observed in the texture maps. We hypothesize that this could be due to phase inversion, the point in the texture map where blend components exchange their discontinuity. The blend with low WG content is SPI continuous. As the WG content increases in the blend, a continuous WG network is formed or a bi-continuous WG network that is entrapping the SPI network. In the dissipation ratio maps, a lower dissipation ratio was observed in the blend compared with the single components, which indicated increased elasticity in the blend. Furthermore, the stress and strain values of SPI and WG in the SPI-WG blend are closer together in the texture and dissipation maps, whereas the PPI and WG phases in the PPI-WG blend show a distinct difference.

### 5.5 Conclusion

The rheological properties of SPI, PPI and blends of these with WG were quantified using texture maps and dissipation ratios obtained from large-deformation Lissajous curves. Different composition and processing conditions were investigated. We showed that the three rheological parameters, (1) stress at the end of the LVE regime, (2) the stress-strain crossover point and (3) the dissipation ratio, provide a useful rheological fingerprint of these food products and materials.

As observed in the maps and schemes, heating induced more elasticity. In PPI-WG blends, PPI has lower strain, stress, and elasticity compared with WG. In SPI-WG blends, the texture properties are almost similar for the two components. SPI-WG blends are tougher and more elastic compared with PPI-WG blends. Mapping the rheological properties at the end of the LVE regime, the crossover point as well as the dissipation ratio as a function of small and large strain amplitudes, is useful for further understanding and use of dense protein blends.

## 5.6 Appendix

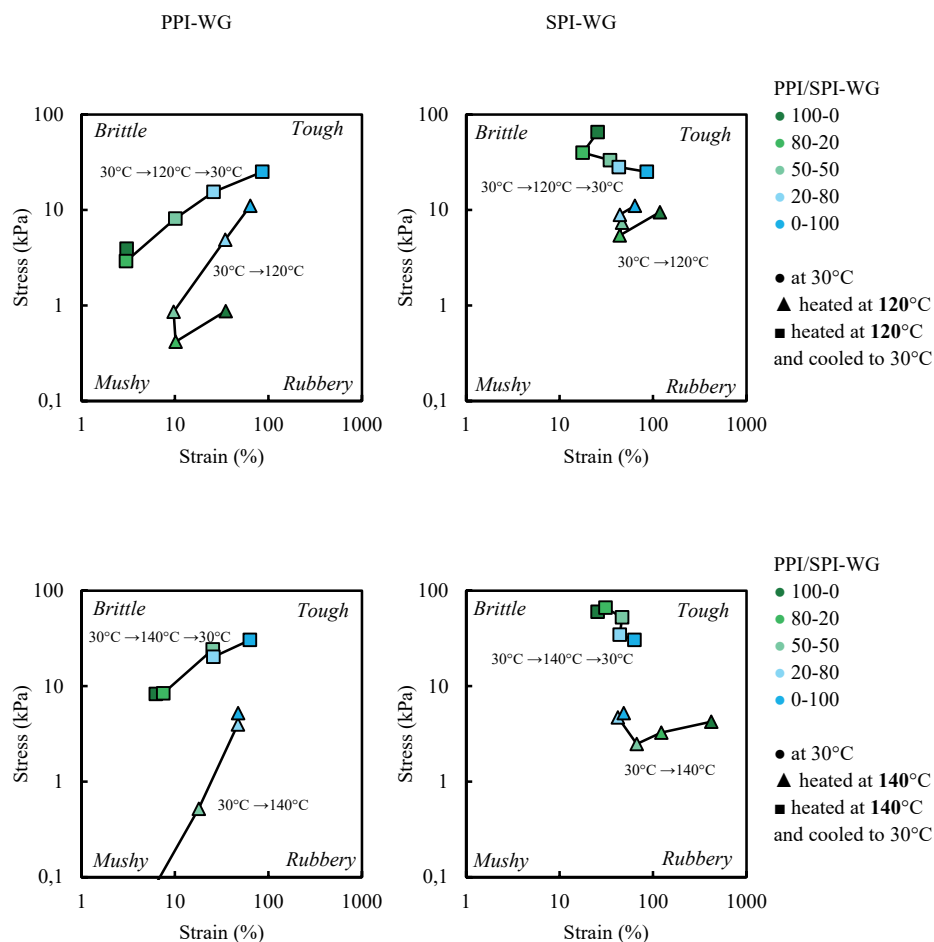


Figure A 5.1. Texture map at the end of the LVE regime for PPI-WG and SPI-WG at 40 wt.% at 120°C and 140°C and heated at 120°C and 140°C and cooled to 30°C. Lines are drawn for visual guidance.



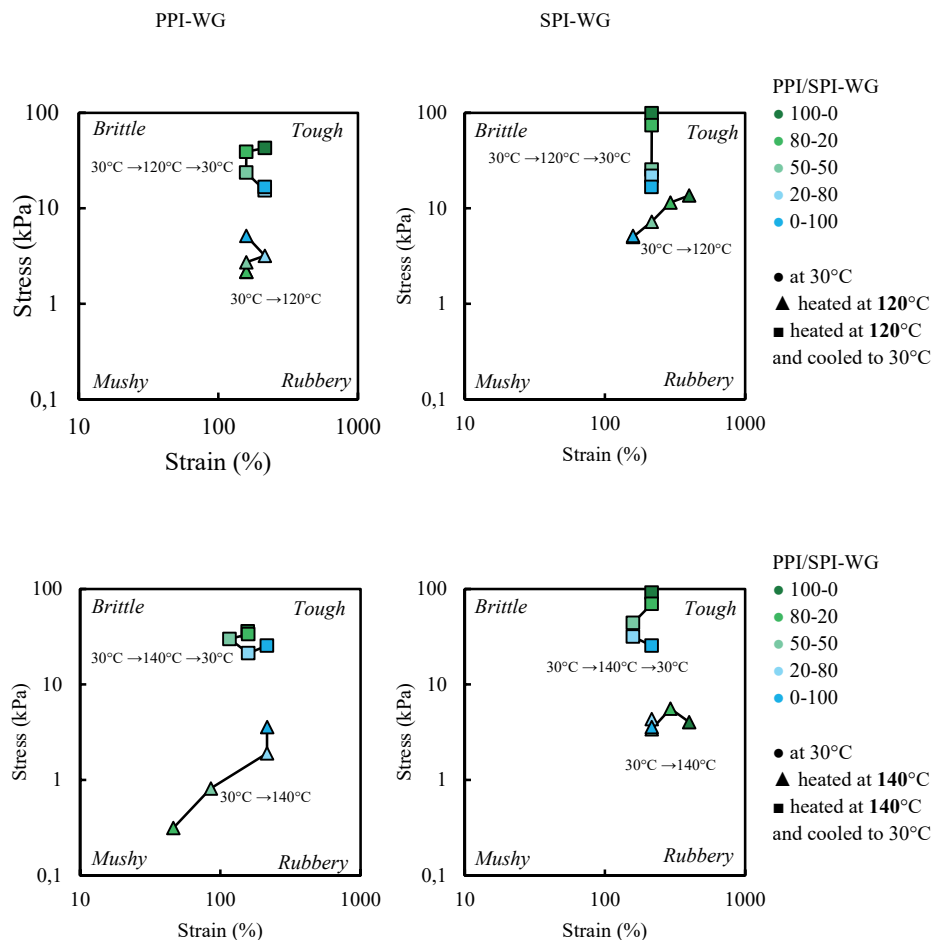


Figure A 5.2. Texture map at the crossover point of PPI-WG and SPI-WG at 40 wt.% at 120°C and 140°C and heated at 120°C and 140°C and cooled to 30°C. Note that the scales of the x-axis and y-axis are different from those in Figures A. 5.4 and 5.5. Lines are drawn for visual guidance.



# *Chapter 6*

*Structure formation and non-linear rheology of blends of  
plant proteins with pectin and cellulose*

*This chapter is submitted as* Structure formation and non-linear rheology of blends of plant proteins with pectin and cellulose, Schreuders, F. K. G., Schlangen M., Bodnár, I., Erni, P., Boom, R. M., & van der Goot, A. J.

## 6.1 *Abstract*

Blends of proteins and carbohydrates are of interest because of their ability to form fibrous products that resemble meat products. Here the structuring potential of pea protein isolate (PPI), soy protein isolate (SPI) and blends of these with pectin/and or cellulose is investigated. A pronounced fibrous structure was formed with blends of SPI/pectin, and PPI/pectin (95:5 and 93:7). In the case of SPI blends, a fibrous product was also anisotropic in terms of mechanical properties (directional tensile strength analysis). For PPI blends, a fibrous morphology did not always lead to mechanical anisotropy.

Differences in structuring potential of the various blends were studied using oscillatory rheological experiments. It was shown that PPI products were mushier than products containing SPI. Also, the addition of carbohydrates to the blend resulted in mushier products. This was most pronounced for blends with pectin, which was attributed to the combined effects of a decrease in pH and/or water redistribution between the two phases. After heating, all blends gained elasticity, which was most pronounced for blends with pectin. This increased elasticity is now likely to be an important factor in the ability of the blends to form fibrous products.

## 6.2 Introduction

Meat analogues that mimic the sensorial properties of meat have recently emerged as a route to help consumers reduce their intake of animal-based products by replacing them with analogous plant-based products (Elzerman, Hoek, van Boekel, et al., 2011; Hoek et al., 2011). High moisture extrusion cooking is often applied to create fibrous meat analogues. Previous research revealed that a fibrous texture could also be created by applying well-defined shear flow on soy protein isolate (SPI)-wheat gluten (WG) blends, SPI/pectin blends, and pea protein isolate (PPI)-WG blends (Dekkers et al., 2018; Dekkers, Nikiforidis, et al., 2016; Grabowska et al., 2014 and Chapter 2). As PPI has a lower environmental impact and it is relatively less allergenic in comparison with SPI (Lam et al., 2018; Stone et al., 2015), it is of interest to study whether PPI can yield anisotropy without using WG, for example, in combination with other components.

PPI/pectin blends have been studied by Lan et al. (2018), at low protein/pectin concentrations to study complex formation. At higher protein/carbohydrate concentrations, mixing of the protein/carbohydrate is less likely to occur as described in a previous study for SPI/pectin blends (Dekkers et al., 2018). It is more appropriate to consider this biopolymer blend as a two-phase product that can be considered as a capillary filled gel. Both phases absorb part of the water, and the blend can be considered as a water-in-water emulsion. Upon shearing a SPI/pectin blend at high temperatures, the pectin domains deform and align in the shear flow direction and after cooling this SPI/pectin blend shows a fibrous product.

Characterizing the rheological properties of the materials during thermomechanical processing is as an important step to further understand the structure formation process. Most studies use small amplitude oscillatory shear (SAOS) analysis to describe the rheological properties of foods. In SAOS, the modulus is independent of the applied strain and strain rate amplitude and provides the properties in the linear viscoelastic (LVE) regime. Large amplitude oscillatory shear (LAOS) measurements can be used to provide insight in the non-LVE regime to gain insight into the structure formation and break down of solid foods as well as the resulting sensorial properties of food products (Alghooneh et al., 2019; Anvari & Joyner (Melito), 2017; Melito et al., 2013). The latter study on cheeses showed that structural differences result in different non-linear behaviour and different texture. Recently, LAOS measurements performed at high temperature provided information relevant for the structure formation processes by quantifying the changes in the properties of the various components

(Chapter 4). A closed-cavity rheometer (CCR) allows accurate determination of the rheological properties of concentrated plant-based protein materials at elevated temperatures (varied from 25°C to 230°C), defined frequency (up to 50 Hz), shear strain (up to 5000%) and pressures (up to 8500 kPa) (Dekkers et al., 2018; Emin & Schuchmann, 2017 and Chapter 3). The CCR was found to mimic the process conditions inside a shear cell or an extruder (Dekkers et al., 2018; Emin & Schuchmann, 2017). In a previous study of single-ingredient systems (SPI, PPI, and WG) as well as blends (PPI/WG and SPI/WG), conditions were used that approach the large-shear deformations responsible for structuring during heating and cooling (Chapter 4 and 5). Here, we extend this analysis to blends containing a protein phase (SPI or PPI), a soluble carbohydrate phase (pectin), and an insoluble carbohydrate phase (cellulose).

In this study, we used LAOS testing to provide information on structure formation as well as physical and chemical changes. The latter are important because a previous study on SPI/pectin blends (Dekkers et al., 2018) revealed that the rheological properties of the blend during processing were not only determined by physical factors. Additional factors were (1) a decrease in the pH due to  $\beta$ -elimination and/or demethoxylation of the pectin, (2) release of galacturonic acid, and (3) water redistribution between the two phases. Both the chemical and physical instabilities can affect the interactions between the two phase in a blend.

Our first question is whether PPI and SPI in combination with carbohydrates (pectin and/or cellulose) can yield a fibrous morphology in a similar manner as reported for SPI/pectin blends previously (Dekkers, Nikiforidis, et al., 2016)? In this article, we relate the shear-induced structures observed on a micro- (~5-300  $\mu\text{m}$ ) and macro- (~1-30 mm) scale and the mechanical properties of the resulting fibrous materials with the non-linear rheology using a closed-cavity rheometer to gain insight into the structure formation as well as physical and chemical changes.

## 6.3 *Materials and methods*

### 6.3.1 *Materials*

Pea protein isolate (PPI) (NUTRALYS® F85G) was purchased from Roquette Frères S.A. (Lestrem, France). Soy protein isolate (SPI) (SUPRO EX 37 IP) was purchased from Solae (St. Louis, MO, USA). PPI consisted of 78.6 wt.% protein ( $N \times 5.7$  (Breese Jones, 1931)), and SPI contained 80.0 wt.% protein ( $N \times 5.7$  (Breese Jones, 1931) on a dry weight basis, according to Dumas measurements (Nitrogen analyzer, FlashEA 1112 series, Thermo Scientific, The Netherlands). The manufacturer's specifications indicated that the PPI contained 1 wt.% dietary fibre, 9 wt.% lipids, 4 wt.% ash; and SPI contained  $\leq 1$  wt.% lipids and  $\leq 5$  wt.% ash. PPI and SPI had an average dry matter content of 93.2 wt.% and 92.8 wt.%, respectively. Pectin from citrus peel (SLBQ6929V) (high methylated, 92.2 wt.% dry matter content), cellulose (S3504, Type 20, 20  $\mu\text{m}$ ) (97.1 wt.% dry matter content) and all chemicals used were obtained from Sigma-Aldrich (Zwijndrecht, the Netherlands).

### 6.3.2 *Preparation of proteinaceous materials*

PPI/carbohydrate and SPI/carbohydrate blends (pectin, cellulose and a combination of pectin and cellulose (1:1)) were studied using a total dry matter content of 45 wt.% for all blends. The total dry matter weight was 1 wt.% sodium chloride, 44 wt.% protein and carbohydrates, implying a fixed moisture content of 55 wt.% added via demi water. The mass ratio of PPI or SPI to carbohydrate was varied by replacing part of the PPI or SPI with the carbohydrate (Table 6.1). The PPI or SPI were prepared by dispersing 44 wt.% PPI or SPI powder in the sodium chloride solution (at room temperature), followed by mixing using a spatula until a homogeneous paste was obtained. The protein material was then covered with Parafilm (Pechiney Plastic Packaging, Chicago, IL, USA) to prevent water evaporation and left to hydrate at room temperature for 30 min. For the blends, the carbohydrate was mixed into the hydrated PPI and SPI dispersion with a spatula directly before processing in the shear cell or the closed cavity rheometer. To change the pH of the blend, a 0.1 M solution of HCl was used instead of water.

Table 6.1. Mass fraction of protein to carbohydrate. \* For PPI/pectin and SPI/pectin only the mass ratio 93:7 was used for SEM and LAOS analysis. \*\* For PPI/pectin/cellulose and SPI/pectin/cellulose, pectin and cellulose were added in a mass ratio 1:1 in the blend.

PPI/carbohydrate blends	Mass ratio Protein:Carbohydrate	SPI/carbohydrate blends	Mass ratio Protein:Carbohydrate
PPI	100 : 0	SPI	100 : 0
PPI/pectin	97 : 3	SPI/pectin	97 : 3
	95 : 5		95 : 5
	93 : 7*		93 : 7*
	91 : 9		91 : 9
PPI/cellulose	93 : 7	SPI/cellulose	93 : 7
PPI/pectin/cellulose**	93 : 7	SPI/pectin/cellulose**	93 : 7

### 6.3.3 High temperature shear cell

A high temperature shear cell (Wageningen University, The Netherlands) was used to structure the PPI/carbohydrate and SPI/carbohydrate blends into fibrous products. The shear cell consists of a rotating bottom cone and a stationary cone which allows defined deformation of the materials at high temperature. The prepared protein blends (90 gram) were processed in a pre-heated shear cell at 140°C and 39 s<sup>-1</sup> (controlled by a Haake PolyLab QC drive, Germany). After 15 min shearing and heating at constant shear rate and temperature, the shear cell was cooled to 25°C within 5 min. Products were released from the shear cell after which those were kept at room temperature in a vacuum-sealed plastic bag for at least 1 h prior to further measurements.

### 6.3.4 Reflective light microscopy

A shear cell product was bended by hand in the parallel direction to the shear flow direction. The resulting deformed material was then observed with a digital microscope (Smartzoom 5) with 10× magnification.

### 6.3.5 Tensile strength analyses

The mechanical properties and the mechanical anisotropy of the products after shear-induced deformation were determined with a tensile strength analyses. Tensile strength analyses were performed with a Texture Analyzer (Instron Corp. 5564, USA) using a static load cell of 100 N. Dog-bone shaped samples (length 25 mm, width 4.4 mm) were cut in two directions in the shear cell product with a dog bone-shaped mould: (1) parallel and (2) perpendicular to the direction of the shear flow. The dimensions (thickness and width) of the tensile bar were



measured and accounted for in the normalized tensile strength determination. The ends of the tensile bars were placed in two clamps, resulting in a sample height of 15.5 mm. A uniaxial tensile test was performed at room temperature with a displacement rate of 1 mm/s. The stress-strain map was created using the tensile stress ( $\sigma$ , kPa) and tensile strain ( $\gamma$ , %) at fracture (Figure 6.1), based on previously reported material resistance equations (Chapter 2). Three parallel and three perpendicular specimens were taken for each sample. This procedure led to nine parallel and nine perpendicular specimens per PPI/carbohydrate or SPI/carbohydrate combination. The results were averaged and the standard deviations were determined based on the variation between the average values of those three samples.

### 6.3.6 Scanning electron microscopy

Scanning electron microscopy (SEM) was performed to provide information on the microstructure (~5-300  $\mu\text{m}$ ) of PPI/carbohydrate and SPI/carbohydrate blends. Rectangular samples (length, 13 mm; width,  $\pm 5$  mm) were placed in 2.5 % (v/v) glutaraldehyde, while gently rotating for 8 h. Next, the samples were soaked in demineralized water overnight and then immersed in a series of solutions of ethanol for at least 1 h per solution (10, 30, 50, 70, 96, and 100 % (v/v)). The materials were dried using critical point drying (CPD 300, Leica, Vienna, Austria) and fractured parallel to the shearing direction. The fractured samples were glued onto sample holders and sputter coated with 15 nm of tungsten (SCD 500, Leica, Vienna, Austria). The surfaces of the products were analysed with a field emission scanning electron microscope (Magellan 400, FEI, Eindhoven, the Netherlands) at magnifications of 250 $\times$  up to 10,000 $\times$  and secondary electron detection of 2.00 kV and 13 pA.

### 6.3.7 Rheological properties

The rheological properties of the PPI/carbohydrate and SPI/carbohydrate blends were measured using a closed-cavity rheometer (CCR) (RPA Elite, TA instruments, New Castle, DE, USA) (Emin & Schuchmann, 2017). Approximately 6 g of the blend was placed between two plastic foils in the closed cavity, which was sealed with a closing pressure of 4.5 bar to prevent water evaporation at high temperature. The CCR cavity has a radius of 22.5 mm, maximum height of the inner cavity of 4 mm and a biconical opening with an opening half angle of 3.35° for homogeneous transmission of the shear stress to the protein materials. The surfaces of the cones are grooved to prevent slippage. The lower cone oscillates in a strain-controlled mode while the upper cone remains stationary. The material was loaded into a pre-heated CCR either set at a temperature of 30°C and 140°C. The latter temperature was chosen

to mimic the shear cell conditions often used to create fibrous materials (Dekkers, Nikiiforidis, et al., 2016). The material was set to either 30°C or 140°C for 2 min without shear treatment and cooled to 30°C using a cooling rate of 5°C/min without shear treatment. After that, strain-sweep experiments were performed at 30°C at a constant frequency (1 Hz). The product was cooled to room temperature in plastic bags, and the pH of these products were then measured. The products were ground and mixed with distilled water to allow good measurement of the pH.

A strain-sweep experiment was used to determine the yield stress and the flow stress of a material. The yield stress is defined as the value of the shear stress at the end of the linear viscoelastic (LVE) regime. We define the yield stress as the point at which  $G'$  differs more than 5% from its strain-independent value in the LVE regime (Figure 6.1). The flow stress is defined as the value of the shear stress at the crossover point where the storage modulus is equal to the loss modulus ( $G' = G''$ ).

### 6.3.8 Large amplitude oscillatory shear (LAOS)

The results of the strain-sweep experiment performed in the CCR were analysed using the MITlaos software (version 2.1 beta, freeware distributed from MITlaos@mit.edu). The strain amplitude varied between 0.01% and 1000% at a constant frequency of 1 Hz at 30°C. The torque is plotted against the deformation in so-called Lissajous curves. Lissajous curves were created to relate the response of the protein materials to the oscillatory strain imposed.

The area enclosed in a Lissajous curve is equal to the energy dissipated per unit volume during one complete cycle of the oscillatory strain imposed. The energy dissipated per unit volume in a single cycle ( $E_d$ ) is a function of the first-order viscous Fourier coefficient ( $G_1''$ ), which can be calculated from the intensity and phase of the first harmonic:

$$E_d = \oint \sigma d\gamma = \pi G_1'' \gamma_0^2 \quad 6.1$$

for a given strain amplitude ( $\gamma_0$ ).

The energy dissipated by a perfectly plastic material in a single cycle ( $(E_d)_{pp}$ ) is equal to

$$(E_d)_{pp} = 4 \gamma_0 \sigma_{\max} \quad 6.2$$

for a maximum stress ( $\sigma_{\max}$ ).

The ratio of the actual dissipated energy and the perfectly plastic dissipation gives the energy dissipation ratio ( $\varphi$ ) as proposed by Ewoldt et al. (2010a):

$$\varphi = \frac{E_d}{(E_d)_{pp}} = \frac{\pi G_1'' \gamma_0}{4 \sigma_{\max}} \quad 6.3$$

### 6.3.9 Texture maps and colour schemes of the dissipation ratio

Texture maps summarize rheological information into two-dimensional plots involving only characteristic key parameters (Chapter 4). Although different parameters can be chosen for these plots, here we used a texture map based on the stress and strain at the end of the LVE regime and another map based on the stress and strain at the crossover point to classify products into four quadrants in each texture map as presented in Figure 6.1 (Hamann & MacDonald, 1992). Materials in the lower left quadrant 1 with low shear stress and shear strain are classified as having a soft, non-shaped texture commonly referred to as “mushy” (e.g. grits and similar food materials). Materials in the lower right quadrant 2 with low shear stress and high shear strain, are often described as “rubbery” (e.g. gelatin). The top right quadrant 3 with high shear stress and shear strain, indicates a “tough” texture (e.g. fruit leather and dried fruits). The top left quadrant 4 with high shear stress and low shear strain, clusters products with a “brittle” texture (e.g. many baked or confectionery food products) (Tunick & Van Hekken, 2010).

The energy dissipation ratio is plotted using colour schemes (Chapter 5), in which values of the dissipation ratio are represented by colours in strain/protein ratio diagrams. When  $\varphi = 0$  (blue), the rheological response is purely elastic;  $\varphi = 1$  (yellow) implies that the material displays perfect plastic (Ptaszek, 2014). A  $\varphi$  of  $\pi/4$  corresponds to a material that behaves as a Newtonian liquid.

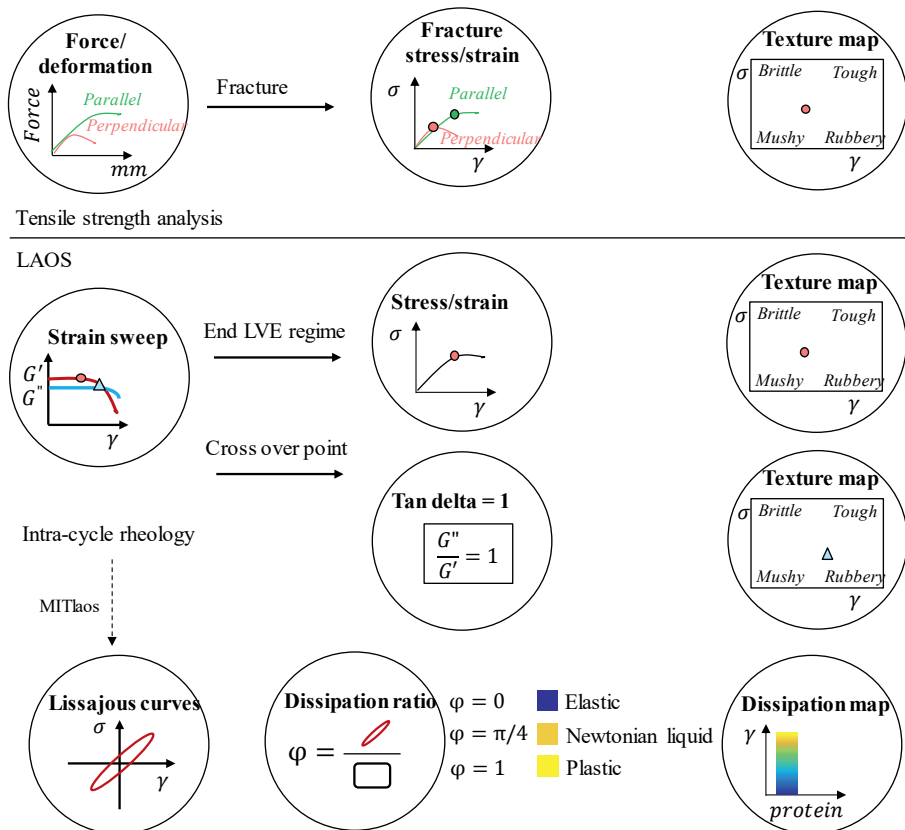


Figure 6.1. Systematic overview of the results of the texture maps and colour schemes that show the dissipation ratio as obtained in Chapter 5. The storage modulus ( $G'$ ) and loss modulus ( $G''$ ) versus strain to define the crossover point ( $G' = G''$ ) and the end of the linear viscoelastic (LVE) regime. The energy dissipation ratio is demonstrated using colour schemes:  $\varphi = 0$ , elastic;  $\varphi = \pi/4$ , Newtonian liquid;  $\varphi = 1$ , perfect plastic.

### 6.3.10 Prediction of the water distribution with rheology

The volume fractions of protein and carbohydrate in a blend were calculated, and the response of the blend can be described with an empirical polymer blending law (Morris, 1992). In several studies (Clark et al., 1983; Fitzsimons et al., 2008; Kasapis & Tay, 2009; Shrinivas et al., 2009), the relative amount of water in each polymeric phase is calculated with the “solvent avidity parameter”,  $p$ . The relative amount of water in each phase is fitted based on the rheological properties with a polymer blending law. The polymer blending law reads in its general form as

$$G_{XY}^n = \phi_X G_X^n + \phi_Y G_Y^n \quad 6.4$$

where  $G_X$ ,  $G_Y$  and  $G_{XY}$  are the moduli of the protein phase  $X$ , the carbohydrate phase  $Y$  and the protein/carbohydrate blend  $XY$ , and  $\phi_X$  and  $\phi_Y$  are the volume fractions of phases  $X$  and  $Y$ . The value of the parameter  $n$  depends on the spatial distribution of the two components in the blended material and their moduli. Here, it is assumed that the protein/carbohydrate blends obey isostrain behaviour, meaning  $n = 1$ . To simplify the calculation for the water distribution, we assume that the contribution of the carbohydrate phase in this equation is low and has therefore a negligible influence on the overall modulus of the blend. This assumption is true when the  $G$  value of the carbohydrate phase is much lower than the  $G$  value of the protein phase, or the volume fraction of the carbohydrate phase is small  $\phi$ . Now, the measured modulus of the PPI/carbohydrate or SPI/carbohydrate blend corresponds to the modulus of the PPI or SPI concentration only. The elastic modulus dependency on the dry matter content can be used to predict the water distribution (and phase volume fraction) in PPI/carbohydrate and SPI/carbohydrate blends, as described by Dekkers, Boom, et al. (2018b) for SPI/pectin blends, using data on how the modulus of PPI and SPI depends on the water content (Chapter 4). Once the moisture content in the protein phase is calculated, a mass balance (explained in Appendix C of Chapter 2, where the  $\rho_{protein}=1330 \text{ kg/m}^3$  and  $\rho_{carbohydrate}=1000 \text{ kg/m}^3$ ) was used to calculate the dry matter fraction in the carbohydrate phase.

## 6.4 Results and discussion

### 6.4.1 Shear-induced structuring

Structured materials were inspected visually by deforming until tear. Figure 6.2 shows the different morphologies of products containing pea protein isolate (PPI) or soy protein isolate (SPI) with pectin and/or cellulose. Without any carbohydrates added, PPI and SPI both resulted in gel-like morphologies (Appendix Figure A 6.2). Those outcomes differ from previous studies on high moisture extrusion cooking with PPI and SPI, where a somewhat fibrous morphology was reported (Osen et al., 2014; Patrick Wittek et al., 2021). The mechanism that could be responsible for anisotropic structure formation is still under debate and may well be different for high moisture extrusion cooking and shear cell deformation (Cornet et al., 2021). In high moisture extrusion cooking, the cooling zone is considered as the area where structure formation takes place. Mechanisms that assume shear during cooling are temperature-induced viscosity gradients and spinodal decomposition and deformation. Those mechanisms cannot be applied in the shear cell, since the lack of shear during the cooling step in the shear cell.

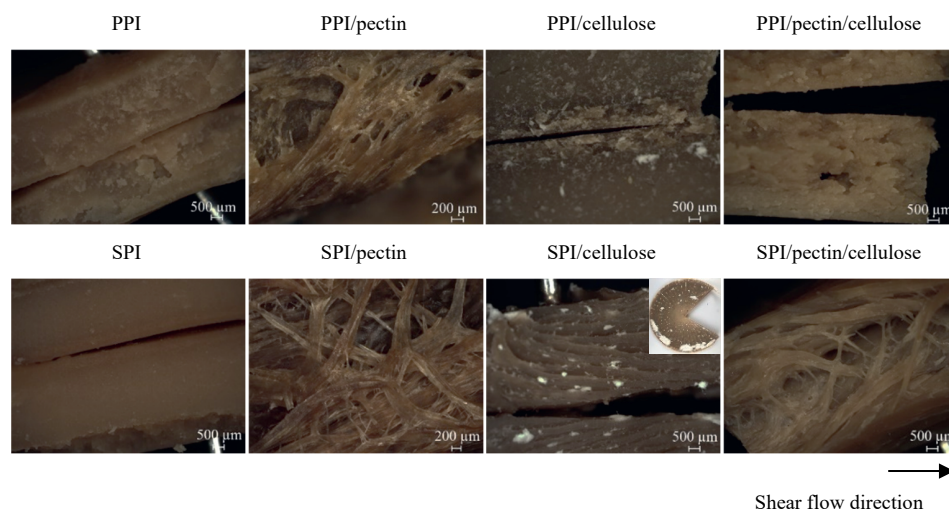


Figure 6.2. Macrostructures after shear-induced structuring of samples consisting of PPI or SPI with pectin, cellulose and pectin/cellulose (ratio 1:1).

Homogeneous gels were also obtained with a mass fraction of both PPI or SPI to pectin of 97:3 (Appendix Figure A 6.1). The mass fraction 95:5 and 93:7 resulted in a fibrous morphology for both PPI/pectin and SPI/pectin blends (Figure 6.2, blends with a mass

fraction of 95:5 were not visualized). The mass fraction PPI/pectin blends of 91:9 resulted in weaker products without any discernible fibrousness. This is different compared with SPI/pectin with the same mass fraction that resulted a fibrous morphology (Appendix Figure A 6.1). SEM images of PPI/pectin blends showed slightly elongated and porous areas parallel to the shear flow direction (Figure 6.3), but the occurrence and elongation of these areas were not as pronounced as in SPI/pectin blends (Dekkers, Nikiforidis, et al., 2016).

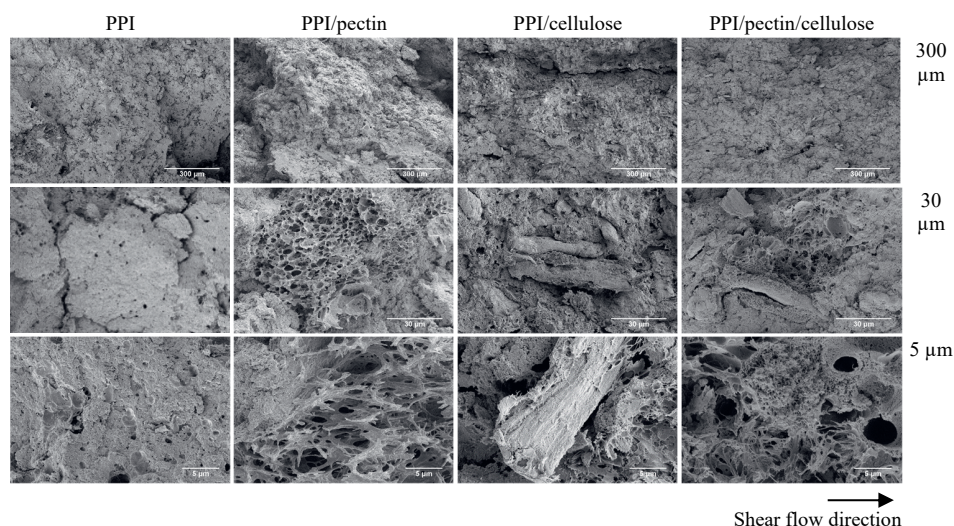


Figure 6.3. Morphology after shear-induced structuring of samples consisting of PPI, PPI/pectin, PPI/cellulose and PPI/pectin/cellulose at magnifications of the images were 1) 250 times, 2) 2500 times, and 3) 10,000 times.

The SPI/cellulose blend resulted in macroscopic phase separation, with white cellulose spots in the matrix and large domains at the rim of the product. The SPI/pectin/cellulose blend showed a fibrous macrostructure. Pectin apparently prevented the macroseparation of cellulose out of the SPI matrix. PPI/cellulose blend did not give macroscale separation and only gave limited fibrous morphology, just like PPI/pectin/cellulose blend. PPI/cellulose blend yielded a visually homogeneous product but with rectangular or parallelepipedal particles included, presumably reflecting the non-deformed cellulose crystals (Appendix Figure A 6.2). The PPI/pectin/cellulose blend also contained non-deformed cellulose rods as well as a few porous areas.

A possible explanation for the different morphologies between PPI and SPI can be found in the rheological properties. As previously shown, PPI is less elastic and weaker compared

with SPI (Chapter 4) and therefore forms a less elastic matrix. Lower elasticity could be a valid reason for absence of macroscopic phase separation of cellulose (Dill, 1979; Peighambardoust et al., 2008; van der Zalm et al., 2012). In addition, a weaker protein phase might induce less orientation of the dispersed phase. This is investigated in more detail in next sections.

#### *6.4.2 Mapping of the mechanical behaviour*

The materials were subjected to tensile strength analysis parallel and perpendicular to the shear flow direction. The ratio of these two is the anisotropy index. Figure 6.4 presents a texture map with the tensile stress and strain at fracture as well as a map of the anisotropy indexes of PPI and SPI and blends with a mass fraction of protein to carbohydrates of 93:7. The tensile stress and strain at fracture of PPI were 2 to 3 times lower than for SPI (Dekkers, Nikiforidis, et al., 2016). The tensile stress and strain at fracture of PPI were slightly higher than for cooked chicken strips (Chapter 2). SPI behaved as relatively tough, whereas PPI was mushy (soft) (Figure 6.4). PPI had an anisotropy index of  $\sim 1.5$  for both tensile stress and strain, whereas SPI showed an anisotropy index of  $\sim 1$ . Remarkably, the anisotropy for PPI as measured with this tensile strength analysis was not accompanied by a fibrous morphology (Figure 6.5).



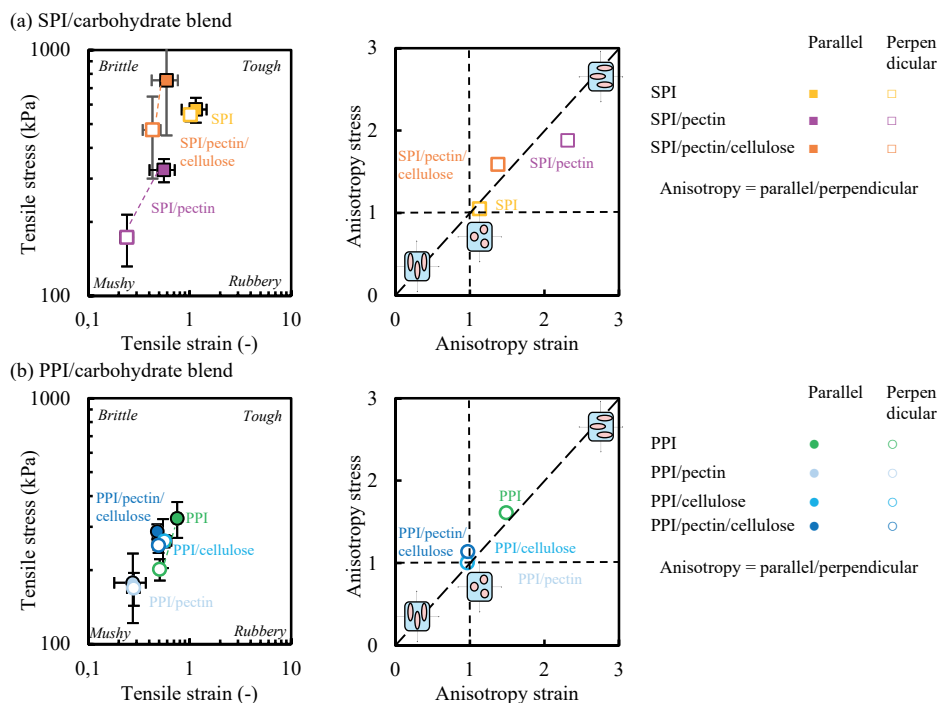


Figure 6.4. Tensile strength analysis including anisotropy of shear-induced structuring of samples consisting of PPI, PPI/pectin, PPI/cellulose and PPI/pectin/cellulose or SPI, SPI/pectin (Dekkers, Nikiforidis, et al., 2016) and SPI/pectin/cellulose at mass fraction protein to carbohydrate 93:7 in parallel and perpendicular direction to the shear flow. The ratio of PPI or SPI and carbohydrate was varied by replacing part of the PPI or SPI with the carbohydrate.

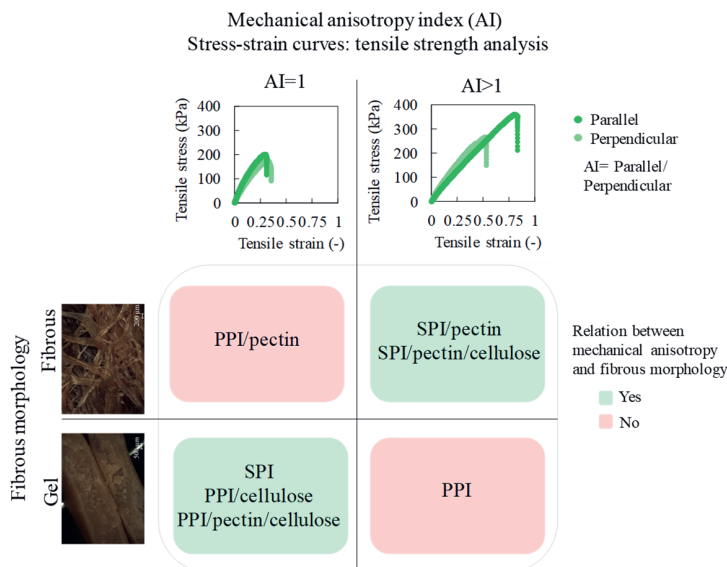
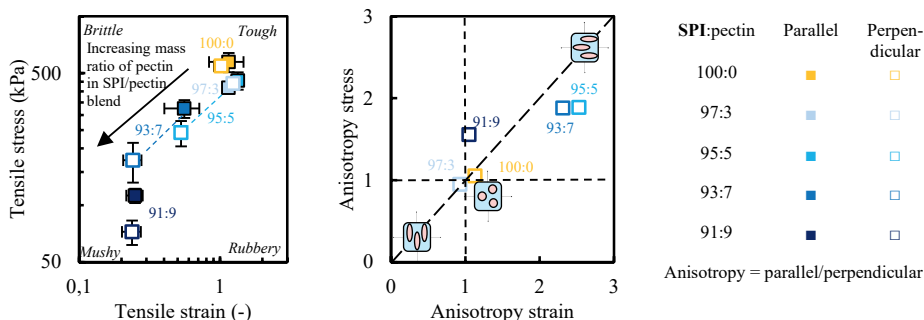


Figure 6.5. Overview of the fibrous morphology observed visually versus the mechanical anisotropy index (AI) measured with a tensile strength analysis.

The addition of carbohydrates to both PPI and SPI resulted in softer materials (Figure 6.4). PPI/cellulose and PPI/pectin/cellulose blends led to lower fracture stress and strain but not as much as with just pectin. An increase in the mass fraction in the PPI/cellulose and PPI/pectin/cellulose blends (91:9) had only a limited effect on the tensile stress and strain as shown in Appendix Figure A 6.2. Pectin added to PPI led to products with a lower tensile stress and strain, just as with SPI (Figure 6.4). Figure 6.6 presents a texture map with the tensile stress and strain at fracture as well as a map of the anisotropy index of blends with different mass fraction of PPI and SPI to pectin. The addition of more pectin resulted in a mushier consistency. With the addition of more pectin, the total volume and surface area of the pectin phase increased and this weakened the matrix both parallel and perpendicular to the shear flow direction. Low mechanical anisotropy indices were found for all PPI/pectin products, whereas for SPI/pectin products at a mass fraction of 95:5 and 93:7, a high anisotropy index was observed. For PPI/pectin blends, no mechanical anisotropy was measured with this tensile strength analysis (parallel/perpendicular tensile stress or strain). However a fibrous morphology was observed for PPI/pectin blends (Figure 6.5). For PPI/pectin blends a fibrous morphology was not always related to mechanical anisotropy. In the case of SPI, a fibrous morphology was related to mechanical anisotropy generally. Similar

mechanical properties in parallel and perpendicular direction (lack of mechanical anisotropy) could indicate fibres in both directions or a less elongated dispersed phase. A higher degree of mechanical anisotropy was related to larger differences in mechanical strength between the continuous and dispersed phase in case of SPI/pectin blends that could be related to the degree of elongation of the dispersed domains.

(a) SPI/carbohydrate blend



(b) PPI/carbohydrate blend

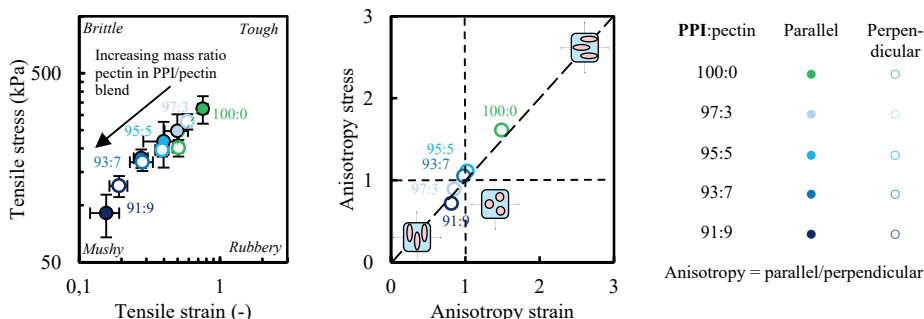


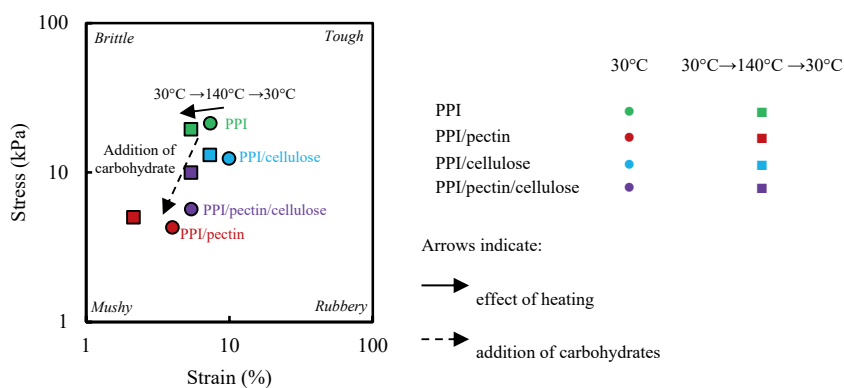
Figure 6.6. Tensile strength analysis including anisotropy of shear-induced structuring of samples consisting of PPI or SPI (Dekkers, Nikiforidis, et al., 2016) with increasing mass fraction of pectin in the blend in parallel and perpendicular direction to the shear flow. Note that the scales of the x-axis and y-axis are different from those shown in Figure 6.4.

### 6.4.3 Mapping of the rheological behaviour

Figure 6.7 presents a texture map with the stress and strain values at the end of the LVE regime for PPI or SPI/carbohydrate blends (93:7) at 30°C and blends heated at 140°C and subsequently cooled to 30°C. It can be seen that SPI is tougher than PPI at 30°C. The addition of carbohydrates leads to lower stress and strain. Pectin gives the biggest shift in the texture map. PPI/pectin/cellulose and SPI/pectin/cellulose blends yielded intermediate toughness and deformability compared with the blends with only pectin or cellulose.

After heating and cooling, the PPI materials became less deformable, whereas SPI became tougher and more deformable. Heating PPI, PPI/pectin and PPI/cellulose led to slightly lower strains compared with the unheated materials. However, for PPI/pectin/cellulose, an increase in stress was observed after heating. The SPI, SPI/pectin, SPI/cellulose and SPI/pectin/cellulose blends all showed higher strain and stress after heating. The results presented here confirm that the SPI/carbohydrate blends are tougher compared with the PPI/carbohydrate blends, and this became more pronounced after heating and cooling.

#### PPI/carbohydrate blends



#### SPI/carbohydrate blends

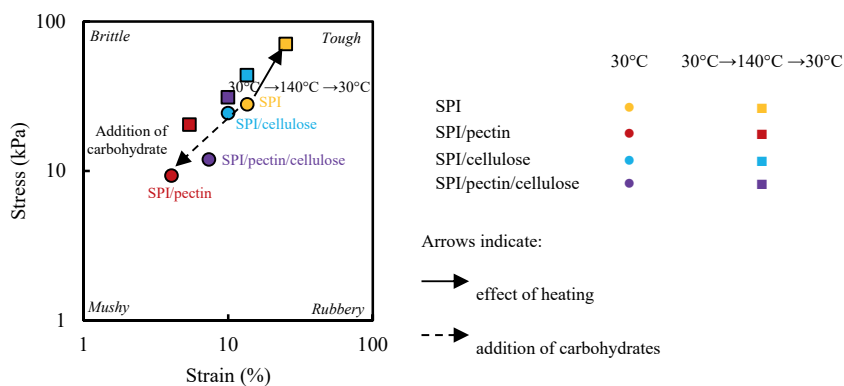
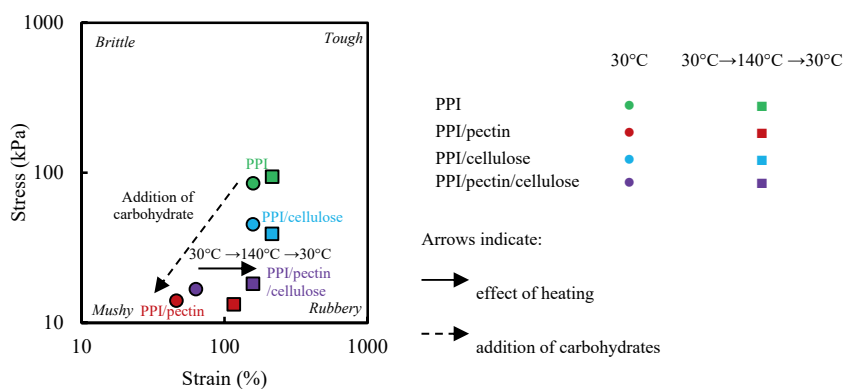


Figure 6.7. Texture map end of the LVE regime of PPI and SPI/carbohydrate blends (93:7) at 30°C and heated at 140°C and cooled to 30°C.

Figure 6.8 presents a texture map with the stress and strain values at the crossover point ( $G' = G''$ ) for PPI or SPI/carbohydrate blends (93:7) at 30°C and after heating to 140°C and subsequently cooling to 30°C. In this texture map weakening has proceeded further compared with the texture map at the end of the LVE regime and thus shows the effect of larger strains in the non-linear regime, which may give more information relevant for the shear-based structuring process. The crossover point with just PPI occurs at a similar strain as with SPI but at lower stress. The addition of cellulose to PPI leads to lower crossover stress. The addition of pectin and pectin/cellulose to PPI and SPI leads to both lower crossover stress and strain, making both products mushier. After heating and cooling, the PPI, PPI/cellulose, SPI and SPI/cellulose products became comparable with the unheated products. Heating and cooling PPI/pectin or SPI/pectin and PPI/pectin/cellulose or SPI/pectin/cellulose resulted in a more deformable product. Those changes in rheological response cannot be explained by considering physical effects only. As explained by Dekkers, Boom, et al. (2018b), factors such as a decrease in the pH due to  $\beta$ -elimination and/or demethoxylation of the pectin could play a role. In addition, further degradation of pectin could lead to the concurrent release of galacturonic acid and altered water redistribution between the two phases. The latter influences the rheological response of the blend.

## PPI/carbohydrate blends



## SPI/carbohydrate blends

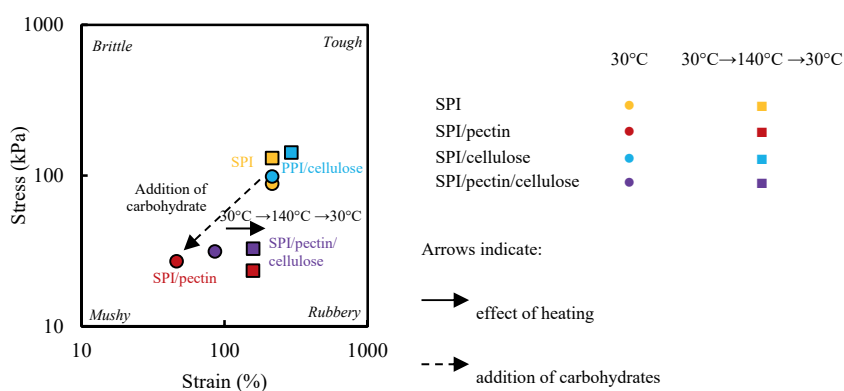


Figure 6.8. Texture map crossover point of PPI and SPI/carbohydrate blends (93:7) at 30°C and heated at 140°C and cooled to 30°C.

We observed similar trends in texture maps of the tensile strength analysis and the CCR: (1) PPI has lower stress and strain at the end of the LVE regime and at fracture compared with SPI, (2) the addition of carbohydrates results in lower yield, flow and fracture stress and strain for both PPI and SPI. This was most pronounced with the addition of pectin.

#### 6.4.4 Large amplitude oscillatory shear: intra-cycle rheology

The dissipation ratio ( $\phi$ ) was calculated to describe the viscous contribution in the response relative to pure plastic behaviour (Ewoldt et al., 2008, 2010; Klost et al., 2020; Tao et al., 2019). Figure 6.9 shows a colour scheme of the dissipation ratio for PPI and SPI/carbohydrate blends with a mass ratio protein to carbohydrate 93:7 at 30°C and at 140°C and cooling to 30°C. At 30°C, PPI and SPI both show a higher dissipation ratio with the strain amplitude. The addition of cellulose to PPI and SPI resulted in a slightly higher dissipation ratio. At equal strain amplitude, the addition of pectin and pectin and cellulose to both PPI and SPI resulted in a higher dissipation ratio, suggesting a less elastic material. Both PPI and SPI showed lower dissipation ratios after heating and cooling, and the products became more elastic at a wider range of strain amplitudes compared with unheated materials. Large deformation led to a sudden onset of viscous/plastic behaviour, which was most pronounced for SPI. The addition of cellulose to PPI and SPI resulted in similar dissipation ratios as with heated and cooled PPI and SPI. PPI/pectin, SPI/pectin, PPI/pectin/cellulose and SPI/pectin/cellulose had a distinct lower dissipation ratio at similar strain amplitudes after heating, indicating induced elasticity. After heating, all blends gained elasticity, which was most pronounced for blends with pectin. Those changes in rheological response cannot be explained by considering physical effects but also the release of galacturonic acid and the altered water redistribution between the two phases.

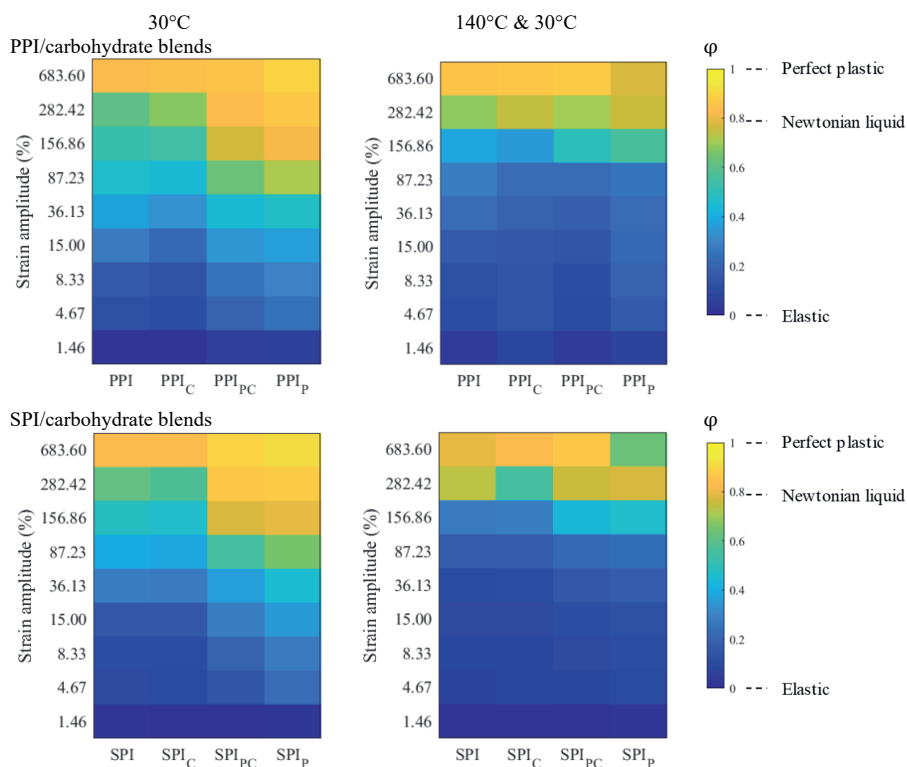


Figure 6.9. Colour schemes that show the dissipation ratio of PPI/carbohydrate and SPI/carbohydrate blends (C (cellulose), PC (pectin +cellulose) and P (pectin)) at 30°C and heated at 140°C and cooled to 30°C. The colour corresponds to the value of the dissipation ratio ( $\phi$ ) in the colour bar:  $\phi = 0$ , elastic;  $\phi = \pi/4$ , Newtonian liquid;  $\phi = 1$ , perfect plastic. The experimental curves are added as supplementary information in Appendix Figure A 6.3.

#### 6.4.5 Connecting non-linear rheology of protein/carbohydrate blends and their link to structure formation

In this study, we analysed blends PPI and SPI mixed with combinations of pectin and cellulose. Concerning the proteins, we found that PPI products were softer than SPI products (Figures 6.4, 6.7 and 6.8), due to relatively lower amounts of cysteines that contributes to the formation of disulphide bonds (O’Kane et al., 2004). Similar differences were described in previous studies albeit at much lower protein concentrations ( $\sim 10$  wt.%) (Batista et al., 2005; Lam et al., 2018; O’Kane et al., 2004). This difference in strength remained after addition of the carbohydrates. The addition of carbohydrates to PPI and SPI always resulted in softer materials as illustrated in all the texture maps for both SPI and PPI (Figures 6.4, 6.7 and 6.8). This decrease was most pronounced with pectin. In the PPI/pectin or SPI pectin blends at neutral pH,  $\beta$ -elimination leads to a lower molecular weight and thus a lower viscosity of the



dispersed phase (Chen et al., 2015; Diaz et al., 2007). Both  $\beta$ -elimination and demethoxylation result in the creation of carboxyl groups, resulting in lowering of the pH (Axelos & Branger, 1993; Renard et al., 2006). Dekkers, Boom, et al. (2018b) showed that a mass fraction of 95:5 SPI/pectin (previously reported as the addition of 2.2 wt.% pectin to SPI) after a time-sweep measurement at 140°C indeed resulted in a decrease in the pH. Therefore, we determined the pH of PPI and SPI materials (7.1 and 6.9, respectively) and of the blends after performing a strain-sweep experiment (Table 6.2). The pH of SPI/pectin and PPI/pectin products was 5.9 and 6.1, respectively, closer to the isoelectric point of both proteins (around 4.5). This decrease of the pH in the products will affect the aggregation of the protein phase. To check this, we dispersed PPI and SPI in 0.1 M HCl, which resulted in a pH of 6.3 for PPI and 6.2 for SPI (Table 6.2). For PPI, this had a limited effect on the stress and strain at the end of the LVE regime; whereas for SPI, the reduction in strength was greater. A previous study of pea protein gels pre-treated at different pHs showed a similar trend (Klost et al., 2020), albeit at a lower protein concentration (~10 wt.%).

*Table 6.2. pH of PPI and SPI/carbohydrate blends. The pH was adjusted using 0.1 M HCl. The corresponding texture properties (end of the LVE regime) are for SPI\* 13.5 % and 47.2 kPa and for PPI\*\* 5.1% and 15.9 kPa.*

	Protein/-	Protein (0.1 M HCl)/-	Protein/pectin	Protein/pectin/cellulose
SPI/carbohydrate	6.9	6.2*	5.9	6.3
PPI/carbohydrate	7.1	6.3**	6.1	6.4

Lower tensile stress and strain values due to the addition of pectin to SPI were previously related to two possible mechanisms (Dekkers, Nikiforidis, et al., 2016). (1) Pectin, when added in small amounts may partially hydrolyse and dissolve in the continuous phase during heating, hindering the crosslinking of SPI and leading to lower tensile stress. (2) Pectin forms a weaker carbohydrate phase or the adhesion between the pectin and SPI is poor. With PPI, the same two mechanisms may occur. Dekkers, Nikiforidis, et al. (2016) found that the strength and volume fraction of the weak phase is important for the formation of a fibrous morphology in a material based on SPI, and that the size of the pectin domains increases due to shear-induced coalescence. Figure 6.3 shows that PPI/pectin product contains smaller and less elongated porous domains than in a SPI/pectin product (Dekkers, Nikiforidis, et al., 2016). In addition to shear-induced coalescence, water redistribution to the pectin phase may increase the size of the dispersed domains. More water in the pectin domain increases the effective protein concentration of the PPI and SPI phases (after Dekkers et al. (2018)). The

modulus of the PPI and SPI-carbohydrate blends were thus matched to the viscoelastic properties at the dry matter content of the single proteins (Chapter 4). Based on the mass balance, the volume fractions of PPI/pectin and SPI/pectin blends are 91%/9% and 89%/11%, respectively (Table 6.3), which implies strong water migration from the protein into the pectin phase. For PPI/pectin and SPI/pectin products, the mass fraction water in the pectin phase increased from 0.55 g/g to 0.71 g/g and 0.55 g/g to 0.65 g/g, respectively.

This leads to two effects: (1) a stronger protein phase and (2) a larger volume fraction of the dispersed pectin phase, which was considered weaker. In a previous study, it was hypothesized that the cohesiveness of the pectin phase or the adhesion between the pectin and SPI phase is weaker than the cohesiveness of the SPI phase itself (Dekkers, Nikiforidis, et al., 2016). The addition of more pectin would result in even more water redistribution, consequently even larger dispersed, weak domains, and thus even weaker materials. Indeed, we saw that the tensile stress and strain values decreased as the pectin concentration increased (Figure 6.6).

Cellulose in a PPI and SPI matrix can be seen as rods with SEM (Figure 6.2). The first expectation is that those cellulose rods would increase the strength of the blend, among others because the water content remained similar in all blends. Cellulose replaced protein. However, a slight weakening was observed after the addition of cellulose, for which several phenomena may be responsible. The mass balance shows that the volume fraction of PPI/cellulose is 97%/3% and SPI/cellulose is 95%/5% (Table 6.3), which is lower than the percentage of protein being replaced by cellulose. This implies that the protein phase (PPI and SPI phase) absorbed more water than cellulose. The protein concentration in the protein phase becomes lower, which can explain the slightly lower stress and strain values.

Table 6.3. Water distribution in PPI and SPI/carbohydrate blends.

	Mass fraction (%/%)	Volume fraction (%/%)		
		Protein/cellulose	Protein/pectin	Protein/pectin/cellulose
SPI/carbohydrate	93/7	95/5	89/11	95/5
PPI/carbohydrate	93/7	97/3	91/9	97/3

However, we saw more complex behaviour for the SPI/cellulose products (Figure 6.2.). Macroscopic phase separation was observed, where cellulose was aggregated into white domains at the rim of the product. For the PPI/cellulose product macroscopic phase separation was not observed. These differences could indicate that PPI is less elastic than SPI (Figure 6.9). Separation of particles to the outer part of a curvilinear shear field as present in the shear cell was also observed when shearing DNA and wheat dough in such flow field (Dill, 1979; Peighambardoust et al., 2008; van der Zalm et al., 2012). There, the elasticity of the material was thought to be responsible for the fact that the application of shear flow led to a net inward force on the large DNA and gluten respectively. In the latter case, starch was expelled from the wheat dough to the rim of the material as a result of inward migration of gluten,. In the SPI/pectin/cellulose product macroscopic phase separation was not observed, implying that pectin prevented or hindered the macroscopic separation of cellulose out of the SPI matrix, possibly due to lower elasticity due to pectin addition.

PPI and SPI are known to be shear thinning and exhibit viscoelasticity. A dispersed phase in a viscoelastic matrix is not only subjected to the viscous stresses but also to the elastic stresses. The latter reduce break up under deformation, and thus form larger domains that are deformed more strongly (Elmendorp & Maalcke, 1985). Mighri et al. (1988) also showed that matrix elasticity increases the deformation of a droplet indirectly by reducing droplet break up, even though some studies show that a Newtonian droplet of the same size deforms less in a viscoelastic matrix (Guido et al., 2002; Sibillo et al., 2004; Verhulst et al., 2007, 2009). Moreover, elasticity also plays an important role in suppressing the relaxation of elongated domains after cessation of flow (Liu et al., 2014; Pawar & Bose, 2015). SPI is slightly more elastic than PPI (Figure 6.9). In Figure 6.5, PPI/pectin shows smaller dispersed phase domains that are less elongated compared with SPI/pectin (Dekkers, Nikiforidis, et al., 2016). Therefore, it was hypothesized that the dispersed phase in PPI weakens the structure isotropically, whereas the more strongly elongated areas in SPI weaken the structure mainly in the perpendicular direction and less in the parallel direction. This results in a fibrous

morphology and larger tensile stress in the parallel direction. The elongated domains can also form fibrousness when they are long enough.

Therefore, although previous studies mostly focus on viscosity (Dekkers et al., 2018; Dekkers, Boom, et al., 2018b; Dekkers, de Kort, et al., 2016), this study reveals the importance of the role of elasticity. Elasticity is hypothesized as important factor in the ability of the blends to form fibrous products, since it promotes deformation and suppress relaxation. This role of matrix elasticity has mostly been studied for non-food extrudates, for example, poly(L-lactide)/poly(amide) blends. A more elastic matrix promotes deformation and extension of the nodules into fibrils (Yousfi et al., 2018); elasticity also suppresses relaxation to isotropic (spherical shape) (Liu et al., 2014; Pawar & Bose, 2015).

## 6.5 Conclusion

In this work, the differences in morphology of shear-induced structures formed with blends of pea protein isolate (PPI) and carbohydrate blends, and soy protein isolate (SPI) and carbohydrates were quantified. Those differences can be connected to differences in rheological properties of both proteins at processing conditions using a closed cavity rheometer. It was found that PPI products were mushier than SPI products and that the addition of carbohydrates to PPI or SPI resulted in mushier products. This was most pronounced for blends with pectin. This was attributed to the combined effects of a decrease in pH and/or water redistribution between the two phases. After heating, all protein/carbohydrate blends showed an increase in elasticity. This was most pronounced for PPI/pectin and SPI/pectin blends. Elasticity was found to be an important factor in the ability of the blends to form fibrous products. These morphology findings and their behaviour during large deformation provide a rheological fingerprint of the protein/carbohydrate blends to guide product design and investigate process/structure relationships. These are important steps towards the design of protein blends suitable for industrial meat analogues applications.

6.6 Appendix A

The following are the Supplementary data to this article:

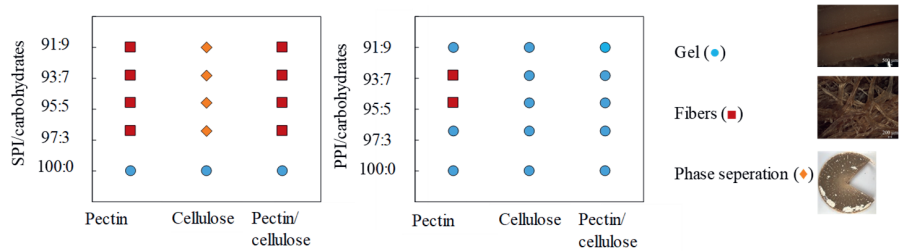


Figure A 6.1. Macrostructures after shear-induced structuring of SPI/carbohydrate and PPI/carbohydrate blends with increasing mass fraction of carbohydrate in the blend.

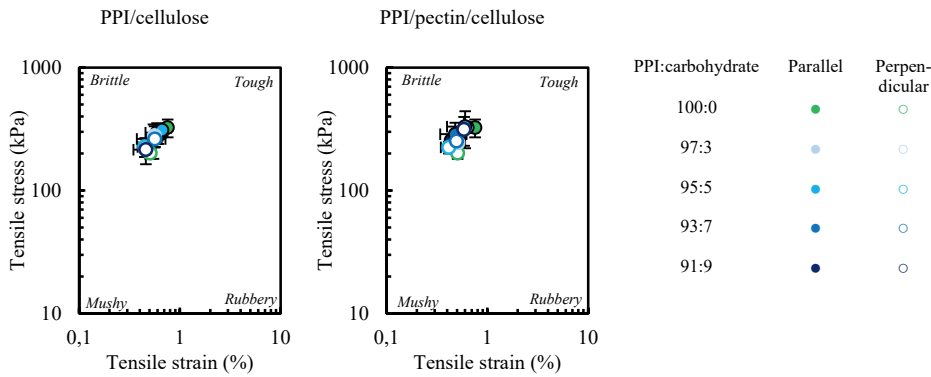


Figure A 6.2. Texture map of tensile strength analysis of shear-induced structuring of PPI with increasing mass fraction of cellulose and pectin/cellulose in the blend parallel and perpendicular direction to the shear flow.

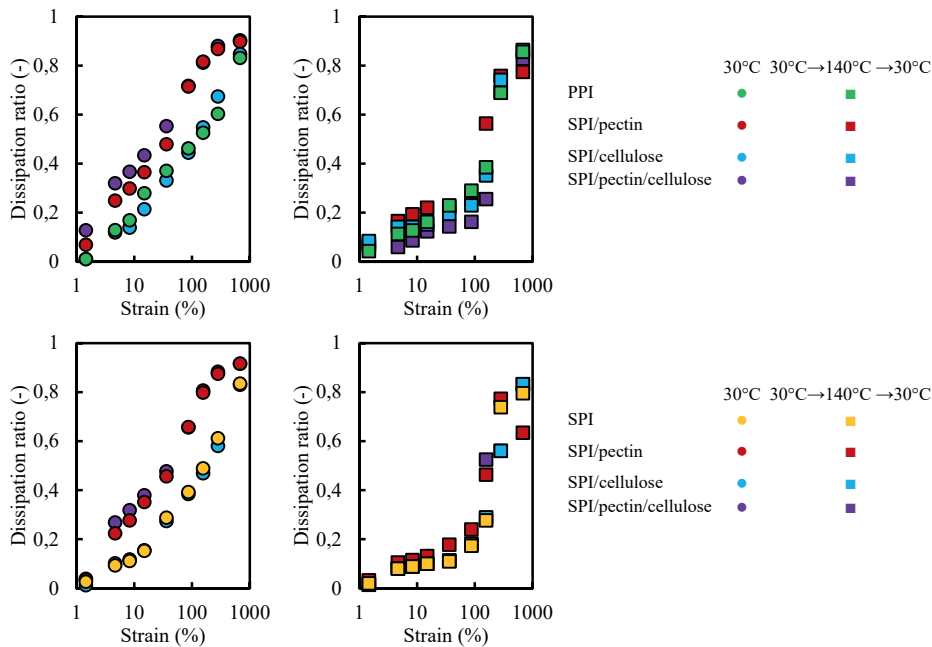


Figure A 6.3. The experimental curves of the dissipation ratio of PPI/carbohydrate and SPI/carbohydrate blends at a mass fraction of protein to carbohydrate of 93:7 at 30°C and heated at 140°C and cooled to 30°C.  $\varphi = 0$ , elastic;  $\varphi = \pi/4$ , Newtonian liquid;  $\varphi = 1$ , perfect plastic.

Table A 6.1. Tensile stress and strain at fracture of PPI and SPI/carbohydrate blends at a mass fraction of protein to carbohydrate of 93:7 (Figure 6.4).

	Stress (kPa)				Strain (-)			
	Parallel		Perpendicular		Parallel		Perpendicular	
PPI	324.44	±53.82	201.46	±20.18	0.76	±0.06	0.51	±0.04
PPI/pectin	177.59	±55.88	169.15	±25.83	0.28	±0.09	0.28	±0.07
PPI/cellulose	263.00	±59.21	262.35	±14.86	0.55	±0.11	0.56	±0.04
PPI/pectin/cellulose	287.03	±20.02	252.12	±17.10	0.48	±0.03	0.49	±0.05
SPI	573.07	±66.55	545.08	±31.77	1.15	±0.32	1.02	±0.11
SPI/pectin	325.20	±35.16	172.99	±41.11	0.56	±0.16	0.24	±0.04
SPI/pectin/cellulose	752.86	±303.40	473.44	±173.46	0.59	±0.17	0.43	±0.09

Table A 6.2. Tensile stress and strain at fracture of PPI/pectin and SPI/pectin blends (Figure 6.6).

	Stress (kPa)				Strain (-)			
	Parallel		Perpendicular		Parallel		Perpendicular	
PPI	324.44	±53.82	201.46	±20.18	0.76	±0.06	0.51	±0.04
PPI/pectin (97:3)	247.15	±55.88	277.74	±25.83	0.50	±0.06	0.59	±0.07
PPI/pectin (95:5)	217.70	±59.21	196.16	±14.86	0.40	±0.09	0.39	±0.04
PPI/pectin (93:7)	177.59	±55.88	169.15	±25.83	0.28	±0.09	0.28	±0.07
PPI/pectin (91:9)	90.91	±23.12	126.77	±16.17	0.16	0.03	0.19	0.03
SPI	573.07	±66.55	545.08	±31.77	1.15	±0.32	1.02	±0.11
SPI/pectin (97:3)	418.48	±14.91	441.10	±22.24	1.15	±0.32	1.24	±0.06
SPI/pectin (95:5)	457.08	±48.08	242.19	±37.26	1.34	±0.10	0.53	±0.05
SPI/pectin (93:7)	325.20	±35.16	172.99	±41.11	0.56	±0.16	0.24	±0.04
SPI/pectin (91:9)	112.52	±9.73	72.37	±10.72	0.25	±0.16	0.24	±0.04







# *Chapter 7*

*Non-linear rheology reveals the importance of elasticity  
in meat and meat analogues*

*This chapter has been submitted as* Non-linear rheology reveals the importance of elasticity  
in meat and meat analogues Schreuders, F. K. G., Sagis, L. M. C., Bodnár, I., Boom, R. M.,  
& van der Goot, A. J.

### 7.1 *Abstract*

The interest in plant-based meat analogues as an alternative to meat is currently growing. We use texture maps and colour schemes to quantify and compare the non-linear rheological behaviour of meat and plant-based meat analogues. Both in texture maps and colour schemes, similarities and differences between rheological responses of meat and meat analogues are apparent. Meat analogues differ in terms of their lower elasticity compared with heated meat, which is likely noticeable for consumers. The changes caused by heating on meat and meat analogues are different as well. Heating of meat resulted in a tougher and more elastic material, while meat analogues only exhibited small effects by heating.

## 7.2 Introduction

Meat analogues are designed to have sensory properties similar to meat but are made from plant proteins (Malav et al., 2015). The unique textural properties of meat are a result of the muscle tissue structure consisting of repeating sarcomere structures that are grouped into muscle fibres and surrounded by connective tissue, the cell membrane, and, depending on the meat type, stored intramuscular fat tissue (Pearson, 2012; Pette & Staron, 1990). Fish muscle is mostly composed of myotomes, which are muscular sheets connected to one another by connective tissues, called myocommata. Myotomes are composed of myosin and actin mainly that form large numbers of muscle fibers (Kazir & Livney, 2021).

Food scientists have mimicked these fibrous structures with plant-based proteins through high moisture extrusion cooking and shear cell technology (Dekkers, Boom, et al., 2018a). Meat analogues often contain blends of textured and non-textured proteins from soy, wheat or pea, as these blends can result in a range of morphologies (Bashi et al., 2019; Jones, 2016). We can roughly distinguish ground meat, and whole-meat products. Some meat analogue products aim at mimicking whole-cut meats, like chicken meat, pork and beef steak, which are characterized by the presence of long fibres or layers. The meat analogues resembling ground and bound meats, like in a hamburger, are first transformed into a meat-like fibre structure that resembles small pieces of meat (e.g. TVP) which is then mixed with other ingredients. These include water (50-70 wt.%), flavourings, oil or fat, binding agents (methylcellulose) and colouring agents (Kyriakopoulou et al., 2021). The structure characteristics of meat have been widely studied. However, methods that quantitatively compare meat and meat analogues are not widely available (Chapter 8). It was recently found that a closed-cavity rheometer developed for the rubber industry allows accurate determination of the rheological properties of concentrated plant-based protein materials (Dekkers, Emin, et al., 2018; Emin & Schuchmann, 2017 and Chapter 3). In a recent study, single ingredient dispersions of soy protein isolate (SPI), pea protein isolate (PPI) and wheat gluten (WG) as well as PPI-WG and SPI-WG blends were studied with this device (Chapter 4 and 5). A combination of texture maps and colour schemes was used to map the properties of the ingredients and the blends. The dissipation ratio as a function of small and large strain amplitudes was useful for understanding the differences in elasticity. Heating of these plant protein blends showed an increase in the elasticity. Here we extend those measurements to

commercial meat and meat analogue products, and especially those that can be considered as whole cut products.

The objective of the current study is therefore to quantify the similarities and differences between meat and meat analogues. The stresses at the ends of the LVE regime and the stress-strain crossover points are captured in texture maps. The energy dissipation ratio is represented by colour contours in strain-temperature diagrams. For the design of plant-based meat analogues, these diagrams may guide the design and selection of plant-based materials to be as similar as possible to meat.

### 7.3 Materials and methods

#### 7.3.1 Materials

Meat and meat analogues were bought from a local supermarket (Albert Heijn) in Wageningen, The Netherlands, which were then stored at 4°C before further analysis within two days. Meat and fish samples used include chicken (more specifically the breast of a chicken), beef, pork, codfish and salmon. The meat analogues used are “Kipstuckjes” (Vegetarian Butcher), “Chick free pea based” (Nutrali Foods), “Stukjes als van Kip” (AH), “Vegetarische basis wokstukjes (AH)” and “Vivera plant stukjes als kip” (Vivera). The manufacturers’ specifications of the composition of meat and meat analogues are presented in Tables 7.1 and 7.2. The specific signatures product of meat analogues and ingredients according to the packaging are presented in Table 7.3.

Table 7.1. Composition of meat and fish.

	Chicken	Beef	Pork	Codfish filet	Salmon
Water	74.7	73.2	72.9	83.1	63.9
Protein	23.6	21.3	23.0	16.0	20.0
Fiber					
Carbohydrate					
Fat	1.6	5.3	4.0	0.7	16.0
Salt	0.1	0.2	0.1	0.2	0.1

Table 7.2. Composition of meat analogues.

	Kipstuckjes	Chick free pea based	Stukjes als van Kip	Vegetarische basis wokstukjes	Vivera plant stukjes als kip
Water	61.1	67.6	61.97	63.6	66.5
Protein	20.0	21.0	23.0	21.0	19.0
Fiber	7.6	2.8	0.2	5.5	5.6
Carbohydrate	5.0	5.8	6.5	4.0	6.7
Fat	4.4	1.7	7.0	4.5	0.5
Salt	1.9	1.1	1.3	1.4	1.7

Table 7.3 Description of meat analogues and ingredients according to the packaging.

Signature product	Company	Ingredients according to packaging	Website
Kipstuckjes	The vegetarian Bucher	88% soy structure (soy protein, water), spice-extract, sunflower oil, natural flavoring	thevegetarian butcher.co.uk
Chick free pea based	Naturli Foods	Water, texturized pea protein concentrate (31%), vegetable bouillon (salt, dextrose, yeast extract, dried vegetables, natural flavouring), fermented dextrose.	naturli-foods.com
Stukjes als van Kip	Albert Heijn	rehydrated vegetable protein (soy, wheat), sunflower oil, free-run egg protein, wheat starch, vinegar, natural flavors, aroma, water, sea salt, salt, maltodextrin, iron, vitamin B12.	ah.nl
Vegetarische basis wokstukjes	Albert Heijn	rehydrated vegetable protein (40% soy, 40% wheat), sunflower oil, free-run egg protein powder, wheat fiber, flavorings, wheat starch, natural flavor, thickener (carrageenan [E407]), diet salt (potassium chloride), dextrose, spices, maltodextrin, yeast extract, onion, salt, iron, vitamin B12.	ah.nl
Vivera Plantaardige kipstuckjes	Vivera	93% rehydrated soy protein, onion extract, natural flavors (contains wheat), pea fiber, salt	vivera.com

### 7.3.2 Rheological properties

The rheological properties were measured with a closed cavity rheometer (CCR) (RPA elite, TA instruments, New Castle, Delaware, USA) (Emin & Schuchmann, 2017). Approximately 6 g of product was placed in between two plastic films in the cavity, which was sealed with a closing pressure of 4.5 bar to prevent water evaporation during heating. The closed cavity rheometer has a radius of 22.5 mm and the maximum height of the inner cavity is 4 mm having a biconical opening with an angle of 3.35° for ensuring a homogeneous shear field. Grooves on the surface of the cones prevent slip. The lower cone oscillates in strain-controlled mode while the upper cone remains stationary. First, the meat and meat analogues were heated for 2 min at 30°C and 65°C without shear shearing. The latter temperature is often considered to be the core temperature of red meat during cooking. Then, strain sweep (0.01-1000%) experiments were performed at these elevated temperatures at a constant frequency (1 Hz). In a second test, the meat and meat analogues were heated at 30°C and 65°C for 2 min and then cooling to 30°C with a cooling rate of 5°C/min without a shear treatment.



Strain sweep experiments were used to determine the yield stress and the flow stress of a material. The yield stress is defined here as the value of the shear stress at the end of the LVE regime. Here we define this stress as the point where  $G'$  differs more than 5% from its strain-independent value in the LVE regime. The flow stress is defined here as the value of the shear stress at the crossover point, where the storage modulus is equal to the loss modulus ( $G' = G''$ ).

### 7.3.3 Large amplitude oscillatory shear (LAOS)

The stress and strain data obtained from the LAOS measurements were analysed using the MITlaos software (Version 2.1 beta, freeware distributed from MITlaos@mit.edu). The strain amplitude was varied in the range of 0.01-1000% at a constant frequency of 1 Hz at 30°C. Lissajous curves were used to relate the response of the protein materials to the imposed oscillatory strain.

The area enclosed by a Lissajous curve can be interpreted as the energy dissipated per unit volume during one complete cycle of the imposed oscillatory strain. The energy dissipated per unit volume in a single cycle ( $E_d$ ) is a function of the first-order viscous Fourier coefficient ( $G_1''$ ; calculated from the intensity and phase of the first-harmonic) only (equation 7.1):

$$E_d = \oint \sigma d\gamma = \pi G_1'' \gamma_0^2 \quad 7.1$$

The energy dissipated by a perfectly plastic material in a single cycle ( $(E_d)_{pp}$ ) is equal to equation 7.2

$$(E_d)_{pp} = 4 \gamma_0 \sigma_{max} \quad 7.2$$

for a given strain amplitude ( $\gamma_0$ ) and maximum stress ( $\sigma_{max}$ ). The ratio of the actual dissipated energy and the perfectly plastic dissipation gives the energy dissipation ratio ( $\varphi$ ) as proposed by Ewoldt et al. (2010) (equation 7.3).

$$\varphi = \frac{E_d}{(E_d)_{pp}} = \frac{\pi G_1'' \gamma_0}{4 \sigma_{max}} \quad 7.3$$

### 7.3.4 Texture maps and dissipation colour schemes

Texture maps summarize rheological information into two-dimensional plots. Here the texture maps are based on the stress and strain at the end of the linear viscoelastic (LVE) regime and the stress and strain at the crossover point, to classify products into four quadrants (Figure 7.1) (Hamann & MacDonald, 1992). Materials in quadrant 1 (Figure 7.1 lower left), with low shear stress and low shear strain, were classified as a soft, non-shaped texture commonly referred to as “mushy” (such as for grits and similar food materials). Materials in quadrant 2 (Figure 7.1 lower right), with low shear stress and high shear strain, are often described as “rubbery” (such as gelatin). Quadrant 3 (Figure 7.1 top right), indicating strong materials with high shear stress and shear strain, indicates a “tough” texture (for example, fruit leather and dried fruits). Quadrant 4 (Figure 7.1 top left), with high shear stress and low shear strain, characterises products with a “brittle” texture (such as many baked or confectionery food products) (Tunick & Van Hekken, 2010).

The energy dissipation ratio is depicted by colour contours in strain-temperature diagrams. When  $\varphi = 0$  (blue), the rheological response is purely elastic, while  $\varphi = 1$  (yellow) implies that the material is a perfect plastic (Ptaszek, 2014). A  $\varphi$  of  $\pi/4$  corresponds to a material that behaves as a Newtonian liquid.

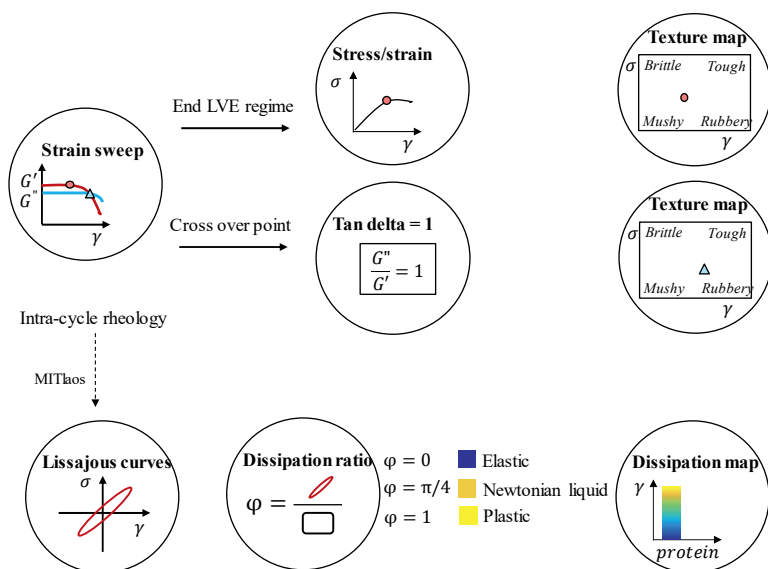


Figure 7.1. The storage modulus ( $G'$ ) and loss modulus ( $G''$ ) versus strain to define the crossover point ( $G' = G''$ ) and the end of the linear viscoelastic (LVE) regime.

## 7.4 *Results and discussion*

### 7.4.1 *Texture maps of meat and meat analogues*

Figure 7.2 presents a texture map using the stress and strain values at the end of the LVE regime of meat and meat analogues at 30°C, and samples heated at 65°C and subsequently cooled to 30°C. At 30°C, meat products behave “mushy” whereas meat analogues are “tough”. Heating and subsequent cooling (i.e. at 65°C and cooled to 30°C) of meat products leads to a shift in the texture map from mushy to tough. This behaviour was most pronounced for chicken and salmon. This is in line with a previous study on chicken meat (Harris & Shorthose, 1988). After heating, the meat products are in the same area of the map as the meat analogues. For meat analogues there was only a small effect by a heat treatment observed in the texture maps, meaning that stress and strain values at the end of the LVE are hardly influenced by heating. Some meat analogues slightly shift into the opposite direction (“tough” to “mushy”), as compared with meat. The limited effect of heating on meat analogues is not unexpected since the commercial meat analogues tested were most likely heated during processing and any denaturation or crosslinking had already been completed.

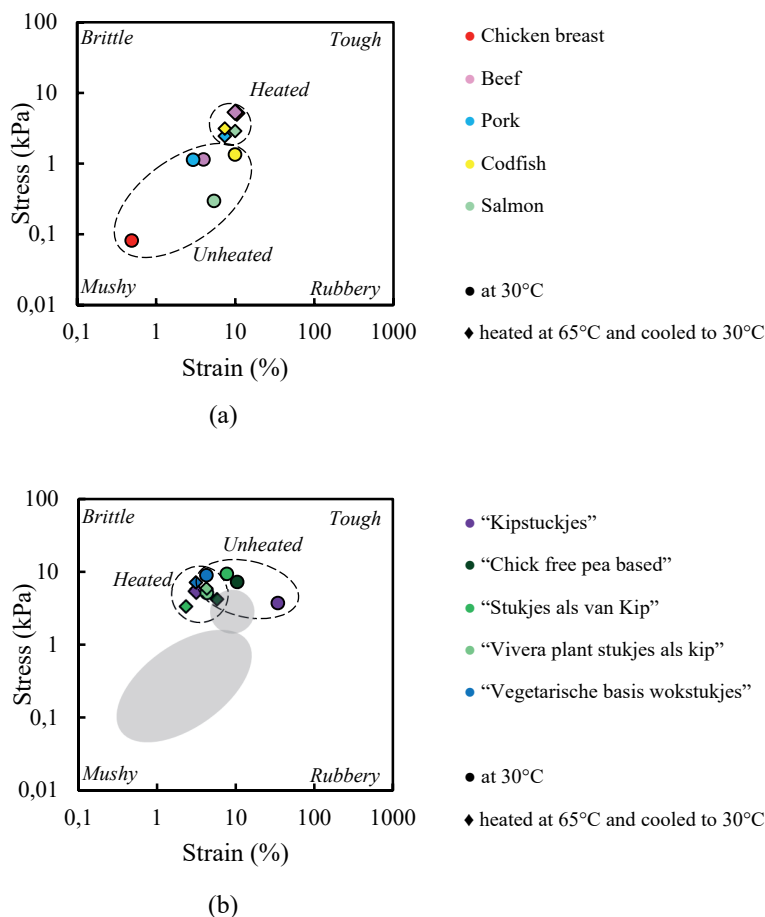


Figure 7.2. Texture map at the end of the LVE regime for meat (a) and meat analogues (b) heated at 30°C and heating to 65°C, and cooling to 30°C. Lines are drawn to guide the eye and shows the outline. The grey area in the texture map of meat analogues shows the outline of meat products, shown also in the Figure 7.2 (a).

Figure 7.3 shows the behaviour at the crossover point ( $G' = G''$ ), where the destructuring has proceeded further. Heating and cooling (i.e. at 65°C and cooled to 30°C) meat products gave a shift in the texture map from mushy to tough. The crossover stresses of different meat analogues at 30°C and pre-heated at 65°C and cooled to 30°C are comparable but the crossover strains are different for each meat analogue.

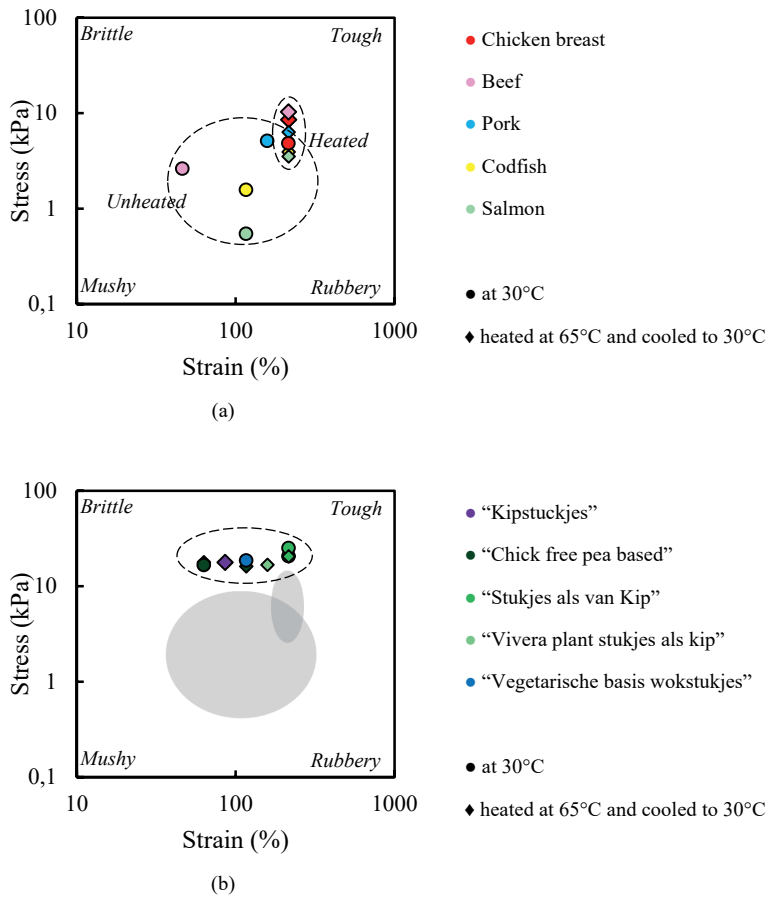


Figure 7.3. Texture map at the crossover point for meat (a) and meat analogues (b) heated at 30°C and heating to 65°C, and cooling to 30°C. Note that the scales of the x-axis and y-axis are different from those in Fig 2. Lines are drawn to guide the eye and shows the outline, the grey area in the texture map of meat analogues shows the outline of meat products shown in Figure 7.3 (b).

#### 7.4.2 Colour scheme to describe the dissipation ratio

A more detailed assessment of the non-linear viscoelastic behaviour of meat and meat analogues was obtained using Lissajous curves. The dissipation ratio was calculated to extract the essence of the non-linear behaviour (Ewoldt et al., 2008, 2010; Klost et al., 2020; Tao et al., 2019). The dissipation values are presented in a colour scheme to facilitate comparison. The upper panel of Figures 7.4 and 7.5 show these colour schemes for meat and meat analogues. The lower panel of Figures 7.4 and 7.5 present the corresponding elastic Lissajous curves for the grid values of imposed strain amplitude and temperature marked by

the crosses in the left-hand panel (colour scheme of the dissipation ratio). As expected, both meat and meat analogues show an increase in the dissipation ratio for increasing strain amplitudes, shown by an enlargement of the area encompassed by the Lissajous curves. Heating made the meat more elastic for all strain amplitudes, but a more sudden transition to viscous/plastic behaviour was observed as well.

For meat, at 30°C, narrow ellipses were observed at low strain amplitude indicating a predominantly elastic behaviour. At higher strain amplitudes these curves showed a gradual transition to a more rhomboidal shape, indicating a transition to plastic behaviour. After heating to 65°C, and cooling, the plots become more narrow than those of the unheated meat samples, indicating an increase of the elasticity in the sample. Compared with the unheated samples we now see a much stronger strain stiffening effect in the intermediate strain range, shown by an inverted sigmoidal shape of the plots. At the highest strains the sigmoidal shape significantly widens, indicating a gradual transition to plastic behaviour. For codfish and salmon similar colour maps and Lissajous curves were found as for meat, including the observation that after heating, the curves attain an inverted sigmoidal shape.

Meat analogues hardly gained elasticity upon heating. Heating did not significantly change the Lissajous curves of meat analogues. Instead, the dissipation ratio for meat analogues transitioned gradually from elastic to plastic as a function of increasing strain amplitudes, in a similar manner as unheated meat analogues.

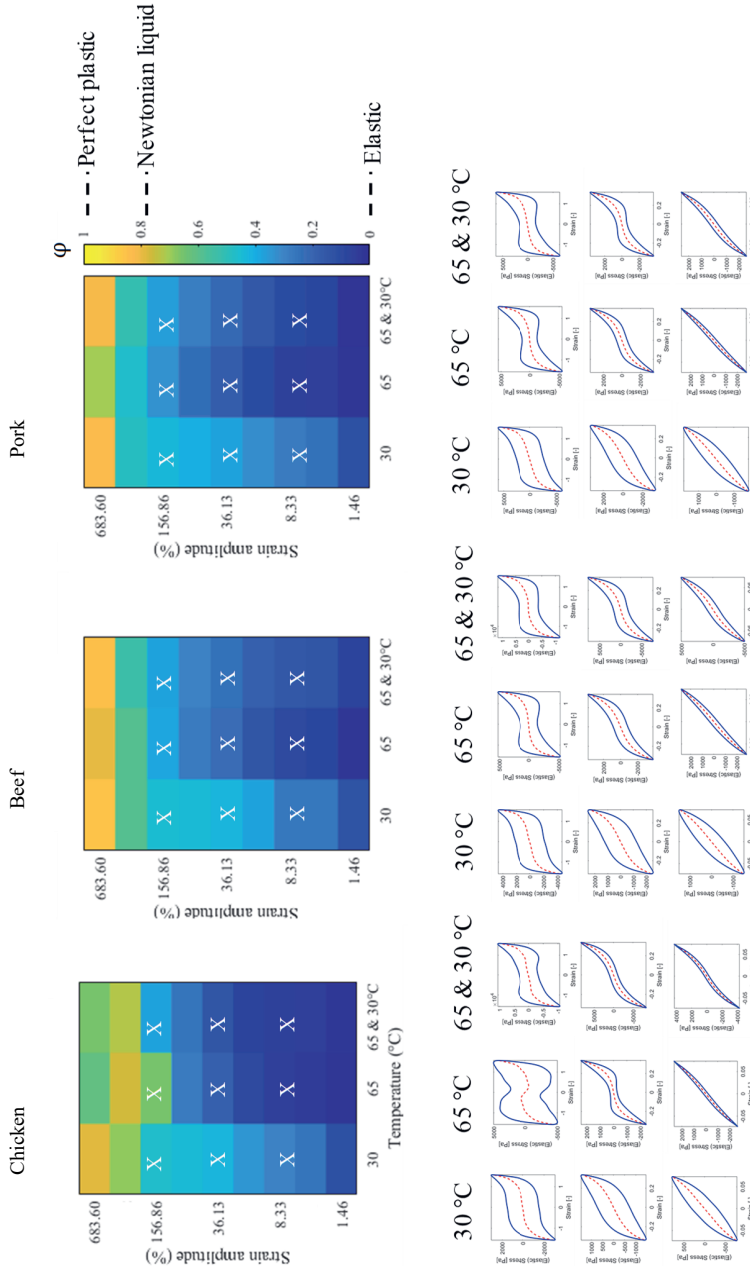


Figure 7.4. Colour scheme of the dissipation ratio ( $\phi$ ) in a strain-temperature diagram for meat and fish at 30°C, heated at 65°C, and cooled to 30°C. The colour corresponds to the value of the dissipation ratio ( $\phi$ ) in the colour bar,  $\phi = 0$ , elastic;  $\phi = \pi/4$ , Newtonian liquid;  $\phi = 1$ , perfect plastic. Lower part: Lissajous curve of stress versus strain amplitude at three different strain amplitudes corresponding to the X symbol in the upper panel (individual plots of normalized stress [solid lines] and elastic stress [dashed lines] vs. strain).

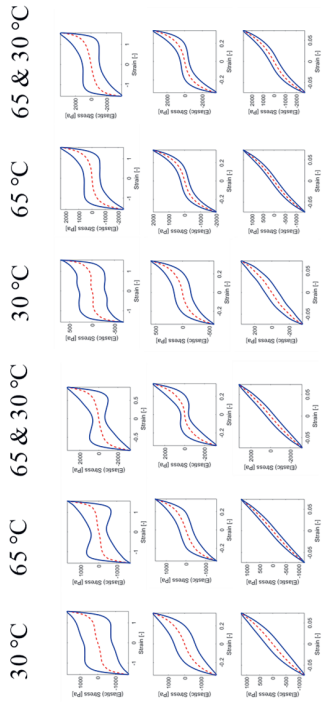
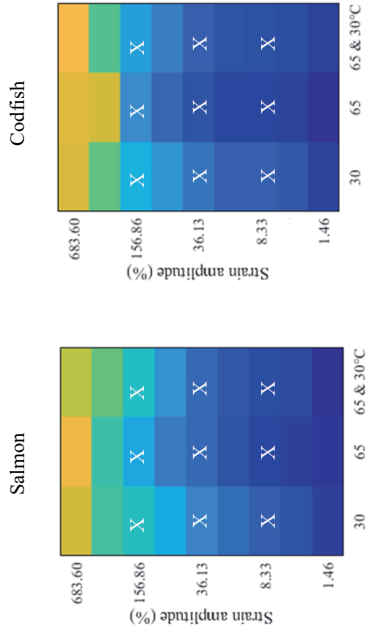


Figure 7.4 (continued)



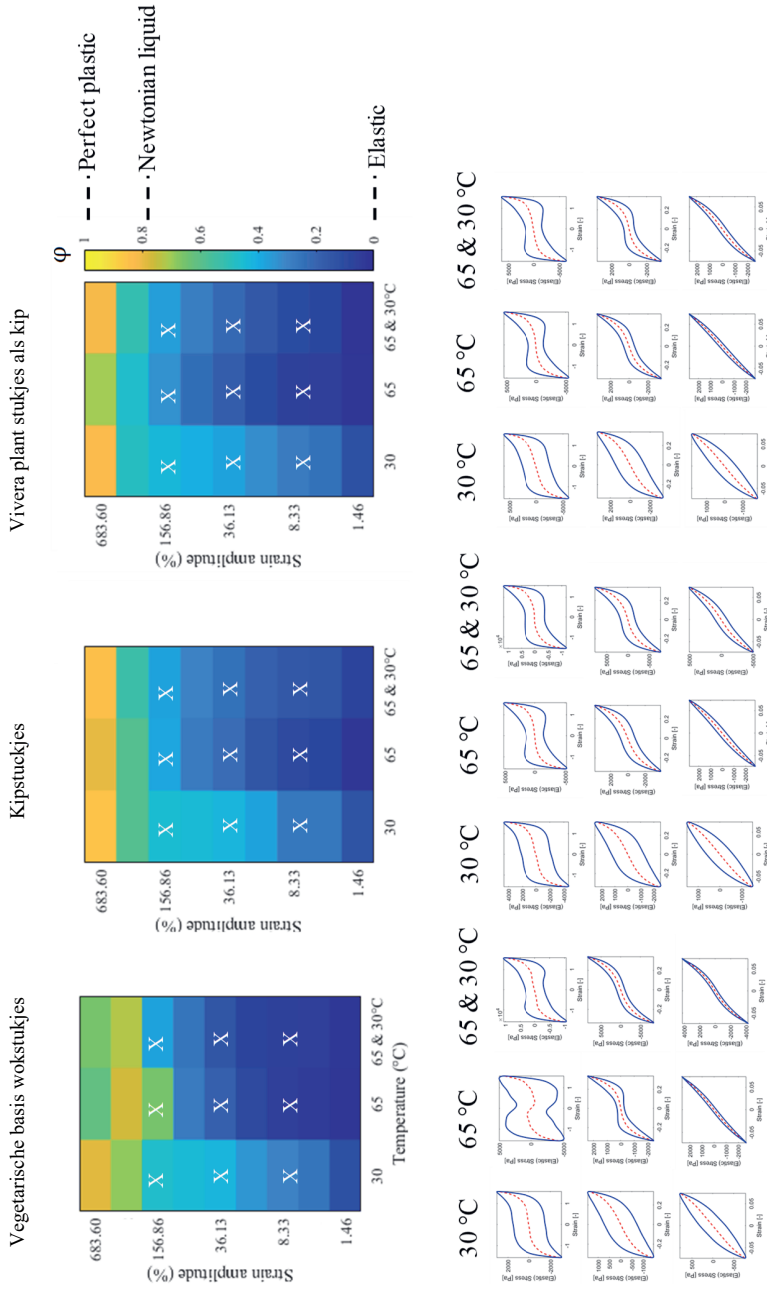
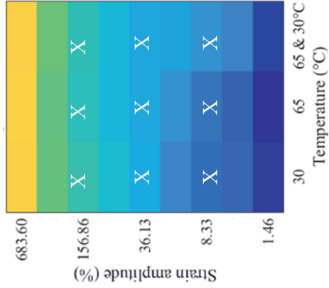
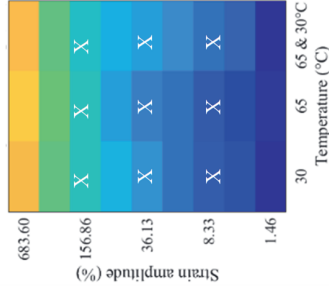


Figure 7.5. Colour scheme of the dissipation ratio ( $\phi$ ) in a strain-temperature diagram for meat analogues at 30°C, heated at 65°C, and cooled to 30°C. The colour corresponds to the value of the dissipation ratio ( $\phi$ ) in the colour bar,  $\phi = 0$ , elastic;  $\phi = \pi/4$ , Newtonian liquid;  $\phi = 1$ , perfect plastic. Lower part: Lissajous curve of stress versus strain amplitude at three different strain amplitudes corresponding to the X symbol in the upper panel (individual plots of normalized stress [solid lines] and elastic stress [dashed lines] vs. strain).

Chick free pea based



Stukjes als van Kip



30 °C    65 °C    65 & 30 °C    30 °C    65 °C    65 & 30 °C

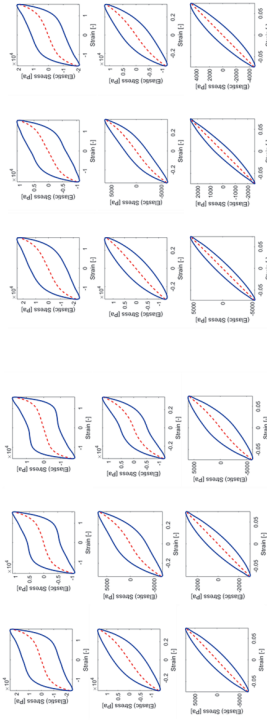


Figure 7.5 (continued)

To describe the local changes of the material inside one strain cycle, the stiffening ratio or S-factor, is introduced in equation (7.4):

$$S = \frac{G'_L - G'_M}{G'_L} \quad (7.4)$$

where  $G'_L$  is the large strain (or secant) modulus, which describes the slope of a line between the origin and the stress at maximum strain in the Lissajous curve. The modulus  $G'_M$  is the slope of the Lissajous curve at zero strain. In the linear regime,  $G'_L = G'_M$ , and therefore  $S = 0$  by definition. In Figure 7.6, the S-factor is plotted as a function of the strain amplitude. For small strain amplitudes, the S-factor is indeed close to zero. With increasing strain amplitude, the S-factor increases indicating intra-cycle strain stiffening. After heating to 65°C and cooling, the meat products (i.e. chicken, pork, beef, salmon and codfish) exhibit a larger S-factor and thus a stronger strain stiffening effect in the intermediate strain range compared to the unheated samples. The meat analogues products clearly showed less strain stiffening upon deformation.

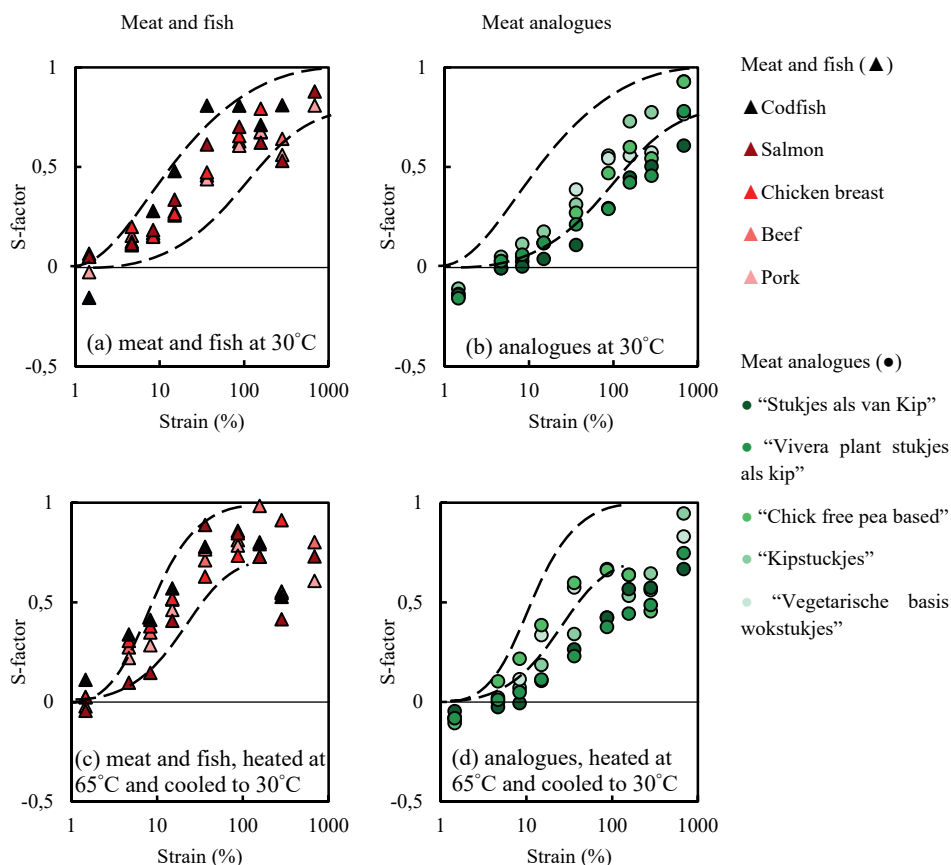


Figure 7.6. Stiffening ratio (S-factor) as a function of strain amplitude for meat and meat analogues. Dashed lines are drawn to guide the eye and show the outlines for the highest and lowest values of meat and fish from the meat analogues graphs.

All materials show apparent stiffening; showing decreasing curves for the  $G'_L$  and  $G'_M$ . For meat and fish, the  $G'_M$  decreases faster than the  $G'_L$  indicating a positive S-factor and stronger apparent strain stiffening in the intermediate strain range (Appendix Figure A 7.1). The meat analogues products show less differences between the  $G'_L$  and  $G'_M$  upon deformation, exhibiting more mild apparent strain stiffening (Appendix Figure A 7.2).

We conclude that meat products have a lower dissipation ratio and a higher S-factor than current meat analogues, especially after heating. It can be expected that the observed differences in elastic properties and stiffness will lead to differences in sensory characteristics. For example, a previous study showed that the non-linear rheology of whey

protein isolate/k-carrageenan gels correlated to sensory and oral processing. The ratio  $G'_L/G'_M$  positively and negatively correlated with oral processing data that including aspects after several chews as well as the first bite (Melito et al., 2013). In other words, the non-linear rheological properties of meat and meat analogues can identify and quantify differences between meat and meat analogues.

Non-linear elasticity, and specifically strain-stiffening, is generic to filament/fibrous networks. The strain at which stiffening becomes significant depends strongly on the persistence length of the filament in a protein-based network. Stiffer filaments, like F-actin or collagen, stiffen at low strains whereas more flexible filaments stiffen only at larger strains (Schofield et al., 1983). The higher stiffening for meat products could be related to its unique hierarchical structure on small length scales. Future developments on meat analogues should therefore focus on routes how to create more stiffness and elasticity, for example through creating more physical and chemical interactions at mesoscopic length scale, thereby to some degree creating a hierarchical structure as well.

### 7.5 *Conclusion*

We quantified the non-linear rheology resemblance of animal meat to their plant-based analogues by using a combination of texture maps and colour schemes. Meat analogues have similar stress and strain values at the end of the LVE regime and crossover point compared with heated meat, but their analogues are less elastic than heated (prepared) meat. In addition, the effect of heating on meat and meat analogues is different. Heating meat results in a tougher and more elastic material. For meat analogues there was only a small effect of a heat treatment observed, which is probably related to their processing history.

## 7.6 Appendix

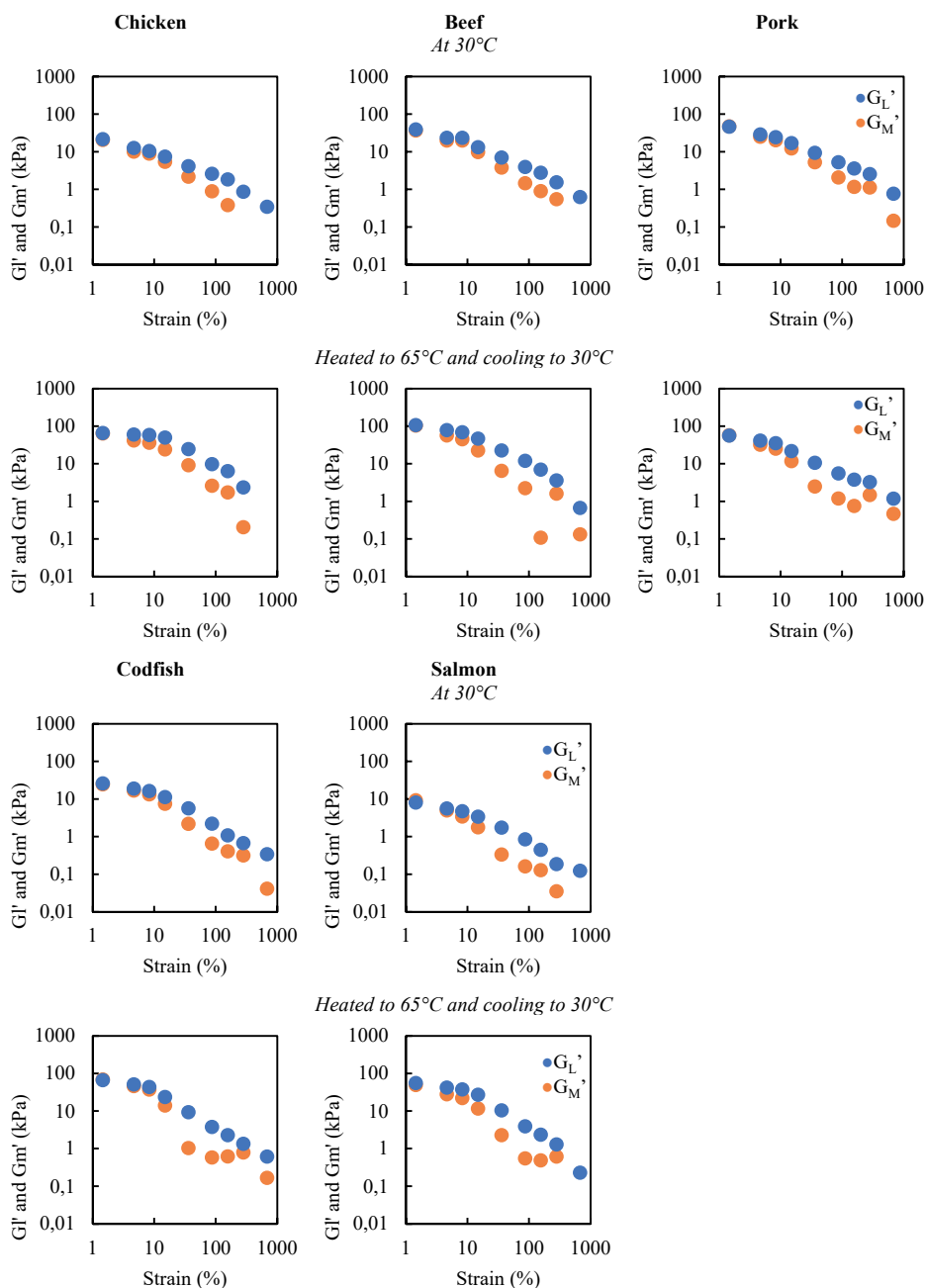


Figure A 7.1. The large strain modulus  $G'_L$  and zero strain modulus  $G'_M$  as function of strain for meat and fish at 30°C, and heated at 65°C and cooled to 30°C.

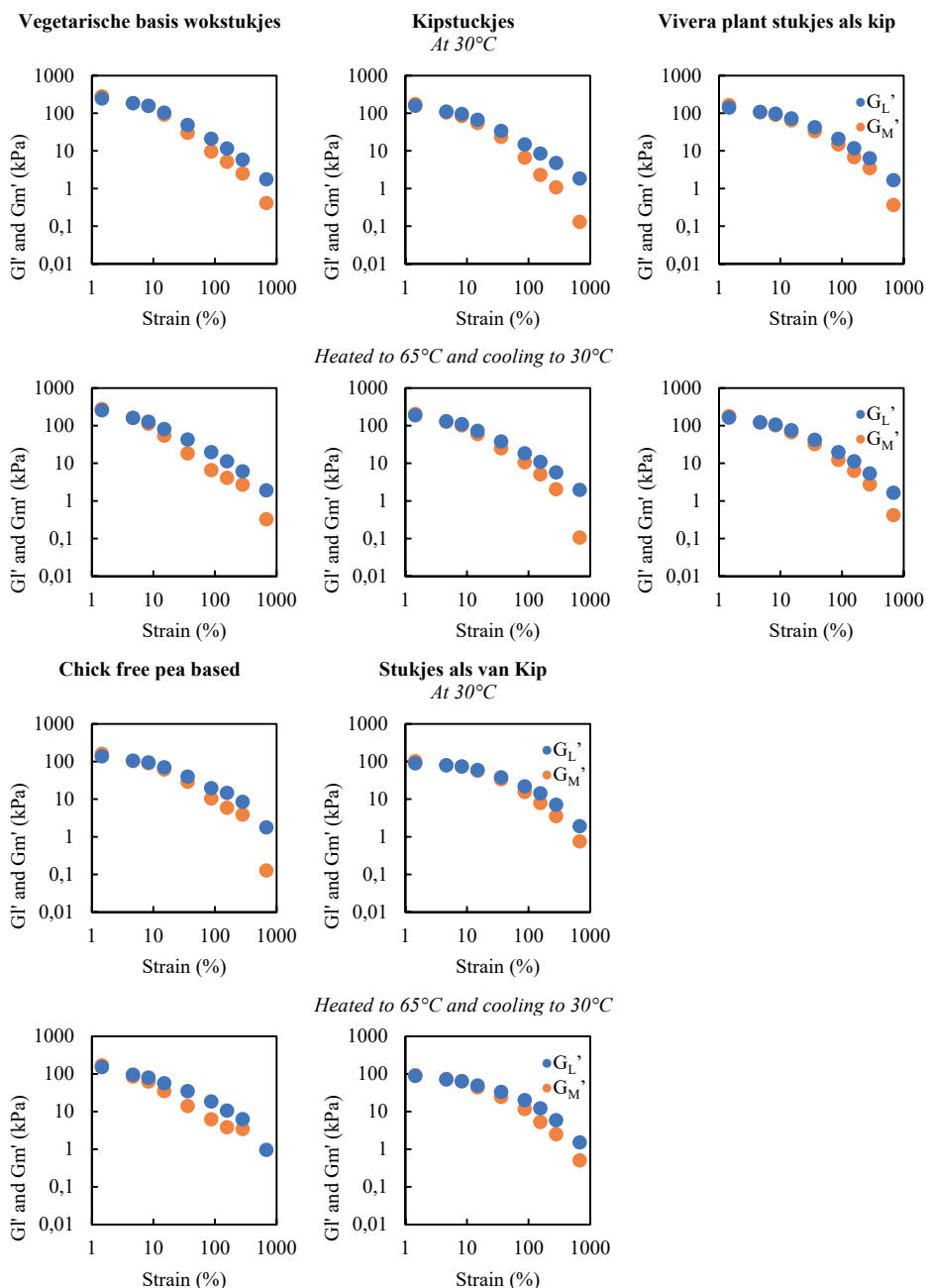


Figure A 7.2. The large strain modulus  $G'_L$  and zero strain modulus  $G'_M$  as function of strain for meat analogues at 30°C, and heated at 65°C and cooled to 30°C







# *Chapter 8*

## *Texture methods for evaluating meat and meat analogue structures: A review*

*This chapter has been published as* Schreuders, F. K. G., Schlangen, M., Kyriakopoulou, K., Boom, R. M., & van der Goot, A. J. (2021). Texture methods for evaluating meat and meat analogue structures: A review. *Food Control*, 108103.

## 8.1 *Abstract*

Meat analogue products are considered to help consumers reducing their meat consumption. Their key success factor is their high similarity in sensory properties compared to meat. Even though the structure and texture characteristics of meat are well documented, dedicated methods used to analyse meat analogues are limited still. This review summarises texture and structure analysis methods of meat and meat analogues: mechanical testing; for example Texture Profile Analysis, spectroscopy; for example NMR and imaging techniques; for example hyperspectral imaging. Furthermore, the advantages and limitations of each texture and structure method are described. Finally, characterizations aspects specific to meat analogues are discussed. Promising methods for future research are described that have potential to get more insight into the fibers of meat analogues and the structure development during thermomechanical processing of meat analogues.

### *Industrial relevance*

To be commercially successful for large groups of consumers, alternatives for meat should be highly similar to meat. That is why meat analogues should resemble existing meat in their texture. It is thus important to understand the texture properties with the help of relevant techniques, such as mechanical, spectroscopy and imaging techniques. In this manuscript, we describe promising texture methods for characterization of properties specific to meat analogues. The development of novel techniques to quantify meat analogue properties will stimulate the development of meat analogues that satisfy the values and wishes of consumers.

## 8.2 Introduction

Plant protein-based meat analogues that mimic the sensory properties of meat could be a route to help consumers to reduce their meat consumption (Elzerman, Hoek, van Boekel, et al., 2011; Hoek et al., 2011; Michel et al., 2021). A reduction of meat consumption might lead to a lower environmental footprint of the diet because meat production leads to intensive use of land, water and energy (Tilman & Clark, 2014; Weinrich, 2019). However, the different nature of plant materials compared to those of meat, renders the imitation of meat texture a challenge. For example, plant proteins do not naturally occur in fibrillar orientation (Fuhrmeister & Meuser, 2003; Sun & Arntfield, 2010; Taherian et al., 2011). Although meat products are widely different in their properties, they do share many characteristics that they do not share with plant proteins. For example, the very small length scale of meat muscle structure consists of myofibrillar protein and myoglobin positioned into a hierarchical fibrillar structure that is not easily replicated in plant-based meat analogues. The unique juiciness of meat is also a result of this hierarchical structure (Frank et al., 2017). Besides, many of the unique meat properties are strongly dependent on the internal structure of the meat, which ranges from 100 nm and 100  $\mu\text{m}$ .

To be commercially successful in the short term, and for large groups of consumers, alternatives should not deviate too much from their current meal and thus resemble existing meat in their texture (Elzerman, Hoek, van Boekel, et al., 2011; Hoek et al., 2011; Michel et al., 2021). As described by Dekkers, Boom, et al. (2018a), two approaches exist to make meat analogues: top-down and bottom-up. The latter approach aims at mimicking the full hierarchical structure of meat, but these methods are laborious and require more resources than the top-down approach. Examples of the top-down approach are the shear cell technology and extrusion. Extrusion is widely used industrially to make currently available meat analogues. However, the fibrousness of meat analogues from plant proteins created via a top-down approach is typically less hierarchical. An important question though is whether similarities on a larger length scale are sufficient for similarities in sensory properties already. The first step towards insights is a characterisation of the structures at different length scales for both meat and meat analogues.

The texture of meat has been widely studied. Many analytical techniques and methods are established for meat and fish, including sensory evaluation and mechanical methods. Therefore, while the existing methods are quite adequate for meat, it is not clear whether

these would also be sufficient to characterize the differences between meat and the plant-based matrices. The objective of this paper is therefore to understand the potential of those analytical methods developed for meat to be used for meat analogues as well. To investigate this, we will review the available methods on their suitability for analysing plant-based meat analogues. We will then assess whether they cover the complete parameter space and describe the need for new techniques specifically for those properties of plant materials that are different from meat products.

### 8.3 *Instrumental techniques for texture of meat and meat analogues*

Although texture is ‘the combination of the rheological and structure (geometrical and surface) attributes of a food product perceptible by means of mechanical, tactile, and where appropriate, visual and auditory receptors’ as defined in 2008 by the International Standards Organization (ISO, 2008), most techniques are focused on instrumental testing. Instrumental techniques to measure the texture of meat and meat analogues are often used instead of sensory experiments, as the latter is expensive, time-consuming and difficult to make quantitative. Instrumental techniques provide objective information on different structural parameters. Meat texture is characterized by different methods. Each method analyses meat products at a certain length scale. Typical approaches to study the texture and structure of meat and meat analogues include mechanical, spectroscopy and imaging characterization methods. This paper summarizes the basic technologies and the most recent advances of those technologies for processing different types of meat (i.e. beef, pork, and poultry) and meat analogues (i.e. shear cell structures and extruded products) (Figure 8.1).

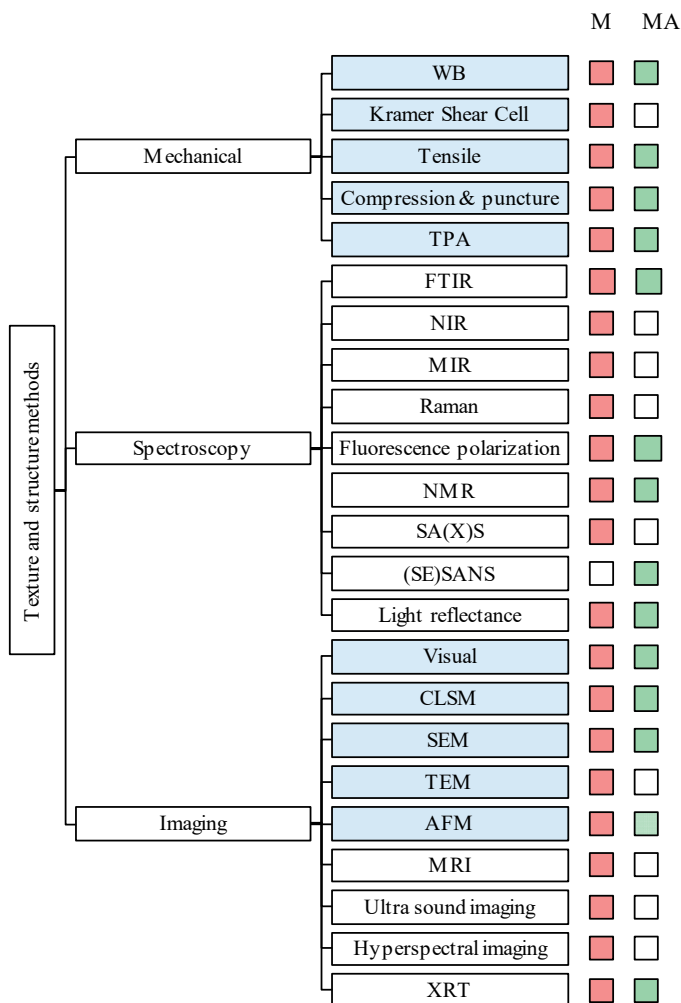


Figure 8.1. Destructive (■) and non-destructive (□) texture and structure methods used for meat (M, ■) and meat analogues (MA, ■). Abbreviations: WB, Warner-Bratzler; TPA, Texture Profile Analysis; NIR, Near-infrared; MIR, Mid-infrared; SA(X)S, Small-angle (X-ray) scattering; (SE)SANS, (Spin-echo) Small-angle neutron scattering; CLSM, Confocal laser scanning microscopy; SEM, Scanning electron microscopy; TEM, Transmission electron microscopy; AFM, Atomic force microscopy; MRI, Magnetic resonance imaging; XRT, X-ray tomography.



### 8.3.1 *Mechanical techniques*

Traditionally, texture is evaluated with mechanical methods. Such methods are used to analyse the mechanical properties of a product through compressing, shearing and/or pulling. Mechanical methods are applied to all kinds of food products, such as cheese, candy, pasta, but also meat and meat analogues. A limitation of the mechanical methods is that they are destructive, hence tested products cannot be used for other applications. A folding test is often performed as the first mechanical test. The test assesses the structural failure of both meat and meat analogue products based on a five-point grading system (Herrero et al., 2008; Kamani et al., 2019). It is an easy and fast method to obtain basic information about the texture of a product, but it is not fully quantitative.

After performing the folding test, one or more of the following tests are done. The Warner-Bratzler test measures the maximum shear force as a function of knife cutting movement through a meat product (Novakovi & Tomaševi, 2017). It is difficult to give a precise physical meaning to the Warner-Bratzler shear force because it measures a combination of shearing, compression and tensile stress, making it more a measurement of overall quality attributes (Voisey, 1976). Nevertheless, the Warner-Bratzler test is used to analyse the texture of different types of meat products, in particular whole muscle products and sausages (Table 8.1). The probe of the Warner-Bratzler test consists of a single blade with a V-shaped notch (Morey & Owens, 2017). This blade is used to cut through the meat product, usually perpendicular to the longitudinal positioning of the muscle fibers, but some studies additionally measure the parallel direction (Cierach & Majewska, 1997). Furthermore, previous studies suggested that differences in the device, blade, product diameter, or settings used, influence the results (Novakovi & Tomaševi, 2017; Pool & Klose, 1969; Voisey & Larmond, 1974; Wheeler et al., 1996). Thus, standardization will be important to obtain results with the Warner-Bratzler method that allows comparison between studies.

A few studies use the Kramer Shear Cell test to measure meat texture in addition to the Warner-Bratzler test (Table 8.1). This test simulates a single bite into a piece of food. The principle is similar to the Warner-Bratzler test, but it has multiple, blunt blades arranged in parallel that correspond to specific slots in the base of the cell (Barbut, 2015; Morey & Owens, 2017). Products, often multiple at once, are placed in the cell; the products are compressed and sheared when the blades push the products through the slots. The resulting parameters are averages of the forces required to shear the full product (Morey & Owens,

2017). This makes it possible to measure products with an uneven surface for example. Similar to the Warner-Bratzler test, the Kramer Shear Cell test does not evaluate a single mechanical property. Instead, it measures a combination of the effects of compression and shear, which could be seen as a limitation of the method. Xiong et al. (2006) compared the potential of the Kramer Shear Cell and the Warner-Bratzler method for the prediction of sensory tenderness of chicken breast, and found that the shear values correlated well with descriptive sensory attributes as well as consumer sensory attributes. Another study also indicated that both methods were successful in evaluating rabbit meat tenderness and presented similar levels of correlation with sensory scores (Bianchi et al., 2007). For both methods, the products need to have a specific thickness. This means that these methods can only be used on meat and meat analogues (extruded products, sheared, patties, sausages, etc.) that fulfil these requirements. While the methods are therefore suitable within a pre-defined range of similar products with a limited variation of parameter values, it is not clear yet whether these methods would also allow the comparison with plant-based meat analogues, which can have quite different properties. The Kramer Shear Cell is not yet used to measure textural properties of meat analogues as far as the authors are aware.

Another mechanical test is the tensile test, which measures the resistance of a product against tearing. A product is mounted between two grips and extended in the tensile direction at a fixed speed until failure. Tensile parameters such as maximum rupture force, breaking strength and energy to fracture can be calculated from obtained stress and strain values. In general, tensile products have a dumbbell or dogbone shape to conduct the stress towards the middle of the product and induce failure at the intended location. Tensile tests are used with a wide product range such as sausages, frankfurters, ham, whole muscle products (Table 8.1) and in the past also meat patties (Beilken et al., 1991; Spadaro & Keeton, 1996). Tensile tests have also been applied to meat analogues (Dekkers, Nikiforidis, et al., 2016 and Chapter 2). The ratio between the tensile strengths parallel and perpendicular to the (muscle-) fiber orientation provides insight into the anisotropy of the product (Barbut, 2015; Dekkers, Nikiforidis, et al., 2016). For both meat and meat analogues a few studies calculate the anisotropic index (Dekkers, Hamoen, et al., 2018; Krintiras et al., 2015 and Chapter 2). Christensen et al. (2000) studied the tensile properties of whole beef meat as well as single muscle fibers and perimysial connective tissue. The use of a mechanical testing method for single muscle fibers is unique and is not realistic with other mechanical testing methods.

Therefore, the tensile test might be able to study the texture of products at a smaller length scale than other mentioned mechanical testing methods. This would allow for measuring the tensile strength of single meat analogue fibers from for example calcium-caseinate materials (Wang et al., 2018).









Another mechanical method to quantify food texture is a single compression test. The single compression test is often performed as an axial compression test between two flat plates (Barbut, 2015). The products have to be smaller than the contact area of the probe in use. Products can be compressed until failure, or to a certain level of deformation. Single compression tests are not used often (Table 8.1) as a double compression test, often called Texture Profile Analysis (TPA), can provide more information within a single experiment. Similar considerations regarding reliability for single compression tests have to be taken as for TPA tests (Lepetit & Culioli, 1994). TPA is a compression technique that combines multiple textural parameters such as hardness, chewiness, adhesiveness, cohesiveness and springiness in a single measurement. The TPA parameters can be divided into primary parameters (hardness, springiness, adhesiveness and cohesiveness) and secondary parameters (gumminess, chewiness, resilience) (Novakovi & Tomaševi, 2017). Primary parameters can be directly determined from the obtained force/time graph, while secondary parameters are derived from the primary parameters. The test is based on simulating the biting action of the mouth by a two-cycle compression series (Barbut, 2015). TPA tests are widely applied on meat analogues and meat products ranging from whole muscle products to emulsified sausage products (Table 8.1). A puncture test is similar to a compression test, but the probe contact area is now much smaller than the size of the product, for example through use of a needle-shaped probe. During a puncture test, the material is compressed to a certain strain by a probe to quantify properties such as maximum force, breaking strength, and the penetration depth. According to Barbut, (2015), it is commonly used for restructured products and emulsified meat products. However, literature only showed the use of a puncture test on chicken breast, meat patties and meat analogue sausages (Table 8.1). Penetration force, as measured with the puncture test, was found to be lower in sausages based on plant proteins than those based on poultry (Kamani et al., 2019). This indicated that the breaking force required to penetrate the outer skin of plant protein sausages is lower than in chicken sausages. In addition, penetration depth of plant-based sausages was used as a measure for the strength of binding agents (Arora et al., 2017). As meat and meat analogues are often heterogenous in structure, it can be hard



to obtain compression type measurements that is representative for the whole product. A recent technique of multi-point indentation characterizes the local mechanical texture of meat and meat analogues by mapping the elastic modules as measured with a spherical probe of radius 1 mm (Boots et al., 2021).

Dolores Romero de Ávila et al. (2014) studied the mechanical properties of commercial cooked meat products by both TPA and tensile tests. They showed that the parameters from the TPA could be used to construct models to predict tensile test parameters such as breaking strength and energy to fracture, removing the need for tensile tests. Furthermore, Ruiz De Huidobro et al. (2005) recommended the TPA method over the Warner-Bratzler method to predict meat texture on basis of a better correlation with sensory data and a higher accuracy. Similar conclusions were drawn by Caine et al. (2003) who showed that TPA parameters correlated better with variations in sensory results of beef tenderness than the Warner-Bratzler test. Similar to the Warner-Bratzler test, the TPA test requires standardized testing methods for trustworthy comparison between studies, and they can probably only make reliable correlations in limited parameter space.

For both meat and meat analogues textural elements can be studied with the Warner-Bratzler test, the tensile test, the TPA test and other compression techniques. The Kramer Shear Cell has only been used to quantify the texture of meat products but offers several benefits, such as the possibility to measure uneven products. Therefore, it might be a future direction for texture analysis of meat analogues. Furthermore, the recently developed multi-point indentation technique shows high potential to characterize heterogeneous meat and meat analogue structures. All described mechanical techniques analyse texture at a macroscale, except for the tensile test which can be used to analyse single muscle fibers at a smaller length scale. Therefore, we believe that the tensile test may also be used to analyse single fibers from meat analogues in the future. Furthermore, there is great importance for standardized testing methods of all mechanical tests described in this review to be able to compare different products (meat and meat analogues) and translate the quantitative analysis in sensory properties.

Table 8.1. Overview of mechanical techniques used in studies on meat and meat analogues from 2005 onwards. The colours in red and green indicate that the method is used for meat and meat analogues, respectively.

Technique	Properties	Product (m/ma)	Reference
Warner-Bratzler  	Warner-Bratzler shear force, slope at yield, shear energy	Steak (m)	(Destefanis et al., 2008; Peña-Gonzalez et al., 2019; Ruiz De Huidobro et al., 2005)
		Chicken breast (m)	(Cavitt, Xiong, et al., 2005; U-Chupaj et al., 2017; Xiong et al., 2006)
		Ham (m)	(Bermúdez et al., 2014; Rizo et al., 2019)
		Meat patty (m)	(Naveena et al., 2006)
		Sausage (m)	(Barbut et al., 2016; Cáceres et al., 2006; Del Nobile et al., 2009; Purohit et al., 2016; Szerman et al., 2015)
		High moisture extruded product (ma)	(Caporgno et al., 2020; Osen et al., 2014; Palanisamy et al., 2018)
		Low moisture extruded product (ma)	(Samard & Ryu, 2019b)
		Patty (ma)	(Forghani et al., 2017)
		Sausage (ma)	(Kamani et al., 2019)
Kramer Shear Cell  	Shear force, maximum slope, total energy	Chicken breast (m)	(Cavitt, Meullenet, et al., 2005; Del Olmo et al., 2010; Xiong et al., 2006)
		Rabbit meat (m)	(Bianchi et al., 2007)
		Meat patty (m)	(Holliday et al., 2011)
Texture Profile Analysis  	Hardness, chewiness, springiness, adhesiveness, gumminess, resilience, etc.	Steak (m)	(Peña-Gonzalez et al., 2019; Ruiz De Huidobro et al., 2005)
		Chicken breast (m)	(Dolores Romero de Ávila et al., 2014; U-Chupaj et al., 2017)
		Ham (m)	(Dolores Romero de Ávila et al., 2014; Rizo et al., 2019)
		Meat patty (m)	(Das et al., 2015)
		Sausage (m)	(Herrero, Ordóñez, et al., 2007; Herrero et al., 2008; Laranjo et al., 2015; Purohit et al., 2016)
		Sausage (ma)	(Arora et al., 2017; Kamani et al., 2019; Majzoobi et al., 2017; Stephan et al., 2018)
		Patty (ma)	(Forghani et al., 2017; Kim et al., 2011; Lee & Hong, 2019)
		High moisture extruded product (ma)	(Hong et al., 2019)
		Low moisture extruded product (ma)	(De Angelis et al., 2020; Samard et al., 2019; Samard & Ryu, 2019b, 2019a)
Single compression  	Stress, maximum compression load	Steak (m)	(Christensen et al., 2011; Panea et al., 2018)
		Sausage (m)	(Alirezalu et al., 2017)

Puncture test 	Puncture force, puncture shear force	Chicken breast (m)	(Cavitt, Meullenet, et al., 2005)
		Meat patty (m)	(Braeckman et al., 2009; Naveena et al., 2006)
		Sausage (ma)	(Arora et al., 2017; Kamani et al., 2019)
Tensile test 	Tensile force, breaking strength	Steak (m)	(Zhang et al., 2019)
		Chicken breast (m)	(Dolores Romero de Ávila et al., 2014)
		Ham (m)	(Dolores Romero de Ávila et al., 2014)
		Sausage (m)	(Daros et al., 2005; Herrero, Ordóñez, et al., 2007; Herrero et al., 2008)
		Shear cell structures (ma)	(Dekkers, Nikiforidis, et al., 2016; Krintiras et al., 2015; Wang et al., 2018)
		High moisture extruded product (ma)	(Pietsch et al., 2019)

### 8.3.2 Spectroscopy

Spectroscopy (infrared, Raman, fluorescence polarization, NMR and light scattering) provides insight into the local composition (mostly surface of the product), intermolecular interaction as well as anisotropy of meat and meat analogues (Table 8.2). Proteins, lipids, water and other substances may be localised and quantified simultaneously. Spectroscopy is direct and non-invasive and requires only small products usually.

Infrared (IR) spectroscopy provides information on the chemical composition by measuring infrared absorption spectra. The spectrum can be used to characterize specific chemical bonds in products and can yield information about the composition, but also about the state of individual substances. In meat products, Fourier Transform IR spectroscopy (FTIR) was used to monitor conformational changes of myofibrillar proteins and connective tissue (Kohler et al., 2007; Perisic et al., 2011). In meat analogues, FTIR was used to identify structural changes after processing in zein, pea and spirulina/lupin protein (like  $\alpha$ -helix and  $\beta$ -sheet) (Beck et al., 2017; Mattice & Marangoni, 2020; Palanisamy et al., 2019).

A near-infrared (NIR) spectrum is often divided into two sections, namely, short wave near-infrared spectral region (SW-NIR) of 780-1100 nm and long wave near-infrared spectral region (LW-NIR) of 1100 - 2526 nm (Cheng et al., 2013). The spectrum shows broad overlapping peaks and large baseline variations, which requires mathematical processing to extract compositional information (Subramanian & Rodriguez-Saona, 2009). In meat products, NIR-spectra were used to subsequently predict the chemical composition (such as

crude protein, intramuscular fat, moisture/dry matter, ash, gross energy, myoglobin and collagen), technological parameters (water holding capacity, Warner-Bratzler and slice shear force) and sensory attributes (juiciness, tenderness or firmness) (Prieto et al., 2009). This would fully eliminate the use of destructive analysis methods like mechanical measurements. However, its prediction is limited to a small range of products and was further hindered by the heterogeneity of intact meat products, and inconsistent product preparation.

The mid-infrared (MIR) spectrum is divided into four sections, namely, the X-H stretching region ( $4000\text{--}2500\text{ cm}^{-1}$ ), the triple bond region ( $2500\text{--}2000\text{ cm}^{-1}$ ), the double bond region ( $2000\text{--}1500\text{ cm}^{-1}$ ), and the fingerprint region ( $1500\text{--}400\text{ cm}^{-1}$ ) (Cheng et al., 2013). MIR spectroscopy was used to obtain information on the conformation of proteins (such as  $\alpha$ -helix or  $\beta$ -sheet) (Carbonaro & Nucara, 2010). Another study showed the analysis of food raw materials (such as skimmed milk powder, chicken meat powder, soy protein isolate (SPI), pea protein isolate (PPI) and wheat flour) on the presence of several potential food adulterants (nitrogen-rich compounds, foreign protein and bulking agent) (da Costa Filho et al., 2020).

Raman spectroscopy provides information on secondary protein conformation (i.e.  $\alpha$ -helix and  $\beta$ -sheets) as well as on the amino acid composition (Overman & Thomas, 1999). In meat products, Raman spectroscopy has been successfully correlated with quality parameters such as protein solubility, apparent viscosity, water holding capacity, instrumental texture methods, and fatty acid composition (Herrero et al., 2008). Furthermore, Raman spectra could be correlated with sensory attributes (i.e. juiciness and chewiness) of pork loins (Wang et al., 2012) and identify structural changes of muscle food components (proteins, lipids and water) due to handling, processing and storage (Pérez-Santaescolástica et al., 2019).

Fluorescence polarization spectroscopy analyses the natural fluorescence from a product. In meat, tryptophan is the major intrinsic fluorophore. It is a constituent of the proteins that have two preferential directions of alignment both parallel and perpendicular to the muscle fiber direction. Fluorescence polarization was used to characterize the structural organization and modifications related to sarcomere length in meat caused by processing (Luc et al., 2008) and in-line detecting of cold shortening in the bovine muscle (Luc et al., 2008). In meat analogues, fluorescence polarization can be used to characterize the anisotropy in high moisture extruded soy protein (Yao et al., 2004). This method is based on the theory that polarization states of fluorescence light are affected by the structure of a product. It was found

that products with a higher degree of fiber formation showed a higher polarization degree (Ranasinghesagara et al., 2005).

Nuclear magnetic resonance spectroscopy (NMR) provides insights into the interaction between molecules (for example water-protein interactions) and thus provides insight into the structural features of meat and meat analogues. Several studies reviewed the application of ( $^1\text{H}$ ,  $^{13}\text{C}$  and  $^{31}\text{P}$ ) NMR in meat (Bertram & Ersten, 2004; Renou et al., 2003). NMR is also used to study water-protein interaction and correlate this with macroscopic properties such as water holding capacity, cooking loss, water and fat content and distribution, and changes associated during processing and storage (such as slaughtering, salting, frozen storage) (Marcone et al., 2013; Micklander et al., 2002). In plant-based materials, Time Domain (TD)-NMR gives an indication of the water-binding capacity of different proteins (wheat gluten (WG), SPI, PPI and lupin protein concentrate) (Peters et al., 2017). In addition, the water distribution was studied in a SPI-WG blend (Dekkers, de Kort, et al., 2016) and PPI-WG blend (Chapter 2).

Small-angle scattering (SAS) methods provide structural information over a size range from nanometer-to-micron length scale, being 0.2-100 nm using light, 1-100 nm using X-rays and 1-20 nm using neutrons (Larson, 1999). In small-angle X-ray scattering (SAXS), an X-ray beam passes through a product and encounters structural obstructions (like collagen or myofibrils). SAXS provides insight into the repetitive structure in a product, such as the structure of the fibrils of actin, myosin and collagen, and potentially provides estimates of the intramuscular fat (Goh et al., 2005; Hoban et al., 2016; Hughes et al., 2019). Small-angle neutron scattering (SANS) is used to investigate the structure on smaller scales and was used to study the internal structure of a fibrous calcium caseinate material (Tian et al., 2020). Spin-echo small-angle neutron scattering (SESANS) based on neutron diffraction can distinguish structures over three orders of magnitude from 10 nm up to 10  $\mu\text{m}$ . SESANS quantified the thickness ( $\pm 138 \mu\text{m}$ ) and the number of fiber layers ( $\pm 36$ ) and the orientation of fibers in SPI-WG blends that were subjected to heat and shear deformation in a Couette Cell (Krintiras et al., 2014). SESANS was also used to study the size and shape of the air bubbles in meat analogues of calcium caseinate (Tian et al., 2018).















The continuous-time random walk (CTRW) theory of light transport has been used to study the spatial distribution of light reflectance on the surface of a (fibrous) product (Weiss et al., 1998). According to this theory, optical scattering depends on the transitional properties of





scattering. The pattern of the scatter recorded by transmission or backscatter contains information on the internal structure of a material, such as meat (Ranasinghesagara & Yao, 2007) and meat analogues (Ranasinghesagara, Hsieh, Huff, & Yao, 2009; Ranasinghesagara, Hsieh, & Yao, 2006). In meat analogues, this method visualizes the degree of fiber formation and fiber orientation which shows potential as a fast, non-destructive method to monitor fiber formation in meat analogues (Ranasinghesagara et al., 2006, 2009). An extension of light scattering is diffusing wave spectroscopy (DWS), in which products with strong multiple scattering can be measured. In this novel DWS technique, the transport of photons through turbid products is treated as a diffusion process (Niu et al., 2019). In meat, DWS has been used to study the gelation process of myofibrillar protein extracted from squid (Niu et al., 2019).

In summary, spectroscopy can yield important information about the overall resolved composition of both meat and meat analogue, as well as intermolecular interactions and even about conformational changes of substances like proteins. It can be expected that the spectra of meat and meat analogues will be quite different because the spectra contain information about molecular properties. This limits its use for the actual comparison of the two types of materials. However, prediction models could be built from the correlation between the spectra and mechanical properties to make indirect comparisons between the materials. Spectroscopy can also give some information on the anisotropy. Light reflectance and SAS are promising methods to explore further for meat analogues to quantify fiber formation as it is relatively simple and easily incorporated into processing equipment, which will help to investigate the formation of the mesoscopic structure. SAXS and (SE)SANS methods typically yield information on smaller scales, but can also help in understanding the way the anisotropy is created from smaller-scale associations. These techniques require however very large infrastructure, and will thus be limited to research purposes.

Table 8.2. Overview of spectroscopy techniques used in studies on meat and meat analogues from 2005 onwards. The colours in red and green indicate that the method is used for meat and meat analogues, respectively.

Technique	Properties	Product (m/ ma)	Reference
FTIR  	Composition and secondary protein conformation	Beef muscle (m) High moisture extruded product (ma)	(Kohler et al., 2007; Perisic et al., 2011) (Beck et al., 2017; Mattice & Marangoni, 2020; Palanisamy et al., 2019)
NIR  	Composition	Pork (m)  Chicken (m)  Beef (m)	(Balage et al., 2013; Fulladosa et al., 2010; Gou et al., 2013; Mabood et al., 2020; Rady & Adedeji, 2018) (Jia et al., 2018; Krepper et al., 2018; Nolasco Perez et al., 2018; Jens Petter Wold et al., 2019) (Bonin et al., 2020; Cafferky et al., 2020; Cozzolino & Murray, 2004; Rady & Adedeji, 2018; Ripoll et al., 2008; Weng et al., 2020)
MIR  	Composition and secondary protein conformation	Beef (m)	(Carbonaro & Nucara, 2010)
Raman  	Secondary protein conformation & amino acid composition	Pork (m)  Beef (m)  Chicken (m) Sheep (m)	(Chen & Han, 2011; Olsen et al., 2007; Pérez-Santaescolástica et al., 2019; Scheier et al., 2015; Wang et al., 2012) (Chen et al., 2020) (Phongpa-Ngan et al., 2014) (Schmidt et al., 2013)
Fluorescence polarization spectroscopy  	Muscle fiber direction	Beef (m)  High moisture extruded product (ma)	(Luc et al., 2008) (Ranasinghesagara et al., 2005)
NMR  	Intermolecular interaction	Pork (m)  Beef (m)  Chicken (m)  Shear cell structures (ma) Low and high moisture extruded product (ma)	(García-García et al., 2019) (Graham et al., 2010; Jung et al., 2010) (Shaarani et al., 2006) (Dekkers et al., 2016 and Chapter 3) (Chen et al., 2010)
SA(X)S  	Insight into repetitive structure	Sheep (m)  Goat (m)  Beef (m)	(Goh et al., 2005; Hoban et al., 2016) (Hoban et al., 2016) (Goh et al., 2005; Hoban et al., 2016; Hughes et al., 2019; Wells et al., 2013)

(SE)SANS 	Fiber orientation	Shear cell structures (ma)	(Krintiras et al., 2014; Tian et al., 2018, 2020)
Light reflectance 	Internal structure and fiber orientation	Beef (m) High moisture extruded product (ma)	(Ranasinghesagara & Yao, 2007) (Ranasinghesagara et al., 2006, 2009)

### 8.3.3 Imaging

Imaging techniques can be used to reveal the structure of meat and meat analogues (Table 8.3). Visual inspection through splitting a meat or meat analogue is commonly used by product developers (Ranasinghesagara, 2008). Visual inspection is fast but destructive, not quantitative and prone to subjectivity. Microscopic (SEM, TEM, CLSM, AFM) characterization is used to construct images on different length scales ranging from macro to nano structure. The main drawback of those techniques is that they are destructive. Imaging using spectroscopic methods, such as MRI, ultrasound, hyperspectral and X-ray imaging does not require sample destruction. Image processing can be used to quantify the colour, shape, size, porosity and surface texture features of meat (Chmiel et al., 2011; Du & Sun, 2006b, 2006a; Li et al., 2016; Li et al., 2001; Ruedt et al., 2020; Taheri-Garavand et al., 2019). In meat analogues, edge detection, Hough transformation and region of interest analysis are used to quantify the fiber index value, which is shown to be strongly correlated with the polarization index (Ranasinghesagara et al., 2005).

Confocal laser scanning microscopy (CLSM) is a fluorescence technique to acquire 2D and limited 3D images of meat and meat analogue products. In meat, CLSM was used to visualize the connective tissue, myofibers and myofilaments and to monitor differences in structure between fresh and cooked meat of pork muscle, comminuted meat gels and beef (Du & Sun, 2009; Liu & Lanier, 2015; Straadt et al., 2007). A combination of CLSM and NMR yielded information about microstructural changes and water distribution in meat (Straadt et al., 2007). In meat analogues, CLSM has been used to visualize the effect of deformation on proteinaceous domains by comparing a sheared and a non-sheared PPI-WG blend (Chapter 2). The domains were aligned along the shear direction in these blends

(Chapter 2), in soy protein concentrate (Grabowska et al., 2016) and SPI-WG (Dekkers, Emin, et al., 2018) after staining with Rhodamine B. Both the SPI, PPI and WG showed fluorescence; the difference in intensity was used to indicate differences in protein concentration in different parts of the products.

Scanning electron microscopy (SEM) produces a surface image with resolution down to ~0.5 nm. In meat products, SEM has been used to reveal process-related changes in meat structure (Cheng & Parrish, 1976; Hearne et al., 1978; Wu et al., 1985). However, extensive sample preparation is needed for materials containing water or fat. These preparations can significantly change the original structure and may cause artefacts. Several techniques have been developed to overcome the disadvantages of high-vacuum SEM, in most cases at the cost of resolution. In cryo-SEM, water is frozen and may remain in that state in the product. Cryofixation is used to observe changes in the microstructure of beef steaks versus several cooking methods like temperature, time and treatments (García-Segovia et al., 2007) and of pork versus freezing rate and frozen storage time (Ngapo et al., 1999). Variable pressure scanning electron microscopy (VP-SEM) is used to examine the microstructure of meat products like the distribution of protein and fat phases in meat products (Liu & Lanier, 2015). Environmental scanning electron microscopy (ESEM) observes wet products at normal vapour pressures. This technique has been successfully used to investigate the microstructural changes of muscle meat in various meat types by heat treatment (Yarmand & Baumgartner, 2000; Yarmand & Homayouni, 2010). The shrinkage of pressure-treated and cooked pork meat structure was observed by ESEM. These ESEM observations were used to provide evidence for a higher shear force as measured with the Warner-Bratzler test (Duranton et al., 2012). SEM analysis combined with Energy-Dispersive X-ray spectroscopy (EDX) may identify the spatially resolved elemental composition of a surface and therefore identify the distribution of different components over the material surface (Ozuna et al., 2013).

SEM has been used to study the microstructure of meat analogues. High moisture extruded SPI-wheat starch revealed a fine and tightly connected network structure (Lin et al., 2002). In SPI/pectin blends, alignment along the shear direction was observed (Dekkers, Nikiforidis, et al., 2016). Soy protein with increasing levels of iota carrageenan showed a more compact network correlated with changes in cooking yield and expressible moisture (Palanisamy et al., 2018). SEM of high moisture extruded lupin protein concentrate and isolate showed that a denser microstructure and higher number of fibrous layers were created by increasing temperature and screw speed along with decreasing water feed (Palanisamy et al., 2019).

Like SEM, transmission electron microscopy (TEM) requires extensive sample preparation. As samples are created by microtoming, TEM provides information about the inner structure

of meat, such as changes in the myofibrillar structure of beef upon cooking (Zhu et al., 2018), the degradation of myofibrillar structure of lean meat by proteolytic action (Gerelt et al., 2000) and calcium chloride addition (Gerelt et al., 2002).

Atomic force microscopy (AFM) explores the local 3D structure of a surface on a nanometer scale. AFM has been widely used to analyse the morphology and mechanical properties of meat proteins for understanding the structure and tenderness/toughness (Soltanizadeh & Kadivar, 2014) and investigates the effects of processing and preservation conditions (ultrasound,  $\text{CaCl}_2$  and sodium tripolyphosphate) on meat proteins (goat muscle fiber) (Gao et al., 2016). AFM-based infrared spectroscopy (AFM-IR) combines the spatial resolution of atomic force microscopy (AFM) with chemical analysis using infrared (IR) spectroscopy (Dazzi & Prater, 2017). For meat analogues, AFM-IR was used to determine the phase distribution of protein and lipids during high moisture extrusion of peanut protein at a nanoscale resolution (10 nm) (Zhang et al., 2019).

Magnetic resonance imaging (MRI) is a non-invasive and non-destructive imaging technique that produces a spatial map of the concentration and relaxation times to give insight into the structural features of meat and meat analogues (Duce et al., 1994; Mitchell et al., 2001). Several studies on meat employed MRI to study the chemical composition, muscle structure as well as carcass compositions, adipose tissue distribution, connective tissue, and muscle fiber type (Marcone et al., 2013). MRI can also visualize the water distribution in meat products and the effect of processing such as freeze-thawing (Guiheneuf et al., 1997) or drying (Fantazzini et al., 2009; Ruiz-Cabrera et al., 2004), moisture loss during processing (Antequera et al., 2007), to quantify changes in the moisture and structure of cooked chicken meat (Shaarani et al., 2006) and allows imaging of the connective network during the cooking of meat (Bouhrara et al., 2011). Magnetic resonance elastography (MRE) is a phase-contrast-based MRI imaging technique that can directly visualize and quantitatively measure localized viscoelastic properties like elasticity and stiffness (Gruwel et al., 2010; Manduca et al., 2001). MRE provides estimates of the mechanical properties such as shear modulus or Young's modulus of tissues (Gruwel et al., 2010; Sapin-De Broses et al., 2010). The analysis of strongly anisotropic beef muscle shows that MRE can distinguish between isotropic (viscous properties) and anisotropic (elastic properties) materials (Sinkus et al., 2005).

Ultrasound imaging can be divided into low power ultrasound (LPU) and high power ultrasound (HPU) (Awad et al., 2012). The latter uses frequencies that are disruptive for the

physical, mechanical, or chemical properties of food products and are therefore promising in food preservation. LPU has been used as a non-invasive analysis method for monitoring food materials during processing or storage. In LPU, sound waves propagate through food materials, which leads to absorption and/or scattering of the waves. Different components will have specific local, acoustic impedance, which is the basis for image production. In the meat industry, LPU is used most often for compositional analysis as quality control of carcasses or live animals (Awad et al., 2012; Silva & Cadavez, 2012). Ultrasound imaging has also been successfully used for measuring the composition of chicken meat (Chanamai & McClements, 1999), carcass composition of pigs (Ayuso et al., 2013) and dry-cured meat products (Corona et al., 2013). Ultrasound imaging of meat and meat products has even been mentioned to provide estimates of localized viscoelastic properties of meat tissues (Biswas & Mandal, 2020). Ultrasound imaging has been used to follow the ripening kinetics of tofu (Ting et al., 2009).

Hyperspectral imaging (HSI) is the combination of multiple wavelengths together with other localised information. Infrared spectroscopy can be combined with microscopy providing spatially resolved compositional analysis (Dazzi & Prater, 2017; Zhang et al., 2019). NIR combined with HSI provides both spectral (NIR spectrum) and localised (for each pixel) details together in the scanned region. This was reviewed for meat and fish to predict quantitatively and qualitative chemical, textural and structural characteristics of meat such as tenderness, water, water holding capacity, fat and protein content (Reis et al., 2018; Wu & Sun, 2013). By combining direct identification of different components and their spatial distribution in the tested product, hyperspectral imaging has the potential for objective quality evaluation of both meat and meat analogues. NIR HSI is already used for the detection and quantification of plant (texturized vegetable protein and gluten) and animal (chicken) based adulterants in minced beef and pork (Rady & Adedeji, 2018, 2020).






Scattering techniques such as X-ray tomography, SAS, or light reflectance provide 3D structural insight. X-ray tomography (XRT) is based on variations in the attenuation of penetrating X-rays. The difference in the degree of X-ray attenuation is determined by the local density and compositional differences, which provides the locally resolved density with a spatial resolution down to 1  $\mu\text{m}$  and at a time scale of minutes. Micro-computed tomography ( $\mu\text{CT}$ ) is used to study the structure of small products with a resolution from mm to  $\mu\text{m}$ . In meat products, XRT is used for microstructural characterization, prediction of salt,

water, (intramuscular) fat content and distribution, and the relationship with hardness (Schoeman et al., 2016). Micro-computed tomography (Mathanker et al., 2013) was used to characterize microstructure, as well as the quantification and prediction of the composition in meat and fish hardness (Schoeman et al., 2016), intramuscular fat level and distribution in beef muscles (Frisullo et al., 2010). In meat analogue products, XRT reveals the porosity in the structure. Air pockets that could be elongated and entrapped were studied in SPI/pectin blends (Dekkers, Hamoen, et al., 2018), SPI-WG and PPI-WG blends (Chapter 2). In extrusion products, expansion (due to water evaporation) of the materials was visualized in extruded rice starch-pea protein in two directions (Philipp et al., 2017). Air bubbles in a composite meat analogue made of calcium caseinate may contribute to fibrous properties (Tian et al., 2018; Zhaojun Wang et al., 2019). In general, XRT depends on differences in density and therefore is not well suited for finding information on the distribution of components that have similar densities. Advanced contrast modalities such as phase-contrast X-ray tomography describes both the meat structure and the different meat components (i.e. water, fat, connective tissue and myofibrils) qualitatively and quantitatively (Miklos et al., 2015). Dual X-ray absorptiometry shows a moderate good correlation with meat tenderness and fat content in pork and beef meat (Brienne et al., 2001; Kröger et al., 2006). The grating-based multimodal X-ray tomography method (including absorption, phase contrast and dark-field tomograms) was used to quantify the composition (i.e. meat matrix, fat, salt, oil droplets) and visualizes the microstructural changes of meat emulsion induced by heat treatment (Einarsdóttir et al., 2014).




As can be concluded from the information described above, imaging reveals important information about the intermolecular interaction, anisotropy and nano to macro structure of meat and meat analogues. While SEM and CLSM are used to reveal the structure of both meat and meat analogues, TEM and AFM have only been used to analyse meat, but not yet meat analogues. The fibrousness of meat analogues from plant proteins created via a top-down approach is typically less hierarchical than meat (Dekkers, Boom, et al., 2018a). This implies that the meat analogues are structured on larger scales than is explored with TEM and AFM. Nevertheless, fibrous proteinaceous materials, such as those based on calcium caseinate may have a finer structure, which could justify further analysis. Given the ubiquity of water in meat analogues, we expect that ESEM and CLSM will be major methods for further structural analysis. CLSM can lead to 3D information through combining a stack of

2D pictures and also yields information on differences in composition, which could provide better insight into the orientation and the length of the structural elements in meat analogues. An important limitation of the microscopy methods is that they require extensive sample preparation, making them less suitable for further analysis. Non-destructive imaging methods like MRI and HSI used for meat provide information on the intermolecular interaction and spatially resolved compositional analysis for meat analogues simultaneously. For both meat and meat analogue products, structural changes have been analysed with XRT. For meat analogue products, XRT was used to quantify and visualize air, while for meat more structural aspects were studied with different types of XRT (like phase-contrast X-ray tomography or grating-based multimodal X-ray tomography).

*Table 8.3 Overview of imaging techniques used in studies on meat and meat analogues from 2005 onwards. The colours in red and green indicate that the method is used for meat and meat analogues, respectively.*

Technique	Properties	Product (m/ ma)	Reference
CLSM 	2D and 3D visualization	Beef (m) Chicken (m) Pork (m) Shear cell structures (ma)	(Du & Sun, 2009) (Liu & Lanier, 2015) (Liu & Lanier, 2015; Straadt et al., 2007) (Dekkers, Emin, et al., 2018; Grabowska et al., 2016 and Chapter 2)
SEM 	Surface image	Beef (m)  Pork (m)  Chicken (m) Goat (m) Shear cell structures (ma) High moisture extruded product (ma)	(García-Segovia et al., 2007; Mulot et al., 2019)  (Duranton et al., 2012; García-García et al., 2019; Larrea et al., 2007; Ozuna et al., 2013) (Liu & Lanier, 2015) (Yarmand & Homayouni, 2010) (Dekkers, Nikiforidis, et al., 2016) (Palanisamy et al., 2018, 2019)
TEM 	Inner structure	Beef (m)  Pork (m)	(Lin et al., 2009; Listrat et al., 2015; Zhu et al., 2018) (Larrea et al., 2007)
AFM 	Local 3D structure of a surface on nanometric scale	Goat (m) Beef (m) Chicken (m) High moisture extruded product (ma)	(Gao et al., 2016) (Wan et al., 2018) (Chen et al., 2016) (Zhang et al., 2019)
MRI 	Spatial map of the concentration and relaxation times	Chicken (m) Pork (m)  Beef (m)	(Shaarani et al., 2006) (Antequera et al., 2007; Fantazzini et al., 2009; Herrero et al., 2007) (Bouhrara et al., 2011)



Ultrasound imaging 	Composition, viscoelastic properties	Pork (m) Dry cured meat products (m)	(Ayuso et al., 2013) (Corona et al., 2013)
Hyperspectral imaging 	Spatially compositional analysis, fiber orientation	Beef (m)  Pork (m)  Lamb (m) Chicken (m)	(Cluff et al., 2008; ElMasry et al., 2011; Rady & Adedeji, 2018, 2020; van Beers et al., 2017) (Barbin et al., 2012, 2013; Cheng et al., 2018; Huang et al., 2017; Kucha et al., 2018; Rady & Adedeji, 2018, 2020; Yang et al., 2017) (Kamruzzaman et al., 2012) (Jia et al., 2018; Rady & Adedeji, 2018, 2020)
X-ray Tomography 	Structure with a resolution from mm to $\mu\text{m}$	Beef (m)  Pork (m)  Chicken (m) High moisture extruded product (ma) Shear cell structures (ma)	(Einarsdóttir et al., 2014; Frisullo et al., 2010; Kröger et al., 2006; Mathanker et al., 2013; Miklos et al., 2015; Schoeman et al., 2016) (Brienne et al., 2001; Einarsdóttir et al., 2014; Frisullo et al., 2010; Kröger et al., 2006; Mathanker et al., 2013; Miklos et al., 2015; Schoeman et al., 2016) (Adedeji & Ngadi, 2011) (Philipp et al., 2017) (Dekkers, Hamoen, et al., 2018; Tian et al., 2018; Zhaojun Wang et al., 2019 and Chapter 2)

#### 8.3.4 Characterization aspects specific to meat analogues

This review focused on the texture and structure of meat and meat analogues as finished products (Figure 8.2). But contradictory to meat, the fibrous structure of meat analogues has to be created in a production process. Therefore we are not just interested in the final structure of meat analogues, but also in the mechanism behind the creation of the fibrous structure. As the fibrous structure of meat analogues is often created during thermomechanical processing, it is important to understand the behaviour of different components during processing. The high temperature and pressure, often used during the production of meat analogues, limit the methods of analysis. However, a combination of different methods could be a route to gain information about the structure formation process. Mechanical methods cannot be used during processing, but spectroscopy and imaging techniques show potential. ESEM and XRT could be promising to study the changes in the structural elements during thermomechanical processing of meat analogues. The application of in-line light reflectance, SAS, NIR, or Raman spectroscopy during the processing of meat analogues could provide insight into structural elements. In-line ultrasound imaging is expected to be a promising method for

studying air bubbles and mechanical properties of meat analogues during processing, as this was previously used for the analysis of dough (Koksel et al., 2016).

Another challenge to characterize meat analogues is the fibrous structure itself. To understand how to create a fibrous structure, knowledge of the fibers in meat analogues is required. So far, it is not completely clear what the geometry, size, binding pattern and adhesion or cohesion of the fibers in meat analogues will look like. The simultaneous use of different mechanical and imaging methods can provide a more holistic view on the fiber properties in meat analogues products. It can also be interesting to refer to meat and also non-food products containing fibers. Meat from different origin such a poultry or beef, consists of fibers with very different shapes and physical characteristics as was revealed with multi-point indentation, which is was used to spatially measure the local elastic modulus (Boots et al., 2021). In non-food products, such as thermoplastic, adhesion and cohesion of fibers in a matrix is studied. A combination of fiber-matrix wetting analysis and interfacial adhesion analysis was found to give a good understanding of the fiber-matrix interface (Tran et al., 2015). Such methods could also be promising in understanding the fibrous structure of meat analogues.

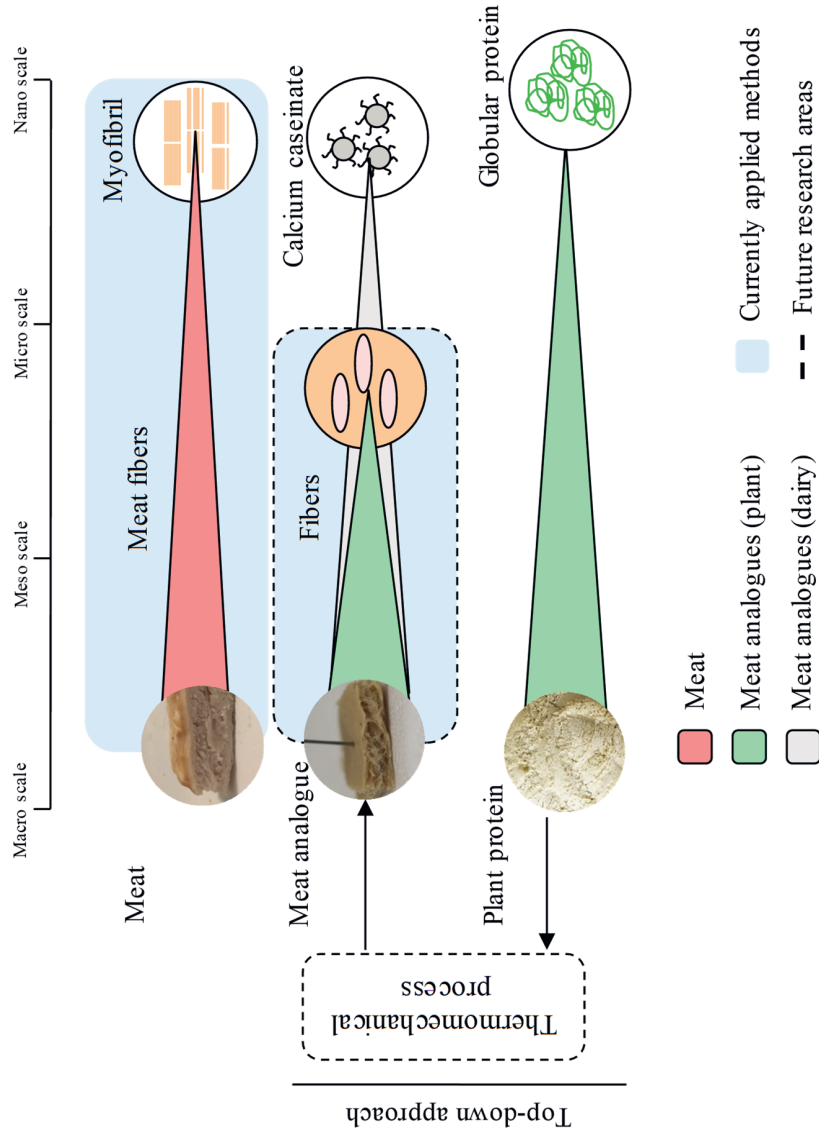


Figure 8.2. Available texture and structure methods ( ) on their suitability for meat (M, ■) and meat analogues (MA, ■) and future potential research areas for meat analogues.

## 8.4 *Conclusion*

An important step towards the development of next-generation meat analogues is a better insight into the texture properties of those products. To quantify those, analytical techniques are necessary. This review summarizes and discusses methods typically used to characterize the properties and quality of meat products and discusses the feasibility to apply those for meat analogues. At this moment the range of methods used for meat analogues is smaller compared to the methods available for meat. However, we conclude that a broad range of methods could be readily employed to analyse meat analogues or slightly modified to make those methods suitable to analyse meat analogues.

Several techniques elucidate structural features. Mechanical methods allow a direct comparison of the texture attributes between meat and meat analogues, tensile analysis, Warner-Bratzler test and compression techniques provide information about the strength of the product and can be applied to both meat and meat analogue products. Spectroscopy methods are non-destructive and fast but more expensive. Most imaging techniques are interesting to compare the structure of both meat and meat analogues. CLSM and XRT reveal 3D information. NIR, MIR, NMR and MIR provide both quantitative information about the structural elements and information of the composition. Tensile analysis, image analysis, fluorescence spectroscopy, SAS and light reflectance, showed to be promising methods to quantify properties of the individual fibers and their formation process. TEM and AFM are interesting for nanoscale structure analysis, but have been applied to meat only so far.

Specifically for meat analogues there is a need to study the texture and structure at processing conditions as well. In-line NIR or ultrasound imaging could be promising to study the changes in the structural elements during thermomechanical processing of meat analogues. Furthermore, future research should focus on characterizing the fibers present in meat analogues with regards to geometry, size and adhesion and cohesion. This approach could optimize the conditions used during the processing of meat analogues process with the final purpose of resembling meat products in terms of texture and structure.





# *Chapter 9*

*Near infrared spectroscopy and chemometrics for non-destructive quantification of fats in dense protein mixes*

## 9.1 *Abstract*

The addition of fat to a meat analogue is important for its juiciness, texture and mouthfeel. Various organic solvent extraction methods have been used to analyse the fat content in meat products. However, these techniques are laborious and environmentally harmful. In the present work, near infrared (NIR) spectroscopy was used for non-destructive, rapid quantification of fats in meat analogue mixes. Two modes of spectroscopy were explored: point spectroscopy and hyperspectral imaging (HSI). Calibration was performed with partial least-square regression (PLSR) analysis to predict the fat and to predict the spatial distribution of fats while processing the HSI data. Models based on 1<sup>st</sup> and 2<sup>nd</sup> CH overtones of the NIR regions were separately developed. Further, variable selection with covariate selection (CovSel) was performed to find the wavelengths that predict the local fat concentration. The results showed that NIR spectroscopy can accurately predict ( $R^2 = 0.99$  and RMSEP = 0.37 %) the total amount of fat in a mixture of fat, proteins and water, which is a composition often used for meat analogues. The 2<sup>nd</sup> CH bond overtone NIR region showed better predictive performance compared to the 1<sup>st</sup> CH bond overtone NIR region. Prediction models based on point spectroscopy performed better in terms of higher  $R^2$  and lower RMSEP compared with HSI. Point spectroscopy could be therefore used as a good alternative to more laborious analytical methods. HIS has potential to map the spatial distribution of the fat in the sample and give insight in the mixing process. Variable selection with CovSel improved the model performance.



## 9.2 Introduction

The addition of fat to meat analogues can enhance the juiciness, texture and mouthfeel of the food, and can be used as carrier for oil soluble flavours and nutrients like vitamin A (Belloque et al., 2002; Egberts & Borders, 2006). A previous study reported that the addition of more than 5 wt.% oil before the extrusion processing results in oil being expelled from the protein matrix (Cheftel et al., 1992) and that this negatively impacts the alignment of proteins because of slippage.

The relevance of the presence and distribution of sufficient fat makes an efficient analysis necessary. The analysis of the fat content in meat and meat analogues is traditionally performed with organic solvent extraction. The official Soxhlet extraction method recommended by the AOAC (1990) is most widely used for determining fat content in food products. For quantification of fat in several meat products, Pérez-Palacios et al. (2008) evaluated the efficiency of several lipid extraction methods. However, these methods are laborious, require many samples, and are hazardous and environmentally harmful (Prevolnik et al., 2011; Tøgersen et al., 2003). In addition, we found earlier that it is not always possible to extract all the oil, as some oil remains encapsulated at the end of the extraction process (Berghout et al., 2014).

As alternative to the organic solvent extraction methods, near infrared (NIR) spectroscopy has potential to quantify fat in meat products (Mishra, Nordon, & Roger, 2021; Wold et al., 2011). NIR spectroscopy is a rapid, low-cost, non-destructive, accurate and reliable analysis method, requires minimal or no sample preparation prior to analysis, and can be used to analyse multiple attributes simultaneously (Klaypradit et al., 2011; Stubbs et al., 2010; Wu et al., 2008). NIR spectroscopy can detect the presence of components such as protein, moisture and fats through the overtones and combinations related to OH, CH and NH bonds captured in the near-infrared range of the electromagnetic spectrum (Osborne, 2000). Furthermore, NIR spectroscopy can provide both spectral and spatial information supported by chemometric modelling when combined with imaging modality as hyperspectral imaging (HSI) (Barbin et al., 2013; Kamruzzaman et al., 2012).

Chemometric modelling is used to resolve overlapping and broad peaks in spectra (Pasquini, 2018). NIR spectroscopy data is multivariate with several peaks overlapping (Pasquini, 2018). Such overlapping peaks pose a multi-collinearity problem in which classical multi-linear techniques do not work well (Mehmood et al., 2012, 2020; Jean Michel Roger &

Boulet, 2018; Saeys et al., 2019). Latent variables (LVs) extraction methods are often used for extracting the relevant chemical components to perform tasks such as regression and classification. Partial least square regression (PLSR) is a common method used for this (Wold et al., 2001). PLSR extracts the LVs by maximizing the covariance between the predictor and response variable. After extraction of each latent variable, the predictor and response variable are orthogonalized with respect to the already explained variance by the previous LV. Subsequently, the process proceeds until no further LVs can be found that bring improvements on the variance in the response variables. The selection of the optimal number of LVs is performed with cross-validation approaches. This has already been shown for the prediction of chemical components in true meat products (Mishra et al., 2021).

In the present work, two modes of NIR spectroscopy i.e. point/area spectroscopy and hyperspectral imaging (HSI) are evaluated for quantification of both the overall fat content and its spatial distribution. Models based on the 1<sup>st</sup> and 2<sup>nd</sup> CH overtones NIR regions are separately developed. To do so, data are analysed by PLSR. Variable selection with the CovSel approach is used to identify the most significant wavelength that explains the fat predication in meat analogues. Finally, image processing was used to obtain images depicting the fat distribution.

### 9.3 Material and methods

#### 9.3.1 Materials

Pea protein isolate (PPI) (NUTRALYS® F85G) was obtained from Roquette Frères S.A., (Lestrem, France). PPI was composed of 78.6 wt.% protein (N x 5.7), WG was composed of 72.4 wt.% protein (N x 5.7) on a dry basis, according to Dumas measurements. PPI had an average dry matter content of 93.2 wt.%. Sunflower oil was purchased from a local supermarket.

#### 9.3.2 Sample preparation

Dispersions of PPI (40 wt.%) and sunflower oil (0-10 wt.%) in water (50-60%) were prepared (Table 9.1). Water was replaced by oil in steps of 1 wt.%. Then PPI was added and thoroughly mixed in with a spatula. The samples were then hydrated for 30 min. Eleven samples with different oil concentrations were prepared in triplicate. All samples were placed in cups with an internal diameter of 2.7 cm and a height of 1.5 cm (Figure 9.1).



Figure. 9.1. Prepared samples with known fat content as used for NIRS measurements.

Table 9.1. A description of samples matrix used in the experiment. The protein content was kept constant, but the water and the oil content were varied.

Material	Composition in each sample (wt.%)										
Protein	40	40	40	40	40	40	40	40	40	40	40
Water	60	59	58	57	56	55	54	53	52	51	50
Oil	0	1	2	3	4	5	6	7	8	9	10

### 9.3.3 NIR spectroscopy measurements

NIR spectroscopy measurements were performed with point spectroscopy and in imaging modality using HSI.

### 9.3.4 Point/area spectroscopy measurements

Point spectral measurements were performed by a Hi-Res, LabSpec spectrometer, ASD, USA. The measurements were performed using the area scan probe (Hi-Brite probe) with the spot size of 10 mm. The probe has an inbuilt 6.5 W halogen light source for illumination and using optical fibers to capture the reflected light. The instrument was controlled using the Indico Pro software, ASD, USA. The integration time was automatically optimized by the Indico Pro software and was defined as 15 ms. Each measurement was an average of ~5 consecutive measurements automatically performed by the Indico Pro software. The white reference was used for the spectral on white standards. The radiometric calibration with white and dark reference was performed automatically by the Indico Pro software.

### 9.3.5 Hyperspectral imaging (HSI)

HSI was performed with Specim's Fx10 spectral camera, Oulu, Finland. Two halogen light sources of 15 W each were used to illuminate the samples. The camera was mounted to an X-Y table and operated using in-house developed software. The camera acquired the images in the spectral wavelength range of 900-1723 nm with the spectral samples of nm. Each sample was analysed at 112 different wavelengths. The imaging was done by placing the samples in the field of view (FOV) of the camera and then moving the camera over the samples to perform the line scan. At the end of the imaging of the samples the white and dark reference were acquired. The images were normalised with equation 9.1:

$$Reflectance = \frac{X - Dark}{White - Dark} \quad 9.1$$

### 9.3.6 Data analysis

All data analysis was performed using MATLAB 2018b, Natick, WA, USA. The analysis was a combination of in-built functions from MATLAB's toolboxes and in-house codes. In the meat analogues mixes, the fat content ranged from 0 - 10 wt.%. The data were partitioned systematically into a calibration set (22 samples) and a validation set (11 samples). Both data sets have comparable ranges of protein, water and fat. The calibration and prediction results were analysed in terms of root mean stand error of calibration (RMSEC), root mean stand

error of prediction (RMSEP), regression coefficient of calibration and regression coefficient of prediction.

### 9.3.7 *Spectral pre-processing*

Prior to regression modelling, the spectra were smoothened using the Savitzky-Golay (SAVGOL) algorithm and the 2<sup>nd</sup> derivative was estimated. This 2<sup>nd</sup> derivative has the benefit of revealing the underlying peaks in the NIRS data to ease the regression modelling (Roger et al., 2020). A window size of 51 was used for the point spectroscopy data and a window size of 15 was used for the HSI data as the spectral resolution of the point spectrometer was larger than the HSI data. The CovSel approach (see section 9.3.9) could be directly based on the raw data.

### 9.3.8 *Partial least-square regression (PLSR) modelling for point spectroscopy data*

PLSR is a commonly used chemometric technique for the interpretation of NIR spectroscopy data (Wold et al., 2001). Particularly, PLSR deals with the multi-co-linearity in the multivariate signal by extracting the underlying peaks to find the inherent latent variables (LVs). The LVs having maximum covariance with the response variables were extracted. PLSR starts by extracting a set of new variables (known as scores) which are based on the projection of the data into the direction of LVs. In the present work, PLSR was implemented with the MATLAB's default 'plsregress' function. A default 10-fold cross validation approach was integrated for optimising the LVs. The LVs were then selected by identifying the inflection point.

### 9.3.9 *Variable selection with CovSel*

CovSel is a popular chemometric technique for filtering important wavelengths (Roger et al., 2011). The CovSel algorithm performs the wavelength selection by iterating two steps. The first step is a search for the variable index that is closest to the response variables. As a second step, the selected wavelength is removed from the predictor and response matrix using the orthogonal projection. The process is then repeated for a specified number of wavelengths. The resulting explained variation plot as the function of wavelengths extracted can be used to decide on the optimal number of variables. Our CovSel implementation was performed using in-house developed code as presented by Roger et al. (2011). Once the wavelengths

were selected, multiple linear regression (MLR) was run to achieve the final calibration model. MLR was implemented using the ‘fitlm’ function in MATLAB.

#### *9.3.10 Hyperspectral image processing*

The images were recorded in the ENVI format and were automatically radiometrically corrected by the software used for the data acquisition. The images were converted into MATLAB format using a combination of ENVI libraries and in-house developed codes. The spectra were extracted using the ‘roipoly’ function in MATLAB to interactively define bounded regions from which the spectra were extracted. In total, 33 regions were defined to extract spectra from the samples. The means were calculated for spectra from each sample to represent the average profile of each sample. The PLS calibration and CovSel variable selection was performed using 22 samples and the testing was performed with the remaining 11 samples. The spectral cube was unfolded and for all pixels the fat content was predicted. The predictions were then refolded to explain the spatial distribution of the fats.

## 9.4 Results

### 9.4.1 Mean spectra of mixes

Figure 9.2 shows the mean spectral profiles of the meat analogue mixes in the complete Visible and NIR spectroscopy (350-2500 nm) (Figure 9.2 A), the 1<sup>st</sup> fat overtone (Figure 9.2 B) and the 2<sup>nd</sup> fat overtones (Figure 9.2 C) range. The differing initial fat contents can be observed. All meat analogues mixes exhibited similar spectral reflectance patterns with differences in the magnitude of reflection throughout the NIR range (350-2500 nm). The differences observed in spectral reflectance mixes were related to the changes in the composition (0-10 wt.% oil and 60-50 wt.% water in meat analogues mixes). The reflectance decreased in the fat overtones region, as the fat content increased. This decrease in reflectance indicates an increase in the absorption of NIR light by the fat.

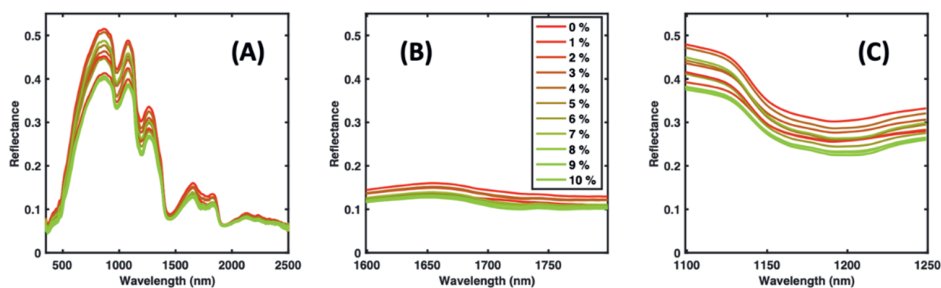


Figure 9.2. Spectral profiles of the meat analogue mixes. The initial fat content in the mixes is indicated with colours ranged from red to green. (A). Complete spectra, (B). First overtones region for CH bonds, and (C), second overtones region for CH bonds.

### 9.4.2 PLSR calibration of point spectroscopy data

A PLSR model was constructed for the three spectral ranges shown in Figure 9.2 i.e. the complete visible and NIR range (350-2500 nm) (Figure 9.2 A), 1<sup>st</sup> fat overtone (Figure 9.2 B) and 2<sup>nd</sup> fat overtones (Figure 9.2 C) range. The results of PLSR modelling are shown in Figure 9.3. In all the cases, the  $R^2$  was 0.98; however, the RMSEP and the prediction bias was higher when the complete spectral range was used. PLSR modelling on 1<sup>st</sup> overtones part of the spectra lowered the RMSEP and the prediction bias by 34 % and 58 % respectively. Further, the modelling on 2<sup>nd</sup> overtones part of the spectra lowered the RMSEP and the prediction bias by 37 % and 54 % respectively. The number of LVs in the case of modelling with 2<sup>nd</sup> overtones part of the spectra was 3 instead of 2 in the case of modelling with full spectral range and the 1<sup>st</sup> overtone part of the spectra.

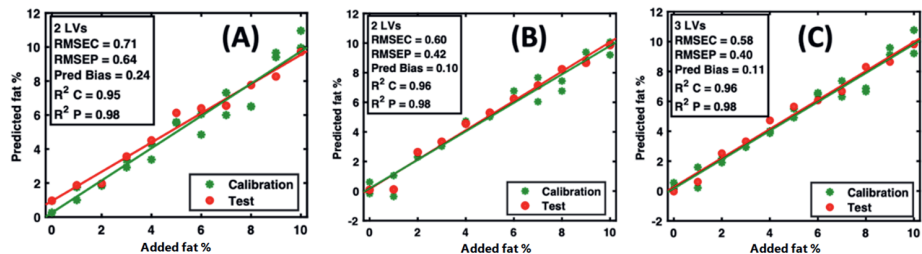


Figure 9.3. PLSR calibration for different spectral ranges. (A) Complete Visible and NIR spectroscopy (350-2500 nm) spectra, (B) first overtones regions, and (C) second overtones region. The samples in green star are the calibration set and the red circle are the test set.

### 9.4.3 CovSel variable selection and MLR

The results from the variable selection with the CovSel are shown in Figure 9.4. In the case of the full spectral range, the CovSel selected 3 wavelengths (1211 nm, 953 nm, 813 nm). In the case of the 1<sup>st</sup> and 2<sup>nd</sup> overtones, the CovSel selected 2 (1646 nm, 1715 nm) and 3 (1099 nm, 1211 nm, 1249 nm) wavelengths, respectively. A summary of selected wavelengths is provided in Table 9.2. The modelling with selected bands was more robust compared with wavelength selection presented in Figure 9.3. The performance for the 2<sup>nd</sup> overtones spectral region with the 3 selected band was the highest with a  $R^2$  of 0.99. The RMSEP and prediction bias were also the lowest at 0.37 % fat and 0.05 % fat respectively. In summary, the variable selection improved the model performance in terms of lowering error and bias and improving the prediction ( $R^2$ ) and gives a clear indication of the wavelengths that are responsible for predicting the fat content in meat analogue mixes.

Table 9.2. A summary of variable selected by CovSel approach for point spectroscopy data.

Spectral range (nm)	Number of bands selected	Selected bands (nm)
350-2500	3	1211, 953, 813
1599-1799	2	1646, 1715
1099-1249	3	1099, 1211, 1249



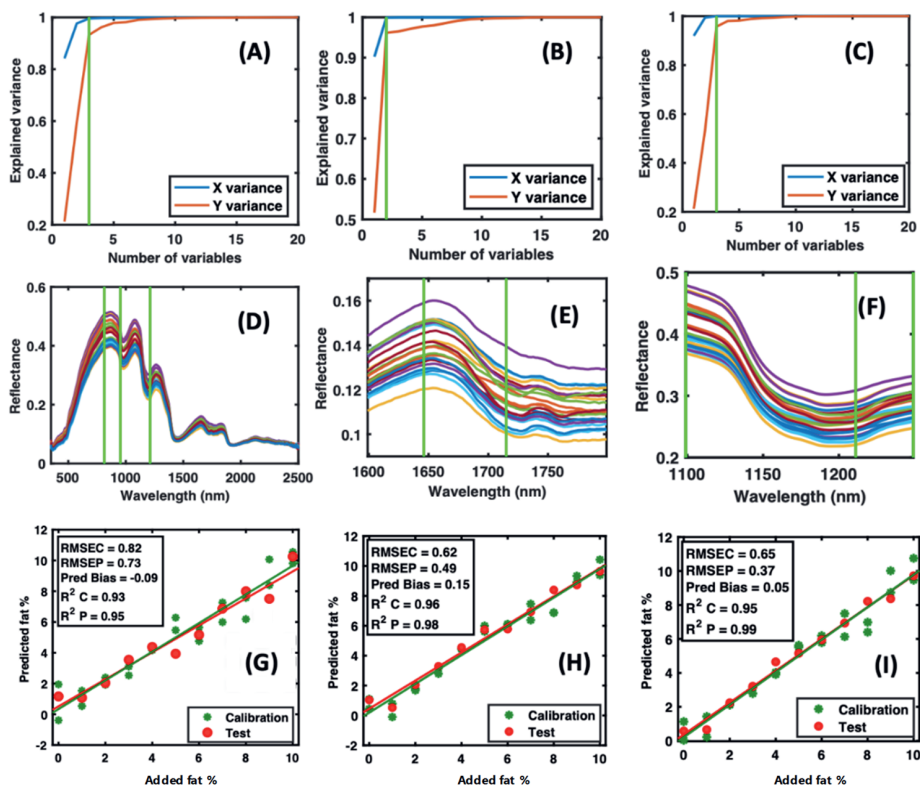


Figure 9.4. CovSel variable selection and calibration models with the selected variables. CovSel on: (A) complete spectra selected 3 bands, (B) first overtone region selected 2 bands, (C) second overtones region selected 3 bands, (D) calibration with 3 bands obtained in (A), (E) calibration with 2 bands obtained in (B), and (F) calibration with 3 bands obtained in (C). The calibration plots with selected wavelengths obtained in (G), (H) and (I). The green star and red circles represent the calibration and test set. The variable selection was performed in the calibration set.

#### 9.4.4 Hyperspectral image analysis

The results discussed in the previous sections were based on using point spectroscopy. The main advantage of HSI is that it contains spectral information in every pixel which can be used for estimating the spatial distribution of the properties. To do this a new PLSR calibration was performed using the mean spectral profiles of the samples. The model performance and the calibration with PLSR on the mean spectral profiles are shown in Figure 9.5. A prediction  $R^2$  of 0.90 was obtained with a RMSEP of 1.20 % and prediction bias of -0.61 %. The PLSR model was used for predicting the concentration in each pixel of the images and the prediction map is shown in Figure 9.5 B. A concentration change (from blue to red) from left to right was expected as the samples from left to right represented a linear

increase in fat content (0-10 %). The top row shows the test set of which no pixels were used in the calibration and tuning step.

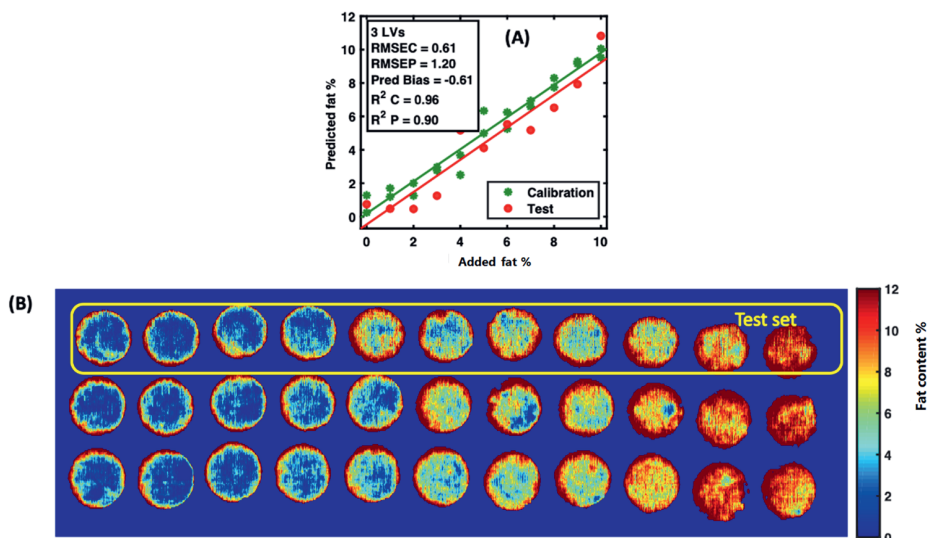


Figure 9.5. PLSR calibration for hyperspectral image. (A) PLSR on mean spectra, and (B) prediction map generated with the PLSR modelling on mean spectra and later using it for predicting concentration of each pixel. The red region at the periphery of the samples are because of the shadow from the sample containers. The colour scale bar is presented from 0-12 % instead of 0-10 % to compensate for the RMSEP.

#### 9.4.5 CovSel wavelength selection on hyperspectral data

The results from the CovSel wavelength selection on hyperspectral data are shown in Figure 9.6. The CovSel selected 2 wavelengths (1215 nm and 1313 nm, Figure 9.6 A) as optimal. A summary of selected wavelengths is shown in Table 9.3. The calibration has similar  $R^2 = 0.90$  compared to obtained with PLSR on complete spectral range of hyperspectral data. However, the model with selected wavelengths reduced the RMSEP and prediction bias by 6 % and 22 % respectively. The developed MLR model with selected two wavelengths was used for predicting the concentration for each pixel of the images and the prediction map is shown in Figure 9.6 D. The prediction maps show a change in colour (from blue to red) from left to right which was expected as the samples from left to right represented a linear increase in fat content (0-10 %).

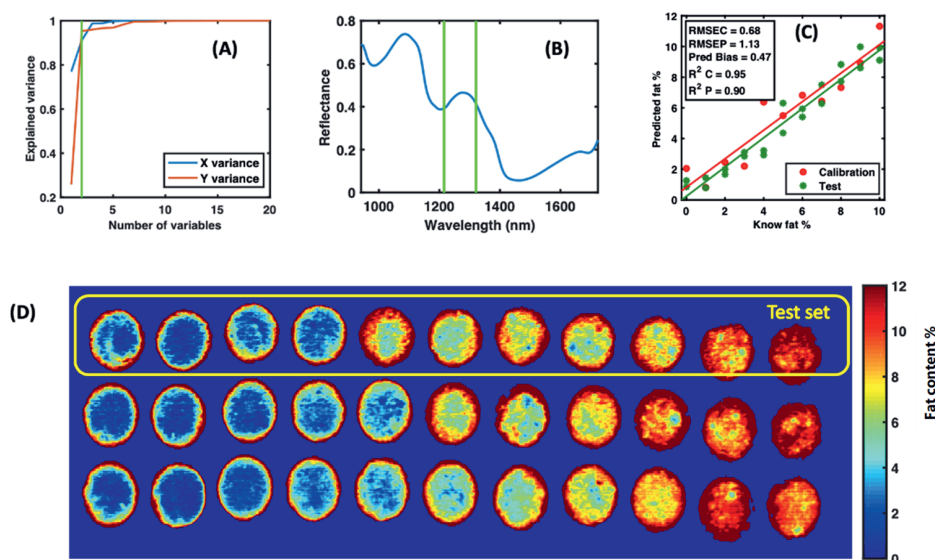


Figure 9.6. CovSel variable selection on hyperspectral images. (A) explained variance plot with green line showing optimal number of wavelengths, (B) selected wavelength highlighted in green, (C) MLR calibration and test on the mean pixels, and (D) prediction maps by using the MLR calibration made on the mean pixels. The red region at the periphery of the samples are because of the shadow from the sample containers.

Table 9.3. A summary of variables selected with CovSel for hyperspectral data.

Spectral range (nm)	Number of bands selected	Selected bands (nm)
942-1723	2	1215, 1313

## 9.5 Discussion

NIRS was used for non-destructive rapid quantification of total fats in meat analogue mixes. Two modes of spectroscopy i.e. point spectroscopy and HSI were explored. The calibrations were developed using PLSR and the variable selection was performed using the CovSel approach. Both point spectroscopy and HSI showed a good correlation ( $>0.90$ ) to predict the total fat in the meat analogue mixes. However, the point/area spectroscopy had much better performance ( $R^2$  up to 0.99) compared to the HSI data. The high accuracy of the point spectroscopy mode is probably due to the high sensitivity of the detector in the point spectrometer compared to the HSI camera.

Fats have multiple C-H bonds and their overtones and stretching can be captured in the NIRS range (Brøndum et al., 2000; Cozzolino & Murray, 2004; Ding & Xu, 2000; Hoving-Bolink

et al., 2005; Skibsted et al., 2005). The most prominent modes in NIRS due to differences in fat content are the C-H stretching overtone associated with fat. The spectral features from fats were dominant in both the 1<sup>st</sup> overtone as well as the 2<sup>nd</sup> overtones regions. In the case of the HSI, due to the limited spectral range only the 2<sup>nd</sup> overtones region was captured. Modelling using different (1<sup>st</sup> and 2<sup>nd</sup>) overtones regions showed comparable performance in terms of  $R^2$ , RMSEP and prediction bias. The wavelength selection with the CovSel approach also identified the 1<sup>st</sup> and the 2<sup>nd</sup> overtones spectral wavelengths correlating with the fat content in the meat analogue mixes.

Wavelength selection with the CovSel approach resulted in improved model prediction and selection of the key wavelengths related to the prediction of fat in meat analogue mixes. This improvement was noticed for both the point spectroscopy as well as with the HSI data. The better performance can be linked to the simpler models that were made on a selected subset of wavelengths compared to the PLSR that was performed on a complete spectral range. In the case of point spectroscopy, the wavelength selection resulted in the selection of just 2 wavelengths compared to the 2151 wavelengths implying a complexity reduction of nearly 1000 times. In the case of HSI, 2 wavelengths were selected out of 112 wavelengths resulting in a reduction of more than 50 times. In the 2<sup>nd</sup> overtones range, the point spectrometer and the HSI identified a common band i.e. ~1211 nm, which is directly related to the C-H bond in fat. Wavelength selection can support the development of inexpensive multi-spectral methods dedicated to the quantification of fat content in the meat analogue mixes.

The concentration maps of the fat in the mixes obtained by HSI demonstrate how this technique may be used to visualise the location of the fat before the structuring process. The maps showed an inhomogeneous distribution of the fat over the surface of the mixes. It was previously impossible to quantify the fat content and especially the distribution of the fat over the mixes with a non-destructive method. Even though the materials were not yet processed, we expect that the technique can be extended to mixes that have been processed by either extrusion or shear cell treatment. A second step would be to extend the method towards different matrices, for example with different types of plant protein. And finally, it is not unreasonable to expect that the method may be used for more than only the fat content.

## 9.6 Conclusions

NIRS offers a rapid and non-destructive prediction of the fat content in meat analogue mixes. We conclude that the higher prediction  $R^2$  and lower error and prediction bias of point spectroscopy compared with HSI offers the possibility of reliably prediction of oil in meat analogues mixes. NIR point spectroscopy can therefore be considered as an alternative to more laborious analytical methods. HIS could be as a non-destructive method to visualize the distribution of fats over the mixes.

Partial least squares regression (PLSR) analyses showed strong performance in predicting fat content. Wavelengths selection further improved the model in terms of higher prediction  $R^2$  and lower RMSEP and prediction bias. The 2<sup>nd</sup> overtones region contained the most valuable information to allow prediction compared to the modelling performed on complete spectra and the 1<sup>st</sup> overtone part of the spectra. The key wavelengths for predicting fat content in meat analogues mixes in the 1<sup>st</sup> overtones region are 1646 and 1715 nm. The key wavelengths for predicting fat content in analogues mixes in the 2<sup>nd</sup> overtones region are 1211 and 1313 nm. The selected wavelengths can be used to develop cheap multi-spectral point/area spectrometer or camera for rapid analysis of fat content in meat analogues mixes.

We expect that the method can be well extended to materials before and after processing, to different types of matrices, and ultimately to be useful not just for the fat content, but also the content of other constituents.



# *Chapter 10*

*General discussion*

## 10.1 *Introduction*

Plant-based meat analogues facilitate the transition from diets based on animal protein towards diets that rely more on plant proteins. Plant protein based foods that can be prepared and enjoyed in the same way as traditional, animal-based foods like meat can help consumer to transition towards plant-based protein foods. This holds especially for consumers who do not yet feel the motivation to explore and to learn how to prepare completely plant-based foods. A fibrous microstructure that is similar to that of meat is therefore essential for meat-replacing products (Hoek et al., 2011; Michel et al., 2021).

Until now, research and development of meat analogues have been mostly limited to soy protein, gluten and dairy proteins. However, both soy and gluten have serious disadvantages. Soy is generally grown in tropical climates and is therefore associated with unsustainable agriculture and deforestation. Both soy and gluten are associated with intolerances or allergies and are increasingly rejected by consumers. This explains why alternative protein sources are being explored. However, the translation to other materials is not trivial, since we do not yet fully understand how the properties of the materials relate to the microstructures obtained during and after thermomechanical treatment, and how this microstructure then relates to the macroscopic characteristics of the meat analogues.

This thesis focuses on the difference in structuring obtained with pea protein, relative to other materials, such as soy. Pea protein is considered a promising alternative, because of its lower allergenic potential, good functionality and lower environmental impact, since it can be grown in temperate climates like our own (Lam et al., 2018; Stone et al., 2015). However, pea protein has different properties than soy protein, and the use of pea protein for preparation of well-structured, fibrous meat analogues is relatively underexplored. This thesis therefore investigates the structuring potential of blends of pea protein isolates (PPI) with selected other biopolymers relevant to the preparation of meat analogues, and compares it to other materials. Shear cell technology was used to study the structuring potential, because this device provides a well-defined thermomechanical preparation method that can yield scientific insights in the structure formation process.



## 10.2 *Main findings and conclusions*

**Chapter 2** discusses the structuring potential of PPI when using shear cell technology. A fibrous structure could be formed with PPI-wheat gluten (WG) blends but only within a narrower window of operating conditions than for soy protein isolate (SPI)-WG blends. The mechanical properties of the PPI-WG blends were in the same range as chicken meat, while SPI-WG blends were tougher. Remarkably, the anisotropy under small deformation (Young's modulus) of chicken meat was larger than the plant protein blends.

In **Chapter 3**, insight into the internal structure of the PPI-WG and SPI-WG blends was obtained by a combination of Time-Domain Nuclear Magnetic Resonance (TD-NMR) and rheological characterization using the polymer blending law. The TD-NMR measurements revealed that water is preferentially taken up by the SPI / PPI phase, leaving less water for WG. Quantification of the rheological properties of the separate phases as a function of the water content showed that the WG inside the blend has a higher apparent modulus than the moduli of the PPI and SPI in a temperature range of 110-140°C. The difference between the moduli of WG and PPI was larger than differences between the moduli of WG and SPI. The dependence of the properties on the real volume fractions revealed that both PPI-WG and SPI-WG blends probably have a bi-continuous morphology when being structured into fibrous products.

**Chapter 4** describes additional rheological characterization of the materials used in this thesis. Small and large amplitude oscillatory shear deformation with a closed cavity rheometer was applied before, during and after thermal treatment, to provide a detailed picture of the rheological changes during thermomechanical treatment, such as extrusion and shear cell treatment. The measurements were visualized with Lissajous curves and the energy dissipation ratio that characterizes the plasticity of the materials. It was found that heating of all proteins induced more elasticity, but the extent of the effect depends on the protein source. Upon heating, PPI loses its elastic properties more than SPI, while WG shows abrupt dissipation after extensive deformation. In addition to these individual proteins, the rheological behaviour of the blends was investigated as well (**Chapter 5**). The rheological properties were visualized using texture maps and colour schemes to summarize the differences between the blends. In PPI-WG blends, PPI has a lower stress and is less elastic compared to WG. In SPI-WG blends, the properties were almost similar.

**Chapter 6** combines the approaches used in Chapters 2 and 4 to better understand the structuring potential of PPI, SPI and blends of these with pectin/and or cellulose. The most pronounced fibrous morphology was formed with PPI/pectin and SPI/pectin at a mass fraction of 93:7 and 95:5. Blends of SPI/pectin/cellulose also showed a fibrous structure. SPI and PPI alone and SPI/cellulose, PPI/cellulose and PPI/pectin/cellulose blends formed products with no visible fibrous morphology. For SPI products, a fibrous morphology also yielded mechanical anisotropy, whereas this relationship was not observed for PPI products. The CCR measurements showed that the PPI products are softer ('mushier') than the SPI products and that pectin addition resulted in mushier products than cellulose in a protein blend. The results suggest that the elasticity of the protein phase is an important factor in the ability of the blends to form fibrous products.

In **Chapter 7**, the methodology developed in Chapter 5 was applied to quantify the non-linear rheological properties of animal meat and meat analogues, especially chicken analogues. This gives both a benchmark for the plant-based materials, and an indication of which properties describe differences between meat and meat analogues best. Meat analogues differ from heated meat by their lower elasticity. In addition, heating of meat resulted in a tougher and more elastic material, while for meat analogues tested there was only a small effect of a heat treatment observed. Future developments on meat analogues should therefore focus on routes to create more elasticity.

**Chapter 8** reviews methods that are typically used to characterize the structure of meat and meat analogue products. The number of available methods used for meat analogues is smaller than for meat, but a range of methods for meat can also be used to analyze meat analogues, albeit after some modification. This could help extend the availability of methods to understand and quantify the structuring and final texture of current and future meat analogues.

**Chapter 9** describes the potential of near-infrared (NIR) and hyperspectral imaging (HSI) to quantify of the composition of blends on their protein and oil content. The methods are non-destructive and allow rapid quantification of the composition and the spatial distribution of the blend using chemometric modelling.

### 10.3 *Critical reflection on methods and results*

PPI and SPI both can lead to fibrous materials, when blended with WG or pectin. PPI and SPI alone were not able to form fibrous structures upon shear-induced structuring. This suggests that for both proteins a two-phase (or multiphase) blend is a prerequisite for fibrous structure formation. A way to characterise the macroscopic anisotropy in these materials, is to measure the tensile strength parallel and perpendicular to the shear flow direction. PPI can exhibit mechanical anisotropy but this was not always related to a fibrous structure. New methods are needed to elucidate the underlying mechanisms, as was highlighted in Chapter 8.

The material behaviour under simple shear flow in a shear cell might differ from that during complex flow conditions in an extruder. It is also possible that formation of fibrous structures follows a different path, which is for example evidenced by the fact that PPI and SPI could be transformed into a fibrous or layered product with high moisture extrusion cooking (Osen et al., 2014; Patrick Wittek et al., 2021). Possibly, protein isolates may still be considered as a two-phase system (Arêas, 1992), for example through the presence of insoluble and non-melting components or aggregates in a protein isolate. In addition, a melt of PPI or SPI and water can decompose into water-rich and protein-rich domains upon entering the cooling die. Third, the material may form regions with different viscosity due to the temperature gradient in the cooling die (Sandoval Murillo et al., 2019; Wittek et al., 2021). For high moisture extrusion cooking, laminar flow (velocity gradient which induces fiber formation parallel to deformation) and elongational flow in the breaker plate (while passing through the breaker plate the dispersed phase is deformed in the flow direction) were also considered structuring mechanisms (Cornet et al., 2021), even though obviously this cannot be the case in a shear cell.

The effect of thermo-mechanical treatment on proteins has been studied extensively on an empirical basis. Many studies just consider the product before and after processing. The TD-NMR method was used to perform measurements at room temperature, while outcomes were applied to plant protein blends that were heated and sheared, and had been cooled and rested again. This was done, because equipment limitations hindered measurement of these protein-water mixture at a high temperature (above 100°C). Also protein-protein interaction of a material is only studied after a thermomechanical treatment. While this may provide insight into final product properties, it does not provide conclusive information on how the structural elements interact during processing, leading to the macroscopic characteristics.

All results and explanations above strongly depend on the results obtained with the ‘closed cavity rheometer’ or CCR. We assumed that the CCR can be used to partly mimic the process conditions in the shear cell. In the CCR, the material is simultaneously subjected to a heat and shear treatment by applying a high frequency and high strain in an oscillation experiment. However, the material behaviour under oscillatory shear in the CCR differs from that during continuous rotational shear as applied in the shear cell or continuous flow in an extruder or cooling die. The large deformations that will truly give rise to structuring, such as the aggregation of a disperse phase such as gluten, cannot be attained when applying oscillation. Nevertheless, we believe that knowledge of the rheological properties at processing conditions does facilitate understanding of the rheological properties and their dependency on the type and amount of proteins, the water content/distribution, temperature and shear applied.

#### 10.4 *New insights in structure formation in protein blends*

Soy protein concentrate and the combination of gluten or pectin and SPI result in mechanical anisotropy with a pronounced fibrous microstructure upon shear cell processing (Dekkers, Nikiforidis, et al., 2016; Grabowska et al., 2016). The design guidelines for fibrous structure formation as described by Dekkers, Hamoen, et al. (2018) were used to study PPI or SPI blends with gluten and pectin, which led to additional insights and an update of the design rules as a consequence. First, insights for blends with wheat gluten are discussed and thereafter blends with pectin since formation of a fibrous structure probably has another origin.

Previous research based on SPI and WG suggested that a fibrous structure requires similar rheological properties between the two phases in a blend during processing, to allow strong deformation of the dispersed phase (Dekkers, Emin, et al., 2018). This was inspired on the well-known principle of the Grace curve, originally meant for purely viscous emulsions, but also applied to viscoelastic systems (Grace, 1982). The Grace curve predicts that a dispersed phase breaks up in smallest domains when the viscosities of the two phases match more or less. It can be assumed that similarities in viscosity will therefore also lead to most elongation of the dispersed phase in case it does not break up. The effect of viscosity of the dispersed and continuous phase on the break-up of the dispersed phase is captured in the graph of critical capillary number versus the viscosity ratio ( $k$ ), which gives a ‘U-shaped’ curve (Figure 10.1). The viscosity ratio ( $k$ ) represents the ratio of the viscosities of the dispersed

( $\eta_d$ ) and the continuous phases ( $\eta_c$ ), when  $k = \frac{\eta_d}{\eta_c} > 4$ , the matrix cannot exert sufficient stress to cause break-up.

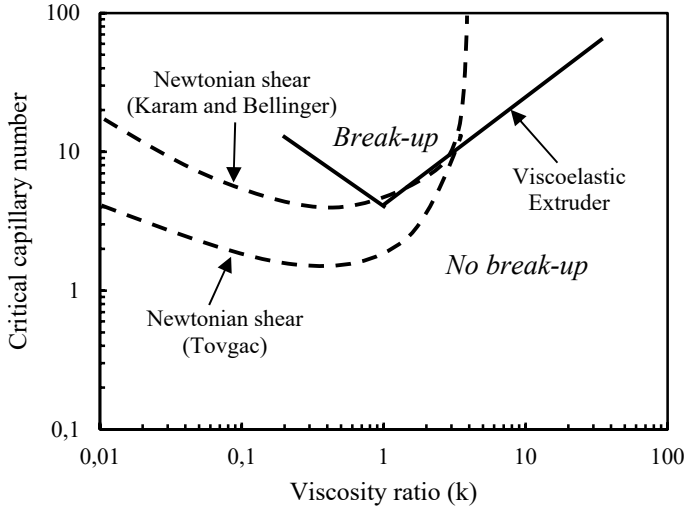


Figure 10.1. Grace curve after Wu, (1987) for a Newtonian liquids in steady uniform shear with those for viscoelastic materials in co-rotating twin screw extruder. The constant  $k$  represents the ratio of the viscosities of the dispersed and the continuous phases ( $k = \eta_d/\eta_c$ ). The capillary number is the ratio of the shear stress to the interfacial tension, given by  $Ca = \eta_c \dot{\gamma} R / \Gamma$ , with  $\eta_c$  the viscosity of the continuous phase,  $\dot{\gamma}$  the shear rate,  $R$  the droplet radius and  $\Gamma$  the interfacial tension.

Dekkers, de Kort, et al. (2016) could indeed show that for SPI and WG, the viscosities matched well enough to expect deformation of the droplets of WG in the SPI matrix into long fiber-like structures. PPI and WG differ in their rheological properties but the blend still resulted in fibrous structures in a narrow temperature interval around 120°C (Chapter 2 and 3). Insight into the internal structure of the blends was obtained by analysis of the polymer blending law. For this polymer blending law, prediction in water distribution of the phases in the blend is obtained with TD-NMR. Similarly to SPI, PPI absorbed more water than WG in a blend. However, this effect led to a large difference in rheological behaviour, contrary to the SPI-WG blend, which makes the deformation of individual droplets less likely. In other words, while a blend of SPI and WG might lead to a protein dispersion close to the minimum value of the U-shaped curved, the blend of PPI and WG will be in a different part of the graph.

Wu (1987) suggested that for viscoelastic materials, the deformation and elongation will be also dependent on the ratio of the elasticities of the two phases ( $k'$ ). This will render the 'U-shaped' curve of the Grace curve sharper, 'V-shaped' as the elasticity of the system increases. This is because the overall time of the stresses should be larger than the typical relaxation time of the materials (Yousfi et al., 2018). The viscoelastic drops will continue to deform and eventually these drops can break-up even for  $k = \frac{\eta_d}{\eta_c} > 4$ . This is presented as the Grace curve becoming more V-shaped if the elasticity increases. Therefore, it seems logical that the dispersed phase will be more elongated as result of elasticity with a viscosity ratio that would not lead to breakage. A droplet-to-fiber transition will be controlled by the viscosity ratio ( $k$ ) between the dispersed and continuous phase (a more viscous continuous phase promotes the breakdown of dispersed phase) and the elasticity ratio ( $k'$ ) between the dispersed and continuous phase (a more elastic continuous phase promotes deformation and extension of the nodules into fibers) and a balance between the relaxation and the deformation (shear or elongation) must be achieved in order to obtain a fibrous morphology (Yousfi et al., 2018).

Since PPI is less elastic than SPI, it is expected that the properties of PPI match less with those of WG than SPI and WG to allow direct deformation of a dispersed phase. Instead, we found that in case of PPI-WG blend, a bi-continuous structure was formed, which might have been the case for SPI-WG blend as well. Therefore, it is expected that the protein domains are largely elongated and interconnect to form a continuous phase; more precisely a bi-continuous network of the two incompatible proteins exists next to each other. A SPI-WG blend could indeed form fibrous materials at a broader processing window. The PPI-WG blend was more critically temperature dependent. We propose based on the polymer blending law results obtained in Chapter 3, that a bi-continuous structure can be formed in a narrow process window. Whether a bi-continuous structure is formed depends on the rheological properties and it may be easier to form a bi-continuous structure if the rheological properties are similar.

We hypothesize that this bi-continuous structure is created through an orthokinetic mechanism, in which the shear flow causes the individual gluten domains to 'collide'. It is expected that gluten will be dispersed initially based on how the protein blend is prepared (gluten is added to the blend of water and SPI and PPI after full hydration). Since the gluten is reactive (sticky), the domains will stick and form a larger elongated aggregate. The more domains collide, the larger and more elongated this structure will become. In the end, this

will result in a continuous, elongated network of aggregated WG domains in a continuous matrix of PPI. It is clear that this will only happen in a relatively narrow range of conditions, and this agrees with the narrow range of conditions found. For SPI, the elastic properties of the SPI match better with those of WG and therefore a broader range of conditions may give rise to a similar structure.

The non-linear rheology analyses that were reported in Chapters 4 and 5, especially the dissipation ratio, showed the importance of the elasticity. Heating at high temperatures is necessary to induce or enhance the elasticity. Upon thermal treatment, PPI lost its elastic properties more quickly than SPI, while WG showed abrupt viscous dissipation after extensive deformation. This rheological fingerprint is consistent with observations from shear deformation processing, in which WG is seen part of an elongated, bi-continuous network. In PPI-WG blends, lower strain, stress and elasticity values were obtained for PPI compared to WG. In SPI-WG blends, the texture properties were almost similar for the two components (Chapter 5).

For blends with WG, we hypothesize that a bi-continuous structure is a prerequisite for a blend to form fibrous products upon shearing, and that orthokinetic aggregation may be the basis of the formation mechanism of such a bi-continuous structure. When a protein is blended with a carbohydrate, the formation of a fibrous structure probably has another origin. In blends with pectin, earlier researchers hypothesized that pectin acts as a weak phase and is the dispersed phase that deforms and aligns in the shear flow direction. Dekkers, Nikiforidis, et al. (2016) found that the pectin phase changes significantly during the thermomechanical structuring process, which will facilitate this alignment. Solidification of the deformed phases after deformation is important to entrap the fibrous structure that is formed; failure to solidify may lead to back relaxation and loss of the structure. The development of elasticity during cooling is indicative of solidification and at some point will suppress the relaxation of deformed domains after flow (Liu et al., 2014; Pawar & Bose, 2015). SPI is more elastic than PPI so therefore it is expected that it suppresses the relaxation pectin domains more effectively. We therefore hypothesize that the formation of a fibrous morphology and the mechanical anisotropy are probably related to the elasticity of the material. Indeed, matching of both the viscous and the elastic behaviour was found by Yousfi et al. (2018) to lead to a fibrillar matrix after extrusion of the viscoelastic blend of polylactide and polyamide.

### 10.5 *Guidelines for protein structuring*

While the creation of a fibrous structure and some degree of anisotropy in the mechanical properties are probably important for the bite and mouthfeel of meat analogues, also other properties are important. In this thesis, meat and meat analogues were found to be quite similar with respect to their textural properties. Nevertheless, two distinct differences were observed: meat shows a stronger anisotropy in the Young modulus and has higher levels of elasticity.

In Chapter 2, it was shown that chicken has similar tensile stress and strain compared to PPI-WG blends, but the high anisotropy index in Young's modulus in chicken meat is missing in plant-based products. So far calcium caseinate is the only material to our knowledge that shows anisotropy in Young's modulus (Tian et al., 2020) and it was indicated that this could be protein alignment at micro-scale. Calcium caseinate products contains micro-fibers with a diameter of ~100 nm and length of ~300 nm that assemble into a macrostructure and show a hierarchical structure of bundled fibres, up to larger scales (Manski et al., 2007; Tian et al., 2020). The top-down strategy for structuring plant-based materials that was followed in this thesis by using shear cell technology creates structure on relatively large length scales. Even though it is a robust and scalable approach and generally is more resource efficient than a bottom-up strategy (Dekkers, Boom, et al., 2018a), its potential might be limited for creating structure on very small scales and subsequently micro-scale anisotropy. Future research on plant proteins for meat analogues could focus on creating a plant protein network on a nano- and mesoscopic length scale and re-arranging them into fibre bundles giving the required properties on a macroscale. Possibly, a pre-processing step could be introduced to create interacting protein aggregates or even micellar-type domains, similar to the calcium caseinate dispersions that we referred to earlier.

In addition to differences in Young's modulus, the use of non-linear rheology also revealed differences in the elasticity and strain stiffening between plant-based blends, meat analogues and meat (Chapter 5 and 7). In Figure 10.2, strain stiffening for chicken meat is observed in Lissajous curves whereas this was not observed for the plant protein-based products. The higher strain stiffening and elasticity for meat products could be related to its unique hierarchical structure on small length scales. Meat products have stiffer filaments, like F-actin or collagen that stiffen at low strains whereas more flexible filaments stiffen only at larger strains (Schofield et al., 1983).



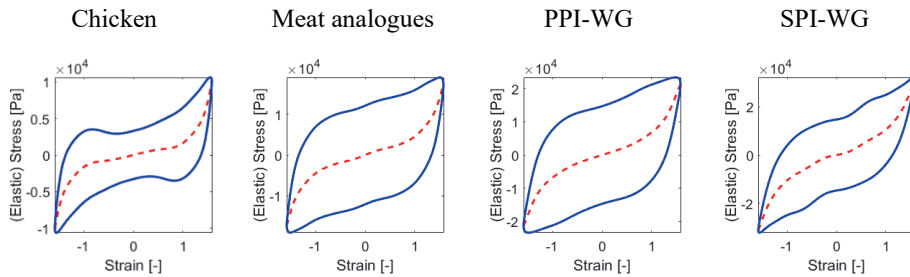


Figure 10.2. Lissajous curve of stress versus strain amplitude at 156.86% strain amplitudes of left to right: Chicken and vegetarian chicken pieces at 65°C and cooled to 30°C and PPI-WG and SPI-WG at 1:1 ratio in the blend at 120°C and cooled to 30°C.

To enhance strain stiffening and elasticity, several options for the design of a structuring process could be considered. For these strategies, it is important to first find the right method and the degree of adapting the interaction between the proteins to enhance elasticity. The second step is then to find the best method to solidify the structure that is created under shear. This could be done by heating or the use of food-grade crosslinkers.

Several strategies can be used to enhance the elasticity and strain stiffening:

- 1) *Modified pH-shifting*; a strong pH shift could result in a high level of protein unfolding, which makes the protein chain flexible and create more active sites to promote molecular interactions including hydrogen bonds and hydrophobic interactions when the protein is neutralized and heated. Strong and elastic pea protein hydrogels formed through pH-shifting method (Zhu et al., 2021). However, the method is necessarily associated with the use of chemicals, which compromises the potential gain in sustainability.
- 2) *Food-grade crosslinkers (transglutaminase)*; Improved toughness and elasticity were reported for pea protein gels made with 19.5% protein and crosslinked by 0.35% transglutaminase with incubation temperatures were between 50-60°C (Shand et al., 2008). The application of transglutaminase during thermomechanical processing is not trivial, because the enzyme is inactivated at high temperatures, which could result in inadequate crosslinking of the proteins.
- 3) *Addition of a highly elastic biopolymer*; The elasticity could be further improved by the addition of highly elastic biopolymers, such as carbohydrates. As an example, a previous study showed that the addition of methylcellulose to SPI led to an increase of the strain stiffening (Witteck et al., 2020).

The above-proposed strategies for developing elasticity in meat analogues are speculative but could form the basis of further developments in the coming years. Major advances will depend on a full understanding of how the chemical and physical interaction of protein particles is affected during processing.

### 10.6 *Future research and product development of meat analogues*

The scientific goal of this work is to gain in-depth understanding of the structure formation process of plant-based proteins. The societal goal is to contribute to the development of even better plant-based meat analogues to help consumers transition at least partially towards plant-based protein foods. This of course involves more than only the fibrous structure that we could obtain with PPI or SPI using shear-induced structuring during heating in the shear cell, and/or during cooling. Other components have to be added to create an edible, palatable food, such as lipids and flavours, and these influence the formation and properties of the morphology as well. New ingredients and novel fractions will also be used. More characterization methods are needed that can be employed during processing to understand the behaviour of these even more complex systems. Future research, development and innovation on meat analogue formulation and production should address these aspects, which can then be the basis for developing even better meat analogues in the future.

#### 10.6.1 *Shear-induced structuring during cooling: link shear cell to high moisture extrusion cooking*

Shear cells can be used to mimic extrusion-relevant conditions and were initially intended for understanding the phenomena occurring during extrusion under well-defined flow (Peighambaroust et al., 2005; van den Einde et al., 2004). In the shear cell, only shear is applied during heating. Structure formation is expected to be completed as soon as the shear stops (Cornet et al., 2021). During HMEC, the cooling die is considered as the “structuring zone” where the formation of the fibrous structure takes place (Akdogan, 1999; Cheftel et al., 1992; Sandoval Murillo et al., 2019; Tolstoguzov, 1993). Therefore it is interesting to investigate the effect of cooling after heat treatment on the structure formation of PPI-based blends for meat analogues. During cooling, the viscosity of the protein phases increases (Chapter 4), and this could influence the alignment and deformation of the protein phases. Research on structure formation during the cooling process with the shear cell could develop new insights into the structuring process during HMEC cooling, which could lead to the development of better fibrous structures (Figure 10.1).



Figure 10.3. Macrostructures of PPI-WG blends heated for 15 min at 120°C and sheared at 13 s<sup>-1</sup> during cooling for 8 min.

### 10.6.2 Addition of lipids to improve juiciness in meat analogues

The incorporation of lipids is desired since it contributes to the juiciness, tenderness and flavour of the product (Egberts & Borders, 2006), but it also influences the formation of the microstructure. A combination of liquid and solid fats (such as sunflower and coconut oil) is typically used to mimic the behavior of animal fat. Dependent on the formulation, oil or fat can be added during the structuring process or later in the process through marination. The addition of more than 5 wt.% oil before the extrusion processing results in lubrication of the material (Cheftel et al., 1992) and this negatively impacts the alignment of the macromolecules because of slippage. In extrusion processes with wheat and almond flour, the oil loss was reduced by the use of emulsifiers such as soy lecithin, sucrose esters, mono-glycerides and mono- and di-glycerides of fatty acids (De Pilli et al., 2007). Emulsification of the oil prior to the processing of meat analogues was reported as well (Joshi & Kumar, 2015; Malav et al., 2015a). Additional binders such as methylcellulose, carrageenan and modified starches in emulsion-type meat analogues can help reduce the oil loss further (Kyriakopoulou et al., 2021).

We investigated the influence of oil on the formation of the microstructure. PPI with 10 wt.% oil in an emulsion stabilized with soluble pea protein resulted in a fibrous morphology (Figure 10.3). This is in agreement with the literature, where extrusion of meat analogues on a gluten basis gave a fibrous morphology with the addition of 4 wt.% oil at the end of the extruder, but resulted in a more rubbery product (Kendler et al., 2021) (Figure 10.3).

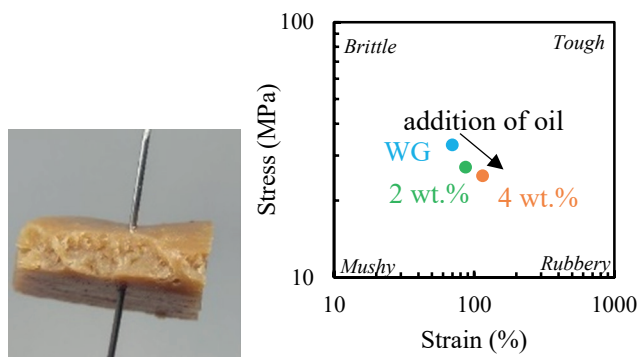


Figure 10.4 A) Macrostructures of 45 wt.% PPI and 10 wt.% oil emulsified with soluble pea protein heated for 15 min at 120°C and sheared at 39 s<sup>-1</sup>. B) Texture map of addition of 0, 2 and 4 wt.% oil to vital wheat gluten in a high moisture extruder (Kendler et al., 2021).

### 10.6.3 Methods to follow structuring during processing

More direct and indirect measurements of material properties inside the cooling die and shear cell are necessary to confirm the mechanism underlying structure formation. Until now, the development of fibrous structures mainly proceeded along a trial-and-error approach with the main focus to study the product before and after thermomechanical processing.

The conditions during processing (like high temperatures) are difficult to duplicate using current analytical methods. This thesis provided a more systematic study of the materials during and after thermomechanical processing. Rheological analysis using a CCR provide the first insight into the functionality of plant protein ingredients at thermomechanical conditions. However, CCR is not able to apply very large deformations, and therefore at best can only partly mimic the process conditions in the shear cell and cooling die. Other characterization methods should be developed that more closely resemble the process conditions. The CCR should be further developed to use continuous rotational instead of oscillatory deformation.

Instead of mimicking the process in an analytical device, one could also insert analytical tools inside the real process. Incorporation of sensors can be incorporated in the extruder to measure the properties inline and to obtain direct measurements of material properties during processing. Inline rheometers, such as capillary or slit die rheometers are considered the most accurate way to offer information during processing (Della Valle et al., 1996; Padmanabhan & Bhattacharya, 1991; Senouci & Smith, 1988; van Lengerich, 1990; Vergnes et al., 1993). However, inline-rheometers are limited in their flexibility, and offer no spatial resolution.

The use of inline spectroscopic methods such as NIR and Raman spectroscopy as well as ultrasound imaging could provide understanding on a molecular level during processing (Chapter 8).

When the results from these inline measurements to the results obtained with offline measurements obtained by devices like a CCR are related, it will be possible to provide researchers and product developers with better understanding of the process and control the product properties to a greater extend. Accurate rheological data at process conditions is necessary for input data for analysis of flow characteristic such as computational fluid dynamics (CFD) (Emin et al., 2020). This provides researchers and product developers tools to develop predictive product responses and could potential limit the number of experiments.

#### *10.6.4 Structure formation of other plant protein*

PPI, SPI and WG are the main ingredients studied for meat analogues. These ingredients are widely available, originally being by-products of already available production lines such as starch or oil. In addition to PPI, SPI and WG, other proteins like potato, peanut, zein, mung bean or faba bean as well as oil-rich seeds as rapeseed, canola and sunflower seed have gained interest (Kyriakopoulou et al., 2021). The comparison of the behaviour of all these different proteins, and correlating this with their individual rheological and (thermo)mechanical properties may well help to further elucidate the different ways that structure is created.

Meat analogues have been mainly based on protein isolates. The isolation process is intensive and is typically done using alkaline dissolution, isoelectric precipitation, neutralization and drying. This process was designed to achieve a high protein purity, not to create the best possible structured meat analogue with the protein. Milder fractionation processes that do take the desired functionality in consideration (Geerts et al., 2018) may be able to provide ingredients that are better suited to create the next-generation plant-based protein ingredients with superior properties, but at the same time a lower ecological footprint due to ingredient processing. New plant proteins as well as novel protein fractions from bacterial, fungal or other single-cell sources could be used to create a variety in products, however these have different functional properties. The translation of the process from PPI or SPI and WG towards these other plant proteins and milder fractions for the creation is the next step. The new insights in structure formation (as described in this chapter) as well as the rheological methodology (described in this thesis) are intended as a starting point to further

systematically identify the determining properties of new plant proteins and novel fractions to the microscopic structures obtained during and after thermomechanical treatment. Those provide then information on the macroscopic characteristics of the matrices created.

### 10.7 *Concluding remarks*

Pea protein is a promising protein for meat-replacing products, it can be used to form fibrous structures in a blend with components like gluten or pectin, yielding similar textural properties as chicken; even though the elasticity is not yet the same. The potential of pea is even enhanced by other aspects that are not studied in this thesis like low allergenicity and recourse efficiency.

This thesis provided new insights into structure formation, especially by investigating the non-linear rheology at conditions that are directly relevant to thermomechanical processing, and compare the properties obtained with PPI, to other materials, such as SPI-based blends and meat. New insight was created in how the specific microstructure is created in blends of PPI with other biopolymers. This insight will be important for further development of even better plant-based meat analogues, using more advanced formulations that will give the best possible consumer experience.







R

## *References*

- Adebiyi, A. P., & Aluko, R. E. (2011). Functional properties of protein fractions obtained from commercial yellow field pea (*Pisum sativum* L.) seed protein isolate. *Food Chemistry*, 128(4), 902–908. <https://doi.org/10.1016/j.foodchem.2011.03.116>
- Adediji, A. A., & Ngadi, M. O. (2011). Microstructural properties of deep-fat fried chicken nuggets coated with different batter formulation. *International Journal of Food Properties*, 14(1), 68–83. <https://doi.org/10.1080/10942910903131423>
- Akdogan, H. (1999). High moisture food extrusion. *International Journal of Food Science & Technology*, 34(3), 195–207. <https://doi.org/10.1046/j.1365-2621.1999.00256.x>
- Akintayo, E. T., Esuoso, K. O., & Oshodi, A. A. (1998). Emulsifying properties of some legume proteins. *International Journal of Food Science and Technology*, 33(3), 239–246. <https://doi.org/10.1046/j.1365-2621.1998.00190.x>
- Alghooneh, A., Razavi, S. M. A., & Kasapis, S. (2019). Classification of hydrocolloids based on small amplitude oscillatory shear, large amplitude oscillatory shear, and textural properties. *Journal of Texture Studies*, June, 520–538. <https://doi.org/10.1111/jtxs.12459>
- Alirezalu, K., Hesari, J., Eskandari, M. H., Valizadeh, H., & Sirousazar, M. (2017). Effect of Green Tea, Stinging Nettle and Olive Leaves Extracts on the Quality and Shelf Life Stability of Frankfurter Type Sausage. *Journal of Food Processing and Preservation*, 41(5), 1–11. <https://doi.org/10.1111/jfpp.13100>
- Altay, F., & Gunasekaran, S. (2013). Gelling properties of gelatin – xanthan gum systems with high levels of co-solutes. *Journal of Food Engineering*, 118(3), 289–295. <https://doi.org/10.1016/j.jfoodeng.2013.04.018>
- Antequera, T., Caro, A., Rodríguez, P. G., & Pérez, T. (2007). Monitoring the ripening process of Iberian ham by computer vision on magnetic resonance imaging. *Meat Science*, 76(3), 561–567. <https://doi.org/10.1016/j.meatsci.2007.01.014>
- Anvari, M., & Joyner (Melito), H. S. (2017). Effect of formulation on structure-function relationships of concentrated emulsions: Rheological, tribological, and microstructural characterization. *Food Hydrocolloids*, 72, 11–26. <https://doi.org/10.1016/j.foodhyd.2017.04.034>
- AOAC. (1990). *Official methods of analysis of the association of official analytical chemists* (K. Helvich (ed.); 15th ed.).
- Arêas, J. A. (1992). Extrusion of food proteins. *Critical Reviews in Food Science and Nutrition*, 32(4), 365–392. <https://doi.org/10.1080/10408399209527604>
- Arora, B., Kamal, S., & Sharma, V. P. (2017). Effect of Binding Agents on Quality Characteristics of Mushroom Based Sausage Analogue. *Journal of Food Processing and Preservation*, 41(5), 1–8. <https://doi.org/10.1111/jfpp.13134>
- Awad, T. S., Moharram, H. A., Shaltout, O. E., Asker, D., & Youssef, M. M. (2012). Applications of ultrasound in analysis, processing and quality control of food: A review. *Food Research International*, 48(2), 410–427. <https://doi.org/10.1016/j.foodres.2012.05.004>
- Axelos, M. A. V., & Branger, M. (1993). The effect of the degree of esterification on the thermal stability and chain conformation of pectins. *Food Hydrocolloids*, 7(2), 91–102. [https://doi.org/10.1016/S0268-005X\(09\)80161-6](https://doi.org/10.1016/S0268-005X(09)80161-6)
- Ayuso, D., González, A., Hernández, F., Corral, J. M., & Izquierdo, M. (2013). Prediction of carcass

- composition, ham and foreleg weights, and lean meat yields of Iberian pigs using ultrasound measurements in live animals. *Journal of Animal Science*, 91(4), 1884–1892. <https://doi.org/10.2527/jas.2012-5357>
- Balage, J. M., Silva, S. da L. e, Bonin, M. de N., Mazon, M. R., & Figueira, A. C. O. L. (2013). Predicting intramuscular fat, moisture, shear force and rating pork tenderness using visible / infrared spectroscopy. *Conference, January*.
- Bandyopadhyay, R., Liang, D., Harden, J. L., & Leheny, R. L. (2006). Slow dynamics, aging, and glassy rheology in soft and living matter. *Solid State Communications*, 139(11–12), 589–598. <https://doi.org/10.1016/j.ssc.2006.06.023>
- Banerjee, S., & Bhattacharya, S. (2012). Critical Reviews in Food Science and Nutrition Food Gels: Gelling Process and New Applications Food Gels: Gelling Process and New Applications. *Critical Reviews in Food Science and Nutrition*, 52, 334–346. <https://doi.org/10.1080/10408398.2010.500234>
- Barbin, D. F., Elmasry, G., Sun, D. W., & Allen, P. (2012). Predicting quality and sensory attributes of pork using near-infrared hyperspectral imaging. *Analytica Chimica Acta*, 719, 30–42. <https://doi.org/10.1016/j.aca.2012.01.004>
- Barbin, D. F., Elmasry, G., Sun, D. W., & Allen, P. (2013). Non-destructive determination of chemical composition in intact and minced pork using near-infrared hyperspectral imaging. *Food Chemistry*, 138(2–3), 1162–1171. <https://doi.org/10.1016/j.foodchem.2012.11.120>
- Barbut, S. (2015). Evaluating Texture and Sensory Attributes. In *The Science of Poultry and Meat Processing* (pp. 16-1-16–39). <https://doi.org/10.2307/973677>
- Barbut, S., Wood, J., & Marangoni, A. (2016). Quality effects of using organogels in breakfast sausage. *Meat Science*, 122, 84–89. <https://doi.org/10.1016/j.meatsci.2016.07.022>
- Bashi, Z., McCullough, R., Ong, L., & Ramirez, M. (2019). Alternative proteins: The race for market share is on. *McKinsey & Company, August*, 1–11.
- Batista, A. P., Portugal, C. A. M., Sousa, I., Crespo, J. G., & Raymundo, A. (2005). Accessing gelling ability of vegetable proteins using rheological and fluorescence techniques. *International Journal of Biological Macromolecules*, 36(3), 135–143. <https://doi.org/10.1016/j.ijbiomac.2005.04.003>
- Beck, S. M., Knoerzer, K., & Arcot, J. (2017). Effect of low moisture extrusion on a pea protein isolate's expansion, solubility, molecular weight distribution and secondary structure as determined by Fourier Transform Infrared Spectroscopy (FTIR). *Journal of Food Engineering*, 214, 166–174. <https://doi.org/10.1016/j.jfoodeng.2017.06.037>
- Beilken, S. L., Eadie, L. M., Griffiths, I., Jones, P. N., & Harris, P. V. (1991). Assessment of the Textural Quality of Meat Patties: Correlation of Instrumental and Sensory Attributes. *Journal of Food Science*, 56(6), 1465–1469. <https://doi.org/10.1111/j.1365-2621.1991.tb08617.x>
- Belloque, J., Garcia, M. C., Torre, M., & Marina, M. L. (2002). Analysis of soyabean proteins in meat products: A review. *Critical Reviews in Food Science and Nutrition*, 42(5), 507–532. <https://doi.org/10.1080/20024091054238>
- Belton, P. S. (1999). Mini Review: On the Elasticity of Wheat Gluten. *Journal of Cereal Science*, 29(2), 103–107. <https://doi.org/10.1006/jcrs.1998.0227>

- Berghout, J. A. M., Boom, R. M., & van der Goot, A. J. (2015). Understanding the differences in gelling properties between lupin protein isolate and soy protein isolate. *Food Hydrocolloids*, 43, 465–472. <https://doi.org/10.1016/j.foodhyd.2014.07.003>
- Berghout, J. A. M., Boom, R. M., & van der Goot, A. J. (2014). The potential of aqueous fractionation of lupin seeds for high-protein foods. *Food Chemistry*, 159, 64–70. <https://doi.org/10.1016/j.foodchem.2014.02.166>
- Bermúdez, R., Franco, D., Carballo, J., & Lorenzo, J. M. (2014). Physicochemical changes during manufacture and final sensory characteristics of dry-cured Celta ham. Effect of muscle type. *Food Control*, 43, 263–269. <https://doi.org/10.1016/j.foodcont.2014.03.028>
- Bertram, H. C., & Ersten, H. J. (2004). Applications of NMR in Meat Science. *Annual Reports on NMR Spectroscopy*, 53(04), 157–202. [https://doi.org/10.1016/S0066-4103\(04\)53003-X](https://doi.org/10.1016/S0066-4103(04)53003-X)
- Betancur-Ancona, D., Gallegos-Tintoré, S., & Chel-Guerrero, L. (2004). Wet-fractionation of Phaseolus lunatus seeds: Partial characterization of starch and protein. *Journal of the Science of Food and Agriculture*, 84(10), 1193–1201. <https://doi.org/10.1002/jsfa.1804>
- Bi, C., Li, D., Wang, L., Wang, Y., & Adhikari, B. (2013). Characterization of non-linear rheological behavior of SPI – FG dispersions using LAOS tests and FT rheology. *Carbohydrate Polymers*, 92(2), 1151–1158. <https://doi.org/10.1016/j.carbpol.2012.10.067>
- Bi, C., Zhang, M., Sun, D., Hua, Z., Zhu, Y., Liu, Y., Huang, Z., & Gao, F. (2019). A novel critical point for isotropic gel in rheological-fractal model. *Journal of Food Engineering*, 244(September 2018), 40–46. <https://doi.org/10.1016/j.jfoodeng.2018.09.023>
- Bianchi, M., Petracci, M., Pascual, M., & Cavani, C. (2007). Comparison between Allo-Kramer and Warner-Bratzler devices to assess rabbit meat tenderness. *Italian Journal of Animal Science*, 6(SUPPL. 1), 749–751. <https://doi.org/10.4081/ijas.2007.1s.749>
- Bildstein, M., Lohmann, M., Hennigs, C., Krause, A., & Hilz, H. (2008). An enzyme-based extraction process for the purification and enrichment of vegetable proteins to be applied in bakery products. *European Food Research and Technology*, 228(2), 177–186. <https://doi.org/10.1007/s00217-008-0921-z>
- Biswas, A. K., & Mandal, P. K. (2020). Current perspectives of meat quality evaluation: Techniques, technologies, and challenges. In *Meat Quality Analysis: Advanced Evaluation Methods, Techniques, and Technologies* (pp. 3–17). Elsevier Inc. <https://doi.org/10.1016/B978-0-12-819233-7.00001-X>
- Bonin, M. de N., da Luz e Silva, S., Bünger, L., Ross, D., Dias Feijó, G. L., da Costa Gomes, R., Palma Rennó, F., de Almeida Santana, M. H., Marcondes de Rezende, F., Vinhas Ítavo, L. C., de Novais, F. J., Surita, L. M. A., de Nadai Bonin, M., Filgueira Pereira, M. W., & Ferraz, J. B. S. (2020). Predicting the shear value and intramuscular fat in meat from Nellore cattle using Vis-NIR spectroscopy. *Meat Science*, 163(February), 108077. <https://doi.org/10.1016/j.meatsci.2020.108077>
- Boots, J. N. M., Humblet-Hua, N. P. K., Tonnejck, L., Fokkink, R., van der Gucht, J., & Kodger, T. E. (2021). Characterization of the local mechanical texture of animal meat and meat replacements using multi-point indentation. *Journal of Food Engineering*, 300(September 2020), 110505. <https://doi.org/10.1016/j.jfoodeng.2021.110505>
- Bouhrara, M., Clerjon, S., Damez, J. L., Chevarin, C., Portanguen, S., Kondjoyan, A., & Bonny, J. M. (2011). Dynamic MRI and thermal simulation to interpret deformation and water transfer in meat

- during heating. *Journal of Agricultural and Food Chemistry*, 59(4), 1229–1235. <https://doi.org/10.1021/jf103384d>
- Braeckman, L., Ronsse, F., Hidalgo, P. C., & Pieters, J. (2009). Influence of combined IR-grilling and hot air cooking conditions on moisture and fat content, texture and colour attributes of meat patties. *Journal of Food Engineering*, 93(4), 437–443. <https://doi.org/10.1016/j.jfoodeng.2009.02.009>
- Breese Jones, D. (1931). Percentages of Nitrogen in Foods and Feeds. *United States Department of Agriculture*, 16–21. [https://doi.org/10.1163/\\_q3\\_SIM\\_00374](https://doi.org/10.1163/_q3_SIM_00374)
- Brienne, J. P., Denoyelle, C., Baussart, H., & Daudin, J. D. (2001). Assessment of meat fat content using dual energy X-ray absorption. *Meat Science*, 57(3), 235–244. [https://doi.org/10.1016/S0309-1740\(00\)00091-7](https://doi.org/10.1016/S0309-1740(00)00091-7)
- Brøndum, J., Munck, L., Henckel, P., Karlsson, A., Tornberg, E., & Engelsen, S. B. (2000). Prediction of water-holding capacity and composition of porcine meat by comparative spectroscopy. *Meat Science*, 55(2), 177–185. [https://doi.org/10.1016/S0309-1740\(99\)00141-2](https://doi.org/10.1016/S0309-1740(99)00141-2)
- Cáceres, E., García, M. L., & Selgas, M. D. (2006). Design of a new cooked meat sausage enriched with calcium. *Meat Science*, 73(2), 368–377. <https://doi.org/10.1016/j.meatsci.2005.12.016>
- Cafferky, J., Sweeney, T., Allen, P., Sahar, A., Downey, G., Cromie, A. R., & Hamill, R. M. (2020). Investigating the use of visible and near infrared spectroscopy to predict sensory and texture attributes of beef *M. longissimus thoracis et lumborum*. *Meat Science*, 159(August 2019), 107915. <https://doi.org/10.1016/j.meatsci.2019.107915>
- Caine, W. R., Aalhus, J. L., Best, D. R., Dugan, M. E. R., & Jeremiah, L. E. (2003). Relationship of texture profile analysis and Warner-Bratzler shear force with sensory characteristics of beef rib steaks. *Meat Science*, 64(4), 333–339. [https://doi.org/10.1016/S0309-1740\(02\)00110-9](https://doi.org/10.1016/S0309-1740(02)00110-9)
- Caporgno, M. P., Böcker, L., Müssner, C., Stirnemann, E., Haberkorn, I., Adelman, H., Handschin, S., Windhab, E. J., & Mathys, A. (2020). Extruded meat analogues based on yellow, heterotrophically cultivated *Auxenochlorella protothecoides* microalgae. *Innovative Food Science and Emerging Technologies*, 59(November 2019), 102275. <https://doi.org/10.1016/j.ifset.2019.102275>
- Carbonaro, M., & Nucara, A. (2010). Secondary structure of food proteins by Fourier transform spectroscopy in the mid-infrared region. *Amino Acids*, 38(3), 679–690. <https://doi.org/10.1007/s00726-009-0274-3>
- Cavitt, L. C., Meullenet, J. F., Gandhapuneni, R. K., Youm, G. W., & Owens, C. M. (2005). Rigor development and meat quality of large and small broilers and the use of Allo-Kramer shear, needle puncture, and razor blade shear to measure texture. *Poultry Science*, 84(1), 113–118. <https://doi.org/10.1093/ps/84.1.113>
- Cavitt, L. C., Xiong, R., & Owens, C. M. (2005). The relationship of razor blade shear, allo-kramer shear, warner-bratzler shear and sensory tests to changes in tenderness of broiler breast fillets. *Journal of Muscle Foods*, 16(479), 223–242. <https://doi.org/10.1111/j.1745-4573.2005.00001.x>
- Chanamai, R., & McClements, D. J. (1999). Ultrasonic determination of chicken composition. *Journal of Agricultural and Food Chemistry*, 47(11), 4686–4692. <https://doi.org/10.1021/jf981349x>
- Cheftel, J. C., Kitagawa, M., & Queguiner, C. (1992). New Protein Texturization Processes by Extrusion Cooking at High Moisture Levels. In *Food Reviews International* (Vol. 8, Issue 2).

- <https://doi.org/10.1080/87559129209540940>
- Chen, F. L., Wei, Y. M., & Zhang, B. (2010). Characterization of water state and distribution in textured soybean protein using DSC and NMR. *Journal of Food Engineering*, 100(3), 522–526. <https://doi.org/10.1016/j.jfoodeng.2010.04.040>
- Chen, H., & Han, M. (2011). Raman spectroscopic study of the effects of microbial transglutaminase on heat-induced gelation of pork myofibrillar proteins and its relationship with textural characteristics. *Food Research International*, 44(5), 1514–1520. <https://doi.org/10.1016/j.foodres.2011.03.052>
- Chen, J., Liu, W., Liu, C. M., Li, T., Liang, R. H., & Luo, S. J. (2015). Pectin Modifications: A Review. *Critical Reviews in Food Science and Nutrition*, 55(12), 1684–1698. <https://doi.org/10.1080/10408398.2012.718722>
- Chen, Q., Zhang, Y., Guo, Y., Cheng, Y., Qian, H., Yao, W., Xie, Y., & Ozaki, Y. (2020). Non-destructive prediction of texture of frozen/thaw raw beef by Raman spectroscopy. *Journal of Food Engineering*, 266(November 2018), 109693. <https://doi.org/10.1016/j.jfoodeng.2019.109693>
- Chen, X., Xu, X., & Zhou, G. (2016). Potential of high pressure homogenization to solubilize chicken breast myofibrillar proteins in water. *Innovative Food Science and Emerging Technologies*, 33, 170–179. <https://doi.org/10.1016/j.ifset.2015.11.012>
- Cheng, C. S., & Parrish, F. C. (1976). Scanning electron microscopy of bovine muscle: effect of heating on ultrastructure. *Journal of Food Science*, 41, 1449–1454. <https://doi.org/10.1111/j.1365-2621.1976.tb01193.x>
- Cheng, J. H., Dai, Q., Sun, D. W., Zeng, X. A., Liu, D., & Pu, H. Bin. (2013). Applications of non-destructive spectroscopic techniques for fish quality and safety evaluation and inspection. *Trends in Food Science and Technology*, 34(1), 18–31. <https://doi.org/10.1016/j.tifs.2013.08.005>
- Cheng, W., Sun, D. W., Pu, H., & Wei, Q. (2018). Heterospectral two-dimensional correlation analysis with near-infrared hyperspectral imaging for monitoring oxidative damage of pork myofibrils during frozen storage. *Food Chemistry*, 248 (August 2017), 119–127. <https://doi.org/10.1016/j.foodchem.2017.12.050>
- Chmiel, M., Słowiński, M., & Dasiewicz, K. (2011). Lightness of the color measured by computer image analysis as a factor for assessing the quality of pork meat. *Meat Science*, 88(3), 566–570. <https://doi.org/10.1016/j.meatsci.2011.02.014>
- Christensen, M., Ertbjerg, P., Failla, S., Sañudo, C., Richardson, R. I., Nute, G. R., Olleta, J. L., Panea, B., Albertí, P., Juárez, M., Hocquette, J. F., & Williams, J. L. (2011). Relationship between collagen characteristics, lipid content and raw and cooked texture of meat from young bulls of fifteen European breeds. *Meat Science*, 87(1), 61–65. <https://doi.org/10.1016/j.meatsci.2010.09.003>
- Christensen, M., Purslow, P. P., & Larsen, L. M. (2000). The effect of cooking temperature on mechanical properties of whole meat, single muscle fibres and perimysial connective tissue. *Meat Science*, 55(3), 301–307. [https://doi.org/10.1016/S0309-1740\(99\)00157-6](https://doi.org/10.1016/S0309-1740(99)00157-6)
- Cierach, M., & Majewska, K. (1997). Comparison of instrumental and sensory evaluation of texture of cured and cooked beef meat. *Nahrung - Food*, 41(6), 366–369. <https://doi.org/10.1002/food.19970410611>

- Clark, A. H., Richardson, R. K., Ross-Murphy, S. B., & Stubbs, J. M. (1983). Structural and Mechanical Properties of Agar/Gelatin Co-gels. Small-Deformation Studies. *Macromolecules*, 16(8), 1367–1374. <https://doi.org/10.1021/ma00242a019>
- Cluff, K., Naganathan, G. K., Subbiah, J., Lu, R., Calkins, C. R., & Samal, A. (2008). Optical scattering in beef steak to predict tenderness using hyperspectral imaging in the VIS-NIR region. *Sensing and Instrumentation for Food Quality and Safety*, 2(3), 189–196. <https://doi.org/10.1007/s11694-008-9052-2>
- Cornet, S. H. V., Snel, S. J. E., Schreuders, F. K. G., Van der, R. G. M., Beyrer, M., & van der Goot, A. J. (2021). Thermo-mechanical processing of plant proteins using shear cell and high-moisture extrusion cooking. *Critical Reviews in Food Science and Nutrition*, 0(0), 1–18. <https://doi.org/10.1080/10408398.2020.1864618>
- Corona, E., Garcia-Perez, J. V., Gomez Alvarez-Arenas, T. E., Watson, N., Povey, M. J. W., & Benedito, J. (2013). Advances in the ultrasound characterization of dry-cured meat products. *Journal of Food Engineering*, 119(3), 464–470. <https://doi.org/10.1016/j.jfoodeng.2013.06.023>
- Cozzolino, D., & Murray, I. (2004). Identification of animal meat muscles by visible and near infrared reflectance spectroscopy. *LWT - Food Science and Technology*, 37(4), 447–452. <https://doi.org/10.1016/j.lwt.2003.10.013>
- da Costa Filho, P. A., Cobuccio, L., Mainali, D., Rault, M., & Cavin, C. (2020). Rapid analysis of food raw materials adulteration using laser direct infrared spectroscopy and imaging. *Food Control*, 113(February), 107114. <https://doi.org/10.1016/j.foodcont.2020.107114>
- Daros, F. G., Masson, M. L., & Amico, S. C. (2005). The influence of the addition of mechanically deboned poultry meat on the rheological properties of sausage. *Journal of Food Engineering*, 68(2), 185–189. <https://doi.org/10.1016/j.jfoodeng.2004.05.030>
- Das, S. K., Prabhakaran, P., Tanwar, V. K., & Biswas, S. (2015). Effect of some plant starches and carrageenan as fat substitutes in chicken patties. *Journal of Animal Science*, 93(7), 3704–3712. <https://doi.org/10.2527/jas.2013-6667>
- Davies, W. E. A. (1971). The theory of elastic composite materials. *Journal of Physics D: Applied Physics*, 4(9), 313. <https://doi.org/10.1088/0022-3727/4/9/313>
- Day, L., & Swanson, B. G. (2013). Functionality of protein-fortified extrudates. *Comprehensive Reviews in Food Science and Food Safety*, 12(5), 546–564. <https://doi.org/10.1111/1541-4337.12023>
- Dazzi, A., & Prater, C. B. (2017). AFM-IR: Technology and applications in nanoscale infrared spectroscopy and chemical imaging. *Chemical Reviews*, 117(7), 5146–5173. <https://doi.org/10.1021/acs.chemrev.6b00448>
- De Angelis, D., Kaleda, A., Pasqualone, A., Vaikma, H., Tamm, M., Tammik, M.-L., Squeo, G., & Summo, C. (2020). Physicochemical and Sensorial Evaluation of Meat Analogues Produced from Dry-Fractionated Pea and Oat Proteins. *Foods*, 9(12), 1754. <https://doi.org/10.3390/foods9121754>
- De Pilli, T., Carbone, B. F., Fiore, A. G., & Severini, C. (2007). Effect of some emulsifiers on the structure of extrudates with high content of fat. *Journal of Food Engineering*, 79(4), 1351–1358. <https://doi.org/10.1016/j.jfoodeng.2006.04.054>
- Dekkers, B.L., Boom, R. M., & van der Goot, A. J. (2018a). Structuring processes for meat analogues.

- Trends in Food Science and Technology*, 81(May), 25–36.  
<https://doi.org/10.1016/j.tifs.2018.08.011>
- Dekkers, B.L., Boom, R. M., & van der Goot, A. J. (2018b). Viscoelastic properties of soy protein isolate - pectin blends: Richer than those of a simple composite material. *Food Research International*, 107(February), 281–288. <https://doi.org/10.1016/j.foodres.2018.02.037>
- Dekkers, B.L., de Kort, D. W., Grabowska, K. J., Tian, B., Van As, H., & van der Goot, A. J. (2016). A combined rheology and time domain NMR approach for determining water distributions in protein blends. *Food Hydrocolloids*, 60, 525–532.  
<https://doi.org/10.1016/j.foodhyd.2016.04.020>
- Dekkers, B.L., Emin, M. A., Boom, R. M., & van der Goot, A. J. (2018). The phase properties of soy protein and wheat gluten in a blend for fibrous structure formation. *Food Hydrocolloids*, 79, 273–281. <https://doi.org/10.1016/j.foodhyd.2017.12.033>
- Dekkers, B.L., Hamoen, R., Boom, R. M., & van der Goot, A. J. (2018). Understanding fiber formation in a concentrated soy protein isolate - Pectin blend. *Journal of Food Engineering*, 222, 84–92.  
<https://doi.org/10.1016/j.jfoodeng.2017.11.014>
- Dekkers, B.L., Nikiforidis, C. V., & van der Goot, A. J. (2016). Shear-induced fibrous structure formation from a pectin / SPI blend. *Innovative Food Science and Emerging Technologies*, 36, 193–200. <https://doi.org/10.1016/j.ifset.2016.07.003>
- Del Nobile, M. A., Conte, A., Incoronato, A. L., Panza, O., Sevi, A., & Marino, R. (2009). New strategies for reducing the pork back-fat content in typical Italian salami. *Meat Science*, 81(1), 263–269. <https://doi.org/10.1016/j.meatsci.2008.07.026>
- Del Olmo, A., Morales, P., Ávila, M., Calzada, J., & Nuñez, M. (2010). Effect of single-cycle and multiple-cycle high-pressure treatments on the colour and texture of chicken breast fillets. *Innovative Food Science and Emerging Technologies*, 11(3), 441–444.  
<https://doi.org/10.1016/j.ifset.2010.01.012>
- Della Valle, G., Colonna, P., Patria, A., & Vergnes, B. (1996). Influence of amylose content on the viscous behavior of low hydrated molten starches. *Journal of Rheology*, 40(3), 347–362.  
<https://doi.org/10.1122/1.550747>
- Destefanis, G., Brugiapaglia, A., Barge, M. T., & Dal Molin, E. (2008). Relationship between beef consumer tenderness perception and Warner-Bratzler shear force. *Meat Science*, 78(3), 153–156.  
<https://doi.org/10.1016/j.meatsci.2007.05.031>
- Diaz, J. V., Anthon, G. E., & Barrett, D. M. (2007). Nonenzymatic degradation of citrus pectin and pectate during prolonged heating: Effects of pH, temperature, and degree of methyl esterification. *Journal of Agricultural and Food Chemistry*, 55(13), 5131–5136.  
<https://doi.org/10.1021/jf0701483>
- Dill, K. A. (1979). Theory for the separation of very large DNA molecules by radial migration. *Biophysical Chemistry*, 10(3–4), 327–334. [https://doi.org/10.1016/0301-4622\(79\)85020-6](https://doi.org/10.1016/0301-4622(79)85020-6)
- Ding, H. B., & Xu, R. J. (2000). Near-infrared spectroscopic technique for detection of beef hamburger adulteration. *Journal of Agricultural and Food Chemistry*, 48(6), 2193–2198.  
<https://doi.org/10.1021/jf9907182>
- Dolores Romero de Ávila, M., Isabel Cambero, M., Ordóñez, J. A., de la Hoz, L., & Herrero, A. M. (2014). Rheological behaviour of commercial cooked meat products evaluated by tensile test and



- texture profile analysis (TPA). *Meat Science*, 98(2), 310–315. <https://doi.org/10.1016/j.meatsci.2014.05.003>
- Du, C. J., & Sun, D. W. (2006a). Automatic measurement of pores and porosity in pork ham and their correlations with processing time, water content and texture. *Meat Science*, 72(2), 294–302. <https://doi.org/10.1016/j.meatsci.2005.07.016>
- Du, C. J., & Sun, D. W. (2006b). Estimating the surface area and volume of ellipsoidal ham using computer vision. *Journal of Food Engineering*, 73(3), 260–268. <https://doi.org/10.1016/j.jfoodeng.2005.01.029>
- Du, C. J., & Sun, D. W. (2009). Retrospective shading correction of confocal laser scanning microscopy beef images for three-dimensional visualization. *Food and Bioprocess Technology*, 2(2), 167–176. <https://doi.org/10.1007/s11947-007-0032-z>
- Duce, S. L., Ablett, S., Guiheneuf, T. M., Horsfield, M. A., & Hall, L. D. (1994). Quantitative Determination of Water and Lipid in Sunflower Oil and Water/Meat/Fat Emulsions by Nuclear Magnetic Resonance Imaging. *Journal of Food Science*, 59(4), 808–812. <https://doi.org/10.1111/j.1365-2621.1994.tb08133.x>
- Durantou, F., Simonin, H., Chéret, R., Guillou, S., & de Lamballerie, M. (2012). Effect of High Pressure and Salt on Pork Meat Quality and Microstructure. *Journal of Food Science*, 77(8), 188–194. <https://doi.org/10.1111/j.1750-3841.2012.02816.x>
- Duvarci, O. C., Yazar, G., & Kokini, J. L. (2017). Trends in Food Science & Technology The comparison of LAOS behavior of structured food materials ( suspensions , emulsions and elastic networks ). *Trends in Food Science & Technology*, 60, 2–11. <https://doi.org/10.1016/j.tifs.2016.08.014>
- Egberts, R., & Borders, C. (2006). Achieving success with meat analogs. *Food Technology*, 60, 28–34.
- Einarsdóttir, H., Nielsen, M. S., Miklos, R., Lametsch, R., Feidenhans’L, R., Larsen, R., & Ersbøll, B. K. (2014). Analysis of micro-structure in raw and heat treated meat emulsions from multimodal X-ray microtomography. *Innovative Food Science and Emerging Technologies*, 24, 88–96. <https://doi.org/10.1016/j.ifset.2013.11.003>
- ElMasry, G., Sun, D. W., & Allen, P. (2011). Non-destructive determination of water-holding capacity in fresh beef by using NIR hyperspectral imaging. *Food Research International*, 44(9), 2624–2633. <https://doi.org/10.1016/j.foodres.2011.05.001>
- Elmendorp, J. J., & Maalcke, R. J. (1985). A study on polymer blending microrheology: Part 1. *Polymer Engineering and Science*, 26(16), 1041–1047. <https://doi.org/10.1002/pen.760251608>
- Elzerman, J. E., Hoek, A. C., a.J.S. van Boekel, M., & Luning, P. a. (2011). Consumer acceptance and appropriateness of meat substitutes in a meal context. *Food Quality and Preference*, 22(3), 233–240. <https://doi.org/10.1016/j.foodqual.2010.10.006>
- Elzerman, J. E., Hoek, A. C., van Boekel, M. J. A. S., & Luning, P. A. (2015). Appropriateness, acceptance and sensory preferences based on visual information: A web-based survey on meat substitutes in a meal context. *Food Quality and Preference*, 42, 56–65. <https://doi.org/10.1016/j.foodqual.2015.01.010>
- Elzerman, J. E., van Boekel, M. A. J. S., & Luning, P. A. (2013). Exploring meat substitutes: consumer experiences and contextual factors. *British Food Journal*, 115(5), 700–710. <https://doi.org/10.1108/00070701311331490>

- Emin, M. A., & Schuchmann, H. P. (2017). A mechanistic approach to analyze extrusion processing of biopolymers by numerical, rheological, and optical methods. *Trends in Food Science and Technology*, 60(October 2017), 88–95. <https://doi.org/10.1016/j.tifs.2016.10.003>
- Emin, M. A., Schwegler, Y., & Wittek, P. (2020). Numerical analysis of thermal and mechanical stress profile during the extrusion processing of plasticized starch by non-isothermal flow simulation. *Journal of Food Engineering*, 294(May 2020), 110407. <https://doi.org/10.1016/j.jfoodeng.2020.110407>
- Ersch, C., ter Laak, I., van der Linden, E., Venema, P., & Martin, A. (2015). Modulating fracture properties of mixed protein systems. *Food Hydrocolloids*, 44, 59–65. <https://doi.org/10.1016/j.foodhyd.2014.09.009>
- Ewoldt, R. H., Hosoi, A. E., & McKinley, G. H. (2008). New measures for characterizing nonlinear viscoelasticity in large amplitude oscillatory shear. *Journal of Rheology*, 52(6), 1427–1458. <https://doi.org/10.1122/1.2970095>
- Ewoldt, R. H., & McKinley, G. H. (2017). Mapping thixo-elasto-visco-plastic behavior. *Rheologica Acta*, 56(3), 195–210. <https://doi.org/10.1007/s00397-017-1001-8>
- Ewoldt, R. H., Winter, P., Maxey, J., & McKinley, G. H. (2010). Large amplitude oscillatory shear of pseudoplastic and elastoviscoplastic materials. *Rheologica Acta*, 49(2), 191–212. <https://doi.org/10.1007/s00397-009-0403-7>
- Fantazzini, P., Gombia, M., Schembri, P., Simoncini, N., & Virgili, R. (2009). Use of Magnetic Resonance Imaging for monitoring Parma dry-cured ham processing. *Meat Science*, 82(2), 219–227. <https://doi.org/10.1016/j.meatsci.2009.01.014>
- Fitzsimons, S. M., Mulvihill, D. M., & Morris, E. R. (2008). Co-gels of whey protein isolate with crosslinked waxy maize starch: Analysis of solvent partition and phase structure by polymer blending laws. *Food Hydrocolloids*, 22(3), 468–484. <https://doi.org/10.1016/j.foodhyd.2007.01.011>
- Forghani, Z., Eskandari, M. H., Aminlari, M., & Shekarforoush, S. S. (2017). Effects of microbial transglutaminase on physicochemical properties, electrophoretic patterns and sensory attributes of veggie burger. *Journal of Food Science and Technology*, 54(8), 2203–2213. <https://doi.org/10.1007/s13197-017-2614-8>
- Frank, D., Oytam, Y., & Hughes, J. (2017). Chapter 27 – Sensory Perceptions and New Consumer Attitudes to Meat. In *New Aspects of Meat Quality*. Elsevier Ltd. <https://doi.org/10.1016/B978-0-08-100593-4.00028-X>
- Frisullo, P., Marino, R., Laverse, J., Albenzio, M., & Del Nobile, M. A. (2010). Assessment of intramuscular fat level and distribution in beef muscles using X-ray microcomputed tomography. *Meat Science*, 85(2), 250–255. <https://doi.org/10.1016/j.meatsci.2010.01.008>
- Fuhrmeister, H., & Meuser, F. (2003). Impact of processing on functional properties of protein products from wrinkled peas. *Journal of Food Engineering*, 56(2–3), 119–129. [https://doi.org/10.1016/S0260-8774\(02\)00241-8](https://doi.org/10.1016/S0260-8774(02)00241-8)
- Fulladosa, E., Santos-Garcés, E., Picouet, P., & Gou, P. (2010). Prediction of salt and water content in dry-cured hams by computed tomography. *Journal of Food Engineering*, 96(1), 80–85. <https://doi.org/10.1016/j.jfoodeng.2009.06.044>
- Fuongfuchat, A., Seetapan, N., Makmoon, T., Pongjaruwat, W., Methacanon, P., & Gamonpilas, C.

- (2012). Linear and non-linear viscoelastic behaviors of crosslinked tapioca starch/polysaccharide systems. *Journal of Food Engineering*, 109(3), 571–578. <https://doi.org/10.1016/j.jfoodeng.2011.10.022>
- Gao, J., Wang, Y., Liu, L., Li, K., Zhang, S., & Zhu, J. (2016). Effects of ultrasound, CaCl<sub>2</sub> and STPP on the ultrastructure of the milk goat longissimus muscle fiber observed with atomic force microscopy. *Scanning*, 38(6), 545–553. <https://doi.org/10.1002/sca.21298>
- García-García, A. B., Cambero, M. I., Castejón, D., Escudero, R., & Fernández-Valle, M. E. (2019). Dry cured-ham microstructure: A T<sub>2</sub> NMR relaxometry, SEM and uniaxial tensile test combined study. *Food Structure*, 19(December 2018), 100104. <https://doi.org/10.1016/j.foostr.2018.100104>
- García-Segovia, P., Andrés-Bello, A., & Martínez-Monzó, J. (2007). Effect of cooking method on mechanical properties, color and structure of beef muscle (M. pectoralis). *Journal of Food Engineering*, 80(3), 813–821. <https://doi.org/10.1016/j.jfoodeng.2006.07.010>
- Geerts, M. E. J., Dekkers, B. L., van der Padt, A., & van der Goot, A. J. (2018). Aqueous fractionation processes of soy protein for fibrous structure formation. *Innovative Food Science and Emerging Technologies*, 45(December 2017), 313–319. <https://doi.org/10.1016/j.ifset.2017.12.002>
- Genovese, D. B., & Rao, M. A. (2003). Vane yield stress of starch dispersions. *Journal of Food Science*, 68(7), 2295–2301. <https://doi.org/10.1111/j.1365-2621.2003.tb05762.x>
- Georgopoulos, T., Larsson, H., & Eliasson, A. C. (2004). A comparison of the rheological properties of wheat flour dough and its gluten prepared by ultracentrifugation. *Food Hydrocolloids*, 18(1), 143–151. [https://doi.org/10.1016/S0268-005X\(03\)00059-6](https://doi.org/10.1016/S0268-005X(03)00059-6)
- Gerelt, B., Ikeuchi, Y., Nishiumi, T., & Suzuki, A. (2002). Meat tenderization by calcium chloride after osmotic dehydration. *Meat Science*, 60(3), 237–244. [https://doi.org/10.1016/S0309-1740\(01\)00126-7](https://doi.org/10.1016/S0309-1740(01)00126-7)
- Gerelt, B., Ikeuchi, Y., & Suzuki, A. (2000). Meat tenderization by proteolytic enzymes after osmotic dehydration. *Meat Science*, 56(3), 311–318. [https://doi.org/10.1016/S0309-1740\(00\)00060-7](https://doi.org/10.1016/S0309-1740(00)00060-7)
- Goh, K. L., Hiller, J., Haston, J. L., Holmes, D. F., Kadler, K. E., Murdoch, A., Meakin, J. R., & Wess, T. J. (2005). Analysis of collagen fibril diameter distribution in connective tissues using small-angle X-ray scattering. *Biochimica et Biophysica Acta - General Subjects*, 1722(2), 183–188. <https://doi.org/10.1016/j.bbagen.2004.12.004>
- Gou, P., Santos-Garcés, E., Høy, M., Wold, J. P., Liland, K. H., & Fulladosa, E. (2013). Feasibility of NIR interactance hyperspectral imaging for on-line measurement of crude composition in vacuum packed dry-cured ham slices. *Meat Science*, 95(2), 250–255. <https://doi.org/10.1016/j.meatsci.2013.05.013>
- Grabowska, K. J., Tekidou, S., Boom, R. M., & van der Goot, A.-J. (2014). Shear structuring as a new method to make anisotropic structures from soy–gluten blends. *Food Research International*, 64, 743–751. <https://doi.org/10.1016/J.FOODRES.2014.08.010>
- Grabowska, K. J., Zhu, S., Dekkers, B. L., De Ruijter, N. C. A., Gieteling, J., & van der Goot, A. J. (2016). Shear-induced structuring as a tool to make anisotropic materials using soy protein concentrate. *Journal of Food Engineering*, 188, 77–86. <https://doi.org/10.1016/j.jfoodeng.2016.05.010>
- Grace, H. P. (1982). Dispersion phenomena in high viscosity immiscible fluid systems and application

- of static mixers as dispersion devices in such systems. *Chemical Engineering Communications*, 14(3–6), 225–277. <https://doi.org/10.1080/00986448208911047>
- Graham, S. F., Kennedy, T., Chevallier, O., Gordon, A., Farmer, L., Elliott, C., & Moss, B. (2010). The application of NMR to study changes in polar metabolite concentrations in beef longissimus dorsi stored for different periods post mortem. *Metabolomics*, 6(3), 395–404. <https://doi.org/10.1007/s11306-010-0206-y>
- Gruwel, M. L. H., Latta, P., Matwiy, B., & Tomanek, B. (2010). Characterization of food stuffs using Magnetic Resonance Elastography. *Food Research International*, 43(8), 2087–2092. <https://doi.org/10.1016/j.foodres.2010.07.015>
- Guido, S., Simeonea, M., & Greco, F. (2002). Effects of matrix viscoelasticity on drop deformation in dilute polymer blends under slow shear flow. *Polymer*, 44(2), 467–471. [https://doi.org/10.1016/S0032-3861\(02\)00763-2](https://doi.org/10.1016/S0032-3861(02)00763-2)
- Guiheneuf, T. M., Parker, A. D., Tessier, J. J., & Hall, L. D. (1997). Authentication of the effect of freezing/thawing of pork by quantitative magnetic resonance imaging. *Magnetic Resonance in Chemistry*, 35(13), S112–S118. [https://doi.org/10.1002/\(SICI\)1097-458X\(199712\)35:13<S112::AID-OMR222>3.0.CO;2-R](https://doi.org/10.1002/(SICI)1097-458X(199712)35:13<S112::AID-OMR222>3.0.CO;2-R)
- Hamann, D. D., & MacDonald, G. A. (1992). Rheology and texture properties of surimi and surimi-based foods. *Surimi Technology*, 429–500.
- Harris, P. V., & Shorthose, W. R. (1988). Meat texture. *Meat Science*, 4, 245–296.
- Harvey, F. ., & Phillips, D. (2020). *A fifth of Brazilian Soy in Europe is Result of Deforestation*. The Guardian. <https://www.theguardian.com/environment/2020/jul/16/a-fifth-of-brazilian-soy-in-europe-is-result-of-deforestation-amazon-jair-bolsonaro>
- Hearne, L. E., Penfield, M. P., & Goertz, G. E. (1978). Heating Effects of Bovine Semitendinosus: Phase Contrast Microscopy and Scanning Electron Microscopy. *Journal of Food Science*, 43(1), 13–16. <https://doi.org/10.1111/j.1365-2621.1978.tb09725.x>
- Herrero, A. M., de la Hoz, L., Ordóñez, J. A., Herranz, B., Romero de Ávila, M. D., & Cambero, M. I. (2008). Tensile properties of cooked meat sausages and their correlation with texture profile analysis (TPA) parameters and physico-chemical characteristics. *Meat Science*, 80(3), 690–696. <https://doi.org/10.1016/J.MEATSCI.2008.03.008>
- Herrero, A. M., Ordóñez, J. A., de Avila, R., Herranz, B., de la Hoz, L., & Cambero, M. I. (2007). Breaking strength of dry fermented sausages and their correlation with texture profile analysis (TPA) and physico-chemical characteristics. *Meat Science*, 77(3), 331–338. <https://doi.org/10.1016/j.meatsci.2007.03.022>
- Hinrichs, R., Bulca, S., & Kulozik, U. (2007). Water mobility during renneting and acid coagulation of casein solutions: A differentiated low-resolution nuclear magnetic resonance analysis. *International Journal of Dairy Technology*, 60(1), 37–43. <https://doi.org/10.1111/j.1471-0307.2007.00290.x>
- Hinrichs, R., Götz, J., & Weisser, H. (2003). Water-holding capacity and structure of hydrocolloid-gels, WPC-gels and yogurts characterised by means of NMR. *Food Chemistry*, 82(1), 155–160. [https://doi.org/10.1016/S0308-8146\(02\)00539-3](https://doi.org/10.1016/S0308-8146(02)00539-3)
- Hoban, J. M., Hopkins, D. L., Kirby, N., Collins, D., Dunshea, F. R., Kerr, M. G., Bailes, K., Cottrell, J. J., Holman, B. W. B., Brown, W., & Ponnampalam, E. N. (2016). Application of small angle

- X-ray scattering synchrotron technology for measuring ovine meat quality. *Meat Science*, 117, 122–129. <https://doi.org/10.1016/j.meatsci.2016.03.005>
- Hoek, A. C., Luning, P. A., Weijzen, P., Engels, W., Kok, F. J., & de Graaf, C. (2011). Replacement of meat by meat substitutes. A survey on person- and product-related factors in consumer acceptance. *Appetite*, 56(3), 662–673. <https://doi.org/10.1016/j.appet.2011.02.001>
- Holliday, D. L., Sandlin, C., Schott, A., Malekian, F., & Finley, J. W. (2011). Characteristics of meat or sausage patties using pulses as extenders. *Journal of Culinary Science and Technology*, 9(3), 158–176. <https://doi.org/10.1080/15428052.2011.594731>
- Hong, J., Loveday, S. M., Hardacre, A. K., & Parker, M. E. (2019). Effects of soy protein to wheat gluten ratio on the physicochemical properties of extruded meat analogues. *Food Structure*, 19(November 2018), 100102. <https://doi.org/10.1016/j.foostr.2018.11.002>
- Hoving-Bolink, A. H., Vedder, H. W., Merks, J. W. M., De Klein, W. J. H., Reimert, H. G. M., Frankhuizen, R., Van Den Broek, W. H. A. M., & Lambooi, E. (2005). Perspective of NIRS measurements early post mortem for prediction of pork quality. *Meat Science*, 69(3), 417–423. <https://doi.org/10.1016/j.meatsci.2004.08.012>
- Hsu, D. L. et al. (1982). Effect of Germination on Electrophoretic, Functional, and Bread-Baking Properties of Yellow Pea, Lentil, and Faba Bean Protein Isolates. *Cereal Chemistry*, 59(5), 344–350.
- Huang, H., Liu, L., & Ngadi, M. O. (2017). Assessment of intramuscular fat content of pork using NIR hyperspectral images of rib end. *Journal of Food Engineering*, 193, 29–41. <https://doi.org/10.1016/j.jfoodeng.2016.07.005>
- Hughes, J., Clarke, F., Li, Y., Purslow, P., & Warner, R. (2019). Differences in light scattering between pale and dark beef longissimus thoracis muscles are primarily caused by differences in the myofibrillar lattice, myofibrillar and muscle fibre transverse spacings. *Meat Science*, 149(May 2018), 96–106. <https://doi.org/10.1016/j.meatsci.2018.11.006>
- Hyun, K., Wilhelm, M., Klein, C. O., Cho, K. S., Nam, J. G., Ahn, K. H., Lee, S. J., Ewoldt, R. H., & McKinley, G. H. (2011). A review of nonlinear oscillatory shear tests: Analysis and application of large amplitude oscillatory shear (LAOS). *Prog. Polym. Sci.*, 36(12), 1697–1753. <https://doi.org/10.1016/j.proppolymsci.2011.02.002>
- ISO. (2008). 5492. *Sensory Analysis — Vocabulary*, 1–107.
- Jia, B., Wang, W., Yoon, S. C., Zhuang, H., & Li, Y. F. (2018). Using a combination of spectral and textural data to measure water-holding capacity in fresh chicken breast fillets. *Applied Sciences (Switzerland)*, 8(3). <https://doi.org/10.3390/app8030343>
- John, J., Ray, D., Aswal, V. K., Deshpande, A. P., & Varughese, S. (2019). Dissipation and strain-stiffening behavior of pectin-Ca gels under LAOS. *Soft Matter*, 15(34), 6852–6866. <https://doi.org/10.1039/c9sm00709a>
- Jones, O. G. (2016). Recent advances in the functionality of non-animal-sourced proteins contributing to their use in meat analogs. *Current Opinion in Food Science*, 7, 7–13. <https://doi.org/10.1016/j.cofs.2015.08.002>
- Joshi, V. K., & Kumar, S. (2015). Meat Analogues: Plant based alternatives to meat products- A review. *International Journal of Food and Fermentation Technology*, 5(2), 107. <https://doi.org/10.5958/2277-9396.2016.00001.5>

- Jung, Y., Lee, J., Kwon, J., Lee, K. S., Ryu, D. H., & Hwang, G. S. (2010). Discrimination of the geographical origin of beef by <sup>1</sup>H NMR-based metabolomics. *Journal of Agricultural and Food Chemistry*, 58(19), 10458–10466. <https://doi.org/10.1021/jf102194t>
- Kamani, M. H., Meera, M. S., Bhaskar, N., & Modi, V. K. (2019). Partial and total replacement of meat by plant-based proteins in chicken sausage: evaluation of mechanical, physico-chemical and sensory characteristics. *Journal of Food Science and Technology*, 56(5), 2660–2669. <https://doi.org/10.1007/s13197-019-03754-1>
- Kamruzzaman, M., ElMasry, G., Sun, D. W., & Allen, P. (2012). Prediction of some quality attributes of lamb meat using near-infrared hyperspectral imaging and multivariate analysis. *Analytica Chimica Acta*, 714, 57–67. <https://doi.org/10.1016/j.aca.2011.11.037>
- Karaca, A. C., Low, N., & Nickerson, M. (2011). Emulsifying properties of chickpea, faba bean, lentil and pea proteins produced by isoelectric precipitation and salt extraction. *Food Research International*, 44(9), 2742–2750. <https://doi.org/10.1016/j.foodres.2011.06.012>
- Kasapis, S., & Tay, S. L. (2009). Morphology of molecular soy protein fractions in binary composite gels. *Langmuir*, 25(15), 8538–8547. <https://doi.org/10.1021/la803290j>
- Kazir, M., & Livney, Y. D. (2021). *Plant-Based Seafood Analogs*. *Molecules*, 26(6), 1559. <https://doi.org/10.3390/molecules26061559>
- Kendler, C., Duchardt, A., Karbstein, H. P., & Emin, M. A. (2021). *Effect of Oil Content and Oil Addition Point on the Extrusion Processing of Wheat Gluten-Based Meat Analogues*. *Foods*, 10(4), 697. <https://doi.org/10.3390/foods10040697>
- Ketz, R. J., Prud'homme, R. K., & Graessley, W. W. (1988). Rheology of concentrated microgel solutions. *Rheologica Acta*, 27(5), 531–539. <https://doi.org/10.1007/BF01329353>
- Khan, S. A., Schnepfer, C. A., & Armstrong, R. C. (1988). Foam Rheology: III. Measurement of Shear Flow Properties. *Journal of Rheology*, 32(1), 69–92. <https://doi.org/10.1122/1.549964>
- Kim, K., Choi, B., Lee, I., Lee, H., Kwon, S., Oh, K., & Kim, A. Y. (2011). Bioproduction of mushroom mycelium of *Agaricus bisporus* by commercial submerged fermentation for the production of meat analogue. *Journal of the Science of Food and Agriculture*, 91(9), 1561–1568. <https://doi.org/10.1002/jsfa.4348>
- Klaypradit, W., Kerdpiroon, S., & Singh, R. K. (2011). Application of Artificial Neural Networks to Predict the Oxidation of Menhaden Fish Oil Obtained from Fourier Transform Infrared Spectroscopy Method. *Food and Bioprocess Technology*, 4(3), 475–480. <https://doi.org/10.1007/s11947-010-0386-5>
- Klost, M., Giménez-Ribes, G., & Drusch, S. (2019). Enzymatic hydrolysis of pea protein: Interactions and protein fractions involved in fermentation induced gels and their influence on rheological properties. *Food Hydrocolloids Submitted*, 105(September 2019). <https://doi.org/10.1016/j.foodhyd.2020.105793>
- Klost, M., Brzeski, C., & Drusch, S. (2020). Effect of protein aggregation on rheological properties of pea protein gels. *Food Hydrocolloids*, 108(January), 106036. <https://doi.org/10.1016/j.foodhyd.2020.106036>
- Kohler, A., Bertrand, D., Martens, H., Hannesson, K., Kirschner, C., & Ofstad, R. (2007). Multivariate image analysis of a set of FTIR microspectroscopy images of aged bovine muscle tissue combining image and design information. *Analytical and Bioanalytical Chemistry*, 389(4),

- 1143–1153. <https://doi.org/10.1007/s00216-007-1414-9>
- Koksel, F., Scanlon, M. G., & Page, J. H. (2016). Ultrasound as a tool to study bubbles in dough and dough mechanical properties: A review. *Food Research International*, 89, 74–89. <https://doi.org/10.1016/j.foodres.2016.09.015>
- Krepper, G., Romeo, F., Fernandes, D. D. de S., Diniz, P. H. G. D., de Araújo, M. C. U., Di Nezio, M. S., Pistonesi, M. F., & Centurión, M. E. (2018). Determination of fat content in chicken hamburgers using NIR spectroscopy and the Successive Projections Algorithm for interval selection in PLS regression (iSPA-PLS). *Spectrochimica Acta - Part A: Molecular and Biomolecular Spectroscopy*, 189, 300–306. <https://doi.org/10.1016/j.saa.2017.08.046>
- Krintiras, G. A., Göbel, J., Bouwman, W. G., van der Goot, A. J., & Stefanidis, G. D. (2014). On characterization of anisotropic plant protein structures. *Food & Function*, 5(12), 3233–3240. <https://doi.org/10.1039/c4fo00537f>
- Krintiras, G. A., Göbel, J., van der Goot, A. J., & Stefanidis, G. D. (2015). Production of structured soy-based meat analogues using simple shear and heat in a Couette Cell. *Journal of Food Engineering*, 160, 34–41. <https://doi.org/10.1016/j.jfoodeng.2015.02.015>
- Kröger, C., Bartle, C. M., West, J. G., Purchas, R. W., & Devine, C. E. (2006). Meat tenderness evaluation using dual energy X-ray absorptiometry (DEXA). *Computers and Electronics in Agriculture*, 54(2), 93–100. <https://doi.org/10.1016/j.compag.2006.09.002>
- Kucha, C. T., Liu, L., & Ngadi, M. O. (2018). Non-destructive spectroscopic techniques and multivariate analysis for assessment of fat quality in pork and pork products: A review. *Sensors (Switzerland)*, 18(2). <https://doi.org/10.3390/s18020377>
- Kyriakopoulou, K., Keppler, J. K., & van der Goot, A. J. (2021). Functionality of Ingredients and Additives in Plant-Based Meat Analogues. *Foods*, 600(10). <https://doi.org/https://doi.org/10.3390/foods10030600> Academic
- Lam, A. C. Y., Can Karaca, A., Tyler, R. T., & Nickerson, M. T. (2018). Pea protein isolates: Structure, extraction, and functionality. *Food Reviews International*, 34(2), 126–147. <https://doi.org/10.1080/87559129.2016.1242135>
- Lan, Y., Chen, B., & Rao, J. (2018). Pea protein isolate–high methoxyl pectin soluble complexes for improving pea protein functionality: Effect of pH, biopolymer ratio and concentrations. *Food Hydrocolloids*, 80, 245–253. <https://doi.org/10.1016/j.foodhyd.2018.02.021>
- Laranjo, M., Agulheiro-Santos, A. C., Potes, M. E., Cabrita, M. J., Garcia, R., Fraqueza, M. J., & Elias, M. (2015). Effects of genotype, salt content and calibre on quality of traditional dry-fermented sausages. *Food Control*, 56, 119–127. <https://doi.org/10.1016/j.foodcont.2015.03.018>
- Larrea, V., Pérez-Munuera, I., Hernando, I., Quiles, A., Llorca, E., & Lluch, M. A. (2007). Microstructural changes in Teruel dry-cured ham during processing. *Meat Science*, 76(3), 574–582. <https://doi.org/10.1016/j.meatsci.2007.01.013>
- Larson, R. G. (1999). *The structure and rheology of complex fluids*. 150.
- Lee, E. J., & Hong, G. P. (2019). Effects of microbial transglutaminase and alginate on the water-binding, textural and oil absorption properties of soy patties. *Food Science and Biotechnology*, 1–6. <https://doi.org/10.1007/s10068-019-00713-6>
- Leonard, M. M., & Vasagar, B. (2014). US perspective on gluten-related diseases. *Clinical and*

- Experimental Gastroenterology*, 7(1), 25–37. <https://doi.org/10.2147/CEG.S54567>
- Lepetit, J., & Culioli, J. (1994). Mechanical properties of meat. *Meat Science*, 36(1–2), 203–237. [https://doi.org/10.1016/0309-1740\(94\)90042-6](https://doi.org/10.1016/0309-1740(94)90042-6)
- Li, H., Kutsanedzie, F., Zhao, J., & Chen, Q. (2016). Quantifying Total Viable Count in Pork Meat Using Combined Hyperspectral Imaging and Artificial Olfaction Techniques. *Food Analytical Methods*, 9(11), 3015–3024. <https://doi.org/10.1007/s12161-016-0475-9>
- Li, J., Tan, J., & Shatadal, P. (2001). Classification of tough and tender beef by image texture analysis. *Meat Science*, 57(4), 341–346. [https://doi.org/10.1016/S0309-1740\(00\)00105-4](https://doi.org/10.1016/S0309-1740(00)00105-4)
- Lin, S., Huff, H. E., & Hsieh, F. (2002). Extrusion process parameters, sensory characteristics, and structural properties of a high moisture soy protein meat analog. *Journal of Food Science*, 67(3), 1066–1072. <https://doi.org/10.1111/j.1365-2621.2002.tb09454.x>
- Lin, W. L., Zeng, Q. X., & Zhu, Z. W. (2009). Different changes in mastication between crisp grass carp (*Ctenopharyngodon idellus* C.et V) and grass carp (*Ctenopharyngodon idellus*) after heating: The relationship between texture and ultrastructure in muscle tissue. *Food Research International*, 42(2), 271–278. <https://doi.org/10.1016/j.foodres.2008.11.005>
- Listrat, A., Lebret, B., Louveau, I., Astruc, T., Bonnet, M., Lefaucheur, L., & Bugeon, J. (2015). How muscle structure and composition determine meat quality. *Productions Animales*, 28(2), 125–136.
- Liu, W., & Lanier, T. C. (2015). Combined use of variable pressure scanning electron microscopy and confocal laser scanning microscopy best reveal microstructure of comminuted meat gels. *LWT - Food Science and Technology*, 62(2), 1027–1033. <https://doi.org/10.1016/j.lwt.2015.02.001>
- Liu, X. Q., Sun, Z. Y., Bao, R. Y., Yang, W., Xie, B. H., & Yang, M. B. (2014). Nanoparticle retarded shape relaxation of dispersed droplets in polymer blends: An understanding from the viewpoint of molecular movement. *RSC Advances*, 4(77), 41059–41068. <https://doi.org/10.1039/c4ra04380d>
- Lu, Z. X., He, J. F., Zhang, Y. C., & Bing, D. J. (2019). Composition, physicochemical properties of pea protein and its application in functional foods. *Critical Reviews in Food Science and Nutrition*, 8398. <https://doi.org/10.1080/10408398.2019.1651248>
- Luc, C., Clerjon, S., Peyrin, F., Lepetit, J., & Culioli, J. (2008). Sarcomere length determination using front-face fluorescence polarization. *Meat Science*, 80(3), 814–818. <https://doi.org/10.1016/j.meatsci.2008.03.030>
- Mabood, F., Boqué, R., Alkindi, A. Y., Al-Harrasi, A., Al Amri, I. S., Boukra, S., Jabeen, F., Hussain, J., Abbas, G., Naureen, Z., Haq, Q. M. I., Shah, H. H., Khan, A., Khalaf, S. K., & Kadim, I. (2020). Fast detection and quantification of pork meat in other meats by reflectance FT-NIR spectroscopy and multivariate analysis. *Meat Science*, 163(September 2019), 108084. <https://doi.org/10.1016/j.meatsci.2020.108084>
- Mackley, M. R., Marshall, R. T. J., Smeulders, J. B. A. F., & Zhao, F. D. (1994). The rheological characterization of polymeric and colloidal fluids. *Chemical Engineering Science*, 49(16), 2551–2565. [https://doi.org/10.1016/0009-2509\(94\)E0082-2](https://doi.org/10.1016/0009-2509(94)E0082-2)
- Majzoobi, M., Talebanfar, S., Eskandari, M. H., & Farahnaky, A. (2017). Improving the quality of meat-free sausages using κ-carrageenan, konjac mannan and xanthan gum. *International Journal of Food Science and Technology*, 52(5), 1269–1275. <https://doi.org/10.1111/ijfs.13394>



- Malav, O. P., Talukder, S., Gokulakrishnan, P., & Chand, S. (2015). Meat Analog: A Review. *Critical Reviews in Food Science and Nutrition*, 55(9), 1241–1245. <https://doi.org/10.1080/10408398.2012.689381>
- Manduca, A., Oliphant, T. E., Dresner, M. A., Mahowald, J. L., Kruse, S. A., Amromin, E., Felmlee, J. P., Greenleaf, J. F., & Ehman, R. L. (2001). Magnetic resonance elastography: Non-invasive mapping of tissue elasticity. *Medical Image Analysis*, 5(4), 237–254. [https://doi.org/10.1016/S1361-8415\(00\)00039-6](https://doi.org/10.1016/S1361-8415(00)00039-6)
- Manski, J. M., van der Goot, A. J., & Boom, R. M. (2007). Formation of fibrous materials from dense calcium caseinate dispersions. *Biomacromolecules*, 8(4), 1271–1279. <https://doi.org/10.1021/bm061008p>
- Marccone, M. F., Wang, S., Albabish, W., Nie, S., Somnarain, D., & Hill, A. (2013). Diverse food-based applications of nuclear magnetic resonance (NMR) technology. *Food Research International*, 51(2), 729–747. <https://doi.org/10.1016/j.foodres.2012.12.046>
- Mathanker, S. K., Weckler, P. R., & Wang, N. (2013). X-ray applications in food and agriculture: a review. *Transactions of the American Society of Agricultural and Biological Engineers*, 56(3), 1213–1226. <https://doi.org/10.13031/trans.56.9390>
- Mattice, K. D., & Marangoni, A. G. (2020). Evaluating the use of zein in structuring plant-based products. *Current Research in Food Science*, 3, 59–66. <https://doi.org/10.1016/j.crfs.2020.03.004>
- McClements, D. J., Weiss, J., Kinchla, A. J., Nolden, A. A., & Grossmann, L. (2021). *Methods for Testing the Quality Attributes of Plant-Based Foods : Meat- and Processed-Meat Analogs*. 1–30. <https://doi.org/10.3390/foods10020260>
- Mehmood, T., Liland, K. H., Snipen, L., & Sæbø, S. (2012). A review of variable selection methods in Partial Least Squares Regression. *Chemometrics and Intelligent Laboratory Systems*, 118, 62–69. <https://doi.org/10.1016/j.chemolab.2012.07.010>
- Mehmood, T., Sæbø, S., & Liland, K. H. (2020). Comparison of variable selection methods in partial least squares regression. *Journal of Chemometrics*, December 2019, 1–14. <https://doi.org/10.1002/cem.3226>
- Melito, H. S., Daubert, C. R., & Foegeding, E. A. (2013). Relating large amplitude oscillatory shear and food behavior: Correlation of nonlinear viscoelastic, rheological, sensory and oral processing behavior of whey protein isolate/κ-carrageenan gels. *Journal of Food Process Engineering*, 36(4), 521–534. <https://doi.org/10.1111/jfpe.12015>
- Michel, F., Hartmann, C., & Siegrist, M. (2021). Consumers' associations, perceptions and acceptance of meat and plant-based meat alternatives. *Food Quality and Preference*, 87(April 2020), 104063. <https://doi.org/10.1016/j.foodqual.2020.104063>
- Micklander, E., Peshlov, B., Purslow, P. P., & Engelsen, S. B. (2002). NMR-cooking: Monitoring the changes in meat during cooking by low-field <sup>1</sup>H-NMR. *Trends in Food Science and Technology*, 13(9–10), 341–346. [https://doi.org/10.1016/S0924-2244\(02\)00163-2](https://doi.org/10.1016/S0924-2244(02)00163-2)
- Mighri, F., Carreau, P. J., & Ajji, A. (1988). Influence of elastic properties on drop deformation and breakup in shear flow. *Journal of Rheology*. <https://doi.org/10.1122/1.550897>
- Miklos, R., Nielsen, M. S., Einarsdóttir, H., Feidenhans'l, R., & Lametsch, R. (2015). Novel X-ray phase-contrast tomography method for quantitative studies of heat induced structural changes in

- meat. *Meat Science*, 100, 217–221. <https://doi.org/10.1016/j.meatsci.2014.10.009>
- Mishra, P., Nordon, A., & Roger, J. M. (2021). Improved prediction of tablet properties with near-infrared spectroscopy by a fusion of scatter correction techniques. *Journal of Pharmaceutical and Biomedical Analysis*, 192, 113684. <https://doi.org/10.1016/j.jpba.2020.113684>
- Mitchell, A. D., Scholz, A. M., Wang, P. C., & Song, H. (2001). Body composition analysis of the pig by magnetic resonance imaging. *Journal of Animal Science*, 79(7), 1800–1813. <https://doi.org/10.2527/2001.7971800x>
- Moreno, H. M., Tovar, C. A., Domínguez-timón, F., Cano-báez, J., Díaz, M. T., Pedrosa, M. M., & Borderías, A. J. (2020). Gelation of commercial pea protein isolate: effect of microbial transglutaminase and thermal processing. *Food Science and Technology*, 2061. <https://doi.org/10.1590/fst.19519>
- Morey, A., & Owens, C. M. (2017). Methods for measuring meat texture. In *Poultry Quality Evaluation: Quality Attributes and Consumer Values* (pp. 115–132). Elsevier Ltd. <https://doi.org/10.1016/B978-0-08-100763-1.00005-2>
- Morris, E. R. (1992). The effect of solvent partition on the mechanical properties of biphasic biopolymer gels: an approximate theoretical treatment. *Carbohydrate Polymers*, 17(1), 65–70. [https://doi.org/10.1016/0144-8617\(92\)90024-K](https://doi.org/10.1016/0144-8617(92)90024-K)
- Mulot, V., Fatou-Toutie, N., Benkhelifa, H., Pathier, D., & Flick, D. (2019). Investigating the effect of freezing operating conditions on microstructure of frozen minced beef using an innovative X-ray micro-computed tomography method. *Journal of Food Engineering*, 262(May), 13–21. <https://doi.org/10.1016/j.jfoodeng.2019.05.014>
- Naveena, B. M., Sen, A. R., Muthukumar, M., Vaithyanathan, S., & Babji, Y. (2006). The effect of lactates on the quality of microwave-cooked chicken patties during storage. *Journal of Food Science*, 71(9). <https://doi.org/10.1111/j.1750-3841.2006.00178.x>
- Ng, T. S. K., & McKinley, G. H. (2008). Power law gels at finite strains: The nonlinear rheology of gluten gels. *Journal of Rheology*, 52(2), 417–449. <https://doi.org/10.1122/1.2828018>
- Ngapo, T. M., Babare, I. H., Reynolds, J., & Mawson, R. F. (1999). Freezing rate and frozen storage effects on the ultrastructure of samples of pork. *Meat Science*, 53(3), 159–168. [https://doi.org/10.1016/S0309-1740\(99\)00051-0](https://doi.org/10.1016/S0309-1740(99)00051-0)
- Niu, F., Ahmad, M., Fan, J., Ritzoulis, C., Chen, J., Luo, Z., & Pan, W. (2019). The application of diffusing wave spectroscopy (DWS) in soft foods. *Food Hydrocolloids*, 96(March), 671–680. <https://doi.org/10.1016/j.foodhyd.2019.06.011>
- Nolasco Perez, I. M., Badaró, A. T., Barbon, S., Barbon, A. P. A., Pollonio, M. A. R., & Barbin, D. F. (2018). Classification of Chicken Parts Using a Portable Near-Infrared (NIR) Spectrophotometer and Machine Learning. *Applied Spectroscopy*, 72(12), 1774–1780. <https://doi.org/10.1177/0003702818788878>
- Novakovi, S., & Tomašević, I. (2017). A comparison between Warner-Bratzler shear force measurement and texture profile analysis of meat and meat products: a review. *IOP Conference Series: Earth and Environmental Science*, 85.
- O’Kane, F. E., Vereijken, J. M., Gruppen, H., & Boekel, M. A. (2005). Gelation behaviour of protein isolates extracted from 5 cultivars of *Pisum sativum* L. *Journal of Food Science*, 70(2). <https://doi.org/10.1111/j.1365-2621.2005.tb07073.x>

- O'Kane, F. E., Happe, R. P., Vereijken, J. M., Gruppen, H., & van Boekel, M. A. J. S. (2004). Heat-Induced Gelation of Pea Legumin: Comparison with Soybean Glycinin. *Journal of Agricultural and Food Chemistry*, 52(16), 5071–5078. <https://doi.org/10.1021/jf035215h>
- Olsen, E. F., Rukke, E. O., Flåtten, A., & Isaksson, T. (2007). Quantitative determination of saturated-, monounsaturated- and polyunsaturated fatty acids in pork adipose tissue with non-destructive Raman spectroscopy. *Meat Science*, 76(4), 628–634. <https://doi.org/10.1016/j.meatsci.2007.02.004>
- Osborne, B. G. (2000). Near-Infrared Spectroscopy in Food Analysis. *Encyclopedia of Analytical Chemistry*, 1–14. <https://doi.org/10.1002/9780470027318.a1018>
- Osen, R., Toelstede, S., Wild, F., Eisner, P., & Schweiggert-Weisz, U. (2014). High moisture extrusion cooking of pea protein isolates: Raw material characteristics, extruder responses, and texture properties. *Journal of Food Engineering*, 127, 67–74. <https://doi.org/10.1016/j.jfoodeng.2013.11.023>
- Overman, S. A., & Thomas, G. J. (1999). Raman markers of nonaromatic side chains in an  $\alpha$ -helix assembly: Ala, Asp, Glu, Gly, Ile, Leu, Lys, Ser, and Val residues of phage fd subunits. *Biochemistry*, 38(13), 4018–4027. <https://doi.org/10.1021/bi982901e>
- Ozuna, C., Puig, A., García-Pérez, J. V., Mulet, A., & Cárcel, J. A. (2013). Influence of high intensity ultrasound application on mass transport, microstructure and textural properties of pork meat (*Longissimus dorsi*) brined at different NaCl concentrations. *Journal of Food Engineering*, 119(1), 84–93. <https://doi.org/10.1016/j.jfoodeng.2013.05.016>
- Padmanabhan, M., & Bhattacharya, M. (1991). Flow behavior and exit pressures of corn meal under high-shear-high-temperature extrusion conditions using a slit die a). *Journal of Rheology*, 35(3), 315–343. <https://doi.org/10.1122/1.550217>
- Palanisamy, M., Töpfl, S., Aganovic, K., & Berger, R. G. (2018). Influence of iota carrageenan addition on the properties of soya protein meat analogues. *LWT - Food Science and Technology*, 87, 546–552. <https://doi.org/10.1016/j.lwt.2017.09.029>
- Palanisamy, M., Töpfl, S., Berger, R. G., & Hertel, C. (2019). Physico-chemical and nutritional properties of meat analogues based on Spirulina/lupin protein mixtures. *European Food Research and Technology*, 245(9), 1889–1898. <https://doi.org/10.1007/s00217-019-03298-w>
- Panea, B., Olleta, J. L., Sañudo, C., del Mar Campo, M., Oliver, M. A., Gispert, M., Serra, X., Renand, G., del Carmen Oliván, M., Jabet, S., García, S., López, M., Izquierdo, M., García-Cachán, M. D., Quintanilla, R., & Piedrafita, J. (2018). Effects of breed-production system on collagen, textural, and sensory traits of 10 European beef cattle breeds. *Journal of Texture Studies*, 49(5), 528–535. <https://doi.org/10.1111/jtxs.12350>
- Pasquini, C. (2018). Near infrared spectroscopy: A mature analytical technique with new perspectives – A review. *Analytica Chimica Acta*, 1026, 8–36. <https://doi.org/10.1016/j.aca.2018.04.004>
- Pawar, S. P., & Bose, S. (2015). Peculiar morphological transitions induced by nanoparticles in polymeric blends: Retarded relaxation or altered interfacial tension? *Physical Chemistry Chemical Physics*, 17(22), 14470–14473. <https://doi.org/10.1039/c5cp01644d>
- Pearson, A. M. (2012). Composition and structure. In *Muscle and Meat Biochemistry* (pp. 1–33).
- Peighambardoust, S. H., Hamer, R. J., Boom, R. M., & van der Goot, A. J. (2008). Migration of gluten under shear flow as a novel mechanism for separating wheat flour into gluten and starch. *Journal*

- of Cereal Science*, 48(2), 327–338. <https://doi.org/10.1016/j.jcs.2007.10.005>
- Peighambardoust, S. H., van der Goot, A. J., Hamer, R. J., & Boom, R. M. (2005). Effect of simple shear on the physical properties of glutenin macro polymer (GMP). *Journal of Cereal Science*, 42(1), 59–68. <https://doi.org/10.1016/j.jcs.2004.12.007>
- Peña-Gonzalez, E., Alarcon-Rojas, A. D., Garcia-Galicia, I., Carrillo-Lopez, L., & Huerta-Jimenez, M. (2019). Ultrasound as a potential process to tenderize beef: Sensory and technological parameters. *Ultrasonics Sonochemistry*, 53(October 2018), 134–141. <https://doi.org/10.1016/j.ultsonch.2018.12.045>
- Pérez-Palacios, T., Ruiz, J., Martín, D., Muriel, E., & Antequera, T. (2008). Comparison of different methods for total lipid quantification in meat and meat products. *Food Chemistry*, 110(4), 1025–1029. <https://doi.org/10.1016/j.foodchem.2008.03.026>
- Pérez-Santaescolástica, C., Fraeye, I., Barba, F. J., Gómez, B., Tomasevic, I., Romero, A., Moreno, A., Toldrá, F., & Lorenzo, J. M. (2019). Application of non-invasive technologies in dry-cured ham: An overview. *Trends in Food Science and Technology*, 86(November 2018), 360–374. <https://doi.org/10.1016/j.tifs.2019.02.011>
- Perisic, N., Afseth, N. K., Ofstad, R., & Kohler, A. (2011). Monitoring protein structural changes and hydration in bovine meat tissue due to salt substitutes by Fourier transform infrared (FTIR) microspectroscopy. *Journal of Agricultural and Food Chemistry*, 59(18), 10052–10061. <https://doi.org/10.1021/jf201578b>
- Peters, J. P. C. M., Vergeldt, F. J., Boom, R. M., & van der Goot, A. J. (2017). Water-binding capacity of protein-rich particles and their pellets. *Food Hydrocolloids*, 65, 144–156. <https://doi.org/10.1016/j.foodhyd.2016.11.015>
- Pette, D., & Staron, R. S. (1990). Cellular and molecular diversities of mammalian skeletal muscle fibers. In *Reviews of Physiology, Biochemistry and Pharmacology, Volume 116* (pp. 1–76). Springer. [https://doi.org/10.1007/3540528806\\_3](https://doi.org/10.1007/3540528806_3)
- Philipp, C., Oey, I., Silcock, P., Beck, S. M., & Buckow, R. (2017). Impact of protein content on physical and microstructural properties of extruded rice starch-pea protein snacks. *Journal of Food Engineering*, 212, 165–173. <https://doi.org/10.1016/j.jfoodeng.2017.05.024>
- Phongpa-Ngan, P., Aggrey, S. E., Mulligan, J. H., & Wicker, L. (2014). Raman spectroscopy to assess water holding capacity in muscle from fast and slow growing broilers. *LWT - Food Science and Technology*, 57(2), 696–700. <https://doi.org/10.1016/j.lwt.2014.01.028>
- Piculell, L., Nilsson, S., & Muhrbeck, P. (1992). Effects of small amounts of kappa-carrageenan on the rheology of aqueous iota-carrageenan. *Carbohydrate Polymers*, 18(3), 199–208. [https://doi.org/10.1016/0144-8617\(92\)90064-W](https://doi.org/10.1016/0144-8617(92)90064-W)
- Pietsch, V. L., Emin, M. A., & Schuchmann, H. P. (2016). Process conditions influencing wheat gluten polymerization during high moisture extrusion of meat analog products. *Journal of Food Engineering*, 198, 28–35. <https://doi.org/10.1016/j.jfoodeng.2016.10.027>
- Pietsch, V. L., Karbstein, H. P., & Emin, M. A. (2018). Kinetics of wheat gluten polymerization at extrusion-like conditions relevant for the production of meat analog products. *Food Hydrocolloids*, 85(July), 102–109. <https://doi.org/10.1016/j.foodhyd.2018.07.008>
- Pietsch, V. L., Werner, R., Karbstein, H. P., & Emin, M. A. (2019). High moisture extrusion of wheat gluten: Relationship between process parameters, protein polymerization, and final product

- characteristics. *Journal of Food Engineering*, 259(January 2018), 3–11. <https://doi.org/10.1016/j.jfoodeng.2019.04.006>
- Pipkin, A. C. (1972). Lectures on Viscoelasticity Theory. *Applied Mathematical Sciences*, 7.
- Pool, M. F., & Klose, A. A. (1969). The Relation of Force to Sample Dimensions in Objective Measurement of Tenderness of Poultry Meat. *Journal of Food Science*, 34(6), 524–526. <https://doi.org/10.1111/j.1365-2621.1969.tb12077.x>
- Precha-Atsawanan, S., Uttapap, D., & Sagis, L. M. C. (2018). Linear and nonlinear rheological behavior of native and debranched waxy rice starch gels. *Food Hydrocolloids*, 85(March), 1–9. <https://doi.org/10.1016/j.foodhyd.2018.06.050>
- Prevolnik, M., Škrlep, M., Janeš, L., Velikonja-Bolta, Š., Škorjanc, D., & Čandek-Potokar-Potokar, M. (2011). Accuracy of near infrared spectroscopy for prediction of chemical composition, salt content and free amino acids in dry-cured ham. *Meat Science*, 88(2), 299–304. <https://doi.org/10.1016/j.meatsci.2011.01.007>
- Prieto, N., Roehe, R., Lavín, P., Batten, G., & Andrés, S. (2009). Application of near infrared reflectance spectroscopy to predict meat and meat products quality: A review. *Meat Science*, 83(2), 175–186. <https://doi.org/10.1016/j.meatsci.2009.04.016>
- Provencher, S. W. (1982). Contin: a general purpose constrained regularization program for inverting noisy linear algebraic and integral equations. *Computer Physics Communications*, 27, 229–242. [https://doi.org/10.1016/0010-4655\(82\)90174-6](https://doi.org/10.1016/0010-4655(82)90174-6)
- Ptaszek, P. (2014). Large amplitudes oscillatory shear (LAOS) behavior of egg white foams with apple pectins and xanthan gum. *Food Research International*, 62, 299–307. <https://doi.org/10.1016/j.foodres.2014.03.002>
- Ptaszek, P. (2015). A geometrical interpretation of large amplitude oscillatory shear (LAOS) in application to fresh food foams. *Journal of Food Engineering*, 146, 53–61. <https://doi.org/10.1016/j.jfoodeng.2014.08.022>
- Purohit, A. S., Reed, C., & Mohan, A. (2016). Development and evaluation of quail breakfast sausage. *LWT - Food Science and Technology*, 69, 447–453. <https://doi.org/10.1016/j.lwt.2016.01.058>
- Rady, A., & Adedeji, A. (2018). Assessing different processed meats for adulterants using visible-near-infrared spectroscopy. *Meat Science*, 136(May 2017), 59–67. <https://doi.org/10.1016/j.meatsci.2017.10.014>
- Rady, A., & Adedeji, A. A. (2020). Application of Hyperspectral Imaging and Machine Learning Methods to Detect and Quantify Adulterants in Minced Meats. *Food Analytical Methods*, 970–981. <https://doi.org/10.1007/s12161-020-01719-1>
- Ranasinghesagara, J. C. (2008). *Optical Reflectance in Fibrous Tissues and Skeletal Muscles* (Issue December). University of Missouri-Columbia.
- Ranasinghesagara, J., Hsieh, F. H., Huff, H., & Yao, G. (2009). Laser scanning system for real-time mapping of fiber formations in meat analogues. *Journal of Food Science*, 74(2). <https://doi.org/10.1111/j.1750-3841.2008.01032.x>
- Ranasinghesagara, J., Hsieh, F., & Yao, G. (2006). A photon migration method for characterizing fiber formation in meat analogs. *Journal of Food Science*, 71(5). <https://doi.org/10.1111/j.1750-3841.2006.00038.x>

- Ranasinghesagara, J., & Yao, G. (2007). Imaging 2D optical diffuse reflectance in skeletal muscle. *Optics Express*, 15(7), 3998. <https://doi.org/10.1364/oe.15.003998>
- Ranasinghesagara, Janaka, Hsieh, F.-H., & Yao, G. (2005). An Image Processing Method for Quantifying Fiber Formation in Meat Analogs Under High Moisture Extrusion. *Journal of Food Science*, 70(8), e450–e454. <https://doi.org/10.1111/j.1365-2621.2005.tb11513.x>
- Reis, M. M., Van Beers, R., Al-Sarayreh, M., Shorten, P., Yan, W. Q., Saeys, W., Klette, R., & Craigie, C. (2018). Chemometrics and hyperspectral imaging applied to assessment of chemical, textural and structural characteristics of meat. *Meat Science*, 144(May), 100–109. <https://doi.org/10.1016/j.meatsci.2018.05.020>
- Renard, D., Velde, F. Van De, & Visschers, R. W. (2006). *The gap between food gel structure, texture and perception*. 20, 423–431. <https://doi.org/10.1016/j.foodhyd.2005.10.014>
- Renou, J. P., Bielicki, G., Bonny, J. M., Donnat, J. P., & Foucat, L. (2003). Assessment of meat quality by NMR. *Special Publication-Royal Society of Chemistry*, 286, 161–171.
- Ripoll, G., Albertí, P., Panea, B., Olleta, J. L., & Sañudo, C. (2008). Near-infrared reflectance spectroscopy for predicting chemical, instrumental and sensory quality of beef. *Meat Science*, 80(3), 697–702. <https://doi.org/10.1016/j.meatsci.2008.03.009>
- Rizo, A., Peña, E., Alarcon-Rojo, A. D., Fiszman, S., & Tarrega, A. (2019). Relating texture perception of cooked ham to the bolus evolution in the mouth. *Food Research International*, 118(October 2017), 4–12. <https://doi.org/10.1016/j.foodres.2018.02.073>
- Roger, J. M., Palagos, B., Bertrand, D., & Fernandez-Ahumada, E. (2011). CovSel: Variable selection for highly multivariate and multi-response calibration. Application to IR spectroscopy. *Chemometrics and Intelligent Laboratory Systems*, 106(2), 216–223. <https://doi.org/10.1016/j.chemolab.2010.10.003>
- Roger, J. M., Boulet, J. C., Zeaiter, M., & Rutledge, D. N. (2020). Pre-processing Methods. In *Reference Module in Chemistry, Molecular Sciences and Chemical Engineering*.
- Roger, J. M., & Boulet, J. C. (2018). A review of orthogonal projections for calibration. *Journal of Chemometrics*, 32(9), 1–16. <https://doi.org/10.1002/cem.3045>
- Ruedt, C., Gibis, M., & Weiss, J. (2020). Quantification of surface iridescence in meat products by digital image analysis. *Meat Science*, 163(January), 108064. <https://doi.org/10.1016/j.meatsci.2020.108064>
- Ruiz-Cabrera, M. A., Gou, P., Foucat, L., Renou, J. P., & Daudin, J. D. (2004). Water transfer analysis in pork meat supported by NMR imaging. *Meat Science*, 67(1), 169–178. <https://doi.org/10.1016/j.meatsci.2003.10.005>
- Ruiz De Huidobro, F., Miguel, E., Blázquez, B., & Onega, E. (2005). A comparison between two methods (Warner-Bratzler and texture profile analysis) for testing either raw meat or cooked meat. *Meat Science*, 69(3), 527–536. <https://doi.org/10.1016/j.meatsci.2004.09.008>
- Saeys, W., Nguyen Do Trong, N., Van Beers, R., & Nicolai, B. M. (2019). Multivariate calibration of spectroscopic sensors for postharvest quality evaluation: A review. *Postharvest Biology and Technology*, 158(August), 110981. <https://doi.org/10.1016/j.postharvbio.2019.110981>
- Samard, S., Gu, B. Y., & Ryu, G. H. (2019). Effects of extrusion types, screw speed and addition of wheat gluten on physicochemical characteristics and cooking stability of meat analogues.

- Journal of the Science of Food and Agriculture*, 99(11), 4922–4931. <https://doi.org/10.1002/jsfa.9722>
- Samard, S., & Ryu, G. H. (2019a). A comparison of physicochemical characteristics, texture, and structure of meat analogue and meats. *Journal of the Science of Food and Agriculture*, 99(6), 2708–2715. <https://doi.org/10.1002/jsfa.9438>
- Samard, S., & Ryu, G. H. (2019b). Physicochemical and functional characteristics of plant protein-based meat analogs. *Journal of Food Processing and Preservation*, 43(10), 1–11. <https://doi.org/10.1111/jfpp.14123>
- Sánchez-Vioque, R., Clemente, A., Vioque, J., Bautista, J., & Millán, F. (1999). Protein isolates from chickpea (*Cicer arietinum* L.): Chemical composition, functional properties and protein characterization. *Food Chemistry*, 64(2), 237–243. [https://doi.org/10.1016/S0308-8146\(98\)00133-2](https://doi.org/10.1016/S0308-8146(98)00133-2)
- Sandoval Murillo, J. L., Osen, R., Hiermaier, S., & Ganzenmüller, G. (2019). Towards understanding the mechanism of fibrous texture formation during high-moisture extrusion of meat substitutes. *Journal of Food Engineering*, 242(August 2018), 8–20. <https://doi.org/10.1016/j.jfoodeng.2018.08.009>
- Sapin-De Broses, E., Gennisson, J. L., Pernot, M., Fink, M., & Tanter, M. (2010). Temperature dependence of the shear modulus of soft tissues assessed by ultrasound. *Physics in Medicine and Biology*, 55(6), 1701–1718. <https://doi.org/10.1088/0031-9155/55/6/011>
- Scheier, R., Scheeder, M., & Schmidt, H. (2015). Prediction of pork quality at the slaughter line using a portable Raman device. *Meat Science*, 103, 96–103. <https://doi.org/10.1016/j.meatsci.2015.01.009>
- Schmidt, H., Scheier, R., & Hopkins, D. L. (2013). Preliminary investigation on the relationship of Raman spectra of sheep meat with shear force and cooking loss. *Meat Science*, 93(1), 138–143. <https://doi.org/10.1016/j.meatsci.2012.08.019>
- Schoeman, L., Williams, P., du Plessis, A., & Manley, M. (2016). X-ray micro-computed tomography ( $\mu$ CT) for non-destructive characterisation of food microstructure. *Trends in Food Science and Technology*, 47, 10–24. <https://doi.org/10.1016/j.tifs.2015.10.016>
- Schofield, J. D., Bottomley, R. C., Timms, M. F., & Booth, M. R. (1983). The effect of heat on wheat gluten and the involvement of sulphhydryl-disulphide interchange reactions. *Journal of Cereal Science*, 1(4), 241–253. [https://doi.org/10.1016/S0733-5210\(83\)80012-5](https://doi.org/10.1016/S0733-5210(83)80012-5)
- Senouci, A., & Smith, A. C. (1988). An experimental study of food melt rheology - I. Shear viscosity using a slit die viscometer and a capillary rheometer. *Rheologica Acta*, 27(5), 546–554. <https://doi.org/10.1007/BF01329355>
- Shaarani, S. M., Nott, K. P., & Hall, L. D. (2006). Combination of NMR and MRI quantitation of moisture and structure changes for convection cooking of fresh chicken meat. *Meat Science*, 72(3), 398–403. <https://doi.org/10.1016/j.meatsci.2005.07.017>
- Shand, P. J., Ya, H., Pietrasik, Z., & Wanasundara, P. K. J. P. D. (2007). Physicochemical and textural properties of heat-induced pea protein isolate gels. *Food Chemistry*, 102(4), 1119–1130. <https://doi.org/10.1016/j.foodchem.2006.06.060>
- Shand, P. J., Ya, H., Pietrasik, Z., & Wanasundara, P. K. J. P. D. (2008). Transglutaminase treatment of pea proteins: Effect on physicochemical and rheological properties of heat-induced protein

- gels. *Food Chemistry*, 107(2), 692–699. <https://doi.org/https://doi.org/10.1016/j.foodchem.2007.08.095>
- Shewry, P. R., & Tatham, A. S. (1997). Disulphide bonds in wheat gluten proteins. *Journal of Cereal Science*, 25(3), 207–227. <https://doi.org/10.1006/jcrs.1996.0100>
- Shrinivas, P., Kasapis, S., & Tongdang, T. (2009). Morphology and mechanical properties of bicontinuous gels of agarose and gelatin and the effect of added lipid phase. *Langmuir*, 25(15), 8763–8773. <https://doi.org/10.1021/la9002127>
- Sibillo, V., Simeone, M., & Guido, S. (2004). Break-up of a Newtonian drop in a viscoelastic matrix under simple shear flow. *Rheologica Acta*, 43(5), 449–456. <https://doi.org/10.1007/s00397-004-0374-7>
- Sicherer, S. H., Morrow, E. H., & Sampson, H. A. (2000). Dose-response in double-blind, placebo-controlled oral food challenges in children with atopic dermatitis. *Journal of Allergy and Clinical Immunology*, 105(3), 582–586. <https://doi.org/10.1067/mai.2000.104941>
- Silva, S. R., & Cadavez, V. P. (2012). Real-time ultrasound (RTU) imaging methods for quality control of meats. In *Computer Vision Technology in the Food and Beverage Industries*. Woodhead Publishing Limited. <https://doi.org/10.1533/9780857095770.3.277>
- Singh, H., & MacRitchie, F. (2001). Application of polymer science to properties of gluten. *Journal of Cereal Science*, 33(3), 231–243. <https://doi.org/10.1006/jcrs.2000.0360>
- Sinkus, R., Tanter, M., Catheline, S., Lorenzen, J., Kuhl, C., Sondermann, E., & Fink, M. (2005). Imaging anisotropic and viscous properties of breast tissue by magnetic resonance-elastography. *Magnetic Resonance in Medicine*, 53(2), 372–387. <https://doi.org/10.1002/mrm.20355>
- Skibsted, E. T. S., Boelens, H. F. M., Westerhuis, J. A., Smilde, A. K., Broad, N. W., Rees, D. R., & Witte, D. T. (2005). Net analyte signal based statistical quality control. *Analytical Chemistry*, 77(22), 7103–7114. <https://doi.org/10.1021/ac048138d>
- Soltanizadeh, N., & Kadivar, M. (2014). Nanomechanical Characteristics of Meat and Its Constituents Postmortem: A Review. *Critical Reviews in Food Science and Nutrition*, 54(9), 1117–1139. <https://doi.org/10.1080/10408398.2011.627518>
- Sosulski, F., Garratt, M. D., & Slimkard, A. E. (1976). Functional Properties of Ten Legume Flours. *Canadian Institute of Food Science and Technology Journal*, 9(2), 66–69. [https://doi.org/10.1016/S0315-5463\(76\)73614-9](https://doi.org/10.1016/S0315-5463(76)73614-9)
- Spadaro, V., & Keeton, J. T. (1996). Qualitative and quantitative textural assessment of cooked ground beef patties. *Journal of Food Science*, 61(1), 235–240. <https://doi.org/10.1111/j.1365-2621.1996.tb14768.x>
- Stephan, A., Ahlborn, J., Zajul, M., & Zorn, H. (2018). Edible mushroom mycelia of *Pleurotus sapidus* as novel protein sources in a vegan boiled sausage analog system: functionality and sensory tests in comparison to commercial proteins and meat sausages. *European Food Research and Technology*, 244(5), 913–924. <https://doi.org/10.1007/s00217-017-3012-1>
- Stone, A. K., Karalash, A., Tyler, R. T., Warkentin, T. D., & Nickerson, M. T. (2015). Functional attributes of pea protein isolates prepared using different extraction methods and cultivars. *Food Research International*, 76(P1), 31–38. <https://doi.org/10.1016/j.foodres.2014.11.017>
- Straadt, I. K., Rasmussen, M., Andersen, H. J., & Bertram, H. C. (2007). Aging-induced changes in



- microstructure and water distribution in fresh and cooked pork in relation to water-holding capacity and cooking loss - A combined confocal laser scanning microscopy (CLSM) and low-field nuclear magnetic resonance relaxation study. *Meat Science*, 75(4), 687–695. <https://doi.org/10.1016/j.meatsci.2006.09.019>
- Strecker, T. D., Cavalieri, R. P., Zollars, R. L., & Pomeranz, Y. (1995). Polymerization and Mechanical Degradation Kinetics of Gluten and Glutenin at Extruder Melt-Section Temperatures and Shear Rates. *Journal of Food Science*, 60(3), 532–537. <https://doi.org/10.1111/j.1365-2621.1995.tb09820.x>
- Stubbs, T. L., Kennedy, A. C., & Fortuna, A. M. (2010). Using NIRS to predict fiber and nutrient content of Dryland cereal cultivars. *Journal of Agricultural and Food Chemistry*, 58(1), 398–403. <https://doi.org/10.1021/jf9025844>
- Subramanian, A., & Rodriguez-Saona, L. (2009). Fourier Transform Infrared (FTIR) Spectroscopy. In *Infrared Spectroscopy for Food Quality Analysis and Control: Vol. 1* (1st ed.). Elsevier Inc. <https://doi.org/10.1016/B978-0-12-374136-3.00007-9>
- Sun, X. D., & Arntfield, S. D. (2010). Gelation properties of salt-extracted pea protein induced by heat treatment. *Food Research International*, 43(2), 509–515. <https://doi.org/10.1016/j.foodres.2009.09.039>
- Szerman, N., Rao, W. L., Li, X., Yang, Y., Vaudagna, S. R., & Zhang, D. Q. (2015). Effects of the Application of Dense Phase Carbon Dioxide Treatments on Technological Parameters, Physicochemical and Textural Properties and Microbiological Quality of Lamb Sausages. *Food Engineering Reviews*, 7(2), 241–249. <https://doi.org/10.1007/s12393-014-9092-9>
- Szopinski, D., & Luinstra, G. A. (2016). Viscoelastic properties of aqueous guar gum derivative solutions under large amplitude oscillatory shear (LAOS). *Carbohydrate Polymers*, 153, 312–319. <https://doi.org/10.1016/j.carbpol.2016.07.095>
- Taheri-Garavand, A., Fatahi, S., Omid, M., & Makino, Y. (2019). Meat quality evaluation based on computer vision technique: A review. *Meat Science*, 156(December 2018), 183–195. <https://doi.org/10.1016/j.meatsci.2019.06.002>
- Taherian, A. R., Mondor, M., Labranche, J., Drolet, H., Ippersiel, D., & Lamarche, F. (2011). Comparative study of functional properties of commercial and membrane processed yellow pea protein isolates. *Food Research International*, 44(8), 2505–2514. <https://doi.org/10.1016/j.foodres.2011.01.030>
- Takayanagi, M., Harima, H., & Iwata, Y. (1963). *Viscoelastic behavior of polymer blends and its Comparison with model experiments*. 129.
- Tao, R., Rice, K. D., Djakeu, A. S., Mrozek, R. A., Cole, S. T., Freney, R. M., & Forster, A. M. (2019). Rheological characterization of next-generation ballistic witness materials for body armor testing. *Polymers*, 11(3). <https://doi.org/10.3390/polym11030447>
- Thrane, M., Paulsen, P. V., Orcutt, M. W., & Krieger, T. M. (2017). Soy Protein: Impacts, Production, and Applications. In *Sustainable Protein Sources*. Elsevier Inc. <https://doi.org/10.1016/B978-0-12-802778-3.00002-0>
- Tian, B., Wang, Z., de Campo, L., Gilbert, E. P., Dalglish, R. M., Velichko, E., van der Goot, A. J., & Bouwman, W. G. (2020). Small angle neutron scattering quantifies the hierarchical structure in fibrous calcium caseinate. *Food Hydrocolloids*, 106(November 2019), 105912. <https://doi.org/10.1016/j.foodhyd.2020.105912>

- Tian, B., Wang, Z., van der Goot, A. J., & Bouwman, W. G. (2018). Air bubbles in fibrous caseinate gels investigated by neutron refraction, X-ray tomography and refractive microscope. *Food Hydrocolloids*, 83, 287–295. <https://doi.org/10.1016/j.foodhyd.2018.05.006>
- Tilman, D., & Clark, M. (2014). Global diets link environmental sustainability and human health. *Nature*, 515(7528), 518–522. <https://doi.org/10.1038/nature13959>
- Ting, C. H., Kuo, F. J., Lien, C. C., & Sheng, C. T. (2009). Use of ultrasound for characterising the gelation process in heat induced  $\text{CaSO}_4 \cdot 2\text{H}_2\text{O}$  tofu curd. *Journal of Food Engineering*, 93(1), 101–107. <https://doi.org/10.1016/j.jfoodeng.2009.01.015>
- Tøgersen, G., Arnesen, J. F., Nilsen, B. N., & Hildrum, K. I. (2003). On-line prediction of chemical composition of semi-frozen ground beef by non-invasive NIR spectroscopy. *Meat Science*, 63(4), 515–523. [https://doi.org/10.1016/S0309-1740\(02\)00113-4](https://doi.org/10.1016/S0309-1740(02)00113-4)
- Tolstoguzov, V. B. (1993). Thermoplastic extrusion—the mechanism of the formation of extrudate structure and properties. *Journal of the American Oil Chemists' Society*, 70(4), 417–424. <https://doi.org/10.1007/BF02552717>
- Traina, M. S., & Breene, W. M. (1994). Composition, functionality and some chemical and physical properties of eight commercial full-fat soy flours. *Journal of Food Processing and Preservation*, 18(3), 229–252. <https://doi.org/10.1111/j.1745-4549.1994.tb00846.x>
- Tran, L. Q. N., Yuan, X. W., Bhattacharyya, D., Fuentes, C., Van Vuure, A. W., & Verpoest, I. (2015). Fiber-matrix interfacial adhesion in natural fiber composites. *International Journal of Modern Physics B*, 29(10–11). <https://doi.org/10.1142/S0217979215400184>
- Truong, V. D., & Daubert, C. R. (2000). Comparative study of large strain methods for assessing failure characteristics of selected food gels. *Journal of Texture Studies*, 31(3), 335–353. <https://doi.org/10.1111/j.1745-4603.2000.tb00294.x>
- Truong, V. D., & Daubert, C. R. (2001). Textural characterization of cheeses using vane rheometry and torsion analysis. *Journal of Food Science*, 66(5), 716–721. <https://doi.org/10.1111/j.1365-2621.2001.tb04627.x>
- Tulbek, M. C., Lam, R. S. H., Wang, Y. C., Asavajaru, P., & Lam, A. (2016). Pea: A Sustainable Vegetable Protein Crop. In *Sustainable Protein Sources*. Elsevier Inc. <https://doi.org/10.1016/B978-0-12-802778-3.00009-3>
- Tunick, M. H., & Van Hekken, D. L. (2010). Rheology and texture of commercial queso fresco cheeses made from raw and pasteurized milk. *Journal of Food Quality*, 33(SUPPL. 1), 204–215. <https://doi.org/10.1111/j.1745-4557.2010.00331.x>
- U-Chupaj, J., Malila, Y., Gamonpilas, C., Kijroongrojana, K., Petracci, M., Benjakul, S., & Visessanguan, W. (2017). Differences in textural properties of cooked caponized and broiler chicken breast meat. *Poultry Science*, 96(7), 2491–2500. <https://doi.org/10.3382/ps/pex006>
- van Beers, R., Aernouts, B., Reis, M. M., & Saeys, W. (2017). Anisotropic light propagation in bovine muscle tissue depends on the initial fiber orientation, muscle type and wavelength. *Optics*
- van den Einde, R. M., Bolsius, A., Van Soest, J. J. G., Janssen, L. P. B. M., van der Goot, A. J., & Boom, R. M. (2004). The effect of thermomechanical treatment on starch breakdown and the consequences for process design. *Carbohydrate Polymers*, 55(1), 57–63. <https://doi.org/10.1016/j.carbpol.2003.07.004>

- van den Einde, R. M., van der Veen, M. E., Bosman, H., van der Goot, A. J., & Boom, R. M. (2005). Modeling macromolecular degradation of corn starch in a twin screw extruder. *Journal of Food Engineering*, 66(2), 147–154. <https://doi.org/10.1016/j.jfoodeng.2004.03.001>
- van der Zalm, E. E. J., Berghout, J. A. M., van der Goot, A. J., & Boom, R. M. (2012). Starch – gluten separation by shearing: Influence of the device geometry. *Chemical Engineering Science*, 73, 421–430. <https://doi.org/10.1016/j.ces.2012.02.009>
- van Lengerich, B. (1990). Influence of Extrusion Processing on In-Line Rheological Behavior, Structure, and Function of Wheat Starch. *Dough Rheology and Baked Product Texture*, 421–471. [https://doi.org/10.1007/978-1-4613-0861-4\\_11](https://doi.org/10.1007/978-1-4613-0861-4_11)
- Vergnes, B., Della Valle, G., & Tayeb, J. (1993). A specific slit die rheometer for extruded starchy products. Design, validation and application to maize starch. *Rheologica Acta*, 32(5), 465–476. <https://doi.org/10.1007/BF00396177>
- Verhulst, K., Cardinaels, R., Moldenaers, P., Afkhami, S., & Renardy, Y. (2009). Influence of viscoelasticity on drop deformation and orientation in shear flow. Part 2: Dynamics. *Journal of Non-Newtonian Fluid Mechanics*, 156(1–2), 44–57. <https://doi.org/10.1016/j.jnnfm.2008.10.003>
- Verhulst, K., Moldenaers, P., & Minale, M. (2007). Drop shape dynamics of a Newtonian drop in a non-Newtonian matrix during transient and steady shear flow. *Journal of Rheology*, 51(2), 261–273. <https://doi.org/10.1122/1.2426973>
- Vogel, R. H. (1988). *SPLMOD user manual, data analysis group, EMBL-DA09, EMBL*.
- Voisey, P. W. (1976). Engineering Assessment and Critique of Instruments used for Meat Tenderness Evaluation. *Journal of Texture Studies*, 7, 11–48. <https://doi.org/10.1111/j.1745-4603.1976.tb01380.x>
- Voisey, P. W., & Larmond, E. (1974). Examination of Factors Affecting Performance of the Warner-Bratzler Meat Shear Test. *Canadian Institute of Food Science and Technology Journal*, 7(4), 243–249. [https://doi.org/10.1016/s0315-5463\(74\)73920-7](https://doi.org/10.1016/s0315-5463(74)73920-7)
- Wan, Y., Wang, H., Wang, W., Zan, L., & Zhu, J. (2018). Effect of Ultrasound and Calcium Chloride on the Ultrastructure and the Warner-Bratzler Shear Force Value of Beef Shank Muscle Fibers. *Food Biophysics*, 13(4), 396–403. <https://doi.org/10.1007/s11483-018-9545-4>
- Wang, N., Bhirud, P. R., & Tyler, R. T. (1999). Extrusion texturization of air-classified pea protein. *Journal of Food Science*, 64(3), 509–513. <https://doi.org/10.1111/j.1365-2621.1999.tb15073.x>
- Wang, Q., Lonergan, S. M., & Yu, C. (2012). Rapid determination of pork sensory quality using Raman spectroscopy. *Meat Science*, 91(3), 232–239. <https://doi.org/10.1016/j.meatsci.2012.01.017>
- Wang, Z., Tian, B., van der Goot, A. J., & Boom, R. (2018). Air bubbles in calcium caseinate fibrous material enhances anisotropy. *Food Hydrocolloids*, 87(submitted), 497–505. <https://doi.org/10.1016/j.foodhyd.2018.08.037>
- Wang, Z., Tian, B., Boom, R., & van der Goot, A. J. (2019). Understanding the role of air and protein phase on mechanical anisotropy of calcium caseinate fibers. *Food Research International*, 121(December 2018), 862–869. <https://doi.org/10.1016/j.foodres.2019.01.009>
- Warner, R. D. (2019). Review: Analysis of the process and drivers for cellular meat production. *Animal*, 13(12), 3041–3058. <https://doi.org/10.1017/S1751731119001897>

- Weinrich, R. (2019). Opportunities for the adoption of health-based sustainable dietary patterns: A review on consumer research of meat substitutes. *Sustainability (Switzerland)*, 11(15). <https://doi.org/10.3390/su11154028>
- Weiss, G. H., Porrà, J. M., & Masoliver, J. (1998). The continuous-time random walk description of photon motion in an isotropic medium. *Optics Communications*, 146(1–6), 268–276. [https://doi.org/10.1016/S0030-4018\(97\)00475-6](https://doi.org/10.1016/S0030-4018(97)00475-6)
- Wells, H. C., Edmonds, R. L., Kirby, N., Hawley, A., Mudie, S. T., & Haverkamp, R. G. (2013). Collagen fibril diameter and leather strength. *Journal of Agricultural and Food Chemistry*, 61(47), 11524–11531. <https://doi.org/10.1021/jf4041854>
- Weng, S., Guo, B., Tang, P., Yin, X., Pan, F., Zhao, J., Huang, L., & Zhang, D. (2020). Rapid detection of adulteration of minced beef using Vis/NIR reflectance spectroscopy with multivariate methods. *Spectrochimica Acta - Part A: Molecular and Biomolecular Spectroscopy*, 230, 118005. <https://doi.org/10.1016/j.saa.2019.118005>
- Wereley, N. M., Chaudhuri, A., Yoo, J. H., John, S., Kotha, S., Suggs, A., Radhakrishnan, R., Love, B. J., & Sudarshan, T. S. (2006). Bidisperse magnetorheological fluids using Fe particles at nanometer and micron scale. *Journal of Intelligent Material Systems and Structures*, 17(5), 393–401. <https://doi.org/10.1177/1045389X06056953>
- Wheeler, T. L., Shackelford, S. D., & Koohmaraie, M. (1996). Sampling, Cooking, and Coring Effects on Warner-Bratzler Shear Force Values in Beef. *Journal of Animal Science*, 74(7), 1553–1562. <https://doi.org/10.2527/1996.7471553x>
- Wittek, P., Zeiler, N., Karbstein, H. P., & Emin, M. A. (2020). Analysis of the complex rheological properties of highly concentrated biopolymers. *Applied Rheology*, 49(0), 64–76. <http://dx.doi.org/10.1515/arh-2020-0107>
- Wittek, P., Zeiler, N., Karbstein, H. P., & Emin, M. A. (2021). *High Moisture Extrusion of Soy Protein : Investigations on the Formation of Anisotropic Product Structure*. <https://doi.org/10.3390/foods10010102>
- Wold, J. P., O'Farrell, M., Høy, M., & Tschudi, J. (2011). On-line determination and control of fat content in batches of beef trimmings by NIR imaging spectroscopy. *Meat Science*, 89(3), 317–324. <https://doi.org/10.1016/j.meatsci.2011.05.001>
- Wold, J. P., Mage, I., Løvland, A., Sanden, K. W., & Ofstad, R. (2019). Near-infrared spectroscopy detects woody breast syndrome in chicken fillets by the markers protein content and degree of water binding. *Poultry Science*, 98(1), 480–490. <https://doi.org/10.3382/ps/pey351>
- Wold, S., Sjöström, M., & Eriksson, L. (2001). PLS-regression: A basic tool of chemometrics. *Chemometrics and Intelligent Laboratory Systems*, 58(2), 109–130. [https://doi.org/10.1016/S0169-7439\(01\)00155-1](https://doi.org/10.1016/S0169-7439(01)00155-1)
- Wu, D., He, Y., Feng, S., & Sun, D. W. (2008). Study on infrared spectroscopy technique for fast measurement of protein content in milk powder based on LS-SVM. *Journal of Food Engineering*, 84(1), 124–131. <https://doi.org/10.1016/j.jfoodeng.2007.04.031>
- Wu, D., & Sun, D. W. (2013). Advanced applications of hyperspectral imaging technology for food quality and safety analysis and assessment: A review - Part II: Applications. *Innovative Food Science and Emerging Technologies*, 19, 15–28. <https://doi.org/10.1016/j.ifset.2013.04.016>
- Wu, F. Y., Dutson, T. R., & Smith, S. B. (1985). A Scanning Electron Microscopic Study of Heat-

- Induced Alterations in Bovine Connective Tissue. *Journal of Food Science*, 50(4), 1041–1044. <https://doi.org/10.1111/j.1365-2621.1985.tb13007.x>
- Wu, S. (1987). Formation of Dispersed Phase in Incompatible Polymer blends: Interfacial and Rheological Effects. *Polymer Engineering and Science*, 7(5), 335–343. <https://doi.org/10.1002/pen.760270506>
- Xiong, R., Cavitt, L. C., Meullenet, J. F., & Owens, C. M. (2006). Comparison of Allo-Kramer, Warner-Bratzler and razor blade shears for predicting sensory tenderness of broiler breast meat. *Journal of Texture Studies*, 37(2), 179–199. <https://doi.org/10.1111/j.1745-4603.2006.00045.x>
- Yang, Q., Sun, D. W., & Cheng, W. (2017). Development of simplified models for nondestructive hyperspectral imaging monitoring of TVB-N contents in cured meat during drying process. *Journal of Food Engineering*, 192, 53–60. <https://doi.org/10.1016/j.jfoodeng.2016.07.015>
- Yao, G., Liu, K. S., & Hsieh, F. (2004). A New Method for Characterizing Fiber Formation in Meat Analogs during High-moisture Extrusion. *Food Engineering and Physical Properties*, 69(7), 450–454. <https://doi.org/10.1111/j.1365-2621.2004.tb13634.x>
- Yarmand, M. S., & Baumgartner, P. A. (2000). Environmental Scanning Electron Microscopy of Raw and Heated Veal Semimembranosus Muscle. *Journal of Agricultural Science and Technology*, 2(3), 217–224.
- Yarmand, M. S., & Homayouni, A. (2010). Quality and microstructural changes in goat meat during heat treatment. *Meat Science*, 86(2), 451–455. <https://doi.org/10.1016/j.meatsci.2010.05.033>
- Yazar, G., Caglar, O., Tavman, S., & Kokini, J. L. (2016). Effect of mixing on LAOS properties of hard wheat flour dough. *Journal of Food Engineering*, 190, 195–204. <https://doi.org/10.1016/j.jfoodeng.2016.06.011>
- Yazar, G., Duvarci, O., Tavman, S., & Kokini, J. L. (2017). Non-linear rheological behavior of gluten-free flour doughs and correlations of LAOS parameters with gluten-free bread properties. *Journal of Cereal Science*, 74, 28–36. <https://doi.org/10.1016/j.jcs.2017.01.008>
- Yousfi, M., Dadouche, T., Chomat, D., Samuel, C., Soulestin, J., Lacrampe, M. F., & Krawczak, P. (2018). Development of nanofibrillar morphologies in poly(l-lactide)/poly(amide) blends: Role of the matrix elasticity and identification of the critical shear rate for the nodular/fibrillar transition. *RSC Advances*, 8(39), 22023–22041. <https://doi.org/10.1039/c8ra03339k>
- Zhang, J., Liu, L., Jiang, Y., Faisal, S., Wei, L., Cao, C., Yan, W., & Wang, Q. (2019). Converting Peanut Protein Biomass Waste into “Double Green” Meat Substitutes Using a High-Moisture Extrusion Process: A Multiscale Method to Explore a Process for Forming a Meat-Like Fibrous Structure [Research-article]. *Journal of Agricultural and Food Chemistry*, 67, 10713–10725. <https://doi.org/10.1021/acs.jafc.9b02711>
- Zhang, Q., Ma, G., Chen, H., Han, L., Yu, Q., Ma, J., & Zhang, W. (2019). Optimization of binding process for premade yak steaks using transglutaminase, sodium caseinate, and carrageenan. *Journal of Food Process Engineering*, 42(5), 1–11. <https://doi.org/10.1111/jfpe.13076>
- Zhou, L., Cook, L. P., & McKinley, G. H. (2010). Probing shear-banding transitions of the VCM model for entangled wormlike micellar solutions using large amplitude oscillatory shear (LAOS) deformations. *Journal of Non-Newtonian Fluid Mechanics*, 165(21–22), 1462–1472. <https://doi.org/10.1016/j.jnnfm.2010.07.009>
- Zhu, P., Huang, W., Guo, X., & Chen, L. (2021). Strong and elastic pea protein hydrogels formed

- through pH-shifting method. *Food Hydrocolloids*, 117(February), 106705. <https://doi.org/10.1016/j.foodhyd.2021.106705>
- Zhu, X., Kaur, L., Staincliffe, M., & Boland, M. (2018). Actinidin pretreatment and sous vide cooking of beef brisket: Effects on meat microstructure, texture and in vitro protein digestibility. *Meat Science*, 145(June), 256–265. <https://doi.org/10.1016/j.meatsci.2018.06.029>







S

*Summary &  
Samenvatting*

Proteins used for meat analogues are at this moment mostly derived from dairy, soy and wheat gluten. Pea protein is considered to be a promising alternative, because of its lower allergenic potential, good functionality and lower environmental impact. The scientific goal of this work was therefore is to gain in-depth understanding in the structure formation process of plant-based proteins and to connect those to the functional properties of pea proteins. To do so, pea protein isolate (PPI) and blends of PPI with other components that are relevant for next generation meat analogues were processed in the shear cell, characterised using non-linear (large deformation) rheological measurements and benchmarked to meat, commercial meat analogues and products based on soy protein isolate (SPI). It was concluded that a common requirement of the fibrous structures that can be obtained by using blends with gluten, is the ability to form a bi-continuous network. The research in this thesis showed the importance of elastic properties of both components in the blend. Heating at high temperature induces elasticity in the proteins during structuring, but the extent of this effect depended on the actual protein source. The mechanical and rheological benchmarking against real meat indicate that the plant-based materials have similar textural properties as chicken, but that their elasticity is not yet the same and therefore an important parameter for future research to the creation of good-quality meat analogues.

In **Chapter 2**, the structuring potential of PPI-wheat gluten (WG) and SPI-WG blends was explored using the shear cell technology. A fibrous structure was formed with PPI-WG blends but only in a narrower processing window than the operating window for SPI-WG blends. Blends with PPI had similar mechanical properties as chicken meat, while SPI-based blends were tougher. Remarkably, the anisotropy in the small deformation (Young's modulus) of chicken meat was larger compared with the plant-based products. In **Chapter 3**, insight into the internal structure of the PPI-WG and SPI-WG blends was obtained by using a combination of Time-Domain Nuclear Magnetic Resonance (TD-NMR) and rheological characterization. Rheological results were interpreted using the polymer blending law. The water distribution of the phases in a blend measured with TD-NMR revealed that water is preferentially taken up by the SPI / PPI phases, leaving less water for WG. A closed cavity rheometer (CCR) was used to quantify the rheological properties of the separate phases as a function of the water content. From that, it was concluded that WG inside the blend has a higher apparent modulus than PPI or SPI at a temperature range 110-140°C. The analysis of the polymer blending is extended by fitting the polymer blending law to the experimental

data. The outcomes of the fitting suggests that both PPI-WG and SPI-WG blends have a bi-continuous morphology when being transformed into fibrous products.

A next step in rheological characterisation was the evaluation of the non-linear properties of the proteinaceous materials used in this thesis at high temperatures, which is described in **Chapter 4**. Large amplitude oscillatory shear (LAOS) measurements were used to provide a detailed picture of the rheological changes that occur during processing (high temperatures and large deformations). The measurements are summarized using Lissajous curves and the energy dissipation ratio that characterizes the plasticity of the materials. Large amplitude oscillatory shear deformation with a closed cavity rheometer was successfully applied before, during and after thermal treatment, giving insight in the rheological changes during processing. It was found that heating induces elasticity in the proteins during structuring, but that the extent of this effect depended on the protein source. PPI lost its elastic properties more quickly than SPI, while WG showed abrupt dissipation after extensive deformation. In addition to these individual proteins, **Chapter 5** describes the rheological behaviour of PPI-WG and SPI-WG blends. The rheological properties were visualized using texture maps and colour schemes to summarize the differences between the blends. In PPI-WG blends, PPI had a lower stress and was less elastic compared with WG. In SPI-WG, the properties were almost similar.

In previous chapters, PPI-WG and SPI-WG blends were investigated for their ability to form fibrous structures. It is of interest to study whether PPI can form these structures with other ingredients than WG as well, such as carbohydrates. Therefore, blends of PPI, SPI with carbohydrates pectin and cellulose were investigated for their structuring potential and the results are presented in **Chapter 6**. A fibrous morphology was formed with PPI/pectin and SPI/pectin at a mass fraction of 93:7 and 95:5. Blends of SPI/pectin/cellulose could also be transformed into a fibrous structure. For SPI-blends, a fibrous morphology was always correlated to mechanical anisotropy, whereas this relationship was not observed for PPI-blends. The linear and non-linear rheological properties of the blends were studied with a closed-cavity rheometer at structuring conditions to gain insight into the structure formation as well as physical and chemical changes. The results indicate that PPI/pectin and SPI/pectin blends formed a mushier softer texture due to water re-distribution and a reduction of pH. Furthermore, the importance of the elasticity of the protein phase was demonstrated as an important factor for predicting the ability of blends to form fibrous products.

In **Chapter 7**, non-linear rheological differences and similarities between various meat and meat analogues (especially chicken analogues) were quantified before and after heating. Meat analogues differed from heated meat in terms of lower elasticity. In addition, heating of meat resulted in a tougher and more elastic product. In contrast, heating hardly altered the properties of meat analogues. Future developments on meat analogues should therefore focus on the creation of more elasticity and possibly allow heating effects on texture.

Literature was reviewed to summarize the texture methods typically used to characterize the structure of meat and meat analogue products (**Chapter 8**). An overview is presented of the available texture methods. Fewer methods are available for meat analogues than for meat, but a range of methods for meat can be used to analyze meat analogues after some modification. The need for new methods to study the structuring and final texture of current and future meat analogues is described.

**Chapter 9** described the potential of Near-infrared (NIR) point spectroscopy and hyperspectral imaging (HSI) to quantify of the composition of blends on their protein and oil content. The methods are non-destructive and allow rapid quantification of the composition using chemometric modelling. NIR point spectroscopy showed good predictions of the composition in the blend and HIS visualized the spatial distribution of the blend.

**Chapter 10** concludes this thesis with a general discussion of the main findings. Those findings are first summarized, after which a critical reflection on the methods and results is given. All insights are integrated into the design rules to create fibrous products. Current developments on new protein structuring are critically discussed and we provide suggestions for future research for meat analogues.

Om de groeiende wereld bevolking op een duurzame manier van voedsel te voorzien is het noodzakelijk dat mensen meer plantaardige producten gaan consumeren. Vleesproductie vereist namelijk intensief gebruik van land, water en energie. Minder vlees en op zijn minst gedeeltelijke overgang naar plantaardige producten zal positief zijn voor het milieu. De consumenten stappen echter nog niet massaal over op deze producten, wat erop wijst dat deze producten nog niet volledig aan hun behoeften en verwachtingen voldoen. Gelukkig zijn er veel ontwikkelingen rondom nieuwe plantaardige producten. Er is vooral veel gaande rondom producten, vaak vleesvervangers genoemd, die vlees benaderen in textuur (vezelachtigheid, beet en mondgevoel). Grote gelijkenis met vlees wordt als een belangrijke factor beschouwd voor consumenten om over te willen stappen naar plantaardig eiwitrijk voedsel. Eiwitten die worden gebruikt voor vleesvervangers zijn op het moment meestal afkomstig van zuivel-, soja- en tarwe. Eiwitten uit erwten wordt beschouwd als een veelbelovend alternatief, vanwege de lagere allergene potentieel, goede functionaliteit en lagere milieu-impact.

Het wetenschappelijke doel van dit werk is dan ook om het structuurvormingsproces van plantaardige eiwitten beter te begrijpen en deze te relateren aan de functionele eigenschappen van erwten eiwitten. Erwteneiwitisolaat (pea protein isolate, PPI) en mengsels van PPI met andere componenten die relevant zijn voor vleesvervangers zijn daarom bewerkt in de shear cell, gekarakteriseerd met behulp van niet-lineaire (grote vervorming) reologische metingen en vergeleken met vlees, commercieel beschikbare vleesvervangers en producten op basis van soja-eiwitisolaat (soy protein isolate, SPI). Een conclusie is dat de vorming van een vezelachtige structuur in een mengsel met gluten (eiwit uit tarwe) hoogstwaarschijnlijk gaat via een bi-continue morfologie. Het onderzoek in dit proefschrift benadrukt ook het belang van elastische eigenschappen van beide componenten in het mengsel. Gebruik van hoge temperaturen induceert elasticiteit in de producten tijdens het structureren, maar de mate van dit effect hangt af van het type eiwit. De uitgevoerde mechanische en reologische benchmarking laat zien dat de plantaardige materialen vergelijkbare textuureigenschappen kunnen hebben als kip, maar dat de elasticiteit nog niet dezelfde is. Het ligt daarom in de lijn der verwachting dat elasticiteit een belangrijke parameter zal zijn in toekomstig onderzoek naar het creëren van kwalitatief goede vleesanalogen.

In **Hoofdstuk 2** zijn de structuurvormende eigenschappen van PPI-tarwegluten (WG) en SPI-WG-mengsels onderzocht met behulp van de shear cell technologie. Met behulp van deze

technologie worden eiwitten in een stromingsveld uitgelijnd in de draairichting. Door dit uitlijnen konden vezelachtige structuren met PPI-WG-blends gevormd worden, maar komt nauwer qua temperatuur dan met SPI-WG-blends. Mengsels met PPI lieten vergelijkbare mechanische eigenschappen zien als kippenvlees, terwijl mengsels die op SPI waren gebaseerd, taaier waren. Interessant is dat de anisotropie bij kleine vervorming (Young's modulus) van kippenvlees groter is dan die van plantaardige producten. **Hoofdstuk 3** beschrijft nieuwe inzichten in de interne structuur van de PPI-WG- en SPI-WG-blends door een combinatie van Time-Domain Nuclear Magnetic Resonance (TD-NMR) en reologische karakterisering met behulp van de polymere meng-wet. De waterverdeling tussen de fasen in een mengsel gemeten met TD-NMR liet zien dat water bij voorkeur wordt opgenomen door de SPI / PPI-fase, waardoor er minder water overblijft voor de WG-fase. Een gesloten reometer ('closed-cavity rheometer'; CCR) werd gebruikt om de reologische eigenschappen van de afzonderlijke fasen te kwantificeren als functie van het watergehalte. Daaruit bleek dat WG in het mengsel een hogere modulus heeft dan PPI of SPI bij een temperatuurbereik van 110-140°C. Verdere analyse van de metingen met behulp van de polymere mengregel liet zien dat zowel PPI-WG- als SPI-WG-mengsels hoogstwaarschijnlijk een bi-continue morfologie hebben.

Een volgende stap in de reologische karakterisering is de evaluatie van de niet-lineaire eigenschappen van de eiwitachtige materialen. Omdat het structureren met een thermomechanische methode per definitie verhitte omvat, wordt dit expliciet meegenomen en beschreven in **Hoofdstuk 4**. Door de reologie ook te bekijken bij grotere afschuivingen via 'large scale oscillatory flow' (LAOS) kan beter zicht worden gekregen op de veranderingen die optreden tijdens het structuurvorming proces, bij hoge temperaturen en simultane grotere vervorming. Lissajous-curven en de energie dissipatie verhouding die de plasticiteit van de materialen kenmerkt, zijn gebruikt om de resultaten samen te vatten. Dergelijke oscillerende afschuiving werd toegepast voor, tijdens en na verhitte, wat inzicht gaf in de reologische veranderingen tijdens structuurvorming. De verhitte induceert elasticiteit tijdens het structureren, maar de mate van dit effect hangt af van het type eiwit. PPI verloor zijn elastische eigenschappen sneller dan SPI, terwijl WG abrupte viskeuze dissipatie liet zien bij grote vervorming. Naast deze individuele eiwitten beschrijft **Hoofdstuk 5** het reologische gedrag van PPI-WG en SPI-WG mengsels. Alle uitkomsten werden samengevat met behulp

van textuurkaarten en kleurenschema's. In PPI-WG-mengsels was PPI zachter en minder elastisch in vergelijking met WG. In SPI-WG waren de eigenschappen vergelijkbaar.

In voorgaande hoofdstukken zijn PPI-WG en SPI-WG mengsels onderzocht op hun vermogen om vezelachtige structuren te vormen. Het is interessant om te onderzoeken of PPI met andere ingrediënten, zoals koolhydraten, ook vezelachtige structuren vormt. De structuurvormende eigenschappen van PPI, SPI en hun mengsels met pectine en/of cellulose werden onderzocht in **Hoofdstuk 6**. PPI/pectine en SPI/pectine leiden tot een vezelachtige structuur bij een massafractie verhouding van 93:7 en 95:5. Mengsels van SPI/pectine/cellulose vertoonden ook een vezelachtige structuur, die bovendien ook mechanische anisotropie gaven. Deze relatie werd niet waargenomen bij PPI-mengsels. Hier werden vezelachtige structuren gevonden die geen mechanische anisotropie gaven. De lineaire en niet-lineaire reologische eigenschappen van de mengsels werden bestudeerd om verder inzicht te krijgen in de structuurvorming. Geconcludeerd werd dat de elasticiteit van de eiwitfase een belangrijke factor is in het vermogen van de mengsels om vezelachtige producten te vormen.

In **Hoofdstuk 7** werden niet-lineaire reologische verschillen en overeenkomsten tussen verschillende vlees- en vleesvervangers (vooral kippenanalogen) voor en na verhitting gekwantificeerd. De vleesvervangers verschilden van verhit (bereid) vlees vooral wat betreft hun lagere elasticiteit. Waar verhitting van vlees de eigenschappen behoorlijk veranderde, veranderden de eigenschappen van vleesvervangers nauwelijks door verhitting. Toekomstige ontwikkelingen op het gebied van vleesvervangers kunnen daarom gericht zijn op het creëren van meer elasticiteit en mogelijk ook de verandering van de eigenschappen door verhitting simuleren.

De in de literatuur bekende textuurmethoden die worden gebruikt om de structuur van vlees en vleesvervangers te karakteriseren worden samengevat en vergeleken in **Hoofdstuk 8**. Het aantal beschikbare methoden voor vleesvervangers is kleiner dan het aantal voor vlees, maar na enige aanpassing is een scala aan methoden voor vlees ook geschikt om vleesvervangers te analyseren.

**Hoofdstuk 9** beschrijft de het gebruik van nabij-infraroodspectroscopie (NIRS) en hyperspectrale beeldvorming (HSI) om de samenstelling van mengsels op hun oliegehalte te kwantificeren. De methoden zijn niet-destructief en maken een snelle kwantificering van de

samenstelling mogelijk. NIRS gaf een goede voorspelling van de samenstelling in het mengsel en HSI visualiseerde de ruimtelijke verdeling van de olie in de mengsels.

**Hoofdstuk 10** vat de belangrijkste bevindingen samen, en reflecteert op de methoden en resultaten. De verkregen inzichten zijn in ontwerpregels voor structureringsprocessen voor vleesvervangers samengevoegd. De huidige ontwikkelingen op het gebied van nieuwe eiwitstructurering worden besproken en suggesties worden gegeven voor toekomstig onderzoek naar vleesvervangers.







A

# Appendices

*Acknowledgments - Dankwoord*

*About the author*

*Publications*

*Overview of completed training activities*

## *Acknowledgments*

With a big smile I am writing these acknowledgements, even earlier than planned, looking back at a period in which I thoroughly enjoyed my research. Conducting my PhD research was not a solo activity, but it is the result of collaboration with the many knowledgeable and nice people around me. I am very grateful for that. Hereby I want to thank everyone who contributed to my work and made its completion possible, starting with my two supervisors, Atze Jan van der Goot and Remko Boom.

Atze Jan van der Goot (promotor), you have given me the support to work as an independent researcher, you taught me to use my qualities and to challenge myself. I would like to thank you for the opportunities you have given me, your committed guidance, genuine interest and valuable advice. Together with Remko Boom, we formed a close team in which we complemented each other and shared research ideas, bringing the project to a higher level. Remko, I also want to thank you for your involvement, inspiring and motivating discussions with many insightful ideas. Thank you both for guiding me smoothly through the PhD process and these four years of continuous learning. I look back at our meetings and trips to Geneva with a big smile on my face.

Also thanks to Firmenich for being actively involved in this project. Igor, thank you for your critical questions and inspiring ideas. Igor and Philip, I value the insightful discussions that greatly contributed to the development of the project. I had the privilege to meet you and other colleagues from Firmenich several times in Geneva and had inspiring meetings. I greatly appreciated our collaboration.

All the collaborators in the Plant Promise Consortium, the past year and a half was very interesting for me. Thanks to everyone involved, especially Laurice and Walter, I learned a lot from all your questions and discussions about the project. I now have the opportunity to see this project from the industrial side, as an employee at Unilever, and see its great value in practice. I am looking forward to continue working together!

During my project, there are also a number of people at Wageningen University who have made their contribution. Leonard, thank you for your suggestions regarding the large amplitude analysis. Birgit thanks for your help in the beginning of my PhD. Jarno, Jos, Frank and Remco, thank you for your help with the analysis. Marjan and Ilona, thank you for the

administrative support. Martin, thanks for all the help with the financial administration and the car trip to Montreal.

To all the students I have worked with over the years, Femke, Paul, Miek, Maartje, Nicole, Caroline, Yihuan, Sophia, Aaron, Carine, Stijn and Rozemarijn: thank you all for your help. I learned a lot from each and every one of you and I am very grateful for your contribution to my work. Yu, Wanqing, Nynke, Birgit, Arianna, Jan, Steven, Anna, Miek, Konstantina, Yafei and Nienke, it was a pleasure sharing our passion for meat analogues. Thank you very much!

It was great to collaborate with many PhDs and postdocs. Many thanks for all the chats during the coffee break, tennis and squash (and other sports) activities, and trips towards conferences and courses. I had so much fun! I would like to specifically thank a number of colleagues for “alle gezelligheid” and a great time at FPE! Thank you, Yu, Lu, Sirinan, Qinhui and Emma for all the laughs, chit chats and relaxing moments in the office. I enjoyed the online coffee chats (Emma and Sten), organizing our (online) young scientist event (Miek and Silvia), the PhD trip (Zulhaj, Isabel, Emma, Maurice and Martin) and of course to be part of the “borrel” committee: Jan, Steven, Jan-Eise, Emma, Nynke, thanks for the great evenings!

A special thanks to Camee for helping me organize the celebration, Simone for the design of my thesis cover and Emma and Saskia for being my paranymphs. Daarnaast wil ik ook al mijn vrienden en familie bedanken! Bedankt voor het proosten op de mijlpalen, de lieve kaartjes, belletjes, etentjes, weekendjes weg, borrels, feestjes en vooral alle gezelligheid!!

Lieve papa, mama en Lotte, bedankt voor al jullie interesse in mijn onderzoek, de gezellige avondjes in Sittard en dat ik altijd op jullie kan rekenen! Tenslotte, Douwe bedankt voor alle liefde, steun, interesse en gezelligheid tijdens het laatste jaar van mijn PhD.



*About the author*

Floor Schreuders was born on 31<sup>st</sup> of July 1994 in Sittard, The Netherlands. She attended “Trevianum” in Sittard, where she obtained her VWO diploma in 2012, with a major in “Natuur en Gezondheid” (Nature and Health).



In 2012, Floor started with her study Food Technology at Wageningen University with in the third year a minor Supply Chain Management. In 2015, Floor started the master Food technology at Wageningen University, with a specialization in sustainable food process engineering. She completed her master thesis entitled “Processing concepts for the use of green leaves as raw materials for the food industry”. After finishing this thesis, Floor moved to Denmark for her internship at DuPont in Aarhus, where she studied the shelf life of ultra-high-temperature treated milk using principal component analysis. She graduated her master in 2017.

After completing her internship, she continued working as a PhD candidate at the Laboratory of the Food Process Engineering group of Wageningen University & Research on the project “Structuring pea towards meat analogues” and the results of this work are described in this thesis. Floor will continue to work as an assistant manager plant meat structuring at Unilever.

## *Publications*

### *This thesis*

**Schreuders, F. K. G.,** Dekkers, B. L., Bodnár, I., Erni, P., Boom, R. M., & van der Goot, A. J. (2019). Comparing structuring potential of pea and soy protein with gluten for meat analogue preparation. *Journal of Food Engineering*, 261, 32-39. <https://doi.org/10.1016/j.jfoodeng.2019.04.022>

**Schreuders, F. K. G.,** Bodnár, I., Erni, P., Boom, R. M., & van der Goot, A. J. (2020). Water redistribution determined by time domain NMR explains rheological properties of dense fibrous protein blends at high temperature. *Food Hydrocolloids*, 101, 105562. <https://doi.org/10.1016/j.foodhyd.2019.105562>

**Schreuders, F. K. G.,** Sagis, L. M. C., Bodnár, I., Erni, P., Boom, R. M., & van der Goot, A. J. (2021). Small and large oscillatory shear properties of concentrated proteins. *Food Hydrocolloids*, 110, 106172. <https://doi.org/10.1016/j.foodhyd.2020.106172>

**Schreuders, F. K. G.,** Sagis, L. M. C., Bodnár, I., Erni, P., Boom, R. M., & van der Goot, A. J. (2021). Mapping the texture of plant protein blends for meat analogues. *Food Hydrocolloids*, 118, 106753. <https://doi.org/10.1016/j.foodhyd.2021.106753>

**Schreuders, F. K. G.,** Schlangen, M., Kyriakopoulou, K., Boom, R. M., & van der Goot, A. J. (2021). Texture methods for evaluating meat and meat analogue structures: A review. *Food Control*, 108103. <https://doi.org/10.1016/j.foodcont.2021.108103>

**Schreuders, F. K. G.,** Schlangen M., Bodnár, I., Erni, P., Boom, R. M., & van der Goot, A. J., Structure formation and non-linear rheology of blends of plant proteins with pectin and cellulose, *submitted*.

**Schreuders, F. K. G.,** Sagis, L. M. C., Bodnár, I., Boom, R. M., & van der Goot, A. J., Non-linear rheology reveals the importance of elasticity in meat and meat analogues, *submitted*.



*Other publications*

Tenorio, A. T., **Schreuders, F. K. G.**, Zisopoulos, F. K., Boom, R. M., & van der Goot, A. J. (2017). Processing concepts for the use of green leaves as raw materials for the food industry. *Journal of cleaner production*, 164, 736-748. <https://doi.org/10.1016/j.jclepro.2017.06.248>

Cornet, S. H., Snel, S. J., **Schreuders, F. K.G.**, van der Sman, R. G., Beyrer, M., & van der Goot, A. J. (2020). Thermo-mechanical processing of plant proteins using shear cell and high-moisture extrusion cooking. *Critical Reviews in Food Science and Nutrition*, 1-18. <https://doi.org/10.1080/10408398.2020.1864618>



## *Overview of completed training activities*

### *Discipline specific activities*

#### *Courses*

Food Extrusion Technology ((HES-SO Valais Wallis school of Engineering, CH)	2018
WUR Rheology course (WUR, NL)	2018
Food proteins: functionality, modifications and analysis (VLAG, NL)	2018
European School on Rheology (KU, BE)	2019
Han-Sur-Lesse physical chemical winterschool (WUR & TU delft, NL)	2019
Multivariate analysis of spectroscopic data (Camo Analytics, NO)	2020

#### *Conferences*

Latest Technology for Producing Meat Analogues (HES-SO Valais Wallis school of Engineering, CH)	2018, 2021
Science and Technology for Meat Analogues (WUR, NL)	2018, 2021
International Symposium on Food Rheology and Structure (ETH-Zürich, CH)	2019
Webinar: Rheology and Food structuring & deconstructing (INRAE, FR)	2021
Webinar: Closed Cavity rheometer: A Novel Approach to the Design of Plant-Based Texturized Foods (TA instruments, USA)	2021
Food Structure and Functionality Symposium (Cork, IE)	2021

#### *General courses*

VLAG PhD week (VLAG, NL)	2018
Competence Assessment (WGS, NL)	2018
Research data management (WGS, NL)	2018
Teaching and supervising thesis students (ESD, NL)	2018
Brain training (WGS, NL)	2018
Introduction to MATLAB for Multivariate Data Analysis (UCPH, DK)	2019
Adobe InDesign (WGS, NL)	2020
Introduction to LaTeX (WGS, NL)	2020
Career Perspectives (WGS, NL)	2020

#### *Other activities*

Preparation of research proposal	2017
PhD study tour to Canada	2018
FPE weekly group meetings	2017-2021
Biweekly journal club on Food Structuring	2019-2021
PlantPromise monthly meetings	2019-2021
VLAG PhD council	2018-2020
Famelab	2019
Organizing committee of first Food science symposium	2020
Organizing committee of the Young Scientist Event during the Science and Technology for Meat Analogues conference	2021

The studies presented in this thesis were financially supported by Firmenich (Chapter 2-4) and within the framework of PlantPROMISE (Chapter 1, 5-10), which is co-financed by Top Consortium for Knowledge and Innovation Agri& Food by the Dutch Ministry of Economic Affairs. The project is registered under contract number TKI-AF- LWV-19027.

*Cover design by* Simone Wenting

*Printed by* ProefschriftMaken || [www.proefschriftmaken.nl](http://www.proefschriftmaken.nl)

